W&M ScholarWorks

Dissertations, Theses, and Masters Projects   Theses, Dissertations, & Master Projects

2003

Chemical bonding in hard and elastic amorphous carbon-nitride films

W. Jason Gammon

College of William & Mary - Arts & Sciences

Follow this and additional works at: https://scholarworks.wm.edu/etd

Part of the Condensed Matter Physics Commons, and the Materials Science and Engineering Commons

Chemical Bonding in Hard and Elastic Amorphous Carbon-Nitride Films

A Dissertation

Presented to

The Faculty of the Department of Physics

The College of William and Mary in Virginia

In Partial Fulfillment

Of the Requirements for the Degree of

Doctor of Philosophy

by

W. Jason Gammon

2003

APPROVAL SHEET

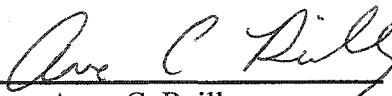This dissertation is submitted in partial fulfillment of

the requirements for the degree of

Doctor of Philosophy

_____
W. Jason Gammon

Approved, May 2003

_____
Anne C. Reilly

_____
Brian C. Holloway

_____
Gina L. Hoatson

_____
William J. Kossler

_____
Robert L. Vold
Applied Science Department

ii

To Mom and Haley.

Table of Contents

v

viii

Acknowledgements

ix

List of Tables

x

List of Figures

xiv

Abstract

In this study, the chemical bonding in hard and elastic amorphous carbon nitride (a-CN$_x$) films is investigated with x-ray photoelectron spectroscopy (XPS) and ^{15}N, ^{13}C, and ^{1}H nuclear magnetic resonance (NMR) spectroscopy. The films were deposited by DC Magnetron sputtering in a pure nitrogen discharge on Si(001) substrates at 300-400 °C. Nanoindentation measurements reveal an elastic modulus of ~50 GPa and a hardness of ~5 GPa, thus confirming our films are highly elastic but resist plastic deformation

Our ^{13}C NMR study demonstrates the absence of sp^3 bonded carbon in this material. Collectively, our N(1s) XPS, ^{13}C NMR, and ^{15}N NMR data suggest a film-bonding model that has an aromatic carbon structure with sp^2-hybridized nitrogen incorporated in heterocyclic rings. We demonstrate that the nitrogen bonding is predominantly in configurations similar to those in pyridine and pyrrole. In addition, the data indicate that the a-CN$_x$ films prepared for this study have low hydrogen content, but are hydrophilic. Specifically, results from ^{15}N and ^{13}C cross polarization (CP) and ^{1}H magic angle spinning (MAS) NMR experiments suggest that nitrogen sites are susceptible to protonation from water absorbed during sample preparation for the NMR experiments. The sensitivity of the surface of a-CN$_x$ to water absorption may impact tribological applications for this material.

In accord with our XPS and NMR spectroscopic studies on a-CN$_x$ films, we propose a film-structure model consisting of buckled graphitic planes that are cross-linked together by sp^2 hybridized carbons. The curvature and cross-linking is attributed to a type of compound defect, which is formed by placing a pentagon next to single-atom vacancy in a graphite layer. Our proposed film structure is called the pentagon-with-vacancy-defect (5VD) model. Using Hartree-Fock calculations, we show that the 5VD, film-structure model is compatible with our XPS, NMR, and nanoindentation measurements and with previous transmission electron microscopy (TEM) and computational work.

Chemical Bonding in Hard and Elastic Amorphous Carbon-Nitride Films

Chapter 1—Introduction

The focus of this research is the study of chemical bonding in amorphous carbon nitride (a-CN$_x$) films that are hard and elastic. A material described as both hard and elastic is unusual. Typically, hard materials are brittle and resist deformation, while elastic materials are soft and plastically deform. Amorphous carbon nitride films are highly elastic and thus deform under load, but resist permanent deformation and therefore recover their original shape when the load is released. Since a-CN$_x$ films absorb impact but also recover, these films should serve well as protective overcoats. However, widespread application of a-CN$_x$ is hindered by the poor understanding of the nature of both its carbon and nitrogen bonding. The objective of this dissertation is to provide a reasonable picture of chemical bonding in a-CN$_x$.

In this study, DC magnetron sputtering was used to fabricate all a-CN$_x$ films. Nanoindentation tests confirm that our films can be described as both hard and highly elastic. The chemical bonding was examined with x-ray photoelectron spectroscopy (XPS) and nuclear magnetic resonance (NMR) spectroscopy. Based on our XPS and NMR data, we propose a film-structure model for a-CN$_x$. In addition, we have used total-energy, Hartree-Fock calculations to demonstrate the plausibility of this model.

2

1.1 Motivation

The interest in carbon nitrides has grown rapidly over the past decade. In 1993, there were less than 25 publications on carbon nitride; at present, this number has grown to more than 1025 publications. The catalyst to this rapid growth was the theoretical work, in 1989, by Liu and Cohen;[1] their calculations predicted that the hypothetical, crystalline compound β-C_3N_4 would be metastable, with a bulk modulus comparable to diamond. The predicted low compressibility of β-C_3N_4 suggests that its hardness may exceed that of diamond.[1,2] Consequently, research on carbon nitride synthesis escalated.

The first attempts to fabricate β-C_3N_4 used high temperature and pressure techniques, [3-5] a logical first choice, since these methods are used to synthesize diamond. However, these initial attempts were unsuccessful. Next, researchers attempted to fabricate β-C_3N_4 using vacuum-based methods for film deposition. Initial results appeared promising; there were several reports of amorphous carbon nitride films with sub-micron sized crystallites embedded in the film's matrix.[6-8] Electron diffraction patterns of these crystallites seemed to be in accord with β-C_3N_4. The plausibility of successful synthesis of β-C_3N_4 is questionable, since film-deposition techniques typically yield carbon nitride films with less than 30 at.% nitrogen concentration,[7] considerably lower than required for the C_3N_4 stoichiometry. Accordingly, researchers argued that the crystallites were embedded in a film-matrix that is nitrogen deficient. Whether or not these embedded crystallites can be attributed to β-C_3N_4 is debatable. Matsumoto et al.[9] and Wang et al.[10] have compared calculated x-ray powder diffraction patterns of various C_3N_4 phases with experimental patterns. Both groups concur that the evidence for

successful synthesis of crystalline C_3N_4 is inconclusive. The important point is that, so far, large-scale synthesis of β-C_3N_4 is unachieved—for example, the presumed C_3N_4 *crystallites* observed in the films by Yu *et al.*[6] take up less than 5% of the film's volume. The pursuit of practical methods to synthesize β-C_3N_4 is an ongoing effort; however, this effort is beyond the scope of this dissertation.

Although attempts to fabricate β-C_3N_4 were unsuccessful, researchers did discover that thin-film techniques yielded a new amorphous carbon-nitride material with a valuable combination of tribological and mechanical properties.[11-15] When deposited under suitable conditions, a-CN_x films can be fabricated with low elastic modulus and high resistance to plastic deformation.[15,16] The material readily deforms under applied load, and when the load is released, the film recovers its original shape. Thus, a-CN_x can be regarded as both an elastic and hard material. This combination of mechanical properties is unusual. Ordinarily, hard materials such as ceramics have high modulus and are brittle, while soft materials such as metals have low modulus and deform plastically. Protective thin-film overcoats with properties similar to a-CN_x are desirable, since the overcoat would absorb impact and afterwards regain its original shape.

Coatings that provide protection from wear are essential, since surface modification by a protective layer provides greater flexibility in the choice of underlying material. Carbon-based films are already found in a variety of thin-film, coating applications. For example, diamond-like carbon (DLC) is used as a protective layer on aerospace window materials to inhibit degradation from particle impact,[17] as a scratch-resistant coating on sunglasses and other optical components,[18] and as a coating on load-

bearing surfaces to decrease wear.[19]   The importance of carbon-based films is well established and provides motivation to investigate other carbon systems, like a-CN$_x$.

Currently, DLC is the industry-standard, wear-resistant layer on magnetic storage media. The carbon layer serves to protect the magnetic medium from impacts due to read-head-to-disk contact. Amorphous, carbon-nitride films are promising candidates to replace DLC wear-layers on magnetic media, since a-CN$_x$ overcoats exhibit a smaller coefficient of friction, lower wear rates, and a lower RMS surface roughness.[11] The better tribological properties of a-CN$_x$ suggest that DLC overcoats can be replaced with a thinner layer of carbon nitride, thus allowing the read-head to be brought closer to the magnetic layer. A shorter spacing between head and disk would allow for an increase in storage density. However as this distance decreases, head-to-disk contact becomes more frequent. Consequently, one expects increased wear, which leads to earlier failure. This example emphasizes the importance of lower wear rates exhibited by a-CN$_x$ films.

Widespread use of a-CN$_x$ films is hindered by the lack of fundamental understanding of its carbon and nitrogen bonding configurations. Careful control of mechanical or tribological properties requires understanding the relationship between these properties and local bonding arrangements. In response to this issue, Sjöström and co-workers have collectively studied the relationship among chemical bonding, film structure, and mechanical properties. Based on XPS, transmission electron microscopy (TEM), and nanoindentation data, Sjöström *et al.* proposed a reasonable film structure for a-CN$_x$, which is consistent with their experimental data.[13] In the next section, a detailed description of their film-structure model is provided.

1.2 Film-Structure Model for Carbon Nitride

In the literature, a film-structure model has been forwarded for a-CN$_x$ films that are deposited by magnetron sputtering.[13] This phenomenological model is consistent with a variety of experimental[13] and computational[13,20] results. In this section, an overview of these important results is provided.

Nitrogen incorporation in amorphous carbon films, thus forming a-CN$_x$, leads to an exceptional improvement in their mechanical properties.[15] Without nitrogen, amorphous sp^2-bonded carbon films have mechanical properties similar to graphite: low elastic modulus, low hardness, and poor recovery. Amorphous carbon nitride also has a low elastic modulus, but it exhibits high hardness and high recovery.[14-16] The nitrogen bonding yields a material that resists plastic deformation. In addition, the mechanical properties of a-CN$_x$ are notably influenced by film fabrication parameters.[14,15] Hellgren et al.[14] noticed that the microstructure (as viewed by TEM) and mechanical properties of a-CN$_x$ films (as measured by nanoindentation) were correlated with substrate temperature, T_s. When T_s is less than 200 $^{\circ}$C, a-CN_x films exhibit lower elastic recovery and an amorphous structure.[14] Films deposited at T_s exceeding 200 $^{\circ}$C were also amorphous but showed increased order; TEM micrographs revealed a structure consisting of segmented graphitic planes with a preferred c-axis that is perpendicular to the film's growth direction. Hellgren et al. also observed that the curvature of the graphitic segments depended on the film's nitrogen content. At low nitrogen concentration (<5%), these segments are flat and planar. However, at higher nitrogen concentration, the graphitic segments became increasingly curved. They concluded that nitrogen incorporation induces buckling, which allows adjacent segments to intersect and form

cross-links.[14] Films with a microstructure of buckled layers were dubbed *fullerene-like*. In accord with nanoindentation results, the cross-linking was deemed responsible for the improved hardness of a-CN$_x$.

Sjöström *et al.* proposed that pentagon incorporation in the graphitic layers could account for the buckled microstructure.[13] This is a reasonable conjecture, since pentagons are responsible for the curvature in fullerenes. This idea was further supported by their semi-empirical, total-energy calculations; they found that the formation energy of a pentagon in a planar carbon cluster is substantially lowered by placing a nitrogen at a pentagon vertex.[13] Their results indicated that the formation of pentagons is more likely in a-CN$_x$ films than in amorphous carbon films. The buckling results in the intersection of adjacent layers, which cross-link at their point of intersection. Using insights provided from a variety of experimental and computational results, Sjöström *et al.* assumed that the cross-links were due to sp^3 carbons.[13] Carbons with sp^3 hybridization have a tetrahedral bonding configuration (diamond-like), which is responsible for the high hardness observed in DLC films. In addition, the high hardness predicted for β-C$_3$N$_4$ is associated with its tetrahedral bonding arrangement.[1,2] Therefore, Sjöström *et al.* proposed that sp^3 carbons were responsible for the hardness in a-CN$_x$ films.[13] Interestingly, the fullerene-like microstructure of their films also suggests the possibility of forming sp^3 cross-links. In particular, consider the azafullerene C$_{59}$N; the monomer is unstable, and it is stabilized by forming a dimer. The intermolecular bond between two C$_{59}$N is formed by an sp^3 carbon cross-link.[21,22] Furthermore, the assumption of sp^3-bonded carbon in a-CN$_x$ is supported by XPS chemical-shift calculations. Computational work indicated that the low-binding-energy component observed in the N(1s) XPS spectra of a-CN$_x$ was

consistent with the chemical shift of sp^3 nitrogen bonded to sp^3 carbons.[20] From this observation, the presence of sp^3 carbons was indirectly inferred. It is noted that direct measurement of the XPS C(1s) spectrum can not be used to determine the relative fraction of sp^3 bonded carbon, since the XPS chemical shifts among the variety of carbon-bonded-only-to-carbon configurations in $a\text{-CN}_x$ are too small to resolve. Collectively their XPS, nanoindentation, and TEM results suggested a film-structure model with buckled graphitic layers due to pentagon formation and with cross-linking between layers by sp^3 carbons.

The above film-structure model is reasonable and consistent with a variety of experimental and computational data. However, this model has not been conclusively proved or disproved. A central theme of this dissertation is to further examine the plausibility of their model, identify its shortcomings, and improve it. Regardless, the model proposed by Sjöström *et al.* highlights an important issue in $a\text{-CN}_x$ research: the identification of the structures responsible for bending and cross-linking adjacent graphitic planes. Prior to work reported here, the hybridization of carbon and nitrogen associated with these structures was unknown.

1.3 Scope of This Dissertation

The scope of this dissertation is to elucidate the predominant nitrogen and carbon bonding configurations in hard and elastic $a\text{-CN}_x$ films. In Chapter 2, a short overview of carbon and nitrogen bonding arrangements is given. Chapter 3 describes the film-fabrication process and deposition conditions for our $a\text{-CN}_x$ films. Chapters 4 and 5 provide an overview of the theory and practical aspects of the experimental techniques—

nanoindentation, XPS, and NMR—that were used to characterize our films. Chapter 6 provides a description of the Hartree-Fock method, which was used to investigate the plausibility of our proposed film-structure model for a-CN$_x$.

The core of this dissertation is embodied by Chapters 7-10. In Chapter 7, the nanoindentation testing results demonstrate that our a-CN$_x$ films are both hard and elastic. The nanoindentation measurements ensure that the a-CN$_x$ characterized in this dissertation has the mechanical properties of interest. In Chapter 8, our XPS study demonstrates the difficulty of making conclusive bonding assignments. In particular, we show that the N(1s) XPS spectra of a-CN$_x$ do not conclusively support a film-structure model with nitrogen bonded to sp^3 (diamond-like) carbons. Our XPS data shows that the presence of sp^3 carbons in a-CN$_x$ is inconclusive and unconfirmed. The inability of XPS to resolve this issue provides impetus for our NMR study.

In Chapter 9, we present the results from a multinuclear solid-state NMR study. The ^{13}C NMR study conclusively demonstrates the absence of sp^3 carbons in hard and elastic a-CN$_x$ films. Together, the ^{13}C and ^{15}N NMR data imply an sp^2 carbon structure with sp^2-hybridized nitrogen incorporated in heterocyclic rings. In addition, results from ^{15}N and ^{13}C cross polarization and ^{1}H magic angle spinning NMR experiments demonstrate that our a-CN$_x$ films have low hydrogen content, but may be hydrophilic. Importantly, the NMR data demonstrate that the film-structure model proposed by Sjöström and co-workers (see Section 1.2) is incompatible with hard and elastic a-CN$_x$. In Chapter 10, we use total-energy, Hartree-Fock calculations to explore the plausibility of a new film-structure model. Our proposed film structure, called the pentagon-with-vacancy-defect (5VD) model, is supported by our theoretical calculations. More

importantly, the proposed film structure is compatible with both XPS and NMR data.

Finally, Chapter 11 summarizes the experimental and computational results and

highlights directions of future work.

1.4 References

1   A. Y. Liu and M. L. Cohen, Science **245**, 84 (1989).

2   A. Y. Liu and M. L. Cohen, Phys. Rev. B **41**, 10727 (1990).

3   A. Badzian and T. Badzian, Diamond Relat. Mater. **5**, 105 (1996).

4   J. H. Nguyen and R. Jeanloz, Mater. Sci. Eng. A **209**, 23 (1996).

5   E. G. Wang, Prog. Mater. Sci. **41**, 241 (1997).

6   K. M. Yu, M. L. Cohen, E. E. Haller, W. L. Hansen, A. Y. Lui, and I. C. Wu, Phys. Rev. B **49**, 5034 (1994).

7   S. Muhl and J. M. Mendez, Diamond and Relat. Mater. **8**, 1809, (1999).

8   C. Niu, Y. Z. Lu, and C. M. Lieber, Science **261**, 334 (1993).

9   S. Matsumoto, E. Q. Xie, and F. Izumi, Diamond Relat. Mater. **8**, 1175 (1999).

10   J. Wang, J. Lei, and R. Wang, Phys. Rev. B **58**, 11890 (1998).

11   E. C. Cutiongco, L. Dong, C. Yip-Wah, and C. S. Bhatia, Transactions of the Asme. Journal of Tribology **118**, 543 (1996).

12   H. Sjostrom, L. Hultman, J. E. Sundgren, S. V. Hainsworth, T. F. Page, and G. Theunissen, J. Vac. Sci. Technol. A **14**, 56 (1996).

13   H. Sjostrom, S. Stafstrom, M. Boman, and J. E. Sundgren, Phys. Rev. Lett. **75**, 1336 (1995).

14   N. Hellgren, M. P. Johansson, E. Broitman, L. Hultman, and J. E. Sundgren, Phys. Rev. B **59**, 5162 (1999).

15   B. C. Holloway, O. Kraft, D. K. Shuh, W. D. Nix, M. Kelly, P. Pianetta, and S. Hagstrom, J. Vac. Sci. Technol. A **18**, 2964 (2000).

16   L. Hultman, S. Stafstrom, Z. Czigany, J. Neidhardt, N. Hellgren, I. F. Brunell, K. Suenaga, and C. Colliex, Phys. Rev. Lett. **87**, 225503/1 (2001).

17   E. J. Coad, C. S. J. Pickles, G. H. Jilbert, and J. E. Field, Diamond Relat. Mater. **5**, 640 (1996).

18   M. Ohring, *The Materials Science of Thin Films* (Academic Press, 1992).

19   Z. M. Zeng, T. Zhang, X. B. Tian, B. Y. Tang, T. K. Kwok, and P. K. Chu, Surf. Coat. Technol. **128**, 236.

20   A. Johansson and S. Stafstrom, J. Chem. Phys. **111**, 3203 (1999).

21   T. Pichler, M. Knupfer, M. S. Golden, S. Haffner, R. Friedlein, J. Fink, W. Andreoni, A. Curioni, K. M. Keshavarz, C. Bellavia-Lund, A. Sastre, J. C. Hummelen, and F. Wudl, Phys. Rev. Lett. **78**, 4249 (1997).

22   H. Kuzmany, W. Plank, J. Winter, O. Dubay, N. Tagmatarchis, and K. Prassides, Phys. Rev. B **60**, 1005 (1999).

Chapter 2—Overview of Carbon and Nitrogen Bonding

Throughout this dissertation, the chemical bonding configurations of carbon and nitrogen are referred to by their *hybridization*. Since these concepts will be used extensively, this chapter provides a review of carbon and nitrogen bonding.

2.1 The Concept of Hybridization

The concept of hybridization provides an intuitive way of visualizing the valence electronic charge density and predicting the geometry of a molecule. An approximate picture of the charge density can be constructed by using hybrid orbitals to describe chemical bonds. A hybrid orbital is formed by taking a linear combination of atomic orbitals that are centered on the same atomic site. Thus, the hybrid orbital is localized at the atomic site that it was formed. The overlap of a pair of hybrid orbitals on adjacent atomic sites can be used to represent a chemical bond. The overlap allows a pair of atoms to form a covalent bond by sharing a pair of electrons—one electron from each atom. This description of bonding assumes the electron pair is localized in space between the bonded atoms; i.e., a covalent bond. Bond formation corresponds to a pileup of charge density between the two atomic cores. Therefore, the hybrid orbital needs to be constructed so that the square of the orbital correctly mimics the charge density between bonded atoms. It is emphasized that a hybrid orbital does not necessarily represent the

11

true molecular orbital. Hybrid orbitals are convenient tools, which aid in visualization of both the charge density and molecular geometry. The geometry and charge density are interrelated, since the charge density has the same symmetry as the molecule. Further details on the above concepts can be found in a variety of entry-level chemistry texts.[1]

In the case of carbon and nitrogen, there are three basic hybridization types to consider: sp, sp^2, and sp^3, and each corresponds to a particular bonding geometry. These ideas are best illustrated by example, and in Section 2.2, carbon bonding is examined in detail. Following that (Section 2.3), a brief summary of nitrogen bonding is provided.

2.2 Carbon Bonding

sp^3 Hybridization: Methane

As a first illustrative example, consider methane (Table 2.1). The carbon atom in methane, CH_4, is bonded to four hydrogens, which are positioned on the vertices of a tetrahedron. The atomic configuration of C is given by $1s^2 2s^2 2p^2$. The four valence electrons in the outer shell ($2s^2 2p^2$) are bonding electrons. A very simple model based on appropriate mixing (hybridization) of the carbon 2s and 2p orbitals can account for the tetrahedral bonding arrangement. By forming linear combinations of the 2s, $2p_x$, $2p_y$, and $2p_z$ orbitals, four orthogonal sp^3 orbitals can be constructed.[2] These hybrid orbitals have identical shape but different directional properties. Each of the sp^3 orbitals is oriented toward a different vertex of a tetrahedron. A C-H bond is described by the overlap of a hydrogen 1s orbital with one of the sp^3 hybrids belonging to the carbon, thus forming four C-H bonds. All the bonds are axially symmetric around the bond axis and are referred to

Table 2.1: Examples of carbon hybridization.

Name	Hybridization	Bond Geometry	Schematic
methane	sp^3	tetrahedral	
ethylene	sp^2	trigonal planar	
acetylene	sp	linear	$HC\equiv CH$
benzene	sp^2	trigonal planar	

as σ (sigma) bonds. Taken together, these bonding orbitals correctly describe the tetrahedral symmetry of methane.

sp² Hybridization: Ethylene and Benzene

Ethylene (C_2H_2) is planar molecule with bond angles of ~120° (Table 2.1). This bonding arrangement can be described using sp^2-hybridized orbitals. Assuming the plane of the molecule is in the *xy*-plane, the 2s, $2p_x$, and $2p_y$ orbitals can be mixed to form three equivalent sp^2 orbitals.[2] The three hybrid orbitals are orthogonal, lie in the *xy*-plane, and are oriented at 120° angles from each other. The fourth orbital is accounted for by the

remaining $2p_z$. Each carbon participates in four bonds. A C-H bond is described by the overlap of a carbon sp^2 orbital with a hydrogen 1s orbital. Each carbon has two C-H bonds, and thus two of the sp^2 orbitals are accounted for. The remaining sp^2 orbital overlaps with the corresponding sp^2 orbital on the neighboring carbon. The three bonds described so far are σ bonds. The remaining fourth bond is described by the overlap of the $2p_z$ orbitals that are centered on the adjacent carbon sites. Since the $2p_z$ orbitals are directed out of molecular plane, the overlap is *side to side*; this sort of bond is called a π (pi) bond.

Benzene (C_6H_6) provides another example of sp^2 hybridized carbons. The chemical structure of benzene, as depicted in Table 2.1, is somewhat misleading, since all six C-C bonds are equivalent. The π bonding in benzene is different from that of ethylene—the π electrons in ethylene are localized between the two carbons. However, in benzene, the π bonds are actually delocalized over the entire circumference of the carbon ring and not in the alternating fashion, as suggested by its schematic. The delocalization of the π electrons in benzene further stabilizes the molecule;[3] cyclic hydrocarbons that are stabilized by this type of bonding are referred to as aromatic.

sp Hybridization: Acetylene

Acetylene (C_2H_2) is a linear molecule (Table 2.1); both carbons are sp hybridized. Orienting the axis of the molecule along the z-direction, the 2s orbital can be mixed with the $2p_z$ orbital to form two sp orbitals. These two sp orbitals are equivalent, orthogonal, and directed 180° from each other.[2] The remaining two orbitals are the unmixed $2p_x$ and $2p_y$. Each carbon atom forms two σ bonds; one is described by the overlap of an sp orbital

with an adjacent hydrogen 1s orbital, and the other by the overlap of sp orbitals on each carbon site. The σ bonds account for two out of the four carbon bonds. The remaining two bonds are π bonds. One is formed from the overlap of the two $2p_x$ orbitals on adjacent carbon sites, and the other from the overlap of the two $2p_y$ orbitals.

Summary of Carbon Bonding

In summary, carbon forms four bonds, and its bonding configuration is described by sp, sp^2, or sp^3 hybridization. Each hybridization corresponds to a particular electron density and bonding geometry. Carbons with sp^3 hybridization have a tetrahedral bonding geometry, and all four bonds are described by σ bonds. Carbons bonded in a trigonal planar arrangement are described by sp^2 hybridization. Each carbon has three σ and one π bond. Finally, the linear bonding arrangement of the carbons in acetylene (Table 2.1) is characteristic of sp hybridization. Each carbon in acetylene has two σ and two π bonds.

2.3 Nitrogen Bonding

The bonding picture that was described for carbon relies on the fact that carbon has an even number of valence electrons; carbon has four valence electrons and forms four bonds. Each bond can be described by a pair of electrons shared between bonded atoms. This is another way of saying that carbon is bonded so that the octet rule is satisfied. This empirical rule states that an atom will form bonds until it has eight valence electrons around it.[1] Typically, nitrogen also bonds in a way so that the octet rule is obeyed. In contrast to carbon, nitrogen has an odd number of valence electrons. The

atomic configuration of N is $(1s^2 2s^2 2p^3)$; thus, it has five valence electrons $(2s^2 2p^3)$.

Fortunately, nitrogen-bonding configurations are similar to those of carbon, and the concepts used to describe carbon bonding are readily extended to this case. To extend these concepts to nitrogen, one must take into account the extra valence electron and keep in mind the octet rule. We will not consider nitrogen configurations that are deviations from the octet rule (e.g., the N bonding in the NO molecule).

Examples of various nitrogen hybridizations are shown in Table 2.2. The nitrogen in ammonia (NH_3) is sp^3 hybridized; the carbon analog to this situation is methane (Table 2.1). This nitrogen is σ-bonded to three hydrogens and has a lone pair in a nonbonding orbital. Three of the sp^3 orbitals are used to describe the N-H bonds, and the fourth sp^3 orbital is *occupied* by the lone pair. The octet rule is evidently satisfied by the three pair of electrons corresponding to the N-H bonds and the lone pair. The ammonia molecule has a distorted tetrahedral geometry with a bond angle between the N-H bonds of $107°$, which is slightly less than a tetrahedral bond angle of $109°$. The geometry distortion is due to the lone pair, which is in a nonbonding orbital and therefore pulled closer to the nitrogen core. Since the lone pair takes up more space around the core, the N-H bond angles distort and contract from the ideal tetrahedral configuration.

Both pyridine and pyrrole are planar molecules (Table 2.2), and their nitrogens are described by sp^2 hybridization. In the case of pyridine (C_5H_5N), two of the nitrogen's sp^2 orbitals are used to form two σ bonds to carbons, and the remaining sp^2 orbital describes the lone pair. Pyridine is aromatic and has six π electrons. Each carbon contributes one π electron, as does the nitrogen. In pyrrole (C_4H_5N), all three of the nitrogen's sp^2 orbitals

Table 2.2: Examples of nitrogen hybridization

Name	Hybridization	Schematic
ammonia	sp^3	
pyridine	sp^2	
pyrrole	sp^2	
hydrogen cyanide	sp	$HC\equiv N:$

are used to describe bonding electrons. The sp^2 orbitals account for the two N-C σ-bonds and the N-H σ-bond. Unlike pyridine, the pyrrole nitrogen does not have a lone pair of electrons in a nonbonding orbital. Pyrrole is aromatic, and its nitrogen contributes two electrons to the π system.

Lastly, hydrogen cyanide (HCN) is a linear molecule, and its nitrogen is sp hybridized. One sp orbital describes the N-C σ-bond and the other sp orbital accounts for the lone pair. The nitrogen also forms two π bonds with the carbon. The bonding in HCN (Table 2.2) is analogous to that of acetylene (Table 2.1).

2.4 References

1   S. S. Zumdahl, *Chemistry* (Heath, Lexington, MA, 1986).

2   D. A. McQuarrie, *Quantum Chemistry* (University Science, Mill Valley, CA, 1983).

3   F. A. Cotton, *Chemical Applications of Group Theory*, 2 ed. (Wiley, New York, 1990).

Chapter 3—Film Fabrication

In the many publications devoted to amorphous carbon nitride films, DC magnetron sputtering is the prevailing technique for film fabrication. Amorphous carbon nitride (a-CN_x) films produced by this method have been examined parametrically for a variety of process conditions [1,2] (e.g., ion flux and substrate temperature). Since DC magnetron sputtering is the best-parameterized technique for fabricating a-CN_x films, this method was used in this research. Additionally, DC magnetron sputtering has the advantage of high deposition rate, which was required to fabricate the large amount of material for the nuclear magnetic resonance measurements (Chapter 9).

In this chapter, the method of DC magnetron sputtering is described, along with a summary of experimental procedures and conditions. Justification of these growth conditions is given by nanoindentation tests (Chapter 7), which demonstrate that these conditions yield a-CN_x films that are hard and elastic.

3.1 DC Magnetron Sputtering

Sputtering is a vacuum-based, film-deposition technique that uses ionized species from a plasma to bombard a target. The energetic ions release or sputter away material from the target. The sputtered material is dispersed into the gas phase and is transported to a substrate, where it condenses to form a film.

19
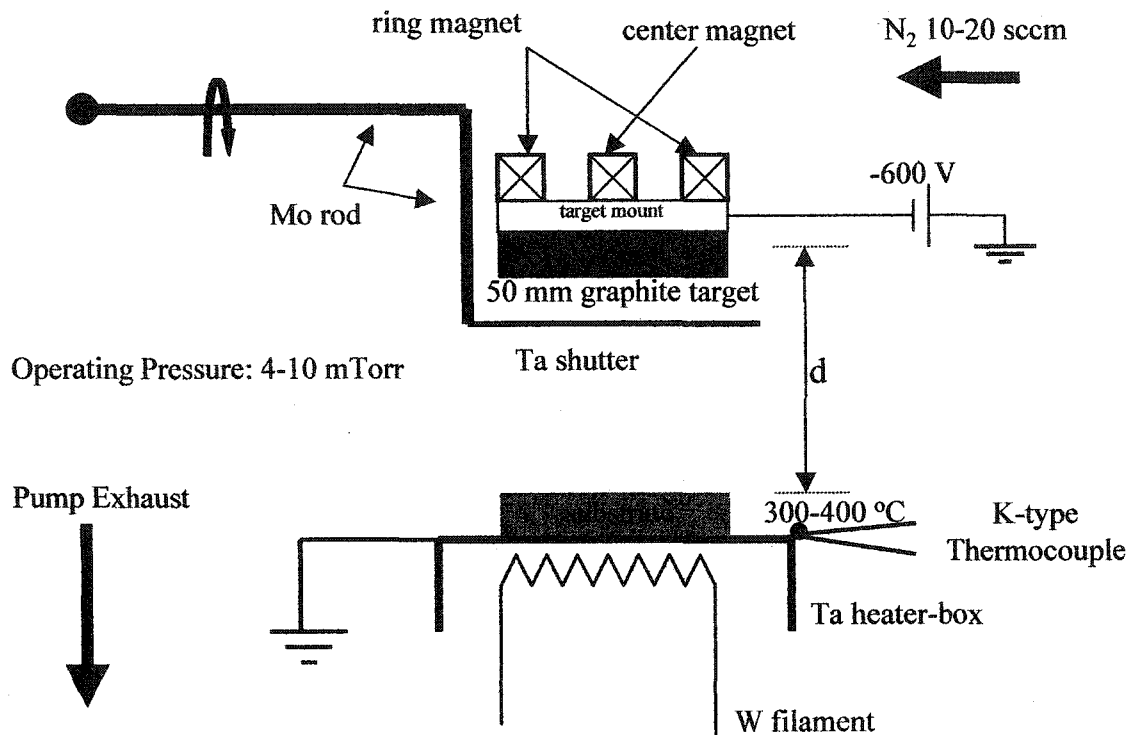
Figure 3.1: A schematic of the DC magnetron sputtering system that was used to fabricate all films.

In the DC magnetron sputtering process, the plasma is sustained by a steady-state electric field assisted by a magnetic field. A schematic of our DC magnetron sputtering system is shown in Figure 3.1. In this arrangement, the target serves as the cathode and the vacuum chamber as the anode. The target is biased with a negative DC potential, and a feedstock gas is admitted into the system. Secondary electrons are emitted from the cathode, and subsequently impact and ionize neutral gas species. This process creates and sustains the plasma. Positioned behind the cathode are two magnets: a center magnet and a ring magnet—the flux of the magnetic field lines is indicated in Figure 3.2a. The magnetic field is used to enhance the ionization process, thus increasing sputtering rates.[3]
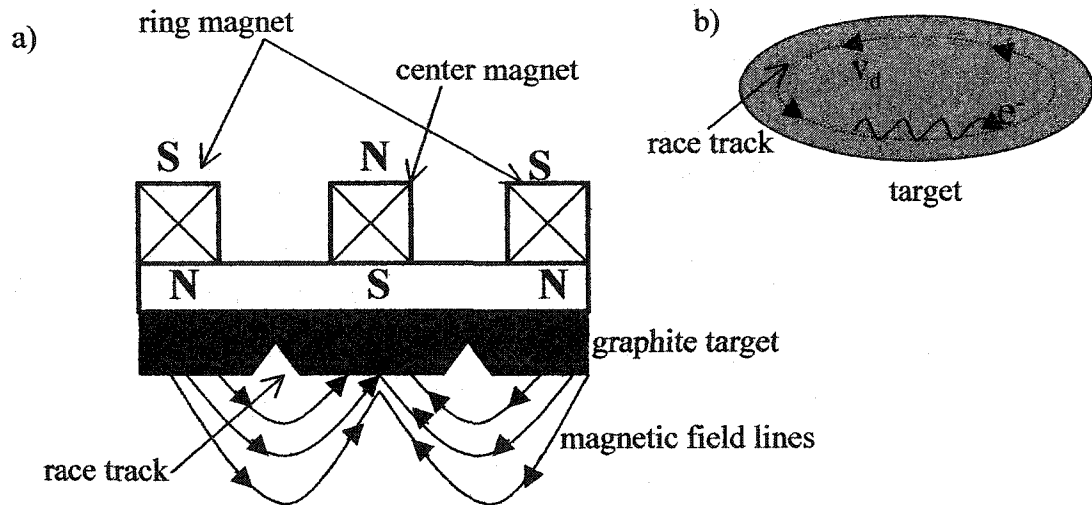
Figure 3.2: a) Schematic of the magnetron source. The magnetic field lines tend to contain the electron density near the target face. b) The drift velocity v_d contains the electron density in an annular region, which is called the racetrack. The electrons also gyrate around this path.

Due to the Lorentz force, the secondary electrons gyrate in cyclic orbits around the magnetic field lines. In addition, the magnetic field tends to trap the secondary electrons near the target face. The trapping is due to the plasma drift velocity: $\vec{v}_d = \vec{E} \times \vec{B} / B^2$, where E and B are the electric and magnetic field strengths, respectively.[3] As sketched in Figure 3.2b, the drift velocity is superimposed on top of the gyrating motion around the field lines. In this arrangement (Figure 3.2), the electron density is contained in an annular region near the target. (Consequently, the erosion zone on the target face has a pattern similar to an annulus and is colloquially known as the *racetrack*.) The containment of the electrons increases their time of travel near the target and, therefore, increases the ionization probability near the target. Thus, the magnetic field assists in sustaining the plasma by increasing the ionization, which allows the plasma to persist at lower operating pressures than in a conventional DC process. Lower operating pressures correspond to

less gas-phase collisions between target and substrate, which allows more sputtered flux (both ions and neutrals) to reach the substrate.

In a reactive sputtering process, the composition of the film incorporates material from both the target and the feedstock gas.[4] In contrast, a conventional sputtering process uses a feedstock gas that is chemically inert (e.g., argon) and, therefore, does not participate in the chemical makeup of the film. In this work, a-CN_x films are fabricated by reactive DC magnetron sputtering—a carbon target is sputtered in the presence of an N_2 feedstock gas. During the process, reactions between the nitrogen gas and carbon atoms can take place at both the substrate and graphite target. Thus, reaction of the gas phase with the target may also influence film properties.

3.2 Background on Sputtered Carbon Nitride Films

Sputtering techniques are the prevailing methods for synthesizing carbon nitride films. Interestingly, the first attempt to fabricate carbon nitride films was made by Cuomo et al., in 1979, using a reactive RF sputtering process.[5] They focused on the preparation of paracynanogen-like films—a soft, amorphous, polymeric material. Their work predates Liu and Cohen's prediction of the hypothetical β-C_3N_4 phase[6] by a decade. Since then, work on sputtered, carbon-nitride films has produced several important results. In this section, we review some of the more relevant work.

Using RF diode sputtering, Yu et al. synthesized carbon nitride films with small crystallites embedded in a polymeric film-matrix.[7] In accord with their electron diffraction results, they suggested the crystallites were β-C_3N_4. However, recent work has

shown that their claim of successful β-C_3N_4 synthesis is unconvincing [8,9] (see discussion in Section 1.1).

Using magnetron sputtering, Cutiongco et al. deposited a-CN_x overcoats on magnetic storage media.[10] They showed that a-CN_x films out-perform amorphous carbon overcoats. Their thin a-CN_x overcoats exhibited a smaller coefficient of friction, lower wear-rates, and a lower RMS surface roughness. They demonstrated that amorphous, carbon-nitride layers are promising candidates to replace the amorphous carbon layer currently used on hard disks. More recently, Li et al. have reported on ultra-smooth 1 nm-thick a-CN_x films for use as a protective overcoat on magnetic media.[11]

In 1995, Sjöström et al. reported the first a-CN_x films with fullerene-like microstructure.[12] These films were deposited by DC magnetron sputtering and the structure was discerned with transmission electron microscopy. This was a very important result, since it allowed the hardness and high elasticity of a-CN_x to be explained in terms of the observed microstructure. The films consisted of a network of buckled graphitic layers that were cross-linked. The fullerene-like structure was consistent with the high elasticity, while the cross-linking could be associated with the material's resistance to plastic deformation (hardness). Hellgren et al. continued this work on fullerene-like carbon nitride,[2] focusing on the relationship among film properties and process parameters (see discussion in Section 1.2). More recently, Hultman et al. have reported the synthesis of a new fullerene-like material consisting of cross-linked nano-onions.[13] At present, all reports on fullerene-like, a-CN_x films have been on materials that were fabricated by DC magnetron sputtering.

3.3 Substrate Preparation

Polished test grade single crystal Si(001) wafers were used as substrates. Silicon was chosen for a variety of reasons: it is reasonably inert to chemical reactions during deposition, does not contaminate the films, has high thermal stability, and is readily available. Furthermore, it has been used extensively as the substrate in previously published studies on a-CN$_x$ films. For the x-ray photoelectron spectroscopy (XPS) study, 1 cm^2 substrates were prepared by dicing a 75 mm wafer, using a score-and-crack technique. The substrates were ultrasonically cleaned sequentially in an acetone and isopropanol baths, for 10 min. each. All substrates were used within 12 hours of cleaning.

The substrate-preparation procedure was altered for the nuclear magnetic resonance (NMR) studies. In this case, the NMR samples were deposited on whole 75 mm-diam. wafers, since large substrate-areas were required to fabricate and collect enough material (~100mg) for NMR measurements. The 75 mm-diam. substrates were placed as received into the vacuum chamber. Solvent rinses to cleanse the whole wafer were avoided, since these substrates were shipped in pristine condition. All substrates— for both the XPS and NMR studies—were visually inspected to ensure the surface was free of dust and particulate before introducing them into vacuum.

3.4 Film Fabrication Conditions

All a-CN$_x$ films were deposited by DC magnetron sputtering in a pure nitrogen discharge, using a 50 mm-Mightymak sputtering gun (U.S. Inc.). The targets were 99.999% pure graphite, hot pressed disks with 50 mm diam. and 6.4 mm thickness. The deposition rate of the material was estimated to be ~1 μm/hr as determined by a thickness

profile measurement using scanning electron microscopy. High material-fabrication rates are crucial for this research, since at least ~100 mg of a-CN_x is required for the NMR measurements. (N.B., the carbon targets used in this work were not ^{13}C enriched.)

The samples were mounted on a radiatively heated substrate-holder, which was positioned in front of the target. The uniformity of the heater was checked by comparing temperature measurements at the center and edge of the plate that held the substrate. The temperature difference from center to edge was less than 50 °C. In all cases, the substrate was electrically grounded during deposition with the target-discharge current limited to 300 mA. In this work, a grounded substrate-bias was implemented for practical reasons. In some previous studies, a-CN_x films have been deposited using a negative substrate-bias with respect to the plasma potential. A negative bias increases the energy of the ions bombarding the sample. Biasing the substrate can result in an improvement of the mechanical properties of the film.[14] However, if the bias is too high (c.a. –200 V), the growth of the film is completely arrested due to resputtering.[15] Although a negative bias may be beneficial, it results in a lower film-deposition rate. As mentioned above, a high deposition rate is critical for this work; therefore, resputtering is undesirable. In addition, higher ion bombardment can cause roughening of the substrate surface, which improves film adhesion. This is also undesirable, since this will make the a-CN_x film more difficult to remove from the substrate for the NMR measurements.

The deposition system was evacuated with a roughing pump backed by a 150 l/s turbomolecular pump. The ultimate pressure of the vacuum system was 2 x 10^{-7} Torr at room temperature, as measured by an ion gauge. This system was thoroughly leaked checked with helium, using a residual gas analyzer. Since this system could only be

operated in a high vacuum regime, precautionary steps were implemented to ensure contamination by water was kept to a minimum. Prior to film deposition, the samples were heated to their deposition temperature and outgassed until the base pressure was at least 1×10^{-6} Torr. Concurrently, an external heating tape was used to outgas water from the chamber walls at 125 $^{\circ}$C. Typically, this preheating period required one hour. Afterwards, the gas lines were evacuated and purged three times with fresh nitrogen. Before deposition, the target was sputter cleaned for 10 min. with a shutter in position to block it from the substrate. During the deposition period, the gas flow was regulated by a precision gas-flow controller. Two flow controllers were required for the a-CN$_x$ films that were fabricated for the ^{15}N NMR study, since a mixture of ^{15}N$_2$ and ^{14}N$_2$ gases was used. After each deposition, the sample temperature was ramped down at a rate of ~50 $^{\circ}$C/min. The samples were allowed to cool to at least 60 $^{\circ}$C before exposing them to atmosphere.

The deposition parameters for the a-CN$_x$ films are displayed in Table 3.1, and are categorized into three columns according to their respective study: XPS, ^{13}C NMR, or ^{15}N NMR. The goal of this research was to investigate a-CN$_x$ films that are highly elastic but hard. In this respect, the litmus test of the quality of the deposition parameters is provided by the nanoindentation results. The justification of these parameters (Table 3.1) is given in Chapter 7, where it is shown that these conditions yield films with desired properties. Regardless, a description of the differences in the parameter set (Table 3.1) is warranted. The first material deposited for this research was for the XPS study; this preliminary work served as a guide for the fabrication process for the NMR experiments. The differences in the various experimental conditions are explained below.

Table 3.1: The deposition parameters used for the films fabricated for the XPS and NMR studies.

Deposition Parameters	XPS Study	^{13}C NMR Study	^{15}N NMR Study
Substrate-target distance, d	4 cm	8 cm	8 cm
Gas-flow rate	20 sccm	10 sccm	10 sccm
Substrate size	1 cm^2	75 mm diam.	75 mm diam.
Deposition time	1-2 hr	8-9 hr	8-9 hr
Pressure	4 mTorr	8 mTorr	8 mTorr
Temperature	400 $^{\circ}$C	300 $^{\circ}$C	300 $^{\circ}$C

The differences between the XPS and NMR film procedures (Table 3.1) primarily reflect the requirement of making a large amount of material for the NMR experiments. Typically, ~100 mg of material is needed to for NMR measurements. The reason for this is twofold. First, only nuclei that possess spin can be observed by NMR. For example, the ^{13}C isotope has a natural abundance of ~1%; this means that the remaining 99% of carbon nuclei are invisible to the ^{13}C NMR measurement. Second, the NMR signal is expected to be very small, which is attributed to the fact that the difference in spin populations is governed by Boltzmann statistics. At room temperature, these population differences are small (tens of ppm), and thus the signal is small.

We now turn our attention to the comparison of the XPS and NMR film fabrication procedures (Table 3.1). A larger substrate-target distance, d, was chosen for the NMR-material process to increase film uniformity over the larger substrate-area (75 mm-diam.). The value of d = 8 cm was the maximum value allowed due to the small size

of the vacuum chamber. A lower gas-flow rate was used for the ^{15}N NMR film-fabrication process, as compared to 20 sccm for the XPS films. The lower rate of flow and the use of a ^{15}N$_2$/^{14}N$_2$ mixture allowed a substantial reduction in cost, since pure isotopic ^{15}N$_2$ gas is very expensive. For the ^{13}C NMR film growth, the flow rate was set to 10 sccm. In this case, a pure ^{14}N$_2$ feedstock gas was used, but identical flow rates were chosen for both NMR fabrication processes for consistency.

Deposition times for the NMR measurements were 8-9 hours, which corresponded to a film thickness of ~8-9 μm. Since extremely long deposition times were used, the long-term stability of the process was an important consideration. The choices of deposition pressure and substrate temperature (Table 3.1) reflect this consideration. For the NMR protocol, the base pressure was set to 9 mTorr, since lower pressures resulted in instabilities in the plasma, which caused the discharge to randomly cease. These instabilities are perhaps associated with changes in the target due to the deep erosion track. This problem was not observed for the films fabricated for the XPS study. In addition, the NMR material was deposited at a lower temperature (300 °C) to prolong the life of the heater.

The compressive stress in a-CN$_x$ films prepared by DC magnetron sputtering is rather large.[2] The stress scales linearly with the film thickness. The large stresses in our thick NMR films aided in the delamination of the material from the substrate. Typically, after deposition, the films were stored at ambient for 24 hrs. During this period, the films would partially delaminate, and the material was harvested from the substrate by gentle scraping. 140 mg of material was obtained for the ^{13}C NMR measurements by depositing three ~9 μm thick films. For the ^{15}N NMR measurements, 180 mg of material was

prepared by depositing four ~8 μm-thick films. After removing the material from the substrates, the films were ground to a fine powder using a mortar and pestle, and then packed into a 5 mm-zirconia rotor for NMR measurements.

3.5 References

1   B. C. Holloway, O. Kraft, D. K. Shuh, W. D. Nix, M. Kelly, P. Pianetta, and S. Hagstrom, J. Vac. Sci. Technol. A **18**, 2964 (2000).

2   N. Hellgren, M. P. Johansson, E. Broitman, L. Hultman, and J. E. Sundgren, Phys. Rev. B **59**, 5162 (1999).

3   J. E. Mahan, *Physical Vapor Deposition of Thin Films* (Wiley, New York, 2000).

4   J. A. Thornton and J. E. Greene, in *Handbook of Deposition Technologies for Films and Coatings*, 2 ed., edited by R. F. Bunshah (Noyes, Westwood, N.J., 1994), p. 29-81.

5   J. J. Cuomo, P. A. Leary, D. Yu, W. Reuter, and M. Frisch, J. Vac. Sci. Technol. **16**, 299 (1979).

6   A. Y. Liu and M. L. Cohen, Science **245**, 841 (1989).

7   K. M. Yu, M. L. Cohen, E. E. Haller, W. L. Hansen, A. Y. Lui, and I. C. Wu, Phys. Rev. B **49**, 5034 (1994).

8   J. Wang, J. Lei, and R. Wang, Phys. Rev. B **58**, 11890 (1998).

9   S. Matsumoto, E. Q. Xie, and F. Izumi, Diamond Relat. Mater. **8**, 1175 (1999).

10   E. C. Cutiongco, L. Dong, C. Yip-Wah, and C. S. Bhatia, Transactions of the Asme. Journal of Tribology **118**, 543 (1996).

11   D. Li and C. Yip-Wah, IEEE Trans. Magn. **39**, 765 (2003).

12   H. Sjostrom, S. Stafstrom, M. Boman, and J. E. Sundgren, Phys. Rev. Lett. **75**, 1336 (1995).

13   L. Hultman, S. Stafstrom, Z. Czigany, J. Neidhardt, N. Hellgren, I. F. Brunell, K. Suenaga, and C. Colliex, Phys. Rev. Lett. **87**, 225503/1 (2001).

14   A. Chowdhury, D. C. Cameron, and M. A. Monclus, Thin Solid Films **355**, 85 (1999).

15   W. T. Zheng, E. Broitman, N. Hellgren, K. Z. Xing, I. Ivanov, H. Sjostrom, L. Hultman, and J. E. Sundgren, Thin Solid Films **308**, 223 (1997).

Chapter 4—Characterization Techniques I: Nanoindentation and X-ray Photoelectron Spectroscopy

4.1 Nanoindentation

Typically, the mechanical properties of a material are determined by placing it under a known force and measuring its response—e.g., clamping the sample in a test-fixture and placing it in under a state of tension or compression. However, conventional test-fixtures can not be used to clamp samples with sub-micron dimensions. Nanoindentation is a technique that was developed to circumvent this problem and is capable of probing the mechanical properties of materials on a sub-micron scale,[1-4] such as thin films. Nanoindentation was used to measure the mechanical properties of the a-CN_x films fabricated for this study. In this chapter, both the theoretical and practical aspects of nanoindentation are described.

4.1.1 Theoretical Considerations

In a nanoindentation experiment, a diamond tip is pushed into the sample surface, and the load-versus-displacement curve is recorded, and information about the material's elastic modulus and hardness is obtained by analysis of the unloading curve. Later in this section, a detailed description of this analysis is given. First, we will consider some of the practical aspects of nanoindentation testing on thin films.

30

Typically, thin films have a thickness of $< 1 \mu m$ and are bonded to a substrate; therefore, if the indenter penetration is too deep, then the substrate will affect the loading behavior. As a rule-of-thumb, this effect can be minimized by ensuring that the indentation depth is less that 10% of the film's thickness.[5] The hardness is a measure of a material's resistance to plastic deformation. Accordingly, a plastic indentation is required to measure hardness. This implies that a minimum indentation depth is needed to compute a reliable hardness value. However, if this minimum depth is too deep, substrate-film interaction takes place and interferes with the hardness measurement.

Because small indentation depths are required, the indenter tip needs to be very sharp in order to obtain a reliable hardness value. A blunt indenter tip requires a large penetration depth to initiate plastic flow; however, this is undesirable because of substrate-film interaction. Whereas, a sharp indenter tip induces plastic flow at shallower depths, and thus helps avoid this interaction. Very sharp diamond indenters can be fabricated, and indenter tips with Berkovich geometry are a popular choice. In this configuration, the tip has a three-sided pyramidal shape, with the sharp end formed by the intersection of the three sides. The angle between the axis of the tip and the line that bisects a side through the tip is 65.3°. Ideally, these three sides intersect at a point to form the tip; however, real indenters are not perfectly sharp, but can be fabricated with a tip that has a radius of curvature of < 300 nm .
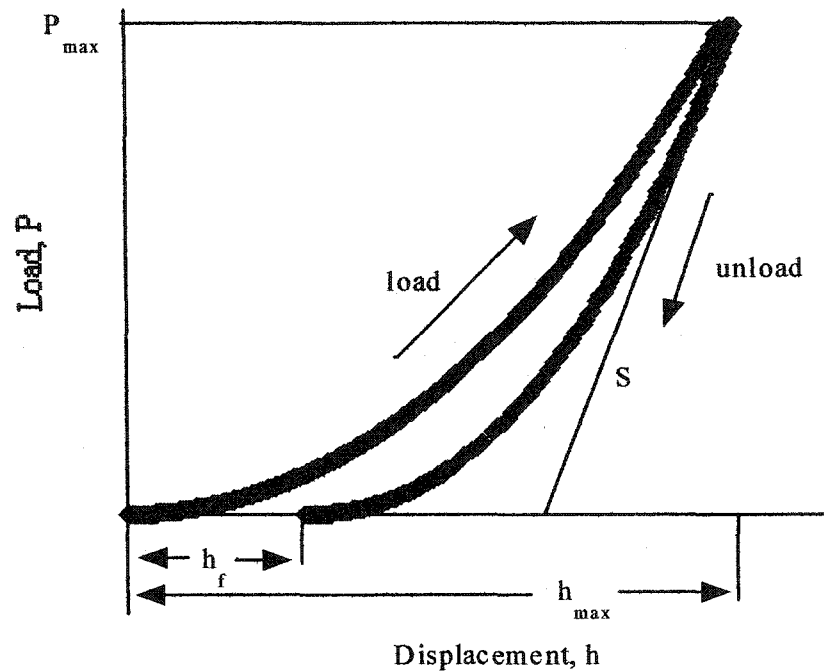
Figure 4.1: A schematic illustration of a nanoindentation-loading curve. The quantities shown in the figure are used to analyze the data and are discussed in the text.

A schematic of a typical nanoindentation loading-curve is shown in Figure 4.1. The indenter tip is usually sharp enough to cause plastic flow throughout the entire portion of the loading curve—except at the initial penetration. Thus, the loading curve exhibits both effects due to plastic and elastic deformation and not surprisingly exhibits a non-linear behavior. As the material is unloaded, its elastic restoring force tends to push the indenter tip out of the material. Thus, analysis of the unloading portion of the curve allows the elastic properties to be determined.[1,3] The non-linear behavior of the unloading curve is attributed to the decreasing contact area of the sample with the indenter tip as it

is removed. Oliver and Pharr [3] have developed a method to analyze the unloading curve, which is described below.

Analysis of the unloading curve allows the hardness, H, and the reduced modulus, E_r, to be computed. The hardness is measure of a material's ability to resist plastic deformation and is defined as the pressure that a material can support under load:[3]

$$H = \frac{P_{max}}{A},$$ (4.1)

where P_{max} is the peak load (see Figure 4.1), and A is the projected contact area of the indenter tip. The other quantity of interest is the reduced modulus, E_r, which provides a measure of the material's compliance:[3]

$$E_r = \frac{\sqrt{\pi}}{2} \frac{S}{\sqrt{A}},$$ (4.2)

where S is the stiffness taken at peak load. It is important to note that the reduced modulus takes into account the elasticity of the indenter tip and the sample. Since the elastic properties of the indenter are known, the elastic properties of the sample can be extracted from E_r (see Eq. 4.8). Further discussion of the reduced modulus is presented later. The key quantities needed to solve Eqs. 4.1 and 4.2 are the peak load, P_{max}, the stiffness, S, and the projected contact area of the indenter tip, A. P_{max} is a directly measured quantity (see Figure 4.1). Analysis of the nanoindentation unloading curve is required to determine A and S.

Determination of S

As illustrated in Figure 4.1, the stiffness, S, is the initial slope of the unloading curve:

$$S = \frac{dP_{max}}{dh_{max}}, \tag{4.3}$$

where h_{max} is the indenter depth at peak load. In early work by Doerner and Nix,[1] the initial slope was determined by a linear fit to the top third of the unloading data. However, Oliver and Pharr [3] pointed out that the slope is rarely linear during the initial stages of unloading. Extending upon the results of Sneddon,[6] Oliver and Pharr proposed that the unloading curve could be fit with a power-law relation of the form:[3]

$$P = \alpha(h - h_f)^m, \tag{4.4}$$

where the constants α, h_f, and m are determined from a least-squares fit to the unloading curve. The fitting parameter, h_f, is the non-recovered residual displacement after the indenter is removed, as shown in Figure 4.1. Thus, once the fitting parameters are determined, the initial stiffness, S, is computed by taking the derivative of Eq. 4.4.

Determination of A

The final quantity needed to complete the analysis is A, the projected contact area of the indenter tip:[3]

$$A = F(h_c). \tag{4.5}$$

Note that A is a function of contact depth, h_c. The contact depth is defined as the depth that the indenter makes contact with the sample at a displacement h (see Figure 4.2). The

Load, P

Surface

h_s

Indenter Tip

h

h_c

Film

Substrate
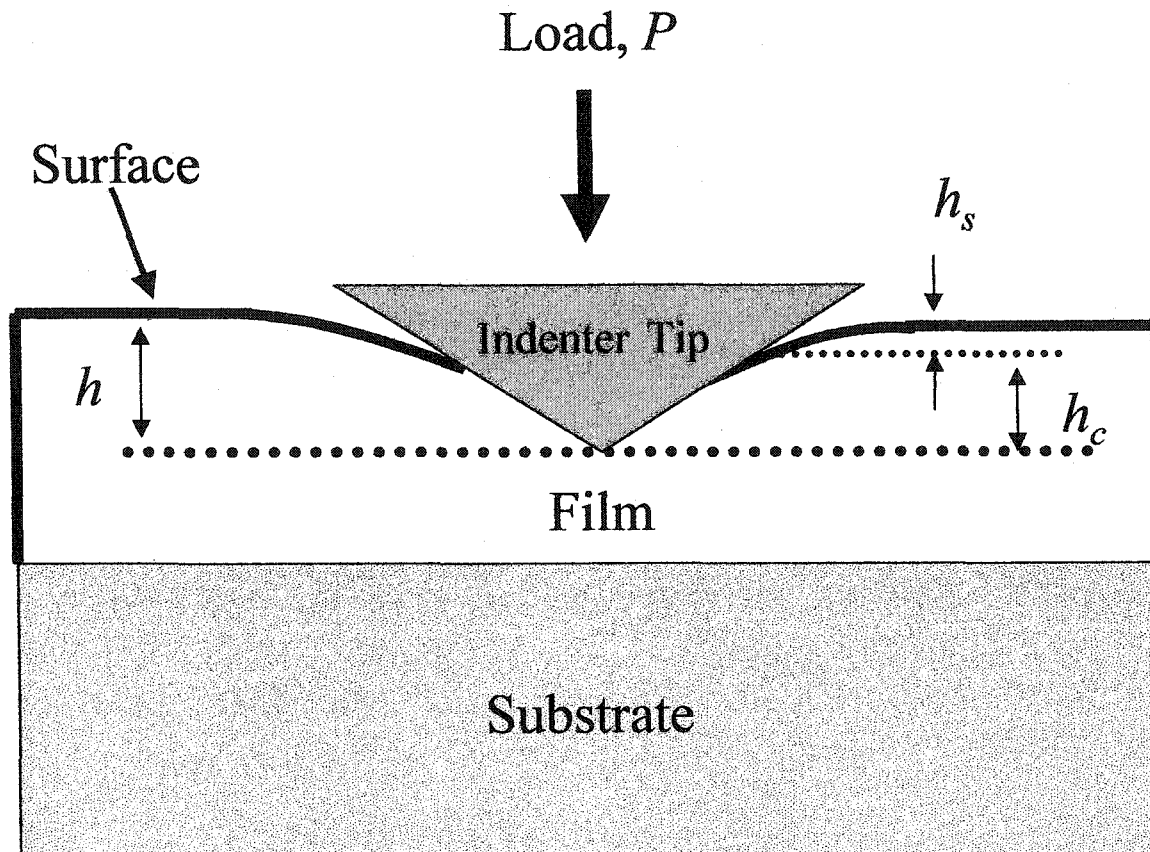
Figure 4.2: A schematic representation of deformation of the sample during a nanoindentation experiment. The quantities that are shown in the figure describe the deflection of the sample surface and are discussed in the text.

Area function of the indenter is determined by prior calibration.[3] According to Eqs. 4.1 and 4.2, our analysis of A is completed by finding the value of h_c at P_{max}. The computation of h_c is described as follows. During unloading, the total displacement of the indenter, h, is written as the sum of two terms: [3]

$$h = h_c + h_s,$$ (4.6)

where h_c is the contact depth and h_s is the displacement of the surface outside the region where the indenter makes contact with the sample. The contact depth and surface

displacement are illustrated schematically in Figure 4.2. The surface displacement, h_s, can be expressed as [3]

$$h_s = \varepsilon P_{max}/S, \tag{4.7}$$

where ε is a constant that describes the indenter geometry. Oliver and Pharr suggest using a value of $\varepsilon = 0.75$ for the Berkovich indenter, which is the only indenter type used in this work. Using Eq. 4.7 with $\varepsilon = 0.75$, the contact depth, h_c, is computed from Eq. 4.6. With h_c known, the projected area, A, is obtained from the predetermined calibration equation Eq. 4.5.

In this section, the method of Oliver and Pharr was described.[3] This method is used to determine the stiffness, S, and the projected contact area, A, of the indenter. With these determined, the hardness, H, and the reduced modulus, E_r, are computed from Eqs. 4.1 and 4.2, respectively. As mentioned earlier, E_r takes into account the elastic properties of the sample as well as the indenter:[3,4]

$$\frac{1}{E_r} = \frac{(1-v^2)}{E} + \frac{(1-v_i^2)}{E_i}. \tag{4.8}$$

Here E and v are the Young's Modulus and Poisson's ratio of the sample, respectively, and E_i and v_i are the same parameters for the indenter. Even if the indenter properties and the reduced modulus are known, knowledge of Poisson's ratio is still needed to compute the Young's modulus for the sample. However, this value is unknown for a-CN$_x$, and its measured modulus is simply reported as $E/(1-v^2)$.

4.1.2 Nanoindentation Methods

Nanoindentation testing was carried out with a MTS NanoXP nanoindentation system using a diamond indenter with Berkovich geometry. All measurements were carried out by O. Kraft at the Max-Planck-Institut fur Metallforschung, Stuttgart, Germany. The indentations were performed under a constant strain rate condition by keeping $\dot{P}/P = 0.01$ s^{-1} where $\dot{P}$ is the load rate and P the load. Multiple indents on the same sample were spaced apart by 50 μm in the x-direction and by 50 μm in the y-direction. The loading sequence consisted of the following steps.[3] First, the sample is preconditioned by pre-loading at 90% of the peak load and then unloading to 10% of the peak load value. The preconditioning step is repeated three times in succession; this step ensures the loading behavior is reversible. After the third preload, the sample remains unloaded at 10% of the peak load for a period of 100 s. This hold period is used to measure the rate of displacement due to thermal expansion. By assuming the thermal drift rate is constant, the displacement data can be corrected.[3] Next, the sample is loaded to its peak value and held at this value for an additional 100 s. The hold period at peak load allows time dependent plastic effects to diminish.[3] Finally, the sample is unloaded—this portion of the curve is analyzed to determine the sample's mechanical properties.

The nanoindentation system can also continuously measure the stiffness during indentation—this technique is called a continuous stiffness measurement.[3] The force on the indenter is modulated by a tiny oscillating signal; consequently, the displacement is also modulated at the same frequency as the force signal. Using a lock-in technique, the displacement modulations are detected. This measurement is used to calculate the stiffness from $S = dP/dh$. One example of this type of measurement is presented later.

4.2 X-ray Photoelectron Spectroscopy

X-ray photoelectron spectroscopy (XPS) is a technique that is based on the emission of electrons from a sample's surface due to x-ray absorption. The electrons that are emitted from the surface are called photoelectrons. The kinetic energy of a photoelectron is dependent on the chemical environment from which it originates. Thus, measurement of the kinetic energy spectrum yields valuable information about chemical bonding. In this work, XPS was used to examine the bonding and composition of hard and elastic amorphous carbon nitride (a-CN_x) films. The following sections provide an overview of the theoretical and practical aspects of XPS.

4.2.1 Theoretical Considerations

XPS is a chemical analysis technique that is based on measuring the kinetic energy of photoelectrons that are emitted from a sample's surface due to x-ray absorption. The incident x-rays with energy hv are absorbed by an electron with binding energy E_b, which is emitted as a photoelectron with kinetic energy, E_k. Conservation of energy requires that the kinetic energy of the photoelectron to be

$$E_k = hv - E_b. \tag{4.9}$$

In the above equation, E_b is referred to the vacuum level. In the final state of this process, the photoelectron leaves behind a positively charged atomic core. Consequently, the charge density relaxes to screen the core-hole left behind by the photoelectron. This screening process lowers the final state energy of the ion, thus providing more kinetic energy to the photoelectron. Taking this final-state effect into account, the binding energy is expressed as [7]

$$E_b = -\varepsilon_k - E_r,\qquad(4.10)$$

where ε_k is the orbital energy, and E_r is the relaxation energy.

In XPS, the photon energy is known (e.g., 1253.6 eV for Mg K-α x-rays), and the kinetic energy spectrum is measured. This allows the binding energy spectrum to be determined (see Eq. 4.9) with respect to a proper reference energy. This is an important point. In Eq. 4.9, the binding energy E_b is referenced to the vacuum level. Experimentally, it is difficult to determine the vacuum level,[8] since this requires accurate knowledge of the work function of the sample, ϕ_s. The difficulty in determining ϕ_s lies in the fact that it is strongly dependent on the condition of the sample's surface.[8] Instead, the measured binding energies are usually referenced to the Fermi level, which for a metal is defined as the energy of the highest occupied level.

For metallic samples, good electrical contact between the sample and spectrometer can be maintained, which allows the zero of the binding energy scale to be conveniently set at the Fermi level. In this case, the Eq. 4.9 is replaced by [7]

$$E_k = h\nu - E_b^F - \phi_{spec},\qquad(4.11)$$

where the superscript F indicates that E_b is referenced to the Fermi level, and ϕ_{spec} is the work function of the spectrometer. For metallic samples, Eq. 4.11 is usually used in determining E_b. However, for insulators or semiconductors, the Fermi level is above the valence band edge; thus, a measurable feature that is associated with the Fermi level can not be distinguished in the spectrum. In addition, insulators have low conductivity, which results in sample charging due to photoelectron emission. As the sample charges, a retarding potential is created on the outgoing photoelectron and lowers its kinetic energy.

Consequently, sample charging shifts the spectrum. For organic samples with low conductivity, the problem of finding a reference energy is often solved by using an internal reference. Typically, all binding energies are referenced to the carbon bonded only to carbon component in the C(1s) spectrum. This reference point is reasonable, since the binding energy of carbons that are bonded to other carbons or hydrogens is insensitive to hybidization and is always near 285.0 eV.[9] This procedure was used in this research, since we are measuring XPS spectra of carbonaceous materials.

XPS can be described as a photon in/electron out spectroscopy. Standard x-ray sources (Mg-Kα and Al-Kα) have photon energies of ~1 KeV. At these energies, photons have penetration depths on the order of 1 μm, which is much larger than the attenuation depth of the photoelectrons.[8] Thus, the depth sensitivity of XPS is controlled by the photoelectron attenuation depth. The photoelectron intensity, I, with kinetic energy E_k that originates from a depth z below the sample's surface is assumed to have the form:[9]

$$I = I_o \exp(-z/\lambda \sin\theta). \tag{4.12}$$

Here, θ is the photoelectron take-off angle, with respect to the plane of the sample's surface. I_o is attenuated by inelastic scattering, as reflected by λ, the inelastic mean free path. Elastic scattering may also lead to a reduction in intensity, since the probability of inelastic scattering increases with longer trajectories. As shown by Eq. 4.12, the surface sensitivity can be increased by measuring the photoelectron intensity emanating at small take-off angle. In addition, λ depends on kinetic energy, which is dependent on the photon energy. X-rays produced by magnesium or aluminum anodes have energies of 1253.6 eV (Mg-Kα) and 1486.6 eV (Al-Kα), respectively. At these x-ray energies, the kinetic energy of an electron ejected from a C(1s) or N(1s) shell is ~ 1 KeV. At 1 KeV,

λ is ~10 nm, as suggested by measurements on a variety of materials.[9] Setting $\theta = \pi/2$ and

$\lambda = 10$ nm in Eq. 4.12 shows that ~95% of the photoelectron intensity comes from the top

30 nm of the sample. Thus, XPS is a surface sensitive technique.

XPS as a Core-level Spectroscopy

In this research, XPS was used solely as a core-level spectroscopy. The binding

energy of core-level electrons is characteristic of the atomic species. Thus, peaks in the

binding energy spectrum are element specific, which allows the chemical composition of

the sample to be determined. In addition to being element specific, the exact core-level

binding energies, E_b, vary slightly (a few tenths of an eV to several eV) with respect to

local chemical bonding environment—this variation is called the chemical shift. Thus,

XPS is a tool that can determine both elemental composition and chemical bonding. In

addition, the relative intensities of core-level spectra allow elemental concentrations to be

identified.

However, before any quantitative information can be obtained, the background

intensity must be subtracted from the spectral components. An iterative Shirley method

was chosen for this purpose.[9,10] The Shirley background is generated by the following

formula:

$$I_n(k) = J(k) - C_n \sum_{l=k+1}^{l \max} I_{n-1}(l) \Delta E, \qquad (4.13)$$

where $J(k)$ is the measured intensity at kinetic energy E_k, $I_n(k)$ is the background corrected

intensity at kinetic energy E_k for the nth iteration, and ΔE is the step size. The constant C_n

is chosen iteratively such that the intensity $I_n(I_{min}) = 0$. The points I_{max} and I_{min} are user

inputs and are chosen a few eV outside the region of the peak. The background intensity at E_k is proportional to the integrated intensity of the portion of the peak at higher kinetic energy (Eq. 4.13); thus, the background steadily increases from high to low kinetic energies. The Shirley formalism assumes that the probability of inelastic scattering is independent of the energy range spanned by the peak and that the scattered electrons lose energy continuously (not discretely) before escaping the surface.

Once a background is subtracted from each peak, the relative concentration, C_x, of a particular element X is determined from the formula:[9]

$$C_X = \frac{I_x / S_x}{\sum_n I_n / S_n},$$

(4.14)

where S_x is the relative sensitivity factor for element X, which depends on the differential photoemission cross-section and analyzer transmission function. The only elements considered in this research were carbon, nitrogen, and oxygen—their corresponding S_n, as given by the instrument manufacturer, are listed in Table 4.1. Note that the relative sensitivity factor of carbon is defined as 1.0.

Interpretation of chemical bonding from the core-level spectra is accomplished by using curve-fitting techniques. After background subtraction, a least-squares fit of Gaussian components can be used to resolve the various sub-peaks that are enclosed in the peak-envelope. The separation in binding energy (the chemical shift) among the various sub-peaks provides insight to identifying bonding. Several factors influence the minimum FWHM, Δ, of a sub-peak:

$$\Delta = \sqrt{\Delta_n^2 + \Delta_p^2 + \Delta_a^2},$$

(4.15)

Table 4.1: Relative sensitivity factors, S_x, for carbon, nitrogen, and oxygen. The relative sensitivity factor of carbon has been defined as 1.0

Element	C	N	O
S_x	1.00	1.68	2.64

where Δ_n is the natural line-width of the core-level, Δ_p is line-width of the x-ray line, and Δ_a is the analyzer resolution.[9] The quadrature form of Eq. 4.15 explicitly assumes that all contributions to the final width have Gaussian distributions. Both standard Mg-Kα and Al-Kα photon sources have line-widths near 1.0 eV (Mg-Kα = 0.70 eV, Al-Kα = 0.85 eV);[9] thus, the resolution between two sub-peaks is not much better than 1.0 eV.

4.2.2 XPS Methods

In this work, XPS was used as a core-level spectroscopy. All measurements were performed *ex-situ*. XPS was carried out on the a-CN$_x$ films and on a variety of reference organic compounds (see compound listing in Table 8.2 of Chapter 8). These reference materials contain nitrogen in a variety of configurations, and the N(1s) peak positions of these materials were compared with the a-CN$_x$ films in an attempt to determine bonding assignments. All measurements were carried out using a VG ESCA lab system with hemispherical energy analyzer and a non-monochromated Mg-Kα source. The analyzer was operated in a constant analyzer energy (CAE) mode, where all the electrons are all retarded to the same energy (the pass energy) before entering the analyzer. The analyzer pass energy was selectable between 5 and 200 eV. As the pass energy increases, resolution diminishes, while sensitivity improves. The x-ray anode was operated at 10 KeV at 20 mA emission current—this choice of operational parameters is clarified. A

rule-of-thumb is to set the anode voltage 10 times higher than the photon energy for efficient x-ray production.[9] This corresponds to an anode voltage of roughly 12 KeV for magnesium (Mg K-α 1253.6 eV). However, voltages higher than 10 KeV resulted in arcing due to condensation build-up on the water cooling lines inside the anode assembly. Therefore, voltages higher than 10 KeV were not used. To ensure efficient cooling, the operating power of the anode was limited to 200 W. Furthermore, the photoelectron currents were all measured at a 70° take-off angle. In this configuration, the sample surface was parallel to the aluminum window of the anode. This allowed the sample to be brought as close as possible to the x-ray source, thus providing better charge compensation from the low-energy secondary electrons emitted from the aluminum window.

Base pressure during analysis was typically 1×10^{-9} Torr for the a-CN$_x$ films. However, due to the higher vapor pressures of the organic powders, spectra were acquired at pressures as high as 1×10^{-7} Torr, with exception to acridine (Table 8.2), which were acquired at $\sim 2 \times 10^{-6}$ Torr due to its high vapor pressure. The spectrometer was calibrated at the Au 4f$_{7/2}$ peak at 84.0 eV with a FWHM of 1.5 eV at 50 eV pass energy. All spectra were collected using 50 eV pass energy, 0.1 or 0.2 eV step size, and a 100 ms dwell time, except for the survey scans which were obtained using a 100 eV pass energy. These settings were chosen so that the spectra of the organic compounds were acquired in a short amount of time. Short data acquisition times were deemed important, since these compounds (Table 8.2) exhibit high vapor pressures, thus lowering the quality of the vacuum with prolonged exposure. Higher resolution settings were available, but were not used since data acquisition times would be significantly increased.

Since the carbon nitride films are amorphous, sputtering is expected to change the local bonding of the material. Moreover, these changes are not reversible by thermal annealing. Thus, no pre-sputter step was carried out preceding spectra acquisition. Consequently, the a-CN_x films retained any surface contamination due to atmosphere exposure, most likely absorbed water. Unfortunately, sample-heating capabilities were not available—mild heat treatment (150 °C) could have been used to desorb water. Recent work indicates that water absorbed due to prolonged exposure to atmosphere only slightly broadens the spectra.[11] Thus, the overall bonding information is retained.

To compensate for sample charging, all binding energies were referenced to the low binding energy component of the C(1s) spectrum, which was assigned a value of 284.6 eV. The reference binding energy was chosen to match the C(1s) binding energy of graphite powder at 284.6 eV, as measured by our XPS system. The position of the low binding energy component of our samples was determined by a least-squares fit of Gaussian components. For the organic compounds listed in Table 8.2, charge compensation was accomplished by fitting the C(1s) spectrum with one or two Gaussian components, depending on the asymmetry of the spectrum. The low binding energy C(1s) component was then charge shifted to 284.6 eV. For the a-CN_x films, the C(1s) spectrum always required a fit with more than one Gaussian component, and in this case, the position of the low binding energy component was determined by a least-squares fit of four components to the C(1s) spectrum, with each constrained to have the same FWHM (usually 2.1 eV). The charge shift correction, as determined by this method was typically 0.3 eV for the a-CN_x films.

The reference organic compounds examined in this study (Table 8.2) were purchased from Aldrich in powder form with a purity of no less than 97%. The powders were pressed into Indium foil and excess material was blown off with compressed air. Care was taken to ensure that the entire Indium surface was completely covered, and that no bare metal surface was exposed. The surfaces of the pressed powders were smooth and glossy. These precautions were taken to eliminate differential charging of the substrate surface during XPS analysis.

Before data analysis, peak backgrounds were subtracted using the Shirley algorithm described in Eq. 4.13—this was custom-programmed using Lab View. The spectra were fit with Gaussian components using the least-squares method that was supplied with the KaleidaGraph software package. Elemental compositions were calculated using Eq. 4.14, with the sensitivity factors in Table 4.1.

4.3 References

1   M. F. Doerner and W. D. Nix, J. Mater. Res. 1, 601 (1986).
2   W. D. Nix, Metallurgical Transactions A 20A, 2217 (1989).
3   W. C. Oliver and G. M. Pharr, J. of Mater. Res. 7, 1564 (1992).
4   F. R. Brotzen, International Material Reviews 39, 24 (1994).
5   O. Kraft, Personal Communication (2000).
6   I. N. Sneddon, Int. J.Engng Sci. 3, 47 (1965).
7   C. S. Fadley, in *Electron Emission Spectroscopy*, edited by W. Dekeyser, L. Fiermans, G. Vanderkelen, and J. Vennik (Reidel, Boston, 1973), p. 151-224.
8   D. P. Woodruff and T. A. Delchar, *Modern Techniques of Surface Science*, 2 ed. (Cambridge, New York, 1994).
9   D. Briggs, *Surface Analysis of Polymers by XPS and Static SIMS* (Cambridge, New York, 1998).
10   A. Proctor and M. A. Sherwood, Anal. Chem. 54, 13 (1982).
11   J. M. Ripalda, N. Diaz, I. Montero, F. Rueda, and L. Galan, J. Appl. Phys. 92, 644 (2002).

Chapter 5—Characterization Techniques II: Nuclear Magnetic Resonance Spectroscopy

In this chapter, an overview of the practical and theoretical aspects of nuclear magnetic resonance (NMR) spectroscopy is provided. The primary objective is to summarize the necessary background for understanding the experiments that were used in this research.

5.1 Basic Considerations

By placing a material in a large external magnetic field B_0, the degeneracy of its nuclear-spin, energy levels is lifted. This phenomenon is known as the Zeeman effect and is shown schematically in Figure 5.1 for a spin-½ nucleus. The classical expression for the energy, E, of an isolated spin in a magnetic field is

$$E = -\vec{\mu} \cdot \vec{B}_o,$$

where $\vec{\mu}$ is the nuclear magnetic moment. Noting the relationship between the magnetic moment and the spin operator, $\vec{I}$:

$$\vec{\mu} = \hbar \gamma \vec{I},$$

a quantum mechanical expression for the energy is obtained:

$$E_z = -\hbar \gamma I_z B_o. \qquad (5.1)$$

47

Here, γ is the magnetogyric ratio of the nucleus, I_z is the spin eigenvalue, and $\vec{B}_o = B_o \hat{z}_o$.

The $(2I+1)$ eigenvalues of I_z allowed by quantum mechanics are

$$I_z = -I, -I+1, \ldots, I-1, I. \tag{5.2}$$

In an atom or molecule, the electrons will circulate in response to the applied external field to generate a small magnetic field, which screens the applied field. Thus, Eq. 5.1 is modified by replacing B_o with a screened field $B_o(1-\sigma)$:

$$E_z = -\hbar \gamma I_z B_o (1 - \sigma). \tag{5.3}$$

Here, σ is the *screening* constant. It is convenient to rewrite the energy (Eq. 5.3) as

$$E_z = -\hbar I_z \omega_o \tag{5.4}$$

$$\omega_o \equiv \gamma B_o (1 - \sigma),$$

where ω_0 is the resonance frequency.

The phenomenon of nuclear magnetic resonance is understood by considering the simple two-state system shown in Figure 5.1. If a continuous radio frequency (RF) field is applied near the resonance frequency ω_0, the probability of spin flips is large and the spin will oscillate between the spin up (↑) and down (↓) states. However, if the frequency is far away from resonance, the probability amplitude of these oscillations is severely damped, and these transitions will not be observed.[1] In addition, there must be an imbalance between the two spin populations (↑ and ↓) to observe these spin oscillations. If there is no population imbalance, then the emission rate equals the absorption rate, and no net effect is observed. However, there will be a population imbalance, since the spin-up eigenstate is lower in energy and is thus energetically favored. The fractional
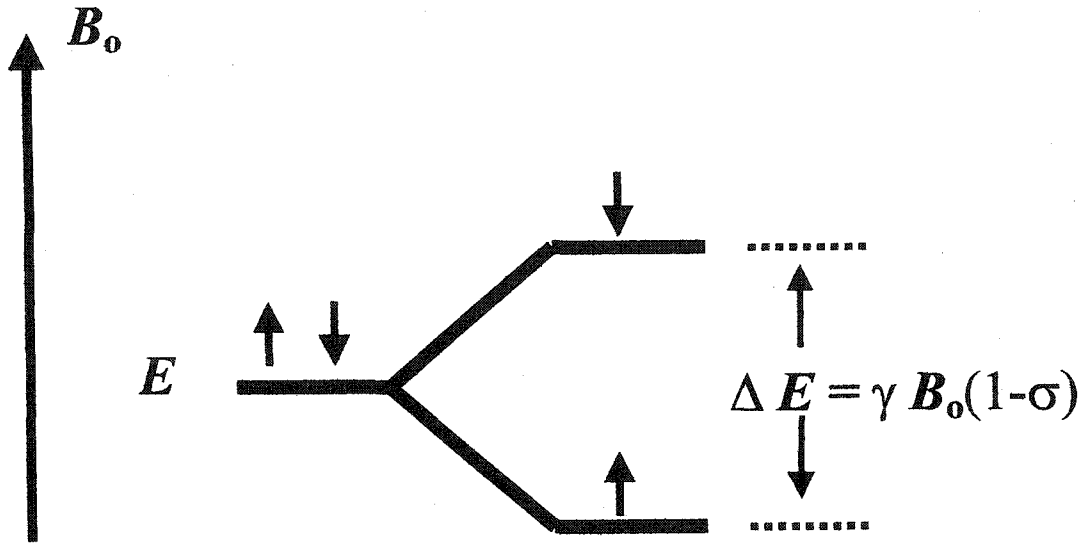
Figure 5.1: The Zeeman effect: the degeneracy of the spin energy levels is lifted by applying an external magnetic field.

population, p_n, for a spin in an eigenstate with energy, E_n, is given by Boltzmann statistics:

$$p_n = \frac{\exp\left(-\dfrac{E_n}{kT}\right)}{Tr\left[\exp\left(-\dfrac{H}{kT}\right)\right]}. \tag{5.5}$$

Here, H is the diagonal matrix of energy eigenvalues, k is the Boltzmann constant, and T is the temperature. Using Eq. 5.5, the population imbalance, for the two-state system (Figure 5.1) is determined from the ratio:

$$\frac{p_\uparrow}{p_\downarrow} = \exp\left[\frac{\hbar \gamma B_o (1-\sigma)}{kT}\right].$$

Expanding the exponential to first order using a Maclaurin series, this ratio is rewritten as

$$\frac{p_\uparrow}{p_\downarrow} \cong 1 + \frac{\hbar \gamma B_o}{kT}; \tag{5.6}$$

this is the so-called high temperature approximation. Using the values of $B_0 = 7.0$ T, $T = 293$ K (room temperature), and $\gamma = 2.68$ rad/Ts (the magnetogyric ratio for protons), calculation gives a net excess of 49 ppm for spins in the lower energy state (spin ↑). Thus, measurement of magnetic resonance relies on a tiny fractional imbalance of spin populations. In the above discussion, the simplest case (spin ½) was considered; however, these arguments are readily extended to nuclei with higher spin by noting that they have $2I(I+1)$ energy levels (by Eq. 5.2).

The use of a continuous wave RF field to induce NMR is now a rarity.[2] Modern NMR experiments use RF pulses to irradiate the nuclei. Near resonance, the field strength B_1 of the RF pulse will induce a torque τ on the spins:

$$\vec{\tau} = \sum \vec{\mu}_j \times \vec{B}_1 = \vec{M} \times \vec{B}_1,\tag{5.7}$$

where $\vec{M}$ is the total magnetic moment, which is given by a sum over nuclear spins. Application of an RF pulse tips the magnetic moment away from the z-axis, as schematically illustrated in Figure 5.2, where B_1 is taken along the positive x-direction. The tip angle Θ (in radians) is proportional to both B_1 and the pulse length τ_p:

$$\Theta = \gamma B_1 \tau_p = \omega_1 \tau_p.\tag{5.8}$$

For example, a $(-\pi/2)_x$ pulse tips the spins into the xy-plane along the y-direction (Figure 5.2)

In a typical NMR experiment, an RF pulse is used to tip the nuclear spins into the plane perpendicular to the external field (xy-plane), where they precess at their characteristic resonance frequency due to the torque acting on the spins by B_0. By placing a pick-up coil in the xy-plane, magnetic resonance is observed by measuring the small
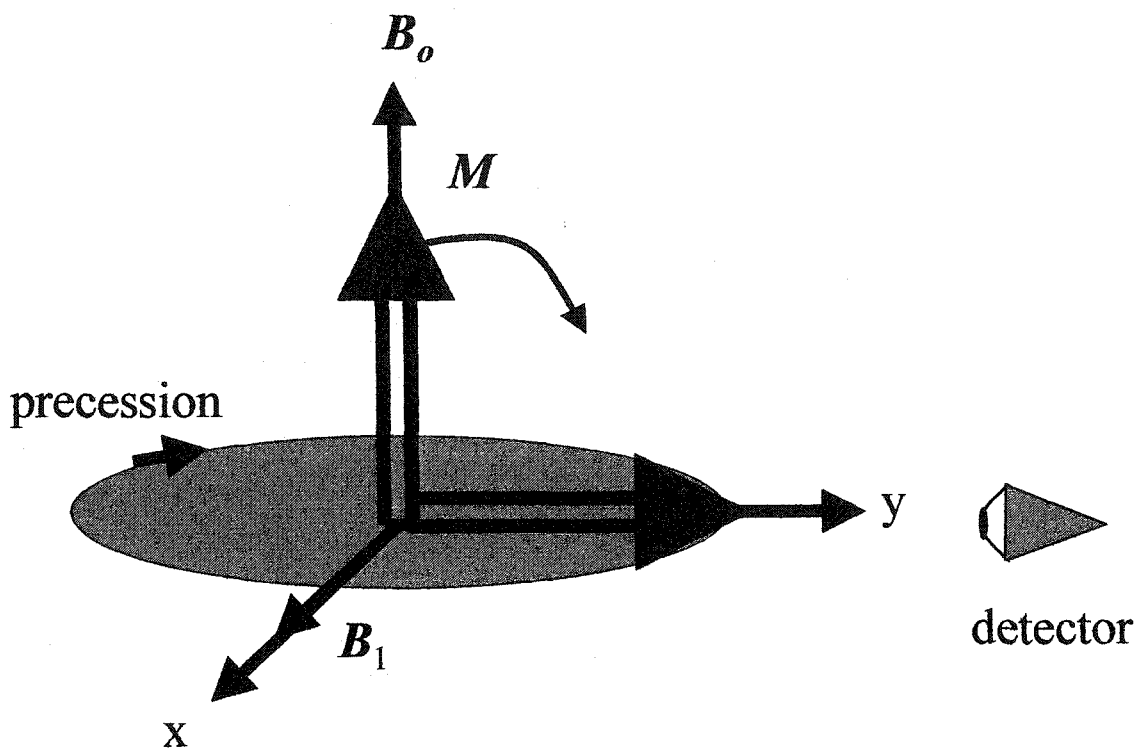
Figure 5.2: A $(-\pi/2)_x$ tips the nuclear spins in the xy-plane along the y-axis. At the end of the pulse, the spins precess around the external field B_0 at their Larmor (resonance) frequency.

current induced by the precessing nuclear spins. The resonance frequency (Eq. 5.4) depends on the chemical-bonding environment in which the nuclei are immersed. Therefore, the width of the RF pulse is chosen to be short enough, so that the entire frequency range of bonding configurations is excited. (The Fourier transform of a square pulse shows that the sinc-function, spectral coverage in the frequency domain is proportional to the reciprocal of the pulse width.)

The spins do not precess indefinitely, but begin to relax as soon as the pulse terminates. After the pulse, the spins return to thermal equilibrium by two relaxation

processes: 1) spin-spin relaxation and 2) spin-lattice relaxation. The spin-spin relaxation process is characterized by the time T_2, which describes the rate the transverse (xy) component of the magnetization returns to its equilibrium value (zero). The spin-lattice relaxation process is characterized by the time T_{1z}, which describes the rate the longitudinal (z) component of the magnetization returns to its equilibrium value. Since the transverse component of the magnetization vanishes at thermal equilibrium, it is always true that $T_{1z} \geq T_2$. As the spins relax, the magnetic resonance signal decays; accordingly, the signal is called a free induction decay (FID). NMR spectra in the frequency domain are obtained by digitizing the FID and then taking its Fourier transform. After the spins return to thermal equilibrium, a second pulse is applied, and the FID is measured again. Good signal to noise ratio is achieved by repeating this process and summing the accumulated FIDs.

In the above discussion, a simple account of the underlying physics of NMR spectroscopy was presented. In later sections, the experimental techniques and pulse-sequences used for this dissertation are described in detail. However, before proceeding in this direction, it is useful to reconsider the pulse-sequence given in Figure 5.2. Once the nuclear spins are rotated in the xy-plane, the spin precession, as a function of time, is determined by the time evolution operator:

$$U(t) = \exp(-iHt / \hbar).$$

This operator is governed by the nuclear spin Hamiltonian, H, which describes all the spin-interactions that affect the system. Accordingly, each spin will precess at its characteristic resonance frequency, which is determined by the various interactions

encompassed by H. Thus, we need to consider the form of the Hamiltonian that describes the spin-system.

For the purposes of this dissertation, the following Hamiltonian suffices:

$$H = H_Z + H_\sigma + H_{dd}.$$ (5.9)

Here, H_Z describes the Zeeman interaction of the spins with the external field, H_σ describes the chemical shielding by the local electron density, and H_{dd} describes the dipolar coupling among nuclear spins. For now, we have not included contributions to the Hamiltonian due to RF pulses—this will be considered when the need arises. The various secular contributions to the Hamiltonian (Eq. 5.9) are given below for a nuclear spin-system consisting of I and S spins—these formulae can be readily generalized to include more spin-types. From here on out, as a matter of convenience, we will consider the energy eigenstates in angular frequency units; thus, the cumbersome factor of $\hbar$ does not appear in the Hamiltonian.

The Zeeman Hamiltonian is given by [3]

$$H_Z = -\omega_Z^I \sum_k I_z^{(k)} - \omega_Z^S \sum_{k'} S_z^{(k')}$$ (5.10)

where k is the nuclear index, and ω_Z^A is the Zeeman frequency, which is defined as

$$\omega_Z^A = \gamma^A B_o.$$ (5.11)

Next, the chemical shielding Hamiltonian is given: [3]

$$H_\sigma = +\omega_Z^I \sum_k I_z^{(k)} \sigma_{Izz}^{(k)}(\alpha_I^{(k)}, \beta_I^{(k)}) + \omega_Z^S \sum_{k'} S_z^{(k')} \sigma_{Szz}^{(k')}(\alpha_S^{(k')}, \beta_S^{(k')}).$$ (5.12)

Here, $\sigma_{Azz}^{(k)}(\alpha^{(k)}, \beta^{(k)})$ is the electronic shielding parameter for the kth nucleus of type A. The polar angle α and the azimuthal angle β describe the orientation of the external

magnetic field ($\vec{B}_o = B_o\hat{z}$) with the principal axis system (PAS) of the shielding tensor.

The functional form of Eqs. 5.10 and 5.12 are similar; thus, it is convenient to combine them together:

$$H_\sigma = -\sum_k \Omega_I^{(k)} I_z^{(k)} - \sum_{k'} \Omega_S^{(k')} S_z^{(k')} \tag{5.13}$$

$$\Omega_A^{(k)} \equiv \omega_z^A (1 - \sigma_{zz}^{(k)}). \tag{5.14}$$

Lastly, the nuclear dipole-coupling Hamiltonian for the I-S spin system is given by

$$H_{dd} = H_{IS} + H_{II} + H_{SS}. \tag{5.15}$$

Here, H_{IS} describes the heteronuclear dipole coupling among I and S spins. H_{II} and H_{SS} describe the homonuclear dipolar coupling of the I spins and S spins, respectively. The secular portion of heteronuclear, dipole-coupling Hamiltonian is given by [3]

$$H_{IS} = \sum_{i,j} \omega_{IS}^{(ij)} (1 - 3\cos^2 \Theta_{IS}^{(ij)}) I_z^{(i)} S_z^{(j)}. \tag{5.16}$$

While, the secular portion of the homonuclear dipole-coupling Hamiltonian is given by [3]

$$H_{II} = \sum_{i<j} \omega_{II}^{(ij)} (1 - 3\cos^2 \Theta_{II}^{(ij)}) I_z^{(i)} I_z^{(j)} - \tfrac{1}{4} \sum_{i<j} \omega_{II}^{(ij)} (1 - 3\cos^2 \Theta_{II}^{(ij)}) (I_+^{(i)} I_-^{(j)} + I_-^{(i)} I_+^{(j)}). \tag{5.17}$$

Similarly, H_{SS} can be obtained from Eq. 5.17 by an interchange of labels indicating nuclear type ($I \leftrightarrow S$). In Eqs. 5.16 and 5.17, the dipolar coupling frequency is

$$\omega_{IS}^{ij} = \frac{\hbar \gamma^I \gamma^S}{r_{ij}^3}, \tag{5.18}$$

where r_{ij} is the inter-nuclear distance between the two dipoles. Lastly, Θ_{IS}^{ij} is the angle between the external field and the line that connects the two nuclear dipoles (I and S).

Typically, nuclei in many different environments contribute to the NMR signal. The salient feature to note is that the line-width of a particular contribution to the

spectrum can be severely broadened by the interactions that arise from H_σ and H_{dd}. The line broadening that arises from H_σ is through the dependence of the chemical shielding, σ_{zz}, on the orientation of the molecule with respect to the external field. Similarly, H_{dd} also depends on Θ_{IS}^{ij}. Moreover, the dipolar coupling splits the energy levels, thus leading to further broadening. Increased line-width can result in many overlapping spectral components, thus producing a single broad featureless peak. Techniques to overcome these problems will be discussed later.

5.2 NMR Techniques

5.2.1 Single π/2 Pulse Sequence

A single π/2 pulse sequence is shown graphically in Figure 5.3. At thermal equilibrium the nuclear spin polarization is aligned parallel to the external field, $B_o\hat{z}$. The $(\pi/2)_y$ pulse rotates the spin polarization along the positive x-direction. Next, the spins are allowed to precess for a time τ before the signal is acquired; the zero time-point corresponds to the end of the pulse (Figure 5.3). The NMR signal is given by the expectation value of the magnetization perpendicular to the applied field $M_\perp(t)$:[4]

$$\langle M_\perp(t) \rangle = Tr\{\rho(t)M_\perp\},\qquad(5.19)$$

where $\rho(t)$ is the reduced density matrix. It is convenient to represent $M_\perp$ using a complex notation:[4]

$$M_\perp = M_x + iM_y.\qquad(5.20)$$
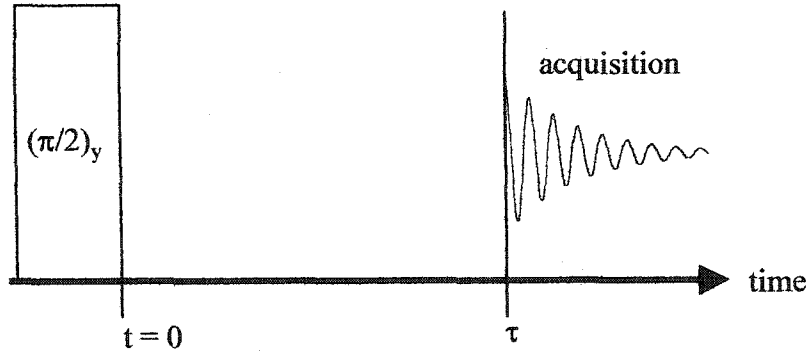
Figure 5.3:A single π/2 pulse-sequence.

This complex representation signifies that the magnetization precesses in the xy-plane, where M_x and M_y differ in phase by $90°$. For simplicity, consider a system of I spins. For this case, $M_\perp$ is rewritten as

$$M_\perp \propto \sum_k (I_x^{(k)} + iI_y^{(k)}) . \tag{5.21}$$

To compute the expectation value, the time evolution of the reduced density matrix is needed:

$$\rho(t) = \exp(-iHt)\rho(0)\exp(+iHt) , \tag{5.22}$$

where $\rho(0)$ is the initial density matrix.

For illustration purposes, we consider a single I spin ½ system in an external magnetic field along the z-direction:

$$H = -\omega_o I_z . \tag{5.23}$$

The $(\pi/2)_y$ pulse rotates the spins to be along the x-direction, so that at $t = 0$, $\rho(0)$ is proportional to I_x. Making use of both Eqs. 5.22 and 5.23, the expectation value of the magnetization (Eq. 5.19), at any time t, is proportional to

$$\left\langle M_{\perp}(t) \right\rangle \propto Tr\{\exp(-iHt)I_x \exp(+iHt)M_{\perp}\}$$

or

$$\left\langle M_{\perp}(t) \right\rangle \propto Tr\{[I_x \cos(\omega_o t) - I_y \sin(\omega_o t)](I_x + iI_y)\}.$$

Taking the trace, the expectation value for the magnetization—our NMR signal—is

$$\left\langle M_{\perp}(t) \right\rangle \propto e^{-i\omega_o t}. \tag{5.24}$$

Using the machinery of quantum mechanics, we have arrived at the anticipated result that

the spins precess around the external field at their Larmor frequency, ω_o.

However, the magnetization begins to decay as soon as the initial pulse ends; this

effect can be included phenomenologically by writing it as

$$\left\langle M_{\perp} \right\rangle \propto e^{-\frac{t}{T_2^*}} e^{-i\omega_o t}, \tag{5.25}$$

where the decay constant, T_2^*, is the transverse relaxation time, which includes effects

due to both homogenous and inhomogeneous broadening.[5] Homogenous decay describes

the loss of the spin signal's coherence due to dephasing from random fluctuation of

microscopic magnetic fields; this decay process is irreversible. While, the inhomogeneous

decay arises because the FID is a superposition of signals from many nuclear spins with

slightly different precessional frequencies. For example, at the end of a $(\pi/2)_y$ pulse, all

the spins are in phase and are aligned along the x-axis. Since the nuclear spins that are

immersed in different chemical environments or field strengths have slightly different

precessional frequencies, the magnetization will dephase over a period of time, and the

superposition of these dephased signals will interfere destructively.

The effect of decay has some very practical consequences. If the time before data

acquisition τ is much greater than T_2^*, most of the signal will be lost. If T_2^* is short, then

the time before data acquisition starts needs to be as short as possible, but the minimum value of τ is limited by magneto-acoustic ringing of the probe and the amplifier dead-time (t_{dead}), which are usually on the order of ~50µs. If $t_{dead} \sim T_2^*$ then the first few time-points in the FID may be lost, corresponding to the loss of broad (high frequency) spectral features in the Fourier transform. This problem is circumvented by using a spin-echo pulse sequence. The spin echo refocuses the magnetization outside the instrumental dead time. Only the part of the signal that has inhomogeneously dephased is refocused by the spin echo. The part of the signal that has irreversibly decayed due to spin-spin relaxation is irrecoverable by the echo.

5.2.2 Spin Echoes

Next, simple pulse sequences that generate spin echoes are described. There are two basic types of spin echoes: the Hahn echo and the solid echo. The differences between these two echoes are explained in the following sections.

5.2.2.1 The Hahn Echo

A Hahn Echo pulse sequence is $[(\pi/2)_y, \tau, \pi_x, \tau]$ and is illustrated in Figure 5.4. For simplicity, a spin-½ system is considered. First, a $(\pi/2)_y$ pulse is applied. The end of this pulse corresponds to the zero-time point at which the nuclear magnetization of the I spins is aligned along the x-direction. Next, the spins are allowed to precess for a time τ. Lastly, a π_x pulse is used to refocus the magnetization at time 2τ. The signal at time 2τ is determined from the time evolution of the reduced density matrix (see Eq. 5.22):
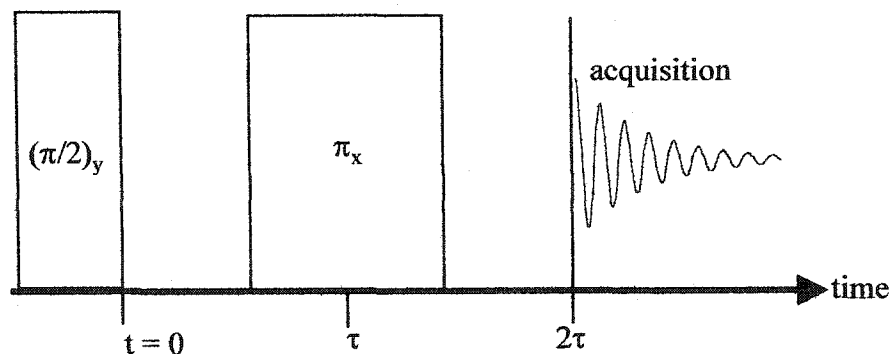
Figure 5.4: A Hahn-echo, pulse sequence.

$$\rho(2\tau) = \exp(-iH\tau)\exp(-i\pi\sum_k I_x^{(k)})\exp(-iH\tau) \times$$
$$\times \rho(0)\exp(iH\tau)\exp(i\pi\sum_k I_x^{(k)})\exp(iH\tau). \tag{5.26}$$

This unitary transformation can be represented symbolically using *arrow notation*:[6,7]

$$\rho(0) \xrightarrow{\;\;H\tau\;\;} \xrightarrow{\;\;\pi\sum_k I_x^{(k)}\;\;} \xrightarrow{\;\;H\tau\;\;} \rho(2\tau). \tag{5.27}$$

For this system, we choose a model Hamiltonian that includes contributions from both the chemical shift and heteronuclear dipolar coupling:

$$H = -\sum_k \Omega_k I_z^{(k)} + \sum_{i,j} \overline{\omega}_{IS}^{i,j} I_z^{(i)} S_z^{(j)}. \tag{5.28}$$

Here, the reduced dipolar coupling frequency, $\overline{\omega}_{IS}^{i,j}$, is defined as

$$\overline{\omega}_{IS}^{i,j} \equiv \omega_{IS}^{i,j}(1 - 3\cos^2\Theta_{IS}^{i,j}). \tag{5.29}$$

In the laboratory frame, the resonance frequency, Ω_k, includes contributions from both the Zeeman and chemical shielding terms in the Hamiltonian. However, it is more convenient to work in the rotating reference frequency (RRF) frame. In this case, Ω_k is regarded as the resonant offset frequency. Using the Hamiltonian (5.28), the *arrow* diagram is expressed as

In the laboratory frame, the resonance frequency, Ω_k, includes contributions from both the Zeeman and chemical shielding terms in the Hamiltonian. However, it is more convenient to work in the rotating reference frequency (RRF) frame. In this case, Ω_k is regarded as the resonant offset frequency. Using the Hamiltonian (5.28), the *arrow* diagram is expressed as

$$\rho(0) \xrightarrow{-\sum_k \Omega_k \tau I_z^{(k)} + \sum_{i,j} \overline{\omega}_{IS}^{(i,j)} \tau I_z^{(i)} S_z^{(j)}} \xrightarrow{\pi \sum_k I_x^{(k)}} \xrightarrow{-\sum_k \Omega_k \tau I_z^{(k)} + \sum_{i,j} \overline{\omega}_{IS}^{(i,j)} \tau I_z^{(i)} S_z^{(j)}} \rho(2\tau)$$

or

$$\rho(0) \xrightarrow{\sum_{i,j} \overline{\omega}_{IS}^{(i,j)} \tau I_z^{(i)} S_z^{(j)}} \xrightarrow{-\sum_k \Omega_k \tau I_z^{(k)}} \xrightarrow{\pi \sum_k I_x^{(k)}} \xrightarrow{-\sum_k \Omega_k \tau I_z^{(k)}} \xrightarrow{\sum_{i,j} \overline{\omega}_{IS}^{(i,j)} \tau I_z^{(i)} S_z^{(j)}} \rho(2\tau)$$

and is simplified with use of the identity for spin-½ operators:

$$\exp(i\Omega\tau I_z)\exp(-i\pi I_x) = \exp(-i\pi I_x)\exp(-i\Omega\tau I_z).$$

This identity is verified by noting that $exp(-i\pi I_x)=-2iI_x$ and that the Pauli operator I_x anticommutes with I_z. Using these identities, the arrow diagram can be rearranged:

$$\rho(0) \xrightarrow{\sum_{i,j} \overline{\omega}_{IS}^{(i,j)} \tau I_z^{(i)} S_z^{(j)}} \xrightarrow{\pi \sum_k I_x^{(k)}} \xrightarrow{+\sum_k \Omega_k \tau I_z^{(k)}} \xrightarrow{-\sum_k \Omega_k \tau I_z^{(k)}} \xrightarrow{\sum_{i,j} \overline{\omega}_{IS}^{(i,j)} \tau I_z^{(i)} S_z^{(j)}} \rho(2\tau)$$

$$\rho(0) \xrightarrow{\sum_{i,j} \overline{\omega}_{IS}^{(i,j)} \tau I_z^{(i)} S_z^{(j)}} \xrightarrow{\pi \sum_k I_x^{(k)}} \xrightarrow{\sum_{i,j} \overline{\omega}_{IS}^{(i,j)} \tau I_z^{(i)} S_z^{(j)}} \rho(2\tau).$$

Repeating a similar simplification step, the *arrow* diagram is reduced to

$$\rho(0) \xrightarrow{\pi \sum_k I_x^{(k)}} \rho(2\tau). \tag{5.30}$$

Noting that $\rho(0) \propto \sum_k I_x^{(k)}$, we can thus write

$$\sum_k I_x^{(k)} \rightarrow \sum_k I_x^{(k)}.$$
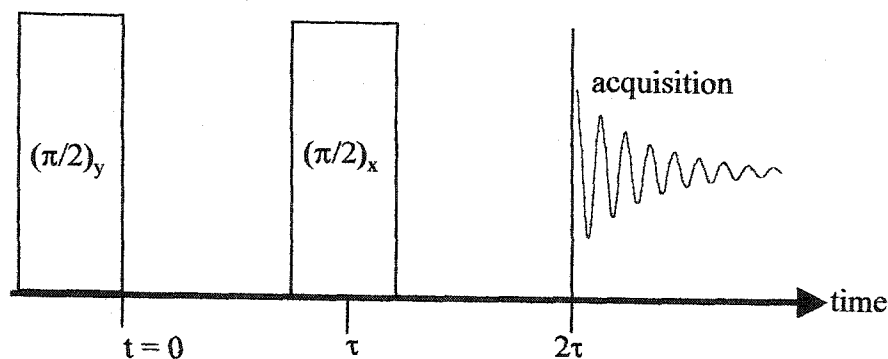
Figure 5.5: A solid echo pulse-sequence.

5.2.2.2 The Solid Echo

The solid echo pulse-sequence is described by $[(\pi/2)_y, \tau, (\pi/2)_x, \tau]$ and is shown in Figure 5.5. The second $\pi/2$ pulse must have a phase difference of $\pi/2$ with respect to the first pulse, and both must be applied on resonance. Taking the zero time-point at the end of the $(\pi/2)_y$ pulse, the time evolution of the reduced density matrix for the solid echo is represented as

$$\rho(0) \xrightarrow{H\tau} \xrightarrow{\frac{\pi}{2}\sum_k I_x^{(k)}} \xrightarrow{H\tau} \rho(2\tau). \tag{5.31}$$

A system of two nuclei with spin ½ is considered and $\rho(0)$ is given by

$$\rho(0) = \sum_{k=1}^{2} I_x^{(k)} = I_x^{(1)} + I_x^{(2)}.$$

For this system, we choose a Hamiltonian that describes chemical shift (Eq. 5.13) and homonuclear dipolar coupling (Eq. 5.17):

$$H = -\sum_{k=1}^{2} \Omega_k I_z^{(k)} + \overline{\omega}_{II}^{(1,2)} [I_z^{(1)} I_z^{(2)} - \frac{1}{4}(I_+^{(1)} I_-^{(2)} + I_-^{(1)} I_+^{(2)})],$$

where $\overline{\omega}_{II}^{(1,2)}$ is the homonuclear dipole coupling frequency—the bar indicates inclusion of the geometrical part (see Eq. 5.29). The solid echo does not refocus resonant offsets, Ω_k (or heteronuclear dipolar coupling).[3] Thus, we consider the case for which resonant offset frequencies vanish ($\Omega_k = 0$):

$$H = \overline{\omega}_{II}^{(1,2)}[I_z^{(1)}I_z^{(2)} - \frac{1}{4}(I_+^{(1)}I_-^{(2)} + I_-^{(1)}I_+^{(2)})]$$

or

$$H = \frac{\overline{\omega}_{II}^{(1,2)}}{2}[3I_z^{(1)}I_z^{(2)} - \vec{I}^{(1)} \cdot \vec{I}^{(2)}]. \tag{5.32}$$

For the above Hamiltonian, the *arrow* diagram is written as

$$(I_x^{(1)} + I_x^{(2)}) \xrightarrow{\frac{3}{2}\overline{\omega}_{II}^{(1,2)}\tau I_z^{(1)}I_z^{(2)}} \xrightarrow{\frac{\pi}{2}\sum_{k=1}^{2}I_x^{(k)}} \xrightarrow{\frac{3}{2}\overline{\omega}_{II}^{(1,2)}\tau I_z^{(1)}I_z^{(2)}} \rho(2\tau).$$

Note that the scalar coupling term, $\vec{I}^{(1)} \cdot \vec{I}^{(2)}$, is dropped, since it commutes with both $I_z^{(1)}I_z^{(2)}$ and ($I_x^{(1)} + I_x^{(2)}$). This diagram is further reduced by the following steps:

$$(I_x^{(1)} + I_x^{(2)}) \xrightarrow{\frac{\pi}{2}\sum_{k=1}^{2}I_x^{(k)}} \xrightarrow{-\frac{\pi}{2}\sum_{k=1}^{2}I_x^{(k)}} \xrightarrow{\frac{3}{2}\overline{\omega}_{II}^{(1,2)}\tau I_z^{(1)}I_z^{(2)}} \xrightarrow{\frac{\pi}{2}\sum_{k=1}^{2}I_x^{(k)}} \xrightarrow{\frac{3}{2}\overline{\omega}_{II}^{(1,2)}\tau I_z^{(1)}I_z^{(2)}} \rho(2\tau)$$

$$(I_x^{(1)} + I_x^{(2)}) \xrightarrow{-\frac{\pi}{2}\sum_{k=1}^{2}I_x^{(k)}} \xrightarrow{\frac{3}{2}\overline{\omega}_{II}^{(1,2)}\tau I_z^{(1)}I_z^{(2)}} \xrightarrow{\frac{\pi}{2}\sum_{k=1}^{2}I_x^{(k)}} \xrightarrow{\frac{3}{2}\overline{\omega}_{II}^{(1,2)}\tau I_z^{(1)}I_z^{(2)}} \rho(2\tau)$$

$$(I_x^{(1)} + I_x^{(2)}) \xrightarrow{\frac{3}{2}\overline{\omega}_{II}^{(1,2)}\tau I_y^{(1)}I_y^{(2)}} \xrightarrow{\frac{3}{2}\overline{\omega}_{II}^{(1,2)}\tau I_z^{(1)}I_z^{(2)}} \rho(2\tau). \tag{5.33}$$

Note that in the first line, a product of exponential factors was inserted that equals unity, and in the third line, the first three arrows are combined. Although the analysis is not worked out explicitly, the above arrow diagram does refocus the magnetization. The refocusing is clearly suggested by noting the commutation relation (for spin-½ operators):

$$\left[I_z^{(1)}I_z^{(2)}, \left[I_y^{(1)}I_y^{(2)}, (I_x^{(1)} + I_x^{(2)})\right]\right] = -(I_x^{(1)} + I_x^{(2)}).$$

Indeed, explicit evaluation of the operator products in Eq. 5.33 demonstrates the solid echo:

$$I_x^{(1)} + I_x^{(2)} \longrightarrow I_x^{(1)} + I_x^{(2)}.$$

This analysis applies to systems with homonuclear coupling between two spins, but can be extended to homonuclear systems with more than two spins, only if the other spin couplings are weak—if the Hamiltonian, described in Eq. 5.32, reasonably approximates the system.

5.2.3 Methods to Suppress Line Broadening

In solid state NMR, line-broadening mechanisms due to dipolar coupling and chemical shift anisotropy greatly limit spectral resolution. To clarify, consider NMR of liquids. The molecules in a liquid flow under shear force and thus have a large range of motion. Consequently, the isotropic molecular motion averages out the dipolar coupling and reduces the chemical shift to its isotropic value. In contrast, this isotropic motional averaging does not occur in solids. Dipolar coupling between spins splits the nuclear energy levels, thus broadening the spectrum. Furthermore, the precessional frequencies of the nuclear spins are dependent on the spin's orientation with respect to the applied field. This orientational dependence is reflected by the angular factor $(1-3\cos^2\theta)$ in the dipolar coupling frequency (see Eqs. 5.16, 17, and 29) and by the functional dependence on the orientation of the principle axis of the shielding tensor, σ_{zz}, with respect to the applied field (see Eq. 5.12).

For a powdered sample, all molecular orientations are possible, and the spectrum will be a broad powder pattern. The problem of line broadening is further exacerbated, if

the sample also includes a distribution of bonding configurations. In this case, the spectrum will consist of many overlapping powder patterns. Moreover, the important discontinuities observed in a single powder pattern will be washed out by spectral overlap.[8] In the following sub-sections, several experimental methods used to suppress line broadening are described.

5.2.3.1 Magic Angle Spinning

By mechanically spinning the sample at a high velocity, line broadening from dipolar coupling and chemical shift anisotropy can be greatly suppressed. If the sample is spun about an axis that makes an angle of $\arccos\sqrt{\frac{1}{3}}$ with respect to the external field, dipolar-coupling interactions can be averaged to zero, and the chemical shielding tensor can be averaged to its isotropic value. Complete averaging is only provided if the spinning rate, v_r, is much greater than the interaction strength to be averaged. This means that ω_r needs to be much greater than both the dipolar coupling strength ω_d, and the anisotropy of the chemical shielding tensor.[8]

The angle $\arccos\sqrt{\frac{1}{3}}$ is known as the magic angle and is the angle at which the angular term $(1-3\cos^2\theta)$ vanishes. These angular factors arise in the dipolar precessional frequencies (Eq. 5.29). By spinning the sample at the magic angle with a rate $\omega_r \gg \omega_d$, the time average of $(1-3\cos^2\theta(t))$ vanishes; thus, the dipolar Hamiltonian is averaged out. The averaging of the chemical shielding tensor by magic angle spinning (MAS) is discussed next.

Table 5.1: A listing of the irreducible spherical tensors that describe the secular terms of the chemical shielding Hamiltonian (Eq. 5.34). [8]

A_{00}	$-\frac{\gamma}{\sqrt{3}} Tr(\sigma_{ij})$
A_{20}	$\frac{\gamma}{\sqrt{6}}\left[3\sigma_{zz} - Tr(\sigma_{ij})\right]$
T_{00}	$-\frac{1}{\sqrt{3}} I_z B_o$
T_{20}	$\frac{2}{\sqrt{6}} I_z B_o$

In a frame fixed to the rotor, the chemical shielding Hamiltonian is conveniently expressed in terms of irreducible spherical tensors as [8]

$$H_\sigma^{Rotor} = A_{00}T_{00} + A_{20}T_{20},$$ (5.34)

where for reference, the A_{kq} and T_{kq} are given in Table 5.1. For convenience, our model system consists of single spin-½ nucleus. In the rotating reference frame (RRF) frame, the chemical shielding Hamiltonian is dependent on time, as imposed by the spinning of the sample. Transforming the Hamiltonian to the RRF frame yields [8]

$$H_\sigma^{MAS} = A_{00}T_{00} + A_{20}(t)T_{20},$$ (5.35)

$$A_{20}(t) = \sum_{q=-2} A_{2q} \exp(-iq\omega_r t) d_{q0}^{(2)}(\beta).$$ (5.36)

Here, $d_{mn}^{(j)}$ is a reduced rotation matrix, $\omega_r t$ and β are the Euler angles specifying the transformation between the RRF and rotor frames (see Figure 5.6 for a schematic). If the spinning rate, ω_r, is much larger than the chemical shift anisotropy, Eq. 5.36 is safely replaced by its time average: [8]

$$\langle A_{20}(t)\rangle = A_{20} d_{00}^{(2)}(\beta)$$

$$= \tfrac{1}{2} A_{20}(3\cos^2\beta - 1).$$ (5.37)
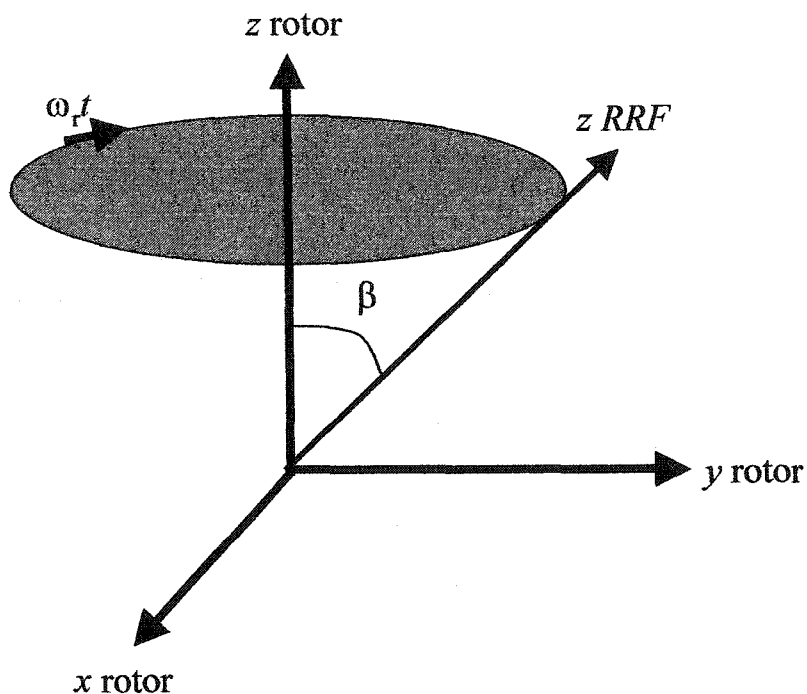
Figure 5.6: A schematic of the orientation between the frame fixed to the rotor and the RRF frame.

If the rotor-axis is oriented at the magic angle $(\beta = \arccos\sqrt{\tfrac{1}{3}})$, $\langle A_{20}(t)\rangle$ vanishes. Then the MAS chemical-shielding Hamiltonian is given by

$$H_\sigma^{MAS} = \frac{\gamma}{3}Tr[\sigma_{ij}]I_z \qquad (5.38)$$

$$= \gamma\sigma_{iso}I_zB_o.$$

Thus, MAS reduces the chemical shielding tensor to its isotropic value, as observed in liquid NMR.

By spinning the sample, the magnetization is modulated by the spinning frequency. These modulations show up as spinning side bands in the frequency domain spectrum. The expectation value of the magnetization has the form:

$$\langle M_\perp(t) \rangle \propto \exp[-i\Psi(t)]$$

$$\Psi(t) = \int \omega(t')dt' \,. \tag{5.39}$$

The above expression is just a generalized version of Eq. 5.24. The time dependence of the phase, $\Psi(t)$, is periodic with the rotor period. Thus, the magnetization can be expanded in a Fourier series that reflects this periodicity:

$$\langle M_\perp(t) \rangle \propto \sum_{N=-\infty}^{\infty} I_N \exp(iN\omega_r t) \,, \tag{5.40}$$

where I_N is the intensity of the Nth spinning side band. In theory, the intensity of the various Fourier components, I_N, can be analyzed to determine the principal elements of the chemical shielding tensor.[8] Although the side bands contain useful information, they can also complicate chemical shift assignments by crowding the spectrum. In particular, if the chemical shift anisotropy is very large or the spinning rate too low, the side bands will not be completely separated from the central band. Thus, the side bands will obscure and overlap with spectral regions of interest. To circumvent these problems, side-band suppression techniques have been developed.[9-11]

5.2.3.2 Total Suppression of Spinning Side bands

Since spinning side bands often complicate chemical shift assignments, total suppression of spinning side band (TOSS) techniques were developed to eliminate them. A schematic of a 4-pulse, TOSS sequence is shown in Figure 5.7. Variations of the 4-pulse, TOSS sequences exist [9-11] as well as others incorporating 5, 6, and 9 pulses.[9,11] However, the 4-pulse TOSS sequence shown in Figure 5.7 is the one used in this dissertation.[10]
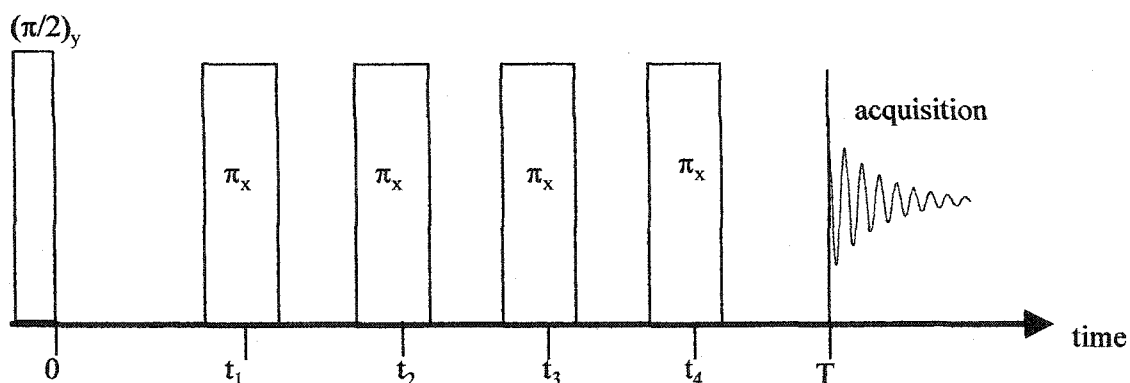
Figure 5.7: A 4-pulse, TOSS sequence follows the initial $(\pi/2)_y$ pulse and consists of four π_x pulses with timings t_1, t_2, t_3, and t_4.

Referring to Figure 5.7, the initial magnetization is prepared along the x-direction in the RRF frame following the $(\pi/2)_y$ pulse, and the TOSS sequence follows with four π_x pulses. By choosing appropriate spacing between the π_x pulses, the side bands are eliminated. A theoretical description of TOSS, which closely follows the treatment given by Antzutkin et al.,[11] is given below.

In this discussion, a powdered sample with many chemically-equivalent, spin-½ nuclei is considered. These sites all have the same chemical shift, but with different orientations in space. It is useful to consider only one carousel of sites at a time. A carousel is defined as follows. Consider the coordinate system attached to the rotor, which spins around its z-axis. A carousel is composed of equivalent sites that are located at the same distance from the origin and are brought into coincidence as the rotor spins.[11] These sites all have the same polar angle, with respect to the rotor's z-axis, but with different azimuthal angles, γ. For members of the same carousel, we are considering those sites whose principal axis system (PAS) comes into coincidence as the sample spins. The

NMR signal for a carousel is obtained by an integral over γ, and the total NMR signal is obtained by summing over contributions from all carousels.

For the 4-pulse TOSS sequence (see Figure 5.7), the total accumulated phase at time T for a spin-packet on a particular carousel is given by [11]

$$\Psi_c(T;\gamma) = \Phi_c(t_1 - 0;\gamma) + e^{i\pi}\Phi_c(t_2 - t_1;\gamma) + \Phi_c(t_3 - t_2;\gamma) + \\ + e^{i\pi}\Phi_c(t_4 - t_3;\gamma) + \Phi_c(T - t_4;\gamma),$$ (5.41)

where the contributing phases are

$$\Phi_c(t_b - t_a;\gamma) = \int_{t_a}^{t_b} dt\, \omega_c(t;\gamma).$$ (5.42)

In the above formulae, the subscript c refers to a particular carousel, and γ refers to azimuthal angle in the rotor frame for a particular spin-packet on the carousel. Since the sample is spinning, with a periodicity of the rotor period, the precessional frequency can be decomposed into a Fourier series.[8,11]

$$\omega_c(t;\gamma) = \sum_{m=-2}^{2} \omega_c^{(m)} \exp[im(\omega_r t + \gamma)].$$ (5.43)

Substituting this Fourier decomposition into Eq. 5.42 and integrating over time gives [11]

$$\Phi_c(t_b - t_a;\gamma) = \omega_c^{(0)}(t_b - t_a) + \xi(t_b;\gamma) - \xi(t_a;\gamma),$$ (5.44)

where the functions $\xi(t;\gamma)$ are defined by [12]

$$\xi(t;\gamma) \equiv \sum_{m \neq 0} \frac{\omega_c^{(m)} \exp[im(\omega_r t + \gamma)]}{im\omega_r}.$$ (5.45)

Using Eqs 5.44-45, the total accumulated phase (Eq. 5.41) is conveniently expressed as

$$\Psi_c(T;\gamma) = \xi(T;\gamma) + [T - 2\sum_{p=1}^{4}(-)^p t_p]\omega_c^{(0)} - [\xi(0;\gamma) + 2\sum_{p=1}^{4}(-)^p \xi(t_p;\gamma)].$$ (5.46)

According to Eq. 5.39, the signal in the time domain, for a spin-packet on carousel c with azimuthal angle γ, has the form:

$$\left\langle M_\perp^c(T+t;\gamma) \right\rangle \propto \exp\{-i[\omega_c^{(0)}t + \xi(T+t;\gamma) - \xi(T;\gamma) + \Psi_c(T;\gamma)]\}. \qquad (5.47)$$

A TOSS sequence is designed to enforce the following requirement on $\Psi_c(T;\gamma)$:[11]

TOSS Condition
$$\xi(0) + 2\sum_p (-)^p \xi(t_p) = 0. \qquad (5.48)$$

If the TOSS condition is satisfied, the time domain signal (Eq. 5.47) is given by

$$\left\langle M_\perp^c(T+t;\gamma) \right\rangle \propto \exp(-i\omega_c^{(0)}(t+\tau_{seq})) \exp(-i\xi(T+t;\gamma)) \qquad (5.49)$$

$$\tau_{seq} \equiv T - 2\sum_p (-)^p t_p .$$

The total TOSS signal for a particular carousel is given by the γ–average over Eq. 5.49 and can be shown to have the form:[11]

$$\overline{\left\langle M_\perp^c(T+t) \right\rangle}_\gamma = \exp[-i\omega_c^{(0)}(t+\tau_{seq})]\overline{f_c}, \qquad (5.50)$$

where $\overline{f_c}$ is a phase function that it is independent of both γ and time. By inspection of Eq. 5.50, it is clear that the only surviving Fourier component is the one for the central band—the side bands are eliminated.

Although not a necessary condition, it is useful to design a TOSS sequence so that

the Hahn-echo condition is satisfied:[11]

$$\tau_{seq} = T - 2\sum_p (-)^p t_p = 0. \tag{5.51}$$

If the Hahn echo condition is satisfied, Eq. 5.50 is replaced by

$$\overline{\langle M_\perp^c(T+t)\rangle_\gamma} = \exp[i\omega_c^{(0)}t]\overline{f_c}. \tag{5.52}$$

The Hahn-echo condition eliminates the need for a phase shift correction due to τ_{seq}, which is dependent on the particular TOSS sequence used.

Making use of Eq. 5.45, the TOSS condition (Eq. 5.48) is written as the following set of equations:

$$\sum_{p=1}^{4}(-)^p \sin m\omega_r t_p = 0 \qquad m = 1, 2$$

$$\sum_{p=1}^{4}(-)^p \cos m\omega_r t_p = \frac{1}{2} \qquad m = 1, 2. \tag{5.53}$$

Solutions to this set of four non-linear equations give the pulse timings, t_p, for the TOSS sequence in Figure 5.7. For a four-pulse sequence, there are four equations and four unknowns; thus, the problem is completely determined. The reader is referred to Lang [10] for a short exposition on the solutions. The pulse timings for the sequence used in this dissertation are given in Table 5.2, and these are expressed in terms of fractional rotor periods:

$$\Theta_p = \frac{\omega_r t_p}{2\pi}. \tag{5.54}$$

It is noted that these pulse timings (Table 5.2) also satisfy the Hahn echo condition (Eq. 5.51).

Table 5.2: The pulse timings used for the 4-pulse TOSS sequence implemented in this research. The pulse timings Θ_p are expressed in terms of fractional rotor periods.

pulse	t_1	t_2	t_3	t_4	T
Θ_p	0.811179	1.769947	2.188821	3.230053	4.000000

For our TOSS sequence, data acquisition does not begin until after four rotor periods. However, in some applications, a long pulse sequence may be disadvantageous. If the spin-spin relaxation time is short, some of the signal intensity will be lost during the time interval before acquisition, thus reducing signal-to-noise ratio. This suggests that high spinning rates should be used to make the rotor period as short as possible. At high spinning rates, the length of the pulse sequence is shortened due to the closer spacing between the t_p. In practice, TOSS sequences at high spinning rates often can not be implemented, because the pulses all have finite width and will overlap if too closely spaced. Our particular choice of TOSS sequence was selected with these considerations in mind. The reader is referred to the literature to compare our choice (Table 5.2) with other TOSS sequences.[9-11]

5.2.3.3 Proton Decoupling

In a MAS experiment, the dipolar coupling is suppressed by mechanically spinning the sample at the *magic angle*. The time average of the dipolar coupling will vanish to first order, and this averaging is complete if the spinning rate is much greater than the dipolar coupling strength. However, since ^1H has a large magnetogyric ratio, ^{13}C or ^{15}N dipolar coupling to protons are often too large to completely average with MAS.
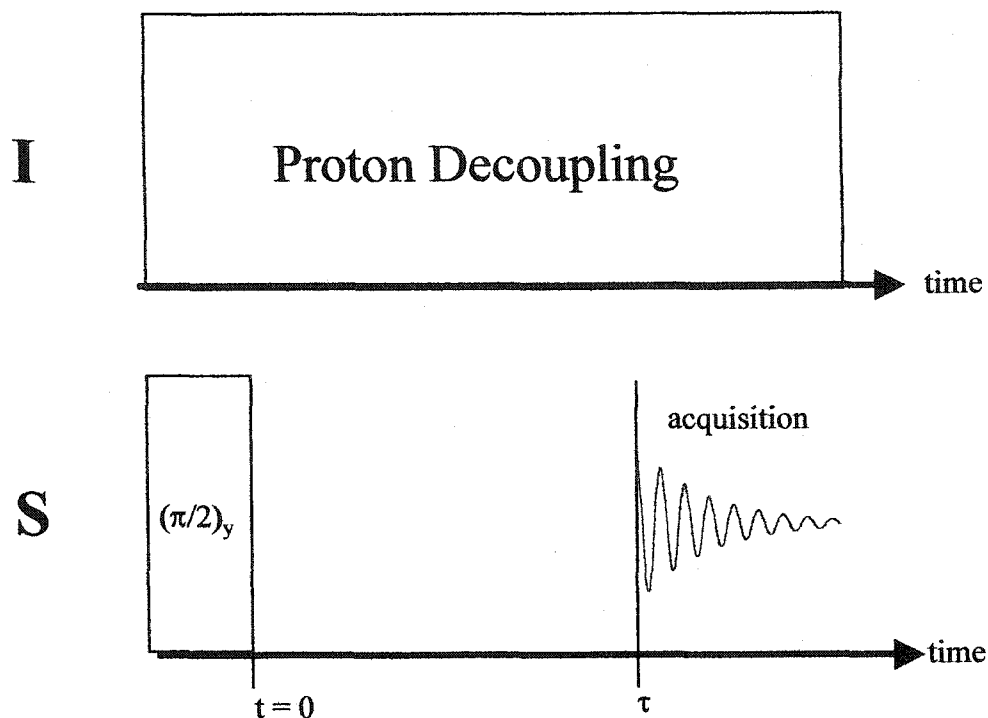
Figure 5.8: A simple $\pi/2$ pulse sequence (S-channel) with proton decoupling (I-channel).

For instance, the ^1H-^{15}N dipolar coupling frequency is on the order of 10 kHz for a directly bonded proton to nitrogen. This interaction strength is ~2.5 times larger for directly bonded ^1H to ^{13}C, since the magnetogyric ratio for ^{13}C is ~2.5 times larger than for ^{15}N. The high mechanical-spinning rates needed to completely average these interactions were unavailable. Typical attainable spinning speeds (used in this work) were 8-10 kHz, and are comparable to ^1H-^{15}N and ^1H-^{13}C dipolar coupling strengths. Therefore, continuous-wave proton decoupling was used to suppress the heteronuclear dipolar couplings to protons.

A simple pulse sequence with continuous-wave proton decoupling is shown in Figure 5.8. The I and S channels are irradiated simultaneously; the I channel corresponds to protons, while the S channel corresponds to ^{13}C or ^{15}N. A single-$\pi/2$-pulse sequence is

shown. During the time that the S spins precess before data acquisition, a continuous, RF, decoupling field is applied simultaneously to the proton (I) channel, throughout the duration of the experiment—including data acquisition of the S-spin signal. By continuously irradiating the protons at their Larmor frequency, the protons rapidly oscillate between their spin-up and spin-down eigenstates. If the strength of the decoupling field is large enough, these oscillations average out ^{1}H-S interaction, thus decoupling the S spins from the protons (I).

As a simple illustration of proton decoupling, we consider the following model Hamiltonian in the doubly rotating frame:

$$H = \overline{\omega}_d I_z S_z + \omega_{1I} I_x, \tag{5.55}$$

where ω_{1I} is the decoupling field strength applied along the x-direction in the proton's RRF frame, and for simplicity, resonance offsets due to chemical shift are neglected. During the course of the experiment, the time evolution of the density matrix is determined by the propagator:

$$\exp(-iHt).$$

Using the Hamiltonian given in Eq. 5.55, the propagator can be split into two terms:

$$\exp(-iHt) = \exp(-i\omega_{1I} I_x t) T \exp\left(-i \int_0^t \overline{\omega}_d t \tilde{I}_z S_z\right). \tag{5.56}$$

The separation of the first factor from the time ordered product is described elsewhere.[7] Here, $\tilde{I}_z$ is expressed in the so-called toggling frame:[7]

$$\tilde{I}_z = \exp(i\omega_{1I} t I_x) I_z \exp(-i\omega_{1I} t I_x)$$

$$\tilde{I}_z = I_z \cos(\omega_{1I} t) + I_y \sin(\omega_{1I} t). \tag{5.57}$$

Applying average-Hamiltonian theory to zero order,[7] the time integral in (Eq. 5.56) vanishes, if the RF decoupling field strength is much greater that the dipolar coupling ($\omega_{1I} \gg \bar{\omega}_d$). In this case, the I spin is decoupled from the S spin, and consequently, the line-shape of the S-spin spectra is narrowed.

From the above example, it may seem reasonable to assume that for the I spins to be decoupled, it is sufficient to ensure that the condition $\omega_{1I} \gg \bar{\omega}_d$ is satisfied. This is true only if the homonuclear coupling among protons can be neglected, as assumed in Eq. 5.55. If these interactions can not be neglected, then the decoupling field strength should also be greater than the I-I coupling strength. The flip-flop terms in the homonuclear dipole-coupling Hamiltonian can modulate the I-S interaction, and in fact, narrow the line-shape.[8] If the decoupling field is not larger than the I-I coupling, the decoupling may instead broaden the spectrum.[8]

5.2.4 Cross Polarization Methods

Cross polarization is an experimental technique that is used to transfer spin polarization from an abundant spin system to a rare spin. Physically, this transfer takes place via the strong, heteronuclear, dipolar interactions that couple the two, spin systems. Cross polarization can lead to a large signal enhancement of the rare spins, thus increasing sensitivity. The limiting value of signal enhancement is determined by the ratio: (γ_I/γ_S). For protons (I) coupled to ^{13}C or ^{15}N nuclei (S), this corresponds to a signal enhancement of c.a. 4 for ^{13}C and c.a. -10 for ^{15}N. This technique is of paramount importance in solid-state NMR spectroscopy. Typical organic samples have a large abundance of protons, which are coupled to sparse ^{13}C or ^{15}N nuclei. Because of the low

natural abundance of ^{13}C and ^{15}N nuclei and their small magnetogyric ratios, the observed signals from these nuclei are usually weak. However, cross polarization techniques can provide a large signal enhancement, thus overcoming the problem of small signal to noise ratios. The physics of cross polarization is explained in the following sub-sections.

5.2.4.1 Polarization Transfer Between a Coupled I-S Spin Pair

In this subsection, a spin system consisting of a coupled I-S spin pair is examined, where the I spin is a proton and S a rare nucleus. This pedagogical example illustrates several quintessential features of the cross-polarization process. A schematic of the pulse sequence used to prepare the I-S spin system is shown in Figure 5.9. An initial $(\pi/2)_y$ pulse rotates the I-spin polarization along the x-axis in the rotating frame of the I nucleus. Next, a continuous RF field locks the I polarization along its x-axis. Simultaneously, a continuous RF field is applied along the x-axis of the S spin in its respective frame; this is the mixing period (Figure 5.9). After the mixing period, proton decoupling is applied to the I channel to suppress the I-S coupling.

During the spin-locking/mixing period, the Hamiltonian is

$$H = \omega_{1I} I_x + \omega_{1S} S_x + \overline{\omega}_d I_z S_z.$$

Here, resonant offsets due to chemical shift are neglected and the RF-field strengths for the I and S spins are ω_{1I} and ω_{1S}, respectively. It is convenient to transform this Hamiltonian to a tilted frame:

$$H = \omega_{1I} I_z + \omega_{1S} S_z + \overline{\omega}_d I_x S_x$$

or equivalently
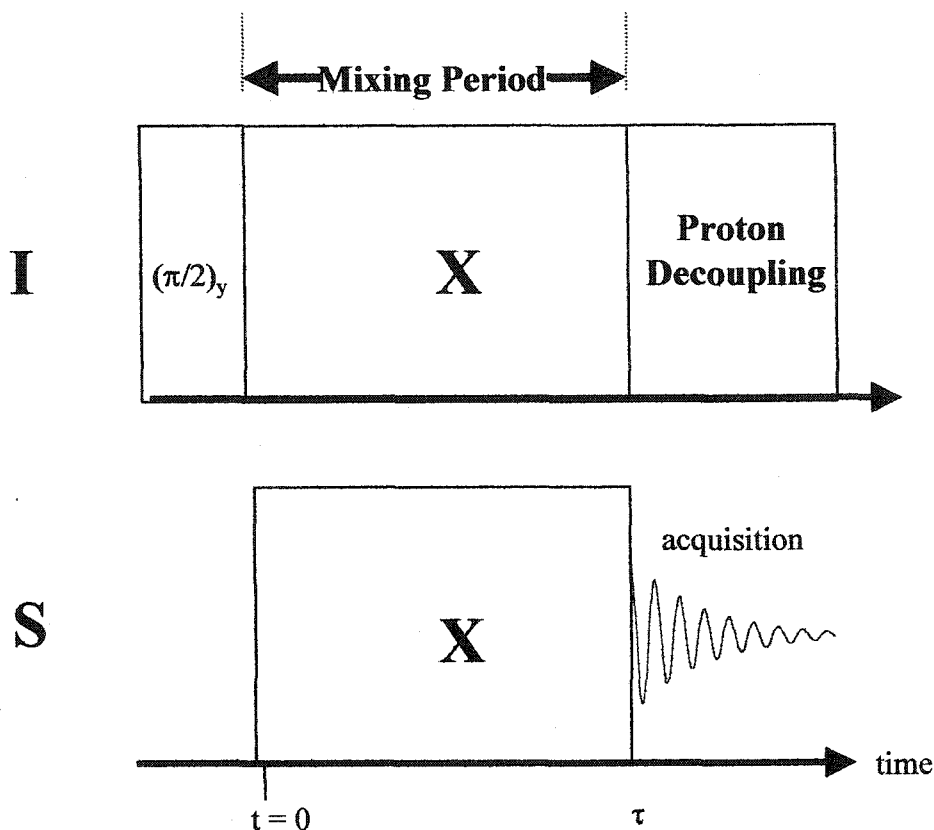
Figure 5.9: A cross-polarization sequence for transferring spin polarization from the I spins to the S spins. First, a $(\pi/2)_y$ pulse rotates the I spins along the x-axis in its the rotating frame. Next, during the mixing period, the I spins are spin-locked along its x-axis. Simultaneously, a continuous RF field is applied along the x-axis of the S spins. Polarization transfer occurs during the mixing period. Data acquisition begins at time τ, during which proton decoupling is applied.

$$H = \omega_{1I} I_z + \omega_{1S} S_z + \overline{\omega}_d (I_x S_x + I_y S_y) - \overline{\omega}_d I_y S_y$$

$$= \omega_{1I} I_z + \omega_{1S} S_z + \frac{\overline{\omega}_d}{2} (I_+ S_- + I_- S_+) - \overline{\omega}_d I_y S_y. \tag{5.58}$$

Here the easiest case is treated; it is assumed that the two, RF-field strengths are equal:

The Hartmann-Hahn Condition $\qquad \omega_{1I} = \omega_{1S}.$ $\qquad\qquad$ (5.59)

This is the Hartmann-Hahn condition. Under this condition, the Hamiltonian in Eq. 5.58 is rewritten as

$$H = \omega_1(I_z + S_z) + \frac{\overline{\omega}_d}{2}(I_+S_- + I_-S_+) . \tag{5.60}$$

It is assumed that the ω_1 term provides the dominant contribution to the Hamiltonian (i.e. $\omega_1 \gg \overline{\omega}_d$). Thus, the non-secular term, the last term in Eq. 5.58, is neglected. In the tilted frame, the signal in the time domain is proportional to

$$\left\langle M_{S_z} \right\rangle = Tr\{S_z \exp(-iHt)\rho(0)\exp(+iHt)\} . \tag{5.61}$$

For this analysis, we assume that the initial density matrix is prepared such that $\rho(0) = I_z$.[7] The initial density matrix is separated into two terms:

$$\rho(0) = \frac{1}{2}(I_z - S_z) + \frac{1}{2}(I_z + S_z) . \tag{5.62}$$

It is convenient to write the density matrix this way, since the term $(I_z + S_z)$ commutes with the Hamiltonian and is, therefore, invariant under the action of the time evolution operator. Thus, the time evolution is completely governed by the first term of $\rho(0)$:

$$\exp(-iHt)\rho(0)\exp(+iHt) = \tfrac{1}{2}\exp(-iHt)(I_z - S_z)\exp(+iHt) + \tfrac{1}{2}(I_z + S_z) . \tag{5.63}$$

Furthermore, with use of the Baker-Hausdorff lemma:[1]

$$\exp(iG\lambda)A\exp(-iG\lambda) = A + i\lambda[G,A] + \frac{i^2\lambda^2}{2!}[G,[G,A]] + \frac{i^3\lambda^3}{3!}[G,[G,[G,A]]] + ... ,$$

it is easy to show that

$$\exp(-iHt)(I_z - S_z)\exp(+iHt) = (I_z - S_z)\cos\overline{\omega}_d t + 2(I_xS_y - I_yS_x)\sin\overline{\omega}_d t . \tag{5.64}$$

Using these results, an expression for the signal is obtained:

$$\left\langle M_{S_z} \right\rangle = \tfrac{1}{2}\sin^2\frac{\overline{\omega}_d}{2}t . \tag{5.65}$$

This shows that under the Hartmann-Hahn condition (Eq. 5.59), half of the I-spin polarization is   transferred to the S spin, with a periodic oscillatory dependence

of $\overline{\omega}_d / 2$. If the Hartmann-Hahn condition is not met, our result (Eq. 5.65) is generalized

to [7]

$$\left\langle M_{S_z} \right\rangle = \tfrac{1}{2}\sin^2 \phi \sin^2 \frac{\sqrt{\Delta^2 + \overline{\omega}_d^2}}{2} t , \tag{5.66}$$

where Δ and the angle ϕ are defined as [7]

$$\Delta \equiv \omega_{1I} - \omega_{1S}$$

$$\tan \phi \equiv \frac{\overline{\omega}_d}{\Delta} . \tag{5.67}$$

According to Eq. 5.66, the Hartmann-Hahn condition is fulfilled when $\phi = \pi/2$. If the RF

fields for the I and S spins are far from the matching condition (Eq. 5.59), the angle ϕ is

small (Eq. 5.67), and the polarization transfer will disappear (Eq. 5.66). In this discussion,

resonant offsets due to chemical shifts were neglected; the monograph by Ernst *et al.*

treats this case in detail.[7] In brief, if the Hartmann-Hahn condition is fulfilled, the effect

of resonant offset is to scale the frequency, such that the period of oscillation becomes

longer.

5.2.4.2 Thermodynamic Treatment of Cross Polarization

If the spin system consists of a single rare spin that is coupled to many abundant

spins, the Hamiltonian describing this situation is very complicated:

$$H = H_I + H_S + H_{IS} + H_{II} .$$

In particular, the presence of many-body interactions makes integration of the Liouville-

von Neuman equation intractable. For this case, a theoretical framework has been

developed to describe the cross-polarization process using a thermodynamic picture.

Before proceeding with this description, it is useful to recall the results obtained for the two-spin, *IS* system discussed in the previous subsection. If the Hartman-Hahn condition is met, the polarization is transferred from the *I* spin to the *S* spin, with an oscillatory dependence determined by half the dipolar coupling frequency (Eq. 5.65). In the case of many *I* spins coupled to a single *S* spin, the oscillations are damped out and the *S* spin obtains a static net polarization.[12]

Cross polarization can also be discussed using a thermodynamic picture. The basic cross-polarization sequence is shown in Figure 5.9. In the preparation step, a $(\pi/2)_y$ pulse rotates the *I* spins along the *x*-axis in its rotating frame. Next the *I* spins are locked along this axis with a continuous RF field applied at the resonance frequency of the *I* spins. Equating the Boltzmann factors for the *I* spins in the lab and rotating frames, the spin temperature of the *I* spins, T_I, is given by [3]

$$T_I = \frac{B_{1I}}{B_o} T_L .$$ (5.68)

Here B_o is the external field, B_{1I} is the RF field applied to the *I* channel, and T_L is the spin-lattice temperature. Since the external field is much larger than the applied RF field $(B_o \gg B_{1I})$, the *I*-spin temperature is much less than the lattice temperature $(T_I \ll T_L)$. During spin locking, the *I-S* spin system can be visualized as two thermal reservoirs (Figure 5.10a). A cool reservoir $(T_I \ll T_L)$ of abundant *I* spins, in accord with Eq. 5.68. The other, a warm reservoir $(T_S = T_L)$ of sparse *S* spins. Obviously, thermal contact between the two reservoirs would allow for polarization transfer to the rare *S* spin system.
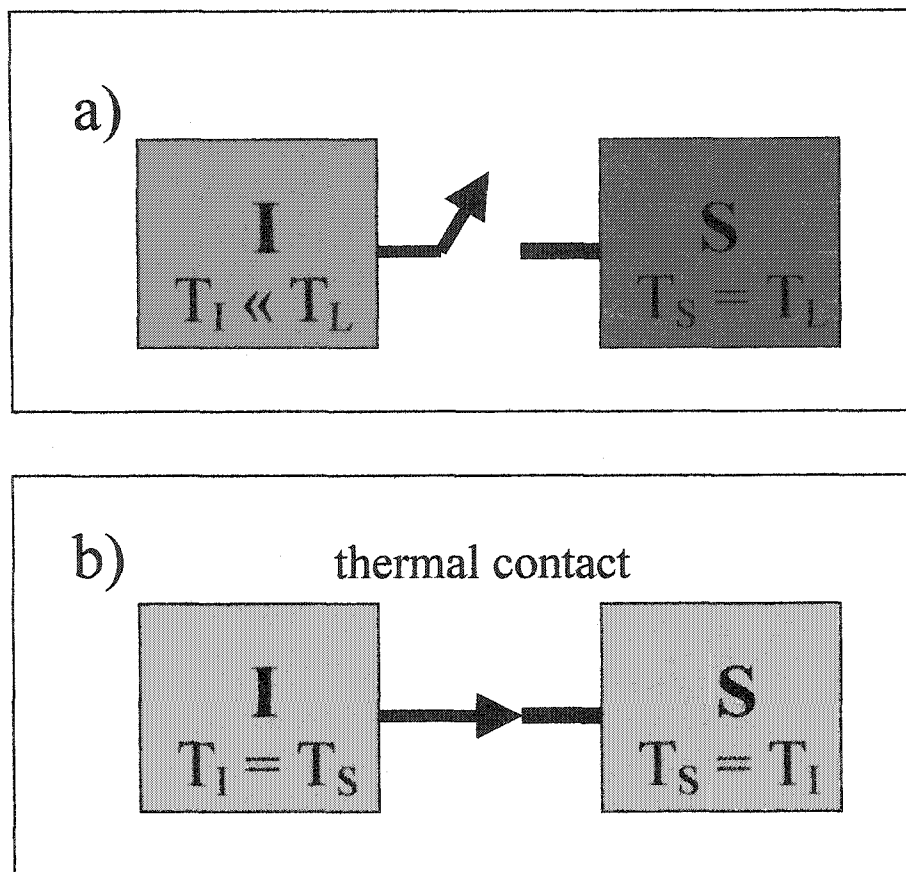
Figure 5.10: A thermodynamic picture of spin-polarization transfer. The I and S spins are visualized as two reservoirs. a) Initially, the I-spin temperature is much less than the lattice temperature ($T_I \ll T_L$), while the S-spins are at thermal equilibrium with the lattice. b) The two, spin reservoirs are allowed to come into thermal contact. This occurs during the mixing period—see Figure 5.9. Thermal contact between the two, spin systems allows polarization transfer. For sufficiently long contact periods, thermal equilibrium ($T_I = T_S$) is established between the two, spin systems.

Thermal contact between the two reservoirs is accomplished during the mixing portion of the cross-polarization sequence (Figure 5.9), and contact between the reservoirs is depicted schematically in Figure 5.10b. To achieve good thermal contact, the RF field strengths that are applied to the I and S channels need to be matched (the Hartmann-Hahn condition). If the contact period is long enough, the temperature of the two, spin reservoirs will reach thermal equilibrium ($T_S = T_I$). Furthermore, if the

Hartmann-Hahn condition is satisfied, then at equilibrium the temperature of the sparse

spins is cooled to [3]

$$T_s = (\frac{\gamma_S}{\gamma_I})(\frac{B_{1S}}{B_o})T_L .$$ (5.69)

This shows that cross polarization lowers T_S by a factor of (γ_S/γ_I) more than can be

obtained by just spin-locking the S spins. The temperature of the S spins that are spin-

locked is given by $T_S = (B_{1S}/B_o)T_L$, which may be obtained from Eq. 5.68 by relabeling $I \rightarrow S$.

Cross polarization is only efficient if the rate of energy exchange between the spin

systems, T_{IS}, is greater than the relaxation rate of the I spins in the rotating frame, $T_{I\rho_f}$.

Mehring [8] derives an approximate expression for $1/T_{IS}$:

$$\frac{1}{T_{IS}} = \frac{\sqrt{\pi}}{4}\sin^2\theta_s \sin^2\theta_I M_2^{IS}\tau_c \exp(-\Delta\omega^2\tau_c^2 / 4)$$

$$\tan\theta_I = \frac{\omega_{1I}}{\Delta\omega_I}$$ (5.70)

$$\tan\theta_S = \frac{\omega_{1S}}{\Delta\omega_S},$$

where M_2^{IS} is the second moment of the is dipole coupling, τ_c is the correlation time, and

$\Delta\omega$ is the measure of mismatch from the Hartmann-Hahn condition. The $\Delta\omega_I$ and $\Delta\omega_S$ are

the resonant offset frequencies for the I and S spins, respectively. This expression

presents a nice summary of the dynamics involved in the polarization-transfer process. It

shows that the reciprocal of the transfer rate, $1/T_{IS}$, is proportional to the square of the

dipolar coupling strength. It also shows that $1/T_{IS}$ drops off monotonically with increasing

mismatch ($\Delta\omega \neq 0$) and is scaled down by resonant offsets.

5.2.4.3 Cross Polarization Combined with Magic Angle Spinning

In this work, all cross polarization experiments were done in conjunction with magic angle spinning (MAS). If the spinning speed is high enough, proton dipolar couplings with the rare spins are suppressed. Consequently, the cross-polarization rate will be altered. At high spinning speeds (~10 kHz), S spins in different bonding environments behave like sub-systems that are coupled to only their nearest neighbor protons.[13] For example, S spins directly bonded to n protons will behave as an isolated SI_n sub-system. In principle, these different sub-systems can be distinguished. Several spectral-editing techniques are based on this principle.[13-15] This motivates our discussion of the spectral-editing technique: cross polarization with population inversion,[13] which is presented next.

5.2.4.4 Cross Polarization with Population Inversion

Standard cross-polarization combined with population inversion (CPPI) is a useful pulse sequence to help resolve components in the NMR spectrum.[13] This sequence is very similar to the standard cross-polarization method; however, the contact period in CPPI is broken into two intervals (Figure 5.11). In the first interval (with CP time τ_{cp}), polarization transfer drives the rare S spins to thermal equilibrium with the abundant I-spin system. During the second contact period τ_{PI}, the phase of the I-spin channel is shifted by π, and the spin temperature is inverted. Consequently, the two spin systems are no longer in thermal equilibrium. Thus, the S-spin magnetization inverts to reestablish a common spin temperature.[13] Typically, several experiments are performed with various
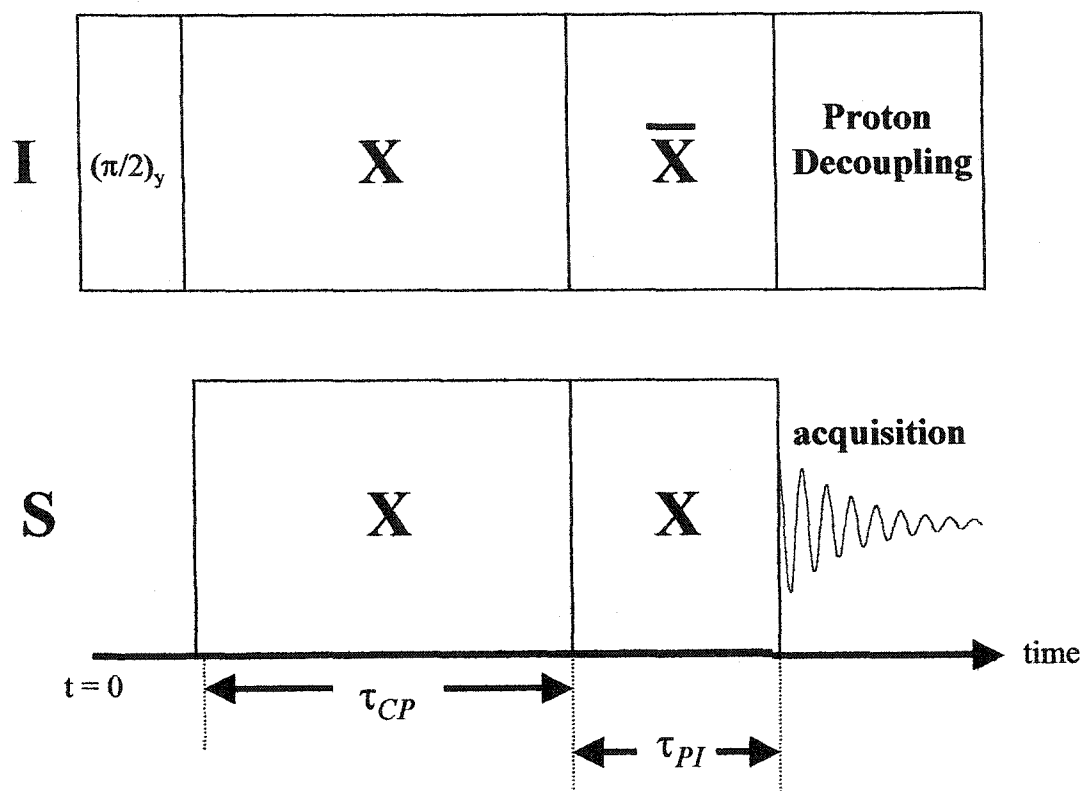
Figure 5.11: A standard cross-polarization sequence combined with population inversion (CPPI).[13]

PI times, and the S-spin magnetization is monitored. As the PI time is increased, the S magnetization first decreases in intensity, next passes through zero, and finally inverts.

The rate at which the S-spin population inverts is related to the proton connectivity in the surrounding environs, thus allowing different bonding configurations to be distinguished. By combining CPPI with MAS, the inversion rate is altered, and this can be taken advantage of to more readily resolve and assign spectral lines. In this work, the CPPI technique was combined with MAS with $v_r = 8$ kHz. At these spinning rates, polarization transfer to a particular S spin system is primarily mediated by the nearest-neighbor protons. S spins directly bonded to n protons behave approximately as an isolated SI_n sub-system, since MAS suppresses dipolar couplings due to the other more-

remote protons. Thus in principle, CPPI with MAS can provide complete spectral editing of the S-components with different proton connectivity. [13]

5.2.5 Rotational-Echo, Adiabatic-Passage, Double Resonance

Rotational-echo, adiabatic-passage, double resonance (REAPDOR) is a MAS NMR experiment designed to determine the dipolar coupling between spin ½ and quadrupolar nuclei.[16-18] The six rotor cycle, ^{13}C-^{14}N REAPDOR, pulse sequence,[18] as used in this study, is shown in Figure 5.12. A xy-train of π pulses is applied to the ^{13}C channel, and each π pulse is separated by half a rotor period. During the first half of the experiment (three rotor cycles), the toggled π pulses introduce dipolar dephasing. If the adiabatic-passage pulse—^{14}N pulse—is not applied, the phase accumulated during the second half of the experiment is equal in magnitude, but opposite in sign of the phase accumulated during the first half. In this case, the phases cancel, and the signal is fully refocused. However, when the adiabatic-passage pulse is applied to the ^{14}N channel, the quadrupolar spins make passages to other eigenstates, thus modifying the dipolar coupling interactions during the second half of the experiment. In this case, the signal is no longer fully refocused, and the dipolar dephasing results in a reduction in intensity. Those ^{13}C nuclei that are directly coupled to ^{14}N nuclei will experience the largest dephasing. While, those ^{13}C spins that are not coupled to ^{14}N spins will not dephase. Thus in its simplest application, REAPDOR allows partial assignment of the spectrum. Those ^{13}C spins that are directly bonded to nitrogen can be distinguished from those that are not.

In the following, a description of REAPDOR theory is provided. We start with the dipolar Hamiltonian in the rotating frame:
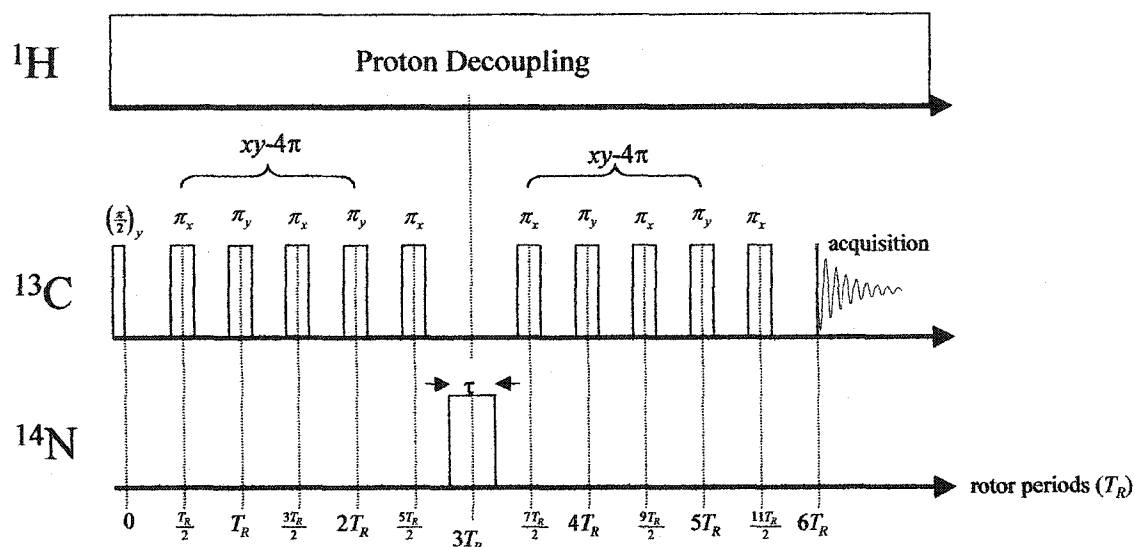
Figure 5.12: A ^{13}C-^{14}N *REAPDOR* pulse sequence.[18] The dephasing pulse (^{14}N channel) alters the ^{13}C-^{14}N dipolar coupling. Consequently, the signal due to ^{13}C spins that are coupled to ^{14}N nuclei is dephased. This experiment is repeated without the dephasing pulse (^{14}N channel), and the two spectra are compared. This comparison allows those ^{13}C spins that are coupled to ^{14}N nuclei to be distinguished from those that are not.

$$H_{IS} = \omega_D (1 - 3\cos^2 \theta) I_z S_z$$

$$= -2\omega_D P_2(\cos\theta) I_z S_z . \tag{5.71}$$

Here, $P_2(\cos\theta)$ is the second order Legendre polynomial, I denotes the ^{14}N spin, and S denotes the ^{13}C spin. θ is the angle between the distance vector separating the I-S spin pair and the z-axis in the lab frame ($\vec{B}_o = B_o \hat{z}$). Under magic angle spinning, θ becomes dependent on time:

$$P_2(\cos\theta) \rightarrow P_2(\cos\theta(t)) .$$

Using the addition theorem for spherical harmonics,[19] the second order Legendre polynomial is expressed as

$$P_2(\cos\theta(t)) = \frac{4\pi}{5} \sum_{m=-2}^{2} Y_{2m}^*(\beta, \omega_r t + \alpha) Y_{2m}(\Theta_M, 0) . \tag{5.72}$$

Here, the orientation of the inter-nuclear vector to the spinning axis is described by the polar angle β and azimuthal angle α, and Θ_M is the magic angle. Substituting Eq. 5.72 into Eq. 5.71, the MAS Hamiltonian for dipolar coupling is rewritten as

$$H = -\omega_D(t) I_z S_z,$$

(5.73)

$$\omega_D(t) = \omega_D \{\sin^2 \beta[\cos(2\omega_r t + 2\alpha)] - \sqrt{2} \sin 2\beta[\cos(\omega_r t + \alpha)]\}.$$

For the above Hamiltonian, the propagator is

$$U(t_2,t_1) = \exp[+i\Phi(t_2,t_1) I_z S_z],$$

(5.74)

where the phase that is accumulated over the period $(t_2 - t_1)$ is given by the integral:

$$\Phi(t_2,t_1) = \int_{t_1}^{t_2} \omega_D(t) dt.$$

(5.75)

Since the dipolar frequency is periodic under MAS:

$$\omega_D(t) = \omega_D(t + \omega_r t_r),$$

the accumulated phase over a rotor period, t_r, has the property:

$$\int_0^{t_r/2} \omega_D(t) dt + \int_{t_r/2}^{t_r} \omega_D(t) dt = 0.$$

Thus, the phase that is accumulated over the first half of a rotor period, $t_r/2$, is opposite in sign to the phase that is accumulated over the second half:

$$\Phi(\tfrac{t_r}{2},0) = -\Phi(t_r,\tfrac{t_r}{2}).$$

(5.76)

For convenience, we define the quantity

$$\Phi(\tfrac{t_r}{2},0) \equiv \phi.$$

(5.77)

Integrating over half the rotor period, an analytical expression for the phase is obtained:

$$\phi = \frac{2\sqrt{2}\omega_D}{\omega_r}\sin\alpha\sin 2\beta \tag{5.78}$$

We will use the above results to track the time evolution of the density matrix for the first half of the REAPDOR sequence (Figure 5.12) in the absence of the dephasing pulse. For the first half of this sequence, the density matrix, ρ, evolves according to the following *arrow* diagram:

$$\rho_0 \xrightarrow{-\phi I_z S_z} \xrightarrow{\pi S_x} \xrightarrow{+\phi I_z S_z} \xrightarrow{\pi S_y} \xrightarrow{-\phi I_z S_z} \xrightarrow{\pi S_x} \xrightarrow{+\phi I_z S_z} \xrightarrow{\pi S_y} \xrightarrow{-\phi I_z S_z} \xrightarrow{\pi S_x} \xrightarrow{+\phi I_z S_z} \rho(3t_r) \tag{5.79}$$

Note the alternating signs in the *arrow* diagram, which is in accord with Eq. 5.76. The *arrow* diagram is simplified with use of the identity:

$$\exp(i\phi I_z S_z)\exp(-i\pi S_x) = \exp(-i\pi S_x)\exp(-i\phi I_z S_z) . \tag{5.80}$$

This identity is easily verified by noting that $exp(-i\pi S_x) = -2iS_x$ and that the Pauli operator S_x anticommutes with S_z. With help of Eq. 5.80, the *arrow* diagram is rearranged:

$$\rho_o \xrightarrow{\pi S_x} \xrightarrow{\pi S_y} \xrightarrow{\pi S_x} \xrightarrow{\pi S_y} \xrightarrow{\pi S_x} \xrightarrow{+6\phi I_z S_z} \rho(3t_r)$$

$$S_x \xrightarrow{+6\phi I_z S_z} \rho(3T) , \tag{5.81}$$

As shown in Eq. 5.81, the phase accumulated over the first half of the REAPDOR experiment is 6ϕ.

If no dephasing pulse is applied to the ^{14}N channel, a similar analysis shows that the phase that is accumulated over the second half of the experiment reverses sign and cancels the phase that is accumulated over the first half. Thus, the signal is fully refocused in the absence of the dephasing pulse.

However, if the dephasing pulse is applied, the ^{14}N spin states can evolve to new eigenstates, and the phase that accumulates over the second half of the experiment no longer cancels. Consider a particular ^{13}C-^{14}N spin pair. Application of the dephasing pulse can be envisioned as causing the magnetic quantum number of the ^{14}N spin to change. Accordingly, the total accumulated phase, Δ, is proportional to the change in magnetic quantum number [18] and is given by

$$\Delta = -(m^{(2)} - m^{(1)})6\phi. \tag{5.82}$$

Here, the quantities $m^{(1)}$ and $m^{(2)}$ are the magnetic quantum numbers for the ^{14}N nuclei during the first half and second half of the experiment, respectively, and the phase 6ϕ is the total accumulated phase over the first half of the experiment. The accumulated phase (Eq. 5.82) depends on the change in eigenstate ($m^{(2)}$-$m^{(1)}$), and the various possibilities [18] are tabulated in Table 5.3. The transition from eigenstate with quantum number $m^{(1)}$ to $m^{(2)}$ is assumed to occur instantaneously; the width of the dephasing pulse is neglected for simplicity.[18]

The dipolar dephasing reduces the signal intensity. The ratio of the reduced signal, S_r, to the full signal, S_0, provides a measure of the strength of the dipolar coupling. This ratio is obtained from the powder average:[18]

$$\frac{S_r}{S_0} = \frac{1}{2\pi} \int_0^{2\pi} d\alpha \int_0^{\pi/2} \frac{1}{6} \sum_1^6 \cos\Delta_i \sin\beta d\beta, \tag{5.83}$$

where the weighted sum is over the six transitions listed in Table 5.3. This measure is convenient since the effect of spin-spin relaxation cancels in the ratio. In the absence of the dephasing pulse, this ratio is unity, since $S_r = S_0$. The REAPDOR pulse sequence

Table 5.3: The total accumula-ted phase Δ for the 6 possible transitions. Δ is determined from Eq. 5.82, and ϕ is given by Eq. 5.78.

Δ_i	Accumulated Phase	Transition
Δ_1	12ϕ	$\|1\rangle \rightarrow \|-1\rangle$
Δ_2	-12ϕ	$\|-1\rangle \rightarrow \|1\rangle$
Δ_3	-6ϕ	$\|0\rangle \rightarrow \|1\rangle$
Δ_4	6ϕ	$\|1\rangle \rightarrow \|0\rangle$
Δ_5	-6ϕ	$\|-1\rangle \rightarrow \|0\rangle$
Δ_6	6ϕ	$\|0\rangle \rightarrow \|-1\rangle$

(Figure 5.12) spans six, rotor periods. The xy-4π pulse train can be used as the basic building block for a REAPDOR experiment. By consecutively repeating these building blocks, longer REAPDOR experiments can be generated. By monitoring the ratio (Eq. 5.83) as a function of number of rotor periods, a REAPDOR curve is generated. In principle, this curve can be fit to obtain the dipolar coupling strength, thus determining the inter-nuclear distances.[18] No such attempt to obtain dipolar-coupling strengths was made in this work. Only a single point on the REAPDOR curve for the six rotor period sequence (Figure 5.12) was obtained. Using a single shot experiment, two portions in the ^{13}C spectrum were distinguished as due to carbon that are strongly and that are weakly coupled to ^{14}N spins.

5.3 Experimental Details

All solid-state NMR measurements were carried out using a custom-built spectrometer (based on an Apollo pulse programmer (Techmag))[20] operating at 7 Tesla (^{1}H Larmor frequency of 300.07 MHz) with a ^{13}C frequency of 75.46 MHz, an ^{14}N frequency of 21.68 MHz, and an ^{15}N frequency of 30.41 MHz. A diagram of the spectrometer setup is illustrated in Figure 5.13. The spectrometer operates in a heterodyne mode. The frequency synthesizer produces a continuous, RF wave at the carrier frequency ($v_L + v_{IF}$), which is subsequently electronically gated by the pulse programmer to generate a pulse. The gating pulses are at an intermediate frequency (v_{IF}) of 30 MHz and are mixed with the continuous, RF wave. Thus, two pulses are produced: one corresponding to the upper side band ($v_L + 2v_{IF}$) and the other corresponding to the lower side band (v_L). The upper side band is removed by a band-pass filter, while the remaining RF pulse at the Larmor frequency (v_L) is amplified and transmitted to the sample coil. Both the phase and length of the pulse can be controlled. The coil, which is housed inside the probe, is also used to pick up the induction signal from the sample. The signal ($v_L + \delta v_L$) is amplified and directed to the receiver, where it is demodulated from RF to audio frequencies (δv_L). The demodulation step is performed in quadrature, which allows phase sensitive detection. This means that the magnitude of δv_L is determined as well as its sign. The demodulated signal corresponds to an observation in the RRF frame; quadrature detection allows signals with frequencies both negative and positive with respect to the Larmor frequency (v_L) to be distinguished.

Computer
Interface

Pulse Programmer
and Digitizer

Channel 1 (Observe)

Synthesizer

$\nu_L + \nu_{IF}$

$\delta\nu_L$

Channel 2

Synthesizer

Receiver

ν_{IF}

ν_{IF}

Transmitter

Transmitter

ν_L

$\nu_L + \delta\nu_L$

Amplifier

$(3/4)\lambda_{CH1}$

Amplifier

$(3/4)\lambda_{CH1}$

$(1/4)\lambda_{CH1}$

Probe

λ_{CH2}
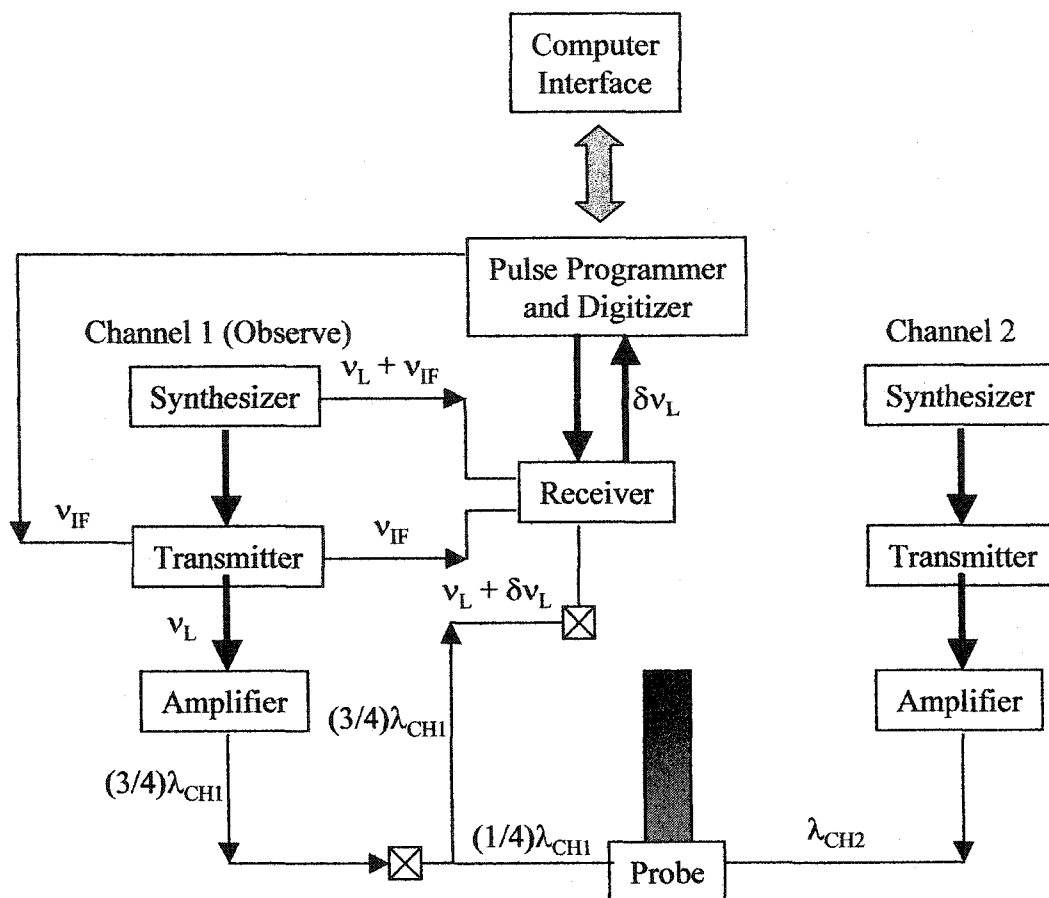
Figure 5.13: A block-diagram of the NMR spectrometer. Two channels are shown to illustrate the setup for a double-resonance experiment. The length of the transmission lines is determined by the wavelength of the signal at the Larmor frequency. The crossed diodes—boxes with X—protect the receiver from the high power pulse and block the signal from the transmitter.

A triple-resonance, Chemagnetics probe with magic angle spinning capability was used for all experiments. The resonant circuits, which are housed inside the probe, are tuned to match the impedance of the cables (50 Ω). For example, the ^{13}C channel is tuned so that it is impedance matched at 75.46 MHz. Impedance matching ensures maximum power transfer and minimizes reflections. The magic angle was set using a ^{13}C enriched (10%) glycine sample and adjusting the angle mechanically until the longest FID was observed, which corresponds to the narrowest line-width in the frequency domain. Spinning stability was typically ± 3 Hz for ν_r = 6-10 kHz. *In situ* sample heating was also

available. This was accomplished by blowing preheated nitrogen past the sample coil, and a fixed temperature was maintained with a LakeShore temperature controller.

Two a-CN$_x$ samples were prepared for the NMR studies. The ^{13}C and ^{1}H experiments were carried out on an unenriched a-CN$_x$ sample—both ^{13}C and ^{15}N are at natural abundance. The ^{15}N experiments were conducted on samples that were fabricated using an enriched ^{15}N$_2$ feedstock gas. A complete description of material fabrication and mechanical testing is provided in Chapter 3 and Chapter 7, respectively. After the films were removed from the substrate, the material was ground and packed into a 5 mm, zirconia rotor. The sample is contained between two, Teflon spacers inside the rotor. Teflon produces a significant background signal to the ^{13}C direct-detection spectra, and this background can be removed by subtraction—details are given later.

In addition, apodization was used to improve signal-to-noise ratio of the spectra. Apodization is a numerical technique for reducing noise in the spectrum; this is accomplished by multiplying the time domain signal (the FID) with an exponential (or other suitable) function before taking the Fourier transform (FT).[16,20] Since the intensity of the exponential decays rapidly for long-time points, multiplication of the signal by an exponential suppresses the noise tail in the FID. The noise suppression is accompanied by a small cost—the spectrum is broadened by $\Delta v = 1/\pi T_2$, where T_2 is the decay time of the exponential.

Unless otherwise mentioned, the 90° pulse widths were 3.5 μs for ^{1}H, 4 μs for ^{13}C, 6 μs for ^{14}N, and 5 μs for ^{15}N. The RF field strength for proton decoupling was 71.4 kHz (90° pulse width of 3.5μs). Spinning speeds were in the range of v_r = 6-10 kHz for the ^{1}H, ^{13}C, and ^{15}N MAS experiments. NMR direct-detection and cross polarization (CP)

spectra were obtained using the Hahn-echo, pulse sequence (90_x–τ_e–180_x) for the ^{15}N and ^{13}C measurements, and a solid-echo sequence (90_x–τ_e–90_y) for the ^1H experiments. In addition, ^{13}C NMR spectra were obtained using a 4-pulse TOSS sequence (section 5.2.3.2). A REAPDOR sequence (see section 5.2.5) was also implemented to determine the contributions to the ^{13}C spectra that are influenced by ^{14}N-^{13}C dipolar coupling. CPPI measurements (see section 5.2.4.4) were used to provide some spectral editing of the ^{15}N spectra. All NMR spectra were obtained at room temperature except for the ^1H spectra, which were obtained at both room temperature and 150 °C. For ^1H NMR experiments at high temperature, the sample was first heated for 20 minutes at 150 °C, and then data were acquired at 150 °C for an additional 22 minutes. Additional experimental details of recycle delays (τ_d), echo spacing times (τ_e), spinning speeds (v_r), number of scans (NS), and apodization by Lorentzian line broadening (LB) for each experiment are included in the figure captions of Chapter 9.

The reported ^{13}C chemical shifts (δ) are referenced to the carboxyl carbon of glycine at 176 ppm on the tetramethylsilane scale (TMS at zero ppm); that is,

$$\delta = \frac{v - v_{ref}}{v_{ref}} \times 10^6,$$

where v and v_{ref} are the resonance frequencies of the sample and reference material, respectively. In addition, ^{15}N chemical shifts are referenced to labeled glycine at -348 ppm on the nitromethane scale (CH_3NO_2 at zero ppm), and the ^1H chemical shifts are referenced to water at 5.3 ppm (TMS at zero ppm). All chemical shifts were referenced externally using literature values.[21] A dwell time (the time interval between data points) of 20 μs was used for all measurements. This corresponds to a spectral width (SW) of ±25 kHz around the center frequency, which is adequate to span all possible bonding configurations.
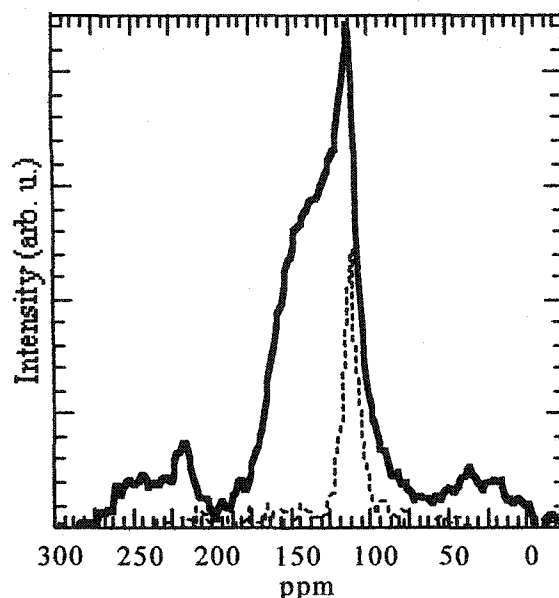
Figure 5.14:A comparison between^{13}C Hahn Echo MAS spectra of a-CN$_X$ (solid line) and an empty rotor (dashed line): τ_d = 10 s; τ_e = 125 μs; v_r = 8 kHz; and NS = 4608. The sharp peak at 111 ppm is due to the Teflon spacers.

Background subtraction

The Teflon spacers contribute a strong background signal to the ^{13}C direct-detection spectrum, as shown in Figure 5.14. The background signal (dashed line) was obtained by measuring the signal of an empty rotor with spacers. The ^{13}C spectrum of amorphous carbon nitride (a-CN$_x$) is shown for comparison. Evidently, the sharp peak near 111 ppm (TMS = 0 ppm) in the a-CN$_x$ spectrum is due to Teflon. Both spectra were obtained using a Hahn-echo, pulse-sequence under the same conditions and after 4608 scans. The background signal is removed by direct subtraction, and the resulting background-corrected, a-CN$_x$ spectra can be viewed in Figure 9.1. No measurable background signal was obtained from ^{13}C CPMAS, ^{15}N CPMAS or ^{15}N direct-detection measurements for our experimental conditions (see Chapter 9).

5.4 References

1   J. J. Sakurai, *Modern Quantum Mechanics* (Benjamin/Cummings, Reading, MA, 1985).

2   D. A. Skoog and J. J. Leary, *Principles of Instrumental Analysis*, 4 ed. (Saunders, New York, 1992).

3   E. O. Stejskal and J. D. Memory, *High Resolution NMR in the Solid State* (Oxford, New York, 1994).

4   T. C. Farrar and J. E. Harriman, *Density Matrix Theory and its Applications in NMR Spectroscopy*, 3 ed. (Farragut Press, Madison, WI, 1998).

5   M. H. Levitt, *Spin Dynamics* (Wiley, New York, 2001).

6   O. W. Sorensen, G. W. Eich, M. H. Levitt, G. Bodenhausen, and R. R. Ernst, Prog. Nucl. Magn. Reson. Spectrosc. **16**, 163 (1983).

7   R. R. Ernst, G. Bodenhausen, and A. Wokaun, *Principles of Nuclear Magnetic Resonance in One and Two Dimensions* (Oxford, Oxford, 1997).

8   M. Mehring, *High Resolution NMR in Solids*, 2 ed. (Springer-Verlag, New York, 1983).

9   D. P. Raleigh, E. T. Olejniczak, and R. G. Griffin, J. Chem. Phys. **89**, 1333 (1988).

10   S. J. Lang, J. of Magn. Reson., Ser. A 104, 345 (1993).

11   O. N. Antzutkin, Z. Song, X. Feng, and M. H. Levitt, J. Chem. Phys. **100**, 130 (1994).

12   L. Muller, A. Kumar, T. Baumann, and R. R. Ernst, Phys. Rev. Lett. **32**, 1402 (1974).

13   X. Wu and K. W. Zilm, J. Magn. Reson, Ser. A **102**, 205 (1993).

14   X. Wu, S. Zhang, and X. Wu, Phys. Rev. B **37**, 9827 (1988).

15   E. De Vita and L. Frydman, J. Magn. Reson. **148**, 327-337 (2001).

16   T. Gullion, Chem. Phys. Lett. **246**, 325-330 (1995).

17   B. Kesling, E. Hughes, and T. Gullion, Solid State Nucl. Magn. Reson. **16**, 1 (2000).

18   B. Yong, K. Hsien-Ming, C. P. Grey, L. Chopin, and T. Gullion, J. Magn. Reson. **133**, 104 (1998).

19   J. D. Jackson, *Classical Electrodynamics*, 3 ed. (Wiley, New York, 1998).

20   D. I. Malyarenko, Ph.D. Dissertation, College of William & Mary (2001).

21   T. M. Duncan, *A Compilation of Chemical Shift Anisotropies* (Farragut Press, Madison, WI, 1990).

Chapter 6—Computational Techniques

In this dissertation, the chemical bonding of hard and elastic amorphous carbon nitride (a-CN_X) films are studied with both x-ray photoelectron spectroscopy (XPS) and nuclear magnetic resonance (NMR) techniques. Based on these measurements, a film-structure model for a-CN_X is proposed. The plausibility of this model is supported using quantum chemical calculations. In this chapter, an overview of the methods and theory behind these calculations are provided. The Hartree-Fock method was implemented for all calculations, using the *Gaussian 98* program.[1]

6.1 Computational Theory

6.1.2 The Electronic Schrödinger Equation

The primary concern of computational quantum chemistry is to solve the Schrödinger equation for a molecule by using a set of reasonable approximations. In this discussion, only the time-independent, non-relativistic, Schrödinger equation needs to be considered. The complete Schrödinger equation for a molecule is given by

$$\hat{H}\Phi(\vec{r},\vec{R}) = E_{TOT}\Phi(\vec{r},\vec{R}) . \qquad (6.1)$$

Here, $\vec{r}$ and $\vec{R}$ represent the set of electronic and nuclear coordinates, respectively. The above Hamiltonian is written as the sum of two contributions:

97

$$\hat{H} = \hat{H}_{el} + \hat{T}_n$$

$$\hat{H}_{el} = -\sum_{i=1}^{N}\frac{1}{2}\nabla_i^2 - \sum_{i=1}^{N}\sum_{A=1}^{M}\frac{Z_A}{r_{iA}} + \sum_{i=1}^{N}\sum_{j>i}^{N}\frac{1}{r_{ij}} + \sum_{A=1}^{M}\sum_{B>A}^{M}\frac{Z_A Z_B}{R_{AB}} \qquad (6.2)$$

$$\hat{T}_n = -\sum_{A=1}^{M}\frac{1}{2M_A}\nabla_A^2 \; .$$

Here $\hat{H}_{el}$ is the electronic Hamiltonian operator, and $\hat{T}_n$ is the kinetic energy operator of the nuclei. $\hat{H}_{el}$ consists of four terms: the first describes the kinetic energy of the electrons, the second describes the Coulomb interaction between electrons and nuclei, the third describes the electron-electron interactions, and the fourth describes the Coulomb interaction between nuclei. In the sums, i and j refer to electronic coordinates, while A and B refer to nuclear coordinates.

To solve the Schrödinger equation (Eq. 6.1), it is assumed that the total wave function is written as a product of an electronic wave function $\Psi_e(\vec{r};\vec{R})$ and a nuclear wave function $\Psi_n(\vec{R})$:

$$\Phi(\vec{r},\vec{R}) = \Psi_e(\vec{r};\vec{R})\Psi_n(\vec{R}) \; . \qquad (6.3)$$

Note that the electronic wave function depends parametrically on the nuclear coordinates, $\vec{R}$. Substituting this ansatz into the Schrödinger equation (Eq. 6.1) gives

$$\Psi_n(\vec{R})\hat{H}_e\Psi_e(\vec{r};\vec{R}) + \hat{T}_n[\Psi_e(\vec{r};\vec{R})\Psi_n(\vec{R})] = E_{TOT}\Psi_e(\vec{r};\vec{R})\Psi_n(\vec{R}) \; ,$$

where the second term can on the left can be expressed as [2]

$$\hat{T}_n[\Psi_e(\vec{r};\vec{R})\Psi_n(\vec{R})] = \Psi_e(\vec{r};\vec{R})\hat{T}_n\Psi_n(\vec{R}) + O(\tfrac{m}{M_A}) \; .$$

In the second line, $O(\tfrac{m}{M_A})$ represents the terms of order (m/M_A), the ratio of the electron mass to nuclear mass. Dropping the higher order terms yields

$$\Psi_n(\vec{R})H_e\Psi_e(\vec{r};\vec{R}) + \Psi_e(\vec{r};\vec{R})\hat{T}_n\Psi_n(\vec{R}) = E_{TOT}\Psi_e(\vec{r};\vec{R})\Psi_n(\vec{R}) \qquad (6.4)$$

Thus by neglecting the kinetic energy of the nuclei (the Born-Oppenheimer approximation), the electronic Schrödinger equation can be separated: [2]

$$H_e\Psi_e(\vec{r};\vec{R}) = E_e(\vec{R})\Psi_e(\vec{r};\vec{R}). \qquad (6.5)$$

The solution describes the motion of the electrons in a static nuclear field. Note that the electronic energy $E_e(\vec{R})$ depends parametrically on the nuclear coordinates. Thus, the ground-state electronic energy is determined by optimizing the molecule such that the set of nuclear coordinates that minimizes $E_e(\vec{R})$ is found. Once the electronic problem is solved (Eq. 6.5), the nuclear motion is determined from:[2]

$$(E_e(\vec{R}) + \hat{T}_n)\Psi_n(\vec{R}) = E_{TOT}\Psi_n(\vec{R}). $$

We are not concerned with nuclear motion; therefore, only solutions to the electronic Hamiltonian (Eq. 6.5) are considered.

6.1.2 The Hartree-Fock Equations

In this section, the solution of the electronic Schrödinger equation (Eq. 6.5) by the Hartree-Fock method is described. The Hartree-Fock method approximates the N-electron wave function, Ψ_e, by a single Slater determinant: [3]

$$\Psi_e(\vec{r}_1,\vec{r}_2,...\vec{r}_N) = (N!)^{-1/2}\begin{vmatrix} \chi_i(\vec{r}_1) & \chi_j(\vec{r}_1) & \cdots & \chi_k(\vec{r}_1) \\ \chi_i(\vec{r}_2) & \chi_j(\vec{r}_2) & \cdots & \chi_k(\vec{r}_2) \\ \vdots & \vdots & & \vdots \\ \chi_i(\vec{r}_N) & \chi_j(\vec{r}_N) & \cdots & \chi_k(\vec{r}_N) \end{vmatrix},$$

or equivalently: $\Psi_e(\vec{r}_1,\vec{r}_2,...\vec{r}_N) = (N!)^{-1/2}\displaystyle\sum_{n=1}^{N!} p_n\hat{\wp}_n\{\chi_i(\vec{r}_1)\chi_j(\vec{r}_2)\cdots\chi_k(\vec{r}_N)\}. \qquad (6.6)$

Here, the operator $\hat{\wp}_n$ generates the nth permutation, and $p_n = 1$ or -1 for even and odd permutations, respectively. It is convenient to express this using a compact notation:

$$\Psi_e(\vec{r}_1, \vec{r}_2, ... \vec{r}_N) = \left| \chi_i(r_1) \chi_j(r_2) \cdots \chi_k(r_N) \right|. \qquad (6.7)$$

In the above, the determinant is represented only by its diagonal elements. Using *bra-ket* notation, Eq. 6.7 is neatly expressed as

$$\left| \Psi_e \right\rangle = \left| ij \cdots k \right\rangle. \qquad (6.8)$$

Furthermore, the electronic wave function is normalized:

$$\left\langle \Psi_e \middle| \Psi_e \right\rangle = 1.$$

The trial wave function (Eq. 6.6) is constructed to satisfy two physical requirements: 1) it is antisymmetric, and 2) it accounts for the indistinguishability of the electrons. However, there is a third requirement that is satisfied by the true electron wave function. Since the coulomb repulsion between two electrons correlates their motion, the probability that two electrons appear at the some point in space vanishes. This requirement is only partially met when the wave function is approximated by a single Slater determinant.[3] Electrons with parallel spin have a vanishing probability of occupying the same point in space. However, electrons with opposite spin have a non-vanishing probability of occupying the same point in space. By describing the wave function by a single Slater determinant, only electrons with parallel spin are correlated. This correlation is called the exchange interaction, which arises because the electron wave function is antisymmetric. The deficiency of Hartree-Fock theory has lead to the development of *electron correlation* methods—examples of these methods are

configuration interaction (CI) methods, Moller-Plesset (MP) perturbation theory and density functional theory (DFT). [2,4] These techniques were not used in this work.

In essence, the Hartree-Fock method finds the best many-electron wave function that is constructed from a single Slater determinant (Eq. 6.6). This is accomplished by using the variational method to minimize the expectation value of the electronic energy:

$$E_e = \langle \Psi_e | H_e | \Psi_e \rangle. \tag{6.9}$$

A variational expression for the energy is obtained by substituting the electronic wave function (Eq. 6.6) and the electronic Hamiltonian (Eq. 6.2) into Eq. 6.9; however, this *direct* method is algebraically cumbersome. Alternatively, an expression for E_e is easily obtained using the very elegant method of second quantization.[3] The electronic Hamiltonian is recast in terms of the creation operators, $a_i^\dagger$, and annihilation operators, a_i:

$$H_e = \sum_{ij} \langle i|h|j \rangle a_i^\dagger a_j + \tfrac{1}{2} \langle ij|\tfrac{1}{r_{12}}|kl \rangle a_i^\dagger a_j^\dagger a_l a_k + V_{NN}$$

$$h(\bar{x}_1) = -\tfrac{1}{2}\nabla_1^2 - \sum_A \frac{Z_A}{r_{1A}} \tag{6.10}$$

$$V_{NN} = \sum_{A=1}^{M} \sum_{B>A}^{M} \frac{Z_A Z_B}{R_{AB}} .$$

Using the above form, the electronic energy (Eq. 6.9) is expressed as

$$E_e = \sum_{ij}^{occupied} \langle i|h|j \rangle \langle \Psi|a_i^\dagger a_j|\Psi \rangle + \tfrac{1}{2} \sum_{ijkl}^{occupied} \langle ij|\tfrac{1}{r_{12}}|kl \rangle \langle \Psi|a_i^\dagger a_j^\dagger a_l a_k|\Psi \rangle + V_{NN} . \tag{6.11}$$

The final form for this expression is obtained by evaluating the two terms:[3]

$$\langle \Psi|a_i^\dagger a_j|\Psi \rangle = \delta_{ij} \langle \Psi|a_i^\dagger a_i|\Psi \rangle$$

$$= \delta_{ij} \langle \Psi|N_i|\Psi \rangle \tag{6.12}$$

$$\langle \Psi|a_i^\dagger a_j^\dagger a_l a_k|\Psi \rangle = \langle \Psi|N_i N_j|\Psi \rangle (\delta_{ik}\delta_{jl} - \delta_{il}\delta_{jk}) .$$

Here N_i is the number operator with eigenvalues 0 if state i is unoccupied or 1 if occupied. Substituting these two terms (Eq. 6.12) into Eq. 6.11 yields the desired form for the electronic energy:

$$E_e = \sum_{ij}^{occupied} \langle i|h|j\rangle + \tfrac{1}{2}\sum_{ijkl}^{occupied} \langle ij\|ij\rangle + \sum_{A=1}^{M}\sum_{B>A}^{M}\frac{Z_A Z_B}{R_{AB}}, \qquad (6.13)$$

$$\langle ij\|ij\rangle \equiv \langle ij|\frac{1}{r_{12}}|ij\rangle - \langle ij|\frac{1}{r_{12}}|ji\rangle.$$

The Hartree-Fock solution for the electronic wave function is found by minimizing the electronic energy (Eq. 6.13) with respect to the spin-orbitals, which are constrained to be orthonormal:

$$\langle i|j\rangle = \delta_{ij}. \qquad (6.14)$$

Thus, the best spin-orbitals are determined by minimizing the functional:[3]

$$L[\{k\}] = E_e[\{k\}] - \sum_{ij} \varepsilon_{ij}\left[\langle i|j\rangle - \delta_{ij}\right]$$

$$\delta L = \delta E_e - \sum_{ij} \varepsilon_{ij}\left[\langle \delta i|j\rangle + \langle i|\delta j\rangle\right] = 0, \qquad (6.15)$$

where the ε_{ij} are Lagrange multipliers. Straightforward evaluation of Eq. 6.15 gives the Hartree-Fock equations:[3]

$$f|\chi_a\rangle = \sum_{b=1} \varepsilon_{ba}|\chi_b\rangle. \qquad (6.16)$$

Here, f is the Fock-operator:

$$f = h + \sum_{b=1}^{N} \tilde{J}_b + \tilde{K}_b$$

$$\tilde{J}_b = \int d\bar{x}_2 \chi_b^*(2)\frac{1}{r_{12}}\chi_b(2) \qquad (6.17)$$

$$\tilde{K}_b|\chi_a\rangle = \left\{\int d\bar{x}_2 \chi_b^*(2)\frac{1}{r_{12}}\chi_a(2)\right\}|\chi_b\rangle.$$

Here, $\tilde{J}_b$ and $\tilde{K}_b$ are the Coulomb and exchange operators, respectively. By choosing a set of canonical spin-orbitals, the Hartree-Fock equation (Eq. 6.16) takes is usual eigenvalue form:[3]

$$f\left|\chi_a^{'}\right\rangle = \varepsilon_a\left|\chi_a^{'}\right\rangle.$$
(6.18)

Specifically, the canonical spin-orbitals, $\chi_a^{'}$, are related to the spin orbitals in Eq. 6.16 by a unitary transformation:

$$\left|\chi_a^{'}\right\rangle = \sum_b\left|\chi_b\right\rangle U_{ba}.$$
(6.19)

The unitary matrix U is chosen to be the one that diagonalizes the matrix with elements ε_{ba} (see Eq 6.16). Since the Fock-operator is invariant under a unitary transformation of spin orbitals,[3] no prime appears on f in Eq. 6.18. A detailed discussion of the unitary transformation that is used to obtain the canonical form of the Hartree-Fock equations (Eq. 6.18) is found elsewhere.[3]

The Hartree-Fock equations (Eq. 6.18) are solved iteratively. Using an initial guess for the spin orbitals, the orbital energies, ε_a, are calculated. In the next iteration, the set of ε_a is used to construct a new set of spin orbitals. This process is repeated until it converges. A detailed description of this computational procedure is given later. To make the Hartree-Fock equations amenable to numerical calculation, the spin variables must first be integrated out. The spin orbital is a direct product of a spatial part and a spin part:

$$\left|\chi_i\right\rangle = \left|\phi_i^{\sigma}\sigma\right\rangle$$
(6.20)

$$\left|\chi_i\right\rangle = \left|\phi_i^{\sigma}\right\rangle \otimes \left|\sigma\right\rangle\,; \sigma = \alpha \text{ or } \beta.$$

Here, the spin index, σ, on the spatial orbital ϕ_i^σ allows for dependence on electron spin. These are called *unrestricted* spatial orbitals. In contrast, *restricted* spatial orbitals are constrained to have the same form for both spin up (α) and spin down (β); i.e., $\phi_i^\alpha = \phi_i^\beta$. Restricted orbitals are simply denoted as ϕ_i by dropping the spin index.

The Fock equation (Eq. 6.18) is now written as

$$f \left| \phi_i^\sigma \sigma \right\rangle = \varepsilon_i^\sigma \left| \phi_i^\sigma \sigma \right\rangle .$$

The spin variables are removed by multiplying both sides of the Fock equation with $\langle \sigma |$ and integrating:

$$f_\sigma \left| \phi_i^\sigma \right\rangle = \varepsilon_i^\sigma \left| \phi_i^\sigma \right\rangle \qquad (6.21)$$

$$f_\sigma \equiv \langle \sigma | f | \sigma \rangle .$$

Carrying out the spin integration in f_σ, the set of equations is obtained:[3]

$$f_\alpha = h + \sum_a^{N_\alpha} [J_a^\alpha - K_a^\alpha] + \sum_a^{N_\beta} J_a^\beta$$

$$f_\beta = h + \sum_a^{N_\beta} [J_a^\beta - K_a^\beta] + \sum_a^{N_\alpha} J_a^\alpha \qquad (6.22)$$

$$J_a^\alpha = \int d\vec{x}_2 \phi_a^{\sigma *}(2) \tfrac{1}{r_{12}} \phi_a^\sigma (2) \,; \sigma = \alpha \text{ or } \beta$$

$$K_a^\sigma \left| \phi_b^\sigma \right\rangle = \left\{ \int d\vec{x}_2 \phi_a^{\sigma *}(2) \tfrac{1}{r_{12}} \phi_b^\sigma (2) \right\} \left| \phi_a^\sigma \right\rangle \,; \sigma = \alpha \text{ or } \beta .$$

In both f_α and f_β, there are two types of sums: a sum over the N_α occupied states with spin α, and a sum over the N_β occupied states with spin β. This set of equations (Eq. 6.22) is the spin-integrated version of the set described by Eq. 6.17. Similarly, the spin-integrated

expression for the total energy is determined by substituting Eq. 6.20 into Eq. 6.11 and integrating over spin:[3]

$$
\begin{aligned}
E_e =& \sum_i^{N_\alpha} \left\langle \phi_i^\alpha \middle| h \middle| \phi_i^\alpha \right\rangle + \sum_i^{N_\beta} \left\langle \phi_i^\beta \middle| h \middle| \phi_i^\beta \right\rangle + \\
&+ \frac{1}{2} \sum_i^{N_\alpha} \sum_j^{N_\alpha} \left\{ \left\langle \phi_i^\alpha \phi_j^\alpha \middle| \frac{1}{r_{12}} \middle| \phi_i^\alpha \phi_j^\alpha \right\rangle - \left\langle \phi_i^\alpha \phi_j^\alpha \middle| \frac{1}{r_{12}} \middle| \phi_j^\alpha \phi_i^\alpha \right\rangle \right\} + \\
&+ \frac{1}{2} \sum_i^{N_\beta} \sum_j^{N_\beta} \left\{ \left\langle \phi_i^\beta \phi_j^\beta \middle| \frac{1}{r_{12}} \middle| \phi_i^\beta \phi_j^\beta \right\rangle - \left\langle \phi_i^\beta \phi_j^\beta \middle| \frac{1}{r_{12}} \middle| \phi_j^\beta \phi_i^\beta \right\rangle \right\} + \\
&+ \sum_i^{N_\alpha} \sum_j^{N_\beta} \left\langle \phi_i^\alpha \phi_j^\beta \middle| \frac{1}{r_{12}} \middle| \phi_i^\alpha \phi_j^\beta \right\rangle + \sum_{i=A}^{M} \sum_{i=B}^{N} \frac{Z_A Z_B}{R_A R_B}
\end{aligned}
\tag{6.23}
$$

Equations 6.21-23 are the important results; these are the framework of Hartree-Fock theory. Physical interpretation of these equations is postponed until later discussion. In the following sections, a description is given of the computational procedures that are used to solve Eq. 6.21-23. At first, our discussion is confined to solution of the Fock equations for a restricted, closed-shell, calculation. Generalization of these results to the unrestricted case is considered afterwards.

6.1.3 The Self-Consistent Field Procedure

The Restricted, Closed-Shell, Hartree-Fock Method

In this method, each orbital is doubly occupied, and the spatial orbitals are constrained to be the same for both spin up (α) and spin down (β). The N-electron system consists of $N/2$ spin pairs—hence a closed shell. The restricted, closed-shell, Fock equations are obtained by inspection of Eqs. 6.21-22:

$$
f \middle| \phi_i \rangle = \varepsilon_i \middle| \phi_i \rangle
$$

$$
f = h(1) + \sum_a^{N/2} [2 J_a(1) - K_a(1)].
\tag{6.24}
$$

In the first line, the eigenvalue equation is obtained by simply dropping the spin index in Eq. 6.21. In the second line, the Fock operator is obtained by selecting one of the pair of Fock operators in Eq. 6.22, noting that $N_\alpha = N_\beta = N/2$, and dropping the spin index. The spin index is no longer necessary, since the spatial orbitals are restricted. Similarly, inspection of Eq. 6.23 yields the restricted, closed-shell energy:

$$E_e = 2\sum_i^{N/2} h_{ii} + \sum_i^{N/2}\sum_j^{N/2} \left(2J_{ij} - K_{ij}\right) + V_{NN}$$

$$h_{ii} = \left\langle \phi_i \left| h \right| \phi_i \right\rangle$$

$$J_{ij} = \left\langle \phi_i\phi_j \left| \tfrac{1}{r_{12}} \right| \phi_i\phi_j \right\rangle \qquad (6.25)$$

$$K_{ij} = \left\langle \phi_i\phi_j \left| \tfrac{1}{r_{12}} \right| \phi_i\phi_j \right\rangle$$

$$V_{NN} = \sum_{i=A}^{M}\sum_{j=B}^{M} \frac{Z_A Z_B}{R_{AB}} .$$

Here, h_{ii} describes the kinetic and potential energy of an electron in the ith shell moving in the bare field of the nuclei. The sum over h_{ii}—first term in the expression for E_e— is called the core Hamiltonian. J_{ij} is the coulomb interaction energy between an electron in shell i with one in shell j. K_{ij} is the exchange correlation energy between electrons with parallel spin—one electron is in shell i and the other in shell j. Since only half of the electrons have parallel spin, the factor of two does not appear in front of K_{ij}.

To see how Eq. 6.25 is applied, a simple example is considered. In Figure 6.1, the energy-level diagram of a Beryllium (Be) atom is shown. The closed-shell configuration for Be consists of a pair of electrons in the 1s shell and a pair in the 2s shell; i.e., $(1s^2 2s^2)$. According to Eq. 6.25, the closed-shell energy for Be is given by

$$E_e = 2h_{11} + 2h_{22} + J_{11} + 4J_{12} + J_{22} - 2K_{12} . \qquad (6.26)$$
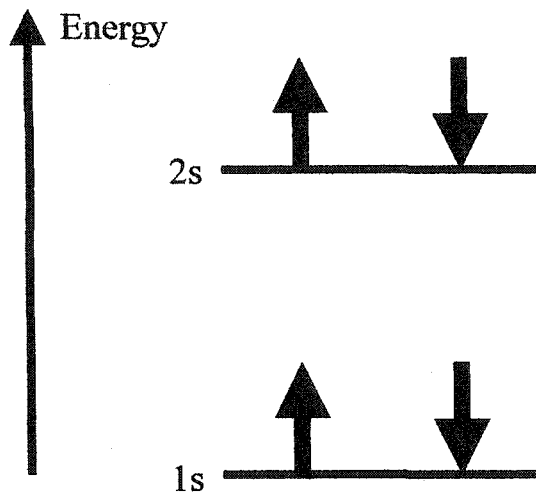
Figure 6.1: Closed-shell, energy-level diagram of a Be atom.

Instead of working with Eq. 6.25 directly, it is easier to obtain E_e by direct inspection of the energy-level diagram (Figure 6.1). The kinetic energy and nuclear attraction energy contributions to E_e for an electron in the 1s shell is given by h_{11}—there are two 1s electrons, so the total contribution is $2h_{11}$. The coulomb interaction between the two 1s electrons contributes J_{11}. By similar arguments, the electrons in the 2s shell contribute the terms $2h_{22}$ and J_{22}. Next, electron-electron interactions between the 1s and 2s shells are considered. There are two electrons in both the 1s and 2s shells; thus, there are four possible interactions between shells, which give the contribution $4J_{12}$. Finally, the exchange interaction is considered. In the Hartree-Fock approximation, only electrons with parallel spin are correlated. There are only two possible ways of pairing electrons with parallel spin: $1s(\alpha)$ with $2s(\alpha)$ and $1s(\beta)$ with $2s(\beta)$. Thus, the exchange correlation

contributes the term minus $2K_{12}$. Adding the above contributions yields Eq. 6.26. This example provides valuable insight into the physical interactions described by Eq. 6.25.

For future reference, it is convenient to write the energy (Eq. 6.25) in terms of the orbital energies, ε_j:

$$E_e = 2\sum_j^{N/2} \varepsilon_j - \sum_{ij}^{N/2} \left\{ 2J_{ij} - K_{ij} \right\} . \tag{6.27}$$

This form is easily obtained by noting that the orbital energies, ε_j, are given by the matrix element $\left\langle \phi_j \middle| f \middle| \phi_j \right\rangle$—see Eq. 6.24.

For quantum chemical calculations, the desired form for the closed-shell, Hartree-Fock equations is obtained by expanding the spatial orbitals in terms of a basis set:

$$\phi_i = \sum_{\mu=1}^{n} c_{\mu i} \psi_\mu . \tag{6.28}$$

Substituting this expansion into Eq. 6.24 yields the Roothaan-Hall equations:[3,4]

$$\sum_{\nu=1}^{n} \left(F_{\mu\nu} - \varepsilon_i S_{\mu\nu} \right) c_{i\nu} = 0, \mu = 1, 2, \ldots N \tag{6.29}$$

or in matrix form:

$$FC = SC\varepsilon . \tag{6.30}$$

Here, S is the overlap matrix:

$$S_{\mu\nu} = \left\langle \psi_\mu \middle| \psi_\nu \right\rangle . \tag{6.31}$$

F is the Fock matrix and is given by:

$$F_{\mu\nu} = H_{\mu\nu}^{core} + G_{\mu\nu} , \tag{6.32}$$
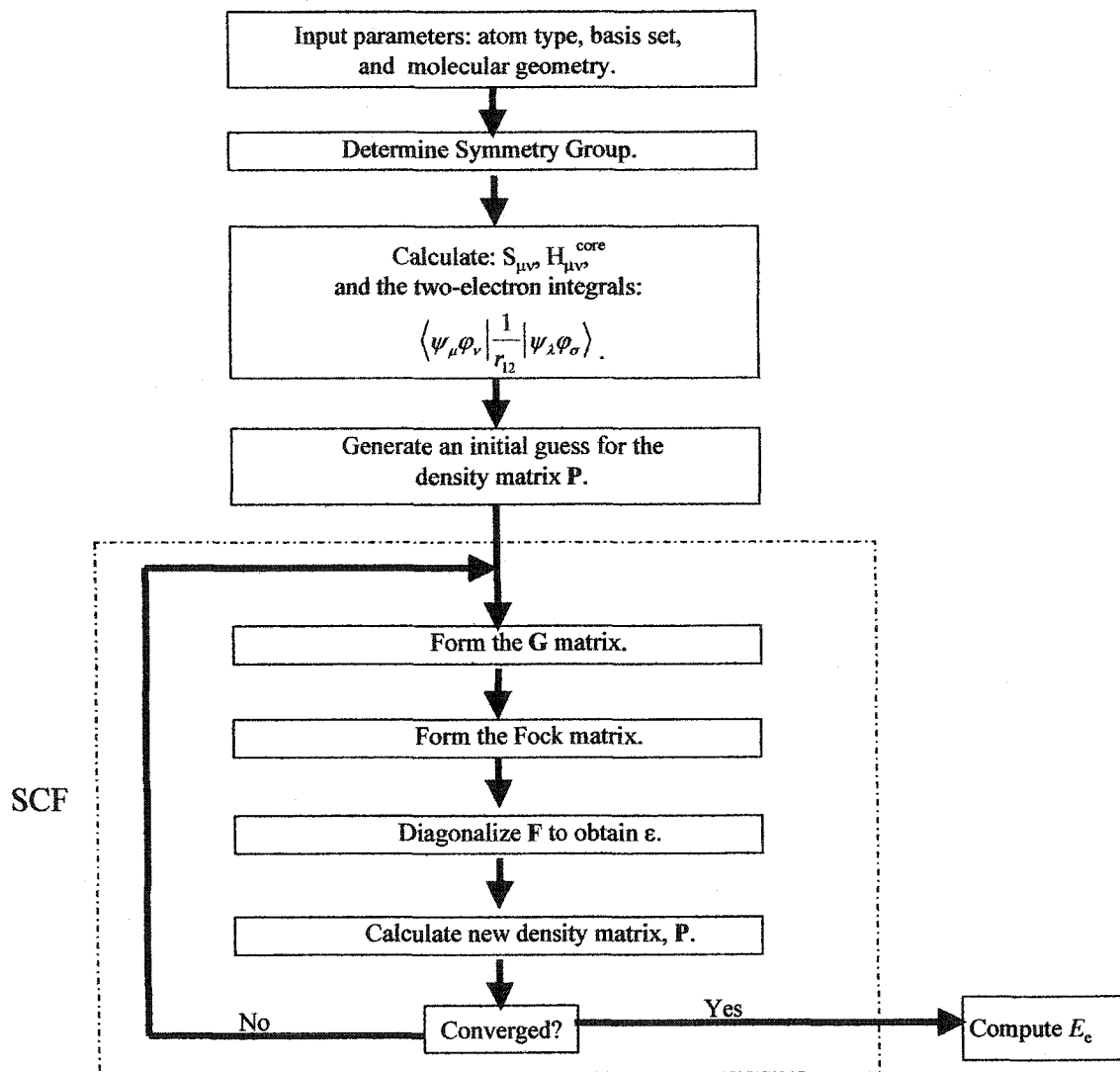
Figure 6.2: Flowchart of the SCF procedure.

where $H_{\mu v}^{core}$ is the core-Hamiltonian matrix, and $G_{\mu v}$ is the two-electron part of the Fock matrix:[3]

$$H_{\mu v}^{core} = \left\langle \psi_\mu \left| h \right| \psi_v \right\rangle,$$ (6.33)

$$G_{\mu v} = \sum_\mu \sum_v P_{\lambda\sigma} \left[\left\langle \psi_\mu \psi_v \left| \tfrac{1}{r_{12}} \right| \psi_\mu \psi_v \right\rangle - \tfrac{1}{2} \left\langle \psi_\mu \psi_v \left| \tfrac{1}{r_{12}} \right| \psi_v \psi_\mu \right\rangle \right].$$ (6.34)

In Eq. 6.34, P is the density matrix and is given by:[3]

$$P_{\lambda\sigma} = 2 \sum_{i=1}^{occupied} c_{\lambda i} c_{\sigma i}^* \ .$$

(6.35)

Numerical solution of the Roothaan-Hall equations (Eq. 6.30) is described in the following. If the matrix of coefficients, C, is known, then the diagonal matrix of eigenvalues, ε, can be computed, or if ε is known, C can be computed. The difficulty in solving the Roothaan-Hall equations is that they are non-linear, since the Fock matrix, $F(C)$, depends on C through $G_{\mu\nu}$. Thus, the Roothaan-Hall equations are solved iteratively—an initial guess is taken for the C matrix and the eigenvalues, ε_i, are computed, these eigenvalues are then used to construct a new C matrix, and this process is repeated until the C matrix converges. This iterative procedure is called the self-consistent field (SCF) method and is outlined in Figure 6.2.

The Unrestricted, Open-Shell, Hartree-Fock Method

So far, this discussion was limited to the solution of the restricted, closed-shell, Hartree-Fock equations—the Roothaan-Hall equations. Solution of an unrestricted set of Hartree-Fock equations is analogous; for this case, the spatial orbitals for spin up and spin down electrons are different (Eq. 6.20). Thus, there are two sets of density matrices: P_α and P_β. Moreover, Eq. 6.22 shows that there are two Fock operators: f_α and f_β. Accordingly, two sets of Fock matrices are obtained for an unrestricted Hartree-Fock calculation:[3,4]

$$F^\alpha C^\alpha = SC^\alpha \varepsilon^\alpha$$

$$F^\beta C^\beta = SC^\beta \varepsilon^\beta \ .$$

(6.36)

Solution of these equations is analogous to the solution of the Roothaan-Hall equations (Eq. 6.30)—see the SCF procedure in Figure 6.2. However, these equations (Eq. 6.36) are coupled; F^α and F^β both depend on C^α and C^β. Thus, both equations (Eq. 6.36) must be solved simultaneously. As expected, solution of the unrestricted, Hartree-Fock equations yields two sets of orbitals and eigenvalues—one set with spin α and the other set with spin β.

6.1.3 Miscellaneous Computational Procedures

Solution of the Hartree-Fock equations is outlined in Figure 6.2. Several features in this flow-chart have yet to be identified. The purpose of this section is to provide a complete description of this flow-chart.

Initial Guess

As indicated in the flow-chart (Figure 6.2), an initial guess must be taken for the wave function before the SCF procedure starts. Typically, this guess is chosen by using the results from a semi-empirical calculation, such as the intermediate neglect of differential overlap (INDO) approximation or extended Hückel Theory (EHT).[2,5] The default method for *Gaussian 98* is the INDO method; however, like the SCF procedure, it is iterative and sometimes fails to converge. In this case, the EHT method is used to calculate an initial guess. This process is fully automated by *Gaussian 98*.[1,5]

Symmetry

In addition, the flow-chart (Figure 6.2) includes an algorithm for computing the symmetry group of the molecule. Information about molecular symmetry is very important, since it can allow for a significant reduction in computational time. A brief discussion of molecular symmetry is given below.

The symmetry group of a molecule provides the list of symmetry operations belonging to that molecule. A symmetry operation reorients the molecule into an equivalent and indistinguishable configuration, thus leaving the energy of the system unchanged. Consequently, a symmetry operation $\hat{R}$ has the very important property of commuting with the Hamiltonian $\hat{H}$: $\left[\hat{R}, \hat{H}\right] = 0$. Since these operators commute, the energy eigenfunctions of the Hamiltonian are also eigenfunctions of the symmetry operators. These eigenfunctions form a basis for the irreducible representations of the symmetry group.[6] Thus, group theoretical arguments can be used to determine which matrix elements of the energy eigenfunctions must vanish. By identifying the vanishing matrix elements beforehand, no attempt is made at calculating these integrals, thus reducing computational effort. The computational time is inversely proportional to the number of symmetry operations.[2]

Geometry Optimization

As shown in Figure 6.2, the molecular geometry is a required input. Usually, an initial guess is taken for the geometry, and this geometry is varied until the best one is found. The best molecular geometry is the one for which E_e is minimum. The task of finding the best geometry is an optimization problem: the energy is treated as function of

nuclear coordinates, which are varied until a stationary point is found. Most geometry optimization methods that are used in quantum chemistry are based on the Newton-Raphson method.[2,7] The energy is expanded in a power series of the displacement vector, $\delta\vec{R}$, from an initial set of nuclear coordinates $\vec{R}_i$:

$$E(\vec{R}_{i+1}) \cong E(\vec{R}_i) + \nabla E(\vec{R}_i) \cdot \delta\vec{R} + \tfrac{1}{2}\delta\vec{R}^T \cdot \tilde{F}(\vec{R}_i) \cdot \delta\vec{R} + \cdots . \qquad (6.37)$$

The optimization algorithm is an iterative procedure, as reflected by the index i, which refers to a particular iteration. In the above equation, $\delta\vec{R}$ is the difference between the vectors of nuclear coordinates from successive iterations:

$$\delta\vec{R} = \vec{R}_{i+1} - \vec{R}_i , \qquad (6.38)$$

and the Hessian $\tilde{F}(\vec{R}_i)$ is the matrix of force constants. An element of the Hessian is given by

$$\tilde{F}_{mn} = \frac{\partial E(\vec{R}_i)}{\partial R_m \partial R_n} . \qquad (6.39)$$

Minimizing the energy (Eq. 6.37) with respect to $\delta\vec{R}$ and solving for $\delta\vec{R}$ yields

$$\delta\vec{R} = -[\tilde{F}(\vec{R}_i)]^{-1} \nabla E(\vec{R}_i) . \qquad (6.40)$$

The displacement vector (Eq. 6.40) determines the new set of nuclear coordinates for the next iteration (i.e., from Eq. 6.38, $\vec{R}_{i+1} = \vec{R}_i + \delta\vec{R}$). Using the new set of nuclear coordinates, a new energy is computed. This process is repeated until a stationary point is found for the energy. In practice, the Newton-Raphson method is numerically intensive, since the matrix of second derivatives (the Hessian) needs to be calculated at every step. Thus, the Newton-Raphson method is not practical for large systems. Instead, most

methods replace the Hessian with a suitable approximation to make the calculation affordable. The interested reader is referred to the literature for details.[2,5] In Figure 6.3, a new flow-chart is introduced, which shows how a geometry optimization routine is integrated with the SCF procedure.

6.2 Basis Sets

In this section, Gaussian basis sets are described. This type of basis set is typical for quantum chemical calculations. Recall in Eq. 6.28, a molecular orbital ϕ_i is approximated by an expansion on n basis functions of the form ψ_μ. For convenience this expansion is repeated here:

$$\phi_i = \sum_{\mu=1}^{n} c_{\mu i} \psi_\mu .$$

(6.41)

The basis functions are normalized and are expanded in terms of Gaussian functions, g_p:

$$\psi_\mu = \sum_p d_{p\mu} g_p ,$$

(6.42)

where $d_{p\mu}$ is a contraction coefficient—the basis function is said to be a contraction of primitive Gaussian functions.[4] A Gaussian function, which is centered at the atomic site $\vec{R}_A$, has the general form:[4]

$$g(\vec{r} - \vec{R}_A, \alpha) = c x^n y^m z^l e^{-\alpha|\vec{r} - \vec{R}_A|^2} ,$$

(6.43)

where c is a normalization constant, which is chosen such that:

$$\int d\vec{r} g^2 = 1 .$$

(6.44)

```
┌─────────────────┐
│  Input Section  │
└─────────────────┘
         │
         ▼
┌──────────────────────────┐
│ Determine Symmetry Group.│
└──────────────────────────┘
         │
         ▼
┌──────────────────────┐
│  Calculate Integrals.│
└──────────────────────┘
         │
         ▼
┌──────────────────────────┐
│  Generate Initial Guess. │
└──────────────────────────┘
         │
         ▼
┌──────────────────┐
│  SCF Procedure   │◄──────────┐
└──────────────────┘           │
    │                          │
    ▼                          │
┌──────────────────┐           │
│ Compute Energy   │           │
│ Derivatives.     │           │
└──────────────────┘           │
    │                          │
    ▼                          │
         ◇                     │
    Geometry        No         │
    Converged? ────────────────┘
         ◇
         │ Yes
         ▼
┌──────────────────────┐
│  Compute Energy Eₑ.  │
└──────────────────────┘
```
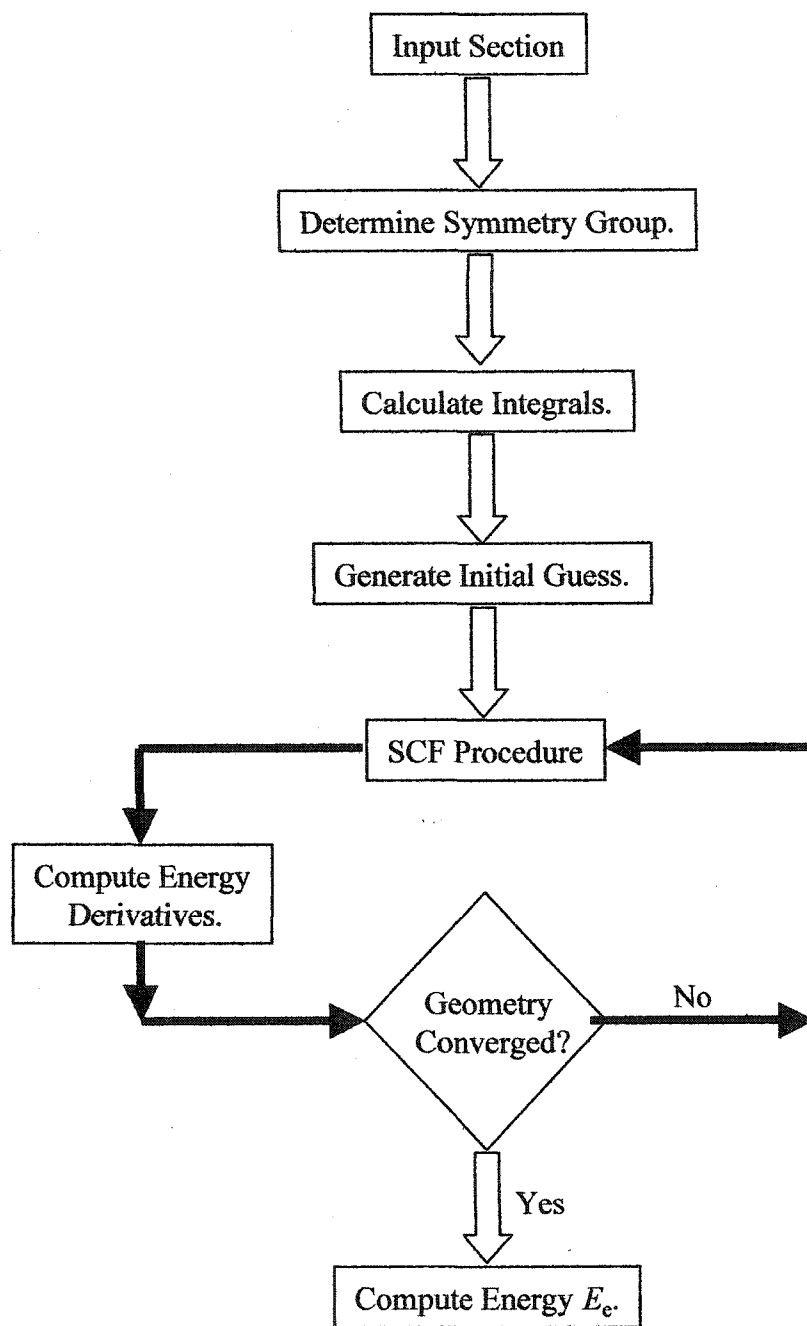
Figure 6.3: SCF procedure with geometry optimization algorithm.

To provide examples, the Gaussian-type atomic orbitals for an s-orbital and a p_z-orbital are given below:[4]

$$g_s = (\vec{r} - \vec{R}, \alpha) = \left(\tfrac{2\alpha}{\pi}\right)^{3/4} e^{-\alpha|\vec{r} - \vec{R}|^2}$$

$$g_{p_z} = (\vec{r} - \vec{R}, \alpha) = \left(\tfrac{128\alpha^5}{\pi^3}\right)^{1/2} z\, e^{-\alpha|\vec{r} - \vec{R}|^2} . \tag{6.45}$$

A single Gaussian orbital is a poor representation of the true atomic orbital. For example, a Gaussian-type s-orbital (first of Eq. 6.45) does not have the correct slope at the nucleus ($\vec{r} = 0$), and the Gaussian s-orbital falls off too rapidly far away from the nucleus.[2,3] Thus, to make up for these deficiencies, the basis function is expanded as a combination of several Gaussians (see Eq. 6.42). Substituting the basis set expansion (6.42) into Eq. 6.41 gives

$$\phi_i = \sum_{\mu=1}^{n} c_{\mu i} \sum_{p} d_{p\mu} g_p . \tag{6.46}$$

The contraction coefficients ($d_{p\mu}$) and Gaussian parameters (α, l, m, and n) are not variational parameters; these are fixed constants, which are optimized to best fit SCF atomic calculations.[2,3] Thus, the contraction is a pre-constructed linear combination of fixed parameters, which define a particular basis set.

The reason for choosing Gaussian basis sets is because they allow efficient and rapid evaluation of the two-electron integrals.[2,3] Evaluation of these integrals is the major difficulty in any Hartree-Fock calculation, simply because there are often millions of integrals to evaluate. The number of two-electron integrals in a calculation scales like $O(N^4/8)$, where N is the number of basis functions.[3] For example, consider a Hartree-Fock calculation on a small system like benzene (C_6H_6), using an STO-3G basis set. This basis

set describes each carbon by five basis functions and each hydrogen by one basis function. Using this basis set, the total electronic wave function of benzene is approximated by 36 basis functions; thus, the number of two-electron integrals is on the order of 209,952. Evidently, evaluation of numerous integrals is time-consuming, which justifies the choice of a Gaussian basis set.

STO-3G, 3-21G, and 6-31G(d) Basis Sets

Three specific types of basis sets are now described. The first is the STO-3G basis set, which is a minimal basis set.[2-5] A minimal basis set consists of the minimum number of basis functions that are required to describe an atom. For example, the atomic configuration of carbon is $(1s^2 2s^2 2p^2)$; thus, a minimal basis set for carbon consists of the five basis functions: 1s, 2s, $2p_x$, $2p_y$, and $2p_z$. These five basis functions are centered at the nuclear site of the carbon. To clarify, consider a C_2 dimer, which has one carbon positioned at $\vec{R}_A$ and the other at $\vec{R}_B$. Using the STO-3G basis set, the wave function of the dimer is expanded as a combination of 10 basis functions—five are centered on $\vec{R}_A$ and the other five on $\vec{R}_B$. The nomenclature STO-3G means that each Slater type orbital (STO) is represented by a contraction of three Gaussians (3G). A description of the STO-3G basis set for C, N, and H is shown in Table 6.1.

The second type is the 3-21G basis set, which is described as a split-valence basis set.[2-5] The 3-21G is a simple extension of the STO-3G basis, but now each valence orbital is described by two basis functions—hence a split valence basis set. The

Table 6.1: Description of the STO-3G, 3-21G, and 6-31G(d) basis sets.

	C or N	H	Number of Basis Functions
STO-3G	$1s$, $2s$, $2p_x$, $2p_y$, $2p_z$	$1s$	C or N: 5 H: 1
3-21G	$1s$, $2s$, $2p_x$, $2p_y$, $2p_z$, $2s'$, $2p_x'$, $2p_y'$, $2p_z'$	$1s$, $1s'$	C or N: 9 H: 2
6-31G(d)	$1s$, $2s$, $2p_x$, $2p_y$, $2p_z$, $2s'$, $2p_x'$, $2p_y'$, $2p_z'$, $3d_{xx}$, $3d_{yy}$, $3d_{zz}$, $3d_{xy}$, $3d_{xz}$, $3d_{yz}$	$1s$, $1s'$	C or N: 15 H: 2

3-21G representation for C, N, and H is shown in Table 6.1. The notation 3-21G means that a contraction of 3 Gaussians describes the core orbitals (number to the left of dash) and that each valence orbital is represented by two sets of functions (numbers to the right of dash). One function is a contraction of 2 Gaussians, and the second is 1 Gaussian.

The third basis is the 6-31G(d) basis set[2-5] (see Table 6.1). The notation 6-31G also indicates a split-valence basis set. Here, the core orbitals are a contraction of 6 Gaussians, and each valence orbital is represented by two functions: one is a contraction of 3 Gaussians, and the other is 1 Gaussian. The d signifies that for the first row elements, the basis includes an additional six Cartesian d-functions: d_{xx}, d_{yy}, d_{zz}, d_{xy}, d_{xz}, and d_{yz}.

In general, larger basis sets provide a better mathematical description of the electronic wave function, and thus, provide more accurate results. However, improved accuracy comes at a significant cost, since CPU time scales roughly as N^4, where N is the number of basis functions. Thus, the size of the basis set that can be used to study a

particular system is constrained by available computational resources as well as the size of the system.[4]

6.3 Computational Details

All calculations were carried using the *Gaussian 98* quantum-chemistry program.[1] A series of carbon clusters—with and without nitrogen—were examined to test the stability of vacancy defects and pentagons incorporated in these clusters. The difference between total energies was used as a measure of stability. All total energies were computed using an unrestricted, Hartree-Fock (UHF) calculation. The UHF method was chosen since some of the clusters had an odd number of electrons—e.g., those clusters with an odd number of nitrogens (see Chapter 10). Since the calculations were all UHF, the *Mix option* was used to generate the initial guess for the SCF procedure—see the *Gaussian 98* literature for details.[4,5]

Except where noted, the UHF calculations were carried out using both the STO-3G and 3-21G basis sets—such calculations are compactly described as UHF/STO-3G and UHF/3-21G, respectively. Typically, geometry optimizations for the clusters were performed at the same level of theory: e.g., UHF/STO-3G//UHF/STO-3G. (The label to the left of the "//" indicates the method used to compute the total energy, while the label to the right indicates the method used to optimize the geometry.) Since the total energies were computed in conjunction with the geometry optimization, the convergence level was set to 10^{-8} Hartrees, which is the default for *Gaussian 98*. However, for single-point, energy calculations, a SCF convergence criterion of 10^{-4} Hartrees sufficed. The geometry optimizations were carried out using the BERNY algorithm,[5,8] using the GDIIS

optimizer.[5,9] The convergence criteria for the geometry optimization were set to minimum computed RMS forces of 0.00001 Hartrees/Bohr and RMS displacements of 0.00004 Bohr.

The cluster-sizes ranged form 24-56 atoms; the hydrogens terminating the clusters are excluded from this count. Most calculations were carried out on a standard desktop computer with a 32-bit x86 Intel processor and 256 MB of RAM. Due to the limited computational resources and large cluster size, the small basis sets (STO-3G and 3-21G) were deemed appropriate. Calculations were first carried using the STO-3G basis set. Although the energies that are computed with the STO-3G basis set are not quantitatively accurate, the basis set is affordable and capable of elucidating qualitative trends. Using the UHF/STO-3G calculation as a starting point, the cluster's geometry was re-optimized with a UHF/3-21G calculation. Comparison between total energies that were obtained with both basis sets demonstrated effects due to basis size. After each calculation, the stability of the ground state was tested, using the algorithm that was provided with the *Gaussian 98* package.[1] The ground state of systems with an even number of electrons was a singlet, while the ground state of those with an odd number was a doublet. The results of this study are found in Chapter 10.

6.4 References

1   *Gaussian 98, Revision A.9*, M. J. Frisch, G. W. Trucks, H. B. Schlegel, G. E. Scuseria, M. A. Robb, J. R. Cheeseman, V. G. Zakrzewski, J. A. Montgomery, Jr., R. E. Stratmann, J. C. Burant, S. Dapprich, J. M. Millam, A. D. Daniels, K. N. Kudin, M. C. Strain, O. Farkas, J. Tomasi, V. Barone, M. Cossi, R. Cammi, B. Mennucci, C. Pomelli, C. Adamo, S. Clifford, J. Ochterski, G. A. Petersson, P. Y. Ayala, Q. Cui, K. Morokuma, D. K. Malick, A. D. Rabuck, K. Raghavachari, J. B. Foresman, J. Cioslowski, J. V. Ortiz, A. G. Baboul, B. B. Stefanov, G. Liu, A. Liashenko, P. Piskorz, I. Komaromi, R. Gomperts, R. L. Martin, D. J. Fox, T. Keith, M. A. Al-Laham, C. Y. Peng, A. Nanayakkara, M. Challacombe, P. M. W. Gill, B. Johnson, W. Chen, M. W. Wong, J. L. Andres, C. Gonzalez, M. Head-Gordon, E. S. Replogle, and J. A. Pople (Gaussian, Inc., Pittsburgh, PA, 1998).

2   F. Jensen, *Introduction to Computational Chemistry* (Wiley, New York, 1999).

3   A. Szabo and N. S. Ostlund, *Modern Quantum Chemistry: Introduction to Advanced Electronic Structure Theory* (Macmillan, New York, 1982).

4   J. B. Foresman and A. Frisch, *Exploring Chemistry with Electronic Structure Methods*, 2 ed. (Gaussian, Inc., Pittsburgh, PA, 1993).

5   A. Frisch and M. J. Frisch, *Gaussian 98 User's Reference*, 2 ed. (Gaussian, Inc., Pittsburgh, PA, 1999).

6   F. A. Cotton, *Chemical Applications of Group Theory*, 2 ed. (Wiley, New York, 1990).

7   G. Fogarasi, X. Zhou, P. Tayor, and P. Pulay, J. Am. Chem. Soc. **114**, 8191 (1992).

8   H. B. Schlegel, J. Comput. Chem. **3**, 214 (1982).

9   P. Csaszar and P. Pulay, J. Mol. Struct. (THEOCHEM) **114**, 31 (1984).

Chapter 7—Nanoindentation Results and Discussion

In this chapter, nanoindentation results on amorphous carbon-nitride (a-CN$_x$) films are discussed. The hardness and reduced elastic modulus were determined by analysis of the unloading curves using the Oliver-Pharr method (see Chapter 4). The data confirm that the a-CN$_x$ films have a low modulus, but high strength. These materials were further characterized with x-ray photoelectron spectroscopy (XPS) and nuclear magnetic resonance (NMR) spectroscopy. The purpose of this nanoindentation study was to validate that our spectroscopic studies were on an a-CN$_x$ material that is both hard and elastic.

7.1 Background

The importance of carbon-based films (e.g., diamond-like carbon films) for use as surface coatings is well established,[1-3] which provides motivation to look at other carbon systems, such as a-CN$_x$. Indeed, researchers have found that incorporating nitrogen into carbon films dramatically alters their mechanical properties.[4,5] When deposited under suitable deposition conditions, a-CN$_x$ films can be fabricated with low modulus, high hardness, and high elastic recovery. The material readily gives under applied load, but resists permanent deformation, therefore, recovering its original shape when the load is released. Ordinarily, hard materials such as ceramics have high modulus and are brittle,

Table 7.1: A comparison of the hardness and elastic modulus, as determined by nanoindentation, for fused silica, aluminum, and a-CN_x.[6]

Material	Hardness (GPa)	Elastic Modulus (GPa)
Fused Silica	10	70
Aluminum	0.4	57
Carbon-Nitride	>6	35-55

while soft materials, such as metals, have low modulus and deform plastically. Therefore, this combination of mechanical properties is unusual. For comparison, the hardness and elastic modulus values for fused silica, aluminum, and a-CN_x are shown [6] in Table 7.1. This comparison shows that a-CN_x films can be elastic like aluminum, but hard like fused silica.

Carbon nitride has received considerable attention because of its potential as a hard coating, and much effort has been put forth to study its mechanical properties. Transmission electron microscopy work on a-CN_x films indicates a fullerene-like microstructure consisting of buckled, graphitic planes that are cross-linked together.[7] This sort of structure is consistent with the mechanical properties of hard and elastic a-CN_x films. The fullerene-like microstructure explains the high elasticity, while the cross-linking explains the material's resistance to plastic deformation. A major focus of a-CN_x research is to determine the chemical bonding of the structures that are responsible for buckling and cross-linking, and in turn to correlate these structures with mechanical properties.[4]

Several nanoindentation studies on a-CN_x with fullerene-like microstructure have been reported in the literature, and the reported values of hardness vary over a

considerable range. For example, Sjöström *et al.* have claimed that their a-CN_x films are super-hard,[7] with an estimated hardness of ~60 GPa, which is ~10 times higher than the hardness of our a-CN_x films. This is somewhat surprising, since the a-CN_x films in both studies were deposited using similar deposition conditions. Their claim of super-hardness seems unlikely, since their hardness values were determined from the nanoindentation unloading curves of 300 nm-thick films at an indentation depth of ~140 nm.[7] At these deep indents, the hardness was certainly overestimated due to substrate-film interaction. The difficulty in obtaining reliable mechanical properties of thin, carbon-nitride films is due to the high elastic response of the material, since even at low loads, deep indents are formed. This suggests that for thin films, a completely plastic indent can not be formed before the substrate affects the measurement. To overcome these problems, Neidhardt *et al.* [8] have evaluated their nanoindentation data of thin (400 nm) carbon-nitride films using a model suggested by Korsunsky *et al.*[9] In their study, nanoindentation data was collected for a series of indentation depths. Next, the Oliver and Pharr method [10] was used to determine the composite mechanical properties of the film-substrate system. The nanoindentation data were then fit with a function [9] to extract the hardness and elastic modulus of the film from the composite values of the film-substrate system. Neidhardt *et al.* reported hardness values in the range of 7-18 GPa; the range of values reflects the dependence on substrate bias and N_2 fraction in the N_2/Ar process gas. In addition, Hultman *et al.* have reported the fabrication of carbon-nitride nano-onions—a new fullerene-like material.[11] This material was reported to have a hardness of 7 GPa.

As mentioned above, the difficulty in determining reliable mechanical properties of thin, carbon-nitride films is due to its highly elastic nature. The high elasticity results

in large displacements at small loads, thus leading to substrate-film interaction. In response to this issue, Zheng *et al.*[12] have suggested that the elastic recovery R can be used as a means to compare mechanical properties:

$$R(\%) = \frac{h_{max} - h_r}{h_{max}} \times 100 \qquad (7.1)$$

Here, h_{max} is the maximum displacement at a particular load, and h_r is the residual displacement after the load is released. As defined, the recovery is not a reliable parameter for comparing literature values among different studies, since the recovery depends on the exact geometry of the indenter tip. Very sharp indenter tips will induce more plastic flow, thereby resulting in a lower recovery. Conversely, a higher recovery will be observed when a blunt tip is used. However, if the same tip is used, a comparison of recoveries provides a useful approach for monitoring film properties.

Nanoindentation tests were used to determine the mechanical properties of our a-CN_x films. Our nanoindentation results are not exhaustive; a detailed analysis of the mechanical properties from systematic parametric study is not presented. The purpose of the nanoindentation measurements was to confirm that the a-CN_x films had a high elasticity and resisted plastic deformation.

7.2 Nanoindentation Results

The nanoindentation results presented in this section are divided into two categories, which are based on the film's deposition parameters. *Category 1*: 1 μm-thick a-CN_x films on 1 cm^2 substrates were deposited at 400 °C, 5 mTorr, and 4 cm substrate-target distance; this material was used in the XPS study (Chapter 8). *Category 2*: 6 μm-

thick a-CN_x films on 75 mm-diam. substrates were deposited at 300 °C, 8 mTorr, and 8 cm substrate-target distance; this material was used in the NMR study (Chapter 9). As discussed in more detail in Chapter 3, these conditions were chosen to balance sample quality and deposition time.

Category 1: Material Used in XPS Study.

The loading behavior of a typical Category-1, a-CN_x film is shown in Figure 7.1. The entire unloading curve was fit with a power-law relation (Eq. 4.4), and this fit (solid line) provides values for the unloading exponent, m, and residual displacement, h_r. Averaging over 6 indents, the exponent m was found to be 2.06 ± 0.08. Using the residual displacements from the fit and Eq. 7.1, an average value for the recovery was determined: $R = 90 \pm 2\%$, for a 120 nm indent at a maximum load of 0.9 mN. Indents at 120 nm gave a hardness of 5.5 ± 0.6 GPa and an elastic modulus of 38 ± 2 GPa. The hardness and elastic modulus were also monitored as a function of indentation depth using continuous-stiffness measurements (Figure 7.2).

Category 2: Material Used in the NMR Study.

The elastic modulus and hardness for a Category-2 film are shown as a function of indentation depth in the upper panel of Figure 7.3. Both the hardness and modulus at each point were obtained using the Oliver-Pharr method.[10] The open squares correspond to testing at the center of the 75 mm-diam. substrate, while the filled squares correspond to testing 10 mm from the edge. A typical load versus displacement curve, illustrating the high elastic recovery of this material, is shown in the lower panel of Figure 7.3.
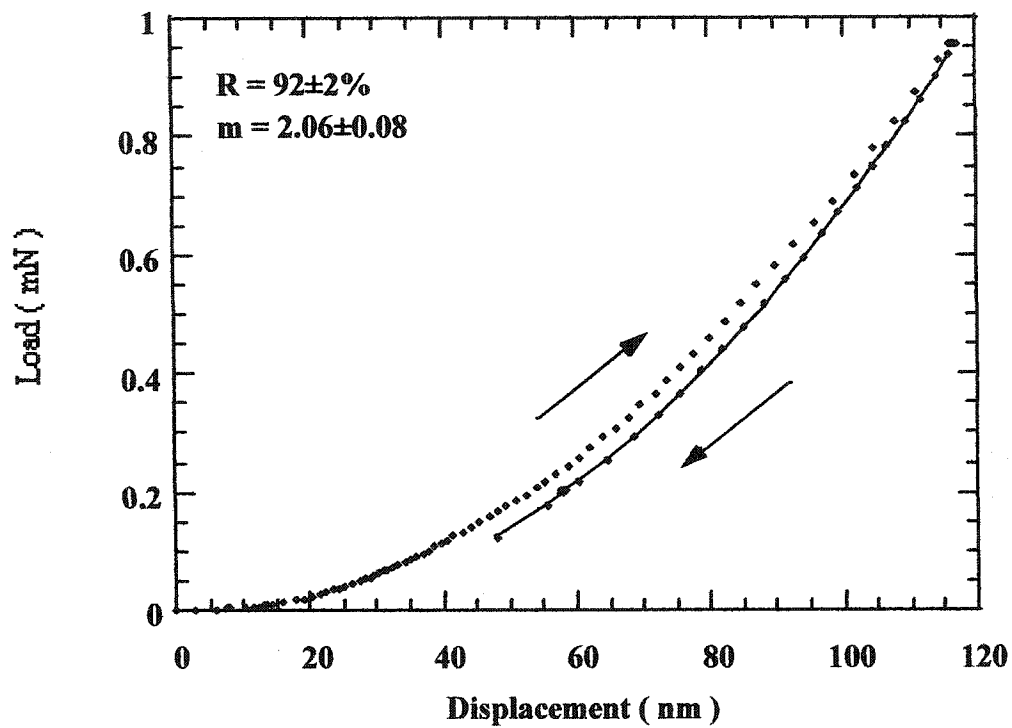
Figure 7.1: A nanoindentation curve for an a-CN$_x$ film that was deposited at 400 °C. The unloading portion of the curve was fit with the power-law relation, as described by Oliver and Pharr.[10]
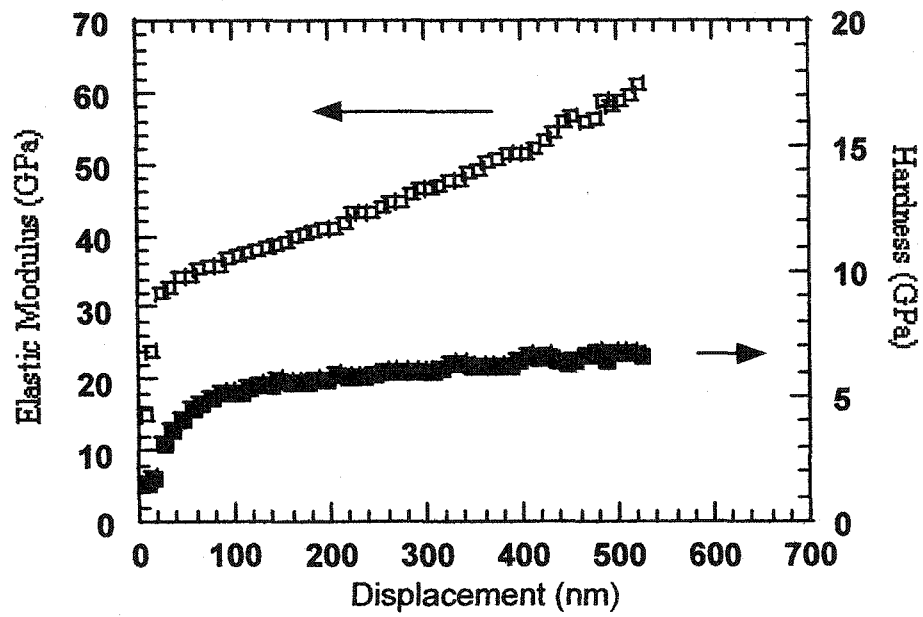
Figure 7.2: The hardness (filled squares) and elastic modulus (open squares) were obtained from continuous stiffness measurements and are shown as a function of indentation depth.
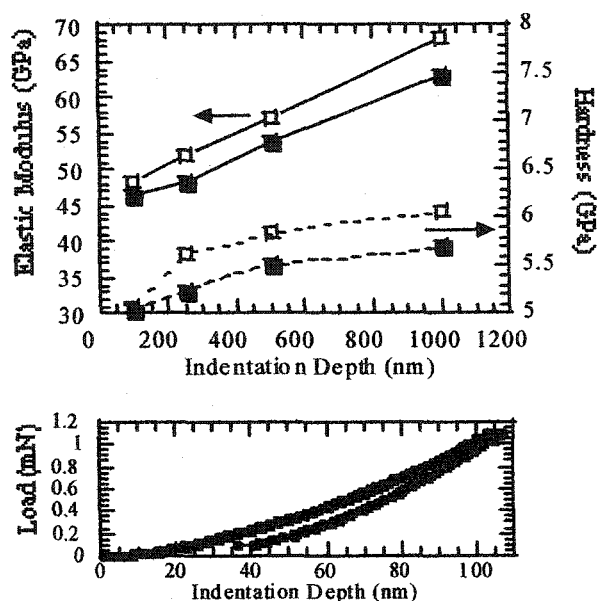
Figure 7.3: Nanoindentation results of a 6 µm-thick, a-CN_x film. In the upper panel, the hardness (symbols with dashed lines) and elastic modulus (symbols with solid lines) are shown as a function of indentation depth. The open squares correspond to results obtained at the center of the 75 mm-diam. substrate, while the filled squares were obtained 10 mm from the edge. The lower panel illustrates a typical load versus displacement curve of this material.

Using the same technique as with the data from Category-1, h_r, m, and thereby R were calculated from a fit to the unloading curve. A comparison of results obtained for indents made at the center and edge of the 75 mm-diam. substrate, as a function of indentation depth, is summarized in Table 7.2; the power-law relation was fit to the entire unloading curve. The notable deviations from m = 2 indicate a very unusual unloading behavior (see discussion section). To clarify the unloading behavior, the fits were repeated using only the top 70% of the unloading curve. In Table 7.3, these results are shown for the 250 and 1000 nm indents that were taken at the center of the 75 mm-diam. film. Notice that now m = 2 for the 250 nm indent. All standard deviations (Table 7.2 and 7.3) were obtained from an average over 10 indents.

Table 7.2: The unloading exponent, m, and the recovery, R, were determined by fitting a power-law relation (Eq. 4.4) to the entire unloading curve. These results provide a comparison of the unloading behavior as a function of indentation depth. Measurements taken at both the center and edge of the 75 mm-diam. substrate are shown. Note the large deviations from $m = 2$.

Center

Indentation Depth (nm)	100	250	500	1000
Exponent, m	2.17±0.06	2.17±0.02	2.29±0.01	2.49±0.02
Recovery, R (%)	79±2	79±1	79.1±0.4	78.0±0.4

Edge

Indentation Depth (nm)	100	250	500	1000
Exponent, m	2.2±0.06	2.21±0.02	2.35±0.01	2.51±0.02
Recovery, R (%)	82±2	80.7±0.5	81.2±0.5	79.3±0.5

Table 7.3: The deviations from m = 2, as shown in Table 7.2, suggest an unusual unloading behavior. In order to clarify the unloading behavior, the power-law fits to the unloading curves for the 250 and 1000 nm indents that were taken at the center of the 75 mm-diam. film were repeated. Instead of using the entire unloading curve, only the top 70% of curve was fit. Notice that now m = 2 for a displacement of 250 nm.

Center

Indentation Depth (nm)	250	1000
Exponent, m	2.00±0.03	2.20±0.03

Table 7.4: The loading behavior of an elastic half-space is dependent on the punch geometry. The loading exponents, *m*, are shown for several indenter geometries. These values were calculated by Sneddon under the constraint of a rigid indenter.[13]

Indenter Geometry	Exponent
Flat	1
Paraboloid	1.5
Cone	2

7.3 Nanoindentation Discussion

From Hertzian analysis, the loading behavior of an elastic half-space is described by a power-law relation,[10,13] for example, see Eq. 4.4. The exponent *m* is characteristic of the indenter's geometry,[10,13] as shown in Table 7.4 for various punch types. Since, we are investigating a very elastic material using a sharp indenter with a shape close to a cone, a value of $m = 2$ is reasonable. Thus, the unloading behavior of the NMR material (Table 7.2) seems unusual, as indicated by the notable deviations from $m = 2$. This is especially surprising at small indents (100 and 250 nm). Notice that $m \sim 2.2$ at a displacement of 250 nm (Table 7.2). At large penetration depths (500 or 1000 nm), deviations from m = 2 are not surprising, since in this regime substrate-film interaction affects the unloading behavior.

In an attempt to clarify this unusual behavior, the fits were repeated using only the top 70% of the unloading curve. In Table 7.3, these results are shown for indents at 250 and 1000 nm taken at the center of a 75 mm-diam. film. For these indents, notice that $m = 2$ for a displacement of 250 nm. Clearly, the unloading behavior of $a\text{-CN}_x$ is modified at small loads, perhaps, indicating that at low loads that the contact area of the

tip is less than expected. Thus in the Oliver and Pharr analysis, we compensated for this effect by using only the top 70% of the unloading data in the fit.

The unusual unloading behavior at low loads was noticed earlier by Garcia and co-workers.[14] They suggest that during the initial loading, the material densifies—the buckled layers are pushed together. As the layers are pushed together, the resistance to deformation then increases due to Coulomb repulsion. Thus, small loads will correspond to larger displacements during the initial loading; then as the layers are pushed together, the deformation behaves in a conventional way. These steps reverse during unloading. As the load is released, the buckled layers spring back into place, thus modifying the behavior during the last stages of unloading.

The most important points from the nanoindentation results are summarized below. The mechanical properties of both carbon-nitride materials can be compared to illustrate their sensitivity to deposition conditions. At an indentation depth of ~100 nm, the NMR material exhibits a hardness of 5.0 GPa and an elastic modulus of 47 GPa, while the XPS material exhibits values of 5.5 GPa and 38.2 GPa. Both materials have approximately the same hardness, but the XPS material is less stiff. The lower stiffness of the XPS material is consistent with its higher recovery. More importantly, both a-CN_x films have high elasticity but resist plastic deformation, as demonstrated by the loading curves in Figures 7.1 and 7.3. This combination of properties demonstrates that our a-CN_x films can be regarded as both hard and elastic. The elastic modulus and hardness, as a function of indentation depth, for the NMR material is shown in Figure 7.3. Notice that the mechanical properties at the center and edge follow very similar trends, except for a constant offset. This constant offset is perhaps attributed to a decreased ion flux near the

edge during the film-fabrication process. It is noted that Hellgren *et al.* have demonstrated that increased ion flux can lead to higher film hardness.[15] Comparison of the mechanical properties between the center and edge of the substrate demonstrates that our material collection process for the NMR experiments was reasonable. We have produced large-area, highly-elastic, a-CN$_x$ films with uniform mechanical properties.

7.4 Conclusions

Nanoindentation measurements confirm that the a-CN$_x$ films are highly elastic but hard. Thus, the major focus of the nanoindentation testing was fulfilled. Furthermore, comparison of indentations between center and edge of the NMR films shows that the deposition process creates material that is mechanically similar over the entire diameter of the film.

7.5 References

1 E. J. Coad, C. S. J. Pickles, G. H. Jilbert, and J. E. Field, Diamond Relat. Mater. 5, 640 (1996).

2 M. Ohring, *The materials science of thin films* (Academic Press, 1992).

3 Z. M. Zeng, T. Zhang, X. B. Tian, B. Y. Tang, T. K. Kwok, and P. K. Chu, Surf. Coat. Technol. 128, 236 (2000).

4 N. Hellgren, M. P. Johansson, E. Broitman, L. Hultman, and J. E. Sundgren, Phys. Rev. B 59, 5162 (1999).

5 B. C. Holloway, O. Kraft, D. K. Shuh, W. D. Nix, M. Kelly, P. Pianetta, and S. Hagstrom, J. Vac. Sci. Technol. A 18, 2964 (2000).

6 B. C. Holloway, Ph.D. Dissertation, Stanford, (1997).

7 H. Sjöström, S. Stafstrom, M. Boman, and J. E. Sundgren, Phys. Rev. Lett. 75, 1336 (1995).

8 J. Neidhardt, Z. Czigany, L. F. Brunell, and L. Hultman, J. Appl. Phys. 93, 3002 (2003).

9 A. M. Korsunsky, M. R. McGurk, S. J. Bull, and T. F. Page, Surf. Coat. Technol. 99, 171 (1998).

10 W. C. Oliver and G. M. Pharr, J. Mater. Res. **7**, 1564 (1992).

11 L. Hultman, S. Stafstrom, Z. Czigany, J. Neidhardt, N. Hellgren, I. F. Brunell, K. Suenaga, and C. Colliex, Phys. Rev. Lett. **87**, 225503/1 (2001).

12 W. T. Zheng, E. Broitman, N. Hellgren, K. Z. Xing, I. Ivanov, H. Sjöström, L. Hultman, and J. E. Sundgren, Thin Solid Films **308**, 223 (1997).

13 I. N. Sneddon, Int. J.Engng. Sci. **3**, 47 (1965).

14 I. A. Garcia, E. G. Berasategui, S. J. Bull, T. F. Page, J. Neidhardt, L. Hultman, and N. Hellgren, Philos. Mag. A **82**, 2133 (2002).

15 N. Hellgren, K. Macak, E. Broitman, M. P. Johansson, L. Hultman, and J. E. Sundgren, J. Appl. Phys. **88**, 524 (2000).

Chapter 8—X-ray Photoelectron Spectroscopy Results and Discussion

In this chapter, the chemical bonding of amorphous carbon-nitride (a-CN$_x$) films is examined by x-ray photoelectron spectroscopy (XPS). Nanoindentation results (Chapter 7) confirm that these films were highly compliant and had high elastic recovery. XPS was used to investigate nitrogen bonding by directly comparing the N(1s) spectra of a-CN$_x$ with the N(1s) peak positions from a variety of organic compounds, which were all characterized in the same XPS system. We show that the N(1s) spectra of a-CN$_x$ do not conclusively support a film-structure model with nitrogen bonded to sp^3 carbons, as suggested by earlier work.[1] We offer an alternate interpretation that is based on the presented data and previous N(1s) XPS chemical-shift calculations. Together the data suggest that hard and elastic a-CN$_x$ consists of an sp^2-carbon network with single-atom vacancy defects, as found in a graphite layer. However, it is emphasized that our XPS data do not dismiss the possibility of sp^3 carbons in a-CN$_x$ films. Instead, our XPS data shows that its presence is inconclusive and unconfirmed. Our XPS work sets the stage for our nuclear magnetic resonance (NMR) study, which is reported in Chapter 9.

8.1 Background

XPS is perhaps the most common technique that has been used to examine the composition and bonding of a-CN$_x$ films. Several groups have measured high-resolution XPS spectra of the C(1s) and N(1s) core-levels in a-CN$_x$.[2-13] The C(1s) spectra are typically described by a broad featureless peak, which becomes more asymmetric and broadened toward higher binding energy with increasing nitrogen concentration in the film.[5,7,8,10,13] The lack of clear and distinguishable features in the C(1s) spectrum makes reliable deconvolution unlikely. Moreover, the binding energy of the carbon-bonded-only-to-carbon (C-C) component is insensitive to hybridization. The C-C component has a binding energy of ~285.0 eV, regardless of hybridization.[14] Thus, the C-C components corresponding to the sp^2 and sp^3 bonding fractions can not be resolved. Because of the inability of in providing reliable peak assignments to the C(1s) spectra, most work has focused on interpretation of the N(1s) spectra.

Typically, the N(1s) spectra are resolved into three intensity contributions by fitting Gaussian line-shapes. The two main components in the N(1s) spectra are typically near 398.5 and 400.6 eV. The relative binding energy and intensity of these peaks are dependent on deposition temperature and are correlated with the mechanical properties of the film.[9] The remaining component is described by a broad, high-binding-energy shoulder near 402 eV.[9] Proposed bonding assignments for these chemically-shifted peaks are still under debate, and interpretation varies widely in the literature.

In the following discussion, we review the literature of the varied assignments of the N(1s) peak. We will focus our attention only on the two main peak components near

398.5 and 400.6 eV, since these components typically make up 88% of the overall intensity (see Table 8.1).

Marton and co-workers reported XPS measurements on carbon-nitride films prepared by a variety of deposition methods (ion beam deposition, DC magnetron sputtering and electron-beam evaporation with an ECR ion source).[3] Based on a comparison of the N(1s) and C(1s) spectra with those of pyridine (C_2H_5N) and urotropine ($C_6H_{12}N_4$), they concluded that their carbon-nitride films consisted of a two-phase system. They assigned the low-binding-energy component at 398.3 eV to sp^3-hybridized nitrogen (3 σ-bonds and a lone pair) and the high-binding-energy component at 400.0 eV to sp^2 nitrogens (pyridine-like—2 σ-bonds, 1 π-bond, and a lone pair).

Rossi *et al.* prepared carbon-nitride films using an ion-beam-assisted magnetron with a nitrogen ion source.[2] They offer another interpretation of the N(1s) core-level spectra. They suggest that the low-binding-energy component at 398.2 eV is due to C≡N (nitrile) and that the component at 400.1 eV is due to C=N (imine).

Ronning *et al.* presented XPS data on carbon-nitride films that were prepared by mass-selected ion-beam deposition.[8] They offer an assignment based on the nitrogen coordination number. They assign the component near 398 eV to nitrogen bonded to two carbons (as in pyridine) and the component near 400 eV to nitrogen bonded to three carbons (as in amines or pyrrole).

Furthermore, Pels *et al.* have reviewed XPS analysis on nitrogen bonding that occurs in coals and chars.[15] They used XPS to investigate the evolution of the nitrogen functionality during the pyrolysis of DE53 coal and other model compounds. The identification of nitrogen bonding in coals and chars provides insight to nitrogen bonding

in other carbonaceous materials, e.g., a-CN_x. In their review, three main nitrogen bonding ranges are distinguished: 1) pyridine-like (398.7 ±0.3 eV); 2) amino groups (near 399.4 eV); and 3) pyrrole-like (400.3 ±0.3 eV). Comparison of these binding energies with the two main components in the N(1s) spectrum of a-CN_x offers an interpretation similar to that of Ronning *et al.* (see above).

The difficulty in making confident XPS peak assignments, as indicated above, for a-CN_x is not surprising. Although XPS is sensitive to chemical bonding, the bonding configurations of interest in a-CN_x are very close in energy and overlap, thus making reliable deconvolution unlikely. To remedy this situation, experimental results have been interpreted with aid of theoretical calculations. In particular, Δ-self-consistent-field binding energy calculations by Johansson and Stafström[16] suggest the following interpretation of the two main N(1s) bonding contributions. They propose that the N(1s) peak at 398.5 eV is due to sp^3 nitrogen threefold coordinated to sp^3 hybridized carbon, and that the N(1s) peak at 400.6 eV is due to sp^2 nitrogen threefold coordinated to sp^2 carbons (as in a substitutional site in a graphene segment). Note that both of these bonding types are three fold coordinated, which contrasts the suggestion made by Ronning *et al.* that N(1s) bonding assignments for a-CN_x can be based on coordination number.[8] Johansson and Stafström's interpretation supports the phenomenological model that the hardness of a-CN_x films are due to cross-linking between graphitic planes by sp^3 bonded carbon.[1] This model is widely accepted in the literature, since it seems reasonable that the improved hardness of a-CN_x can be accounted for by the presence of a diamond-like (sp^3) carbons.

Computational work by Snis and Matar[17] on the model compound $C_{11}N_4$ offers another interpretation of the ~2 eV chemical shift between the two main peak components in the N(1s) spectrum. $C_{11}N_4$ is a planar cluster with a structure similar to graphite; however, the plane of the cluster is perforated with single-atom vacancies. Along the perimeter of the vacancy, there are two non-equivalent sites at which nitrogen can be coordinated. Nitrogen can be located at sites that are either twofold or threefold coordinated to carbons. Using a full-potential, linearized-augmented-plane-wave method, they calculated the binding-energy ranges of nitrogen at these two sites. The nitrogen bonding configurations correspond to sp^2 N bonded to two aromatic carbons—pyridine-like—(398.3-398.8 eV), and to sp^2 N bonded to three sp^2 carbons (400.8-401.3 eV).[17]

Snis and Matar's computational work forward a very important point: pyridine-like nitrogen is assigned to the low-binding-energy component, not the high-binding-energy component. In contrast, other computational studies by Johansson and Stafström [16] and by Souto et al.[6] suggest that the binding energy of pyridine-like nitrogen is ~1 eV too high to account for the low-binding energy feature at ~398.5 eV in a-CN_x. In addition, several experimental studies (see above) attribute pyridine-like nitrogen to the high binding energy component in the a-CN_x spectra.[3,6] Insight into this issue is one focus of our XPS study. The low-binding-energy N(1s) component accounts for nearly 48% of the overall spectral intensity (see Table 8.1). Conclusive assignment of this intensity to only sp^2 or sp^3 nitrogen would be a major step in understanding the chemical bonding of carbon nitride.

In this work, we have measured XPS spectra of several organic compounds, which are representative of various nitrogen-bonding configurations in carbon and nitrogen

materials. The reference spectra were compared with the XPS data of hard and elastic a-CN_x films. We show that the assignment of the low-binding-energy N(1s) component as due to nitrogen bonded to sp^3 carbons is inconclusive, and we suggest that this component is instead due to pyridine-like nitrogens bonded at the perimeter of a vacancy defect. This defect may be similar to a single-atom vacancy in a graphite layer.

8.2 X-ray Photoelectron Spectroscopy Results

A representative survey scan is shown in Figure 8.1. The C(1s), N(1s), and O(1s) core-level and C(KLL), N(KLL), and O(KVV) Auger peaks are identified. Oxygen is the only detectable contaminant appearing in the spectrum, as expected, since all XPS measurements were performed *ex situ*. The presence of oxygen is attributed to atmosphere exposure prior to XPS analysis and is most likely due to absorbed water (not from the film fabrication process). This assumption is reasonable, since the ultimate pressure of the vacuum system was ~2 X 10^{-7} Torr and the deposition pressure was ~4 mTorr. Under these conditions, a rough estimate of oxygen contamination from the deposition process is 0.005%. We would have liked to test this hypothesis by measuring the intensity of the O(1s) peak as a function of sample temperature to see if the intensity of the O(1s) peak could be depleted by thermal desorbtion of water. However, *in situ* sample heating was unavailable. Typically, oxygen contamination was in the range of 4-8 at.%, as measured by XPS.

The N(1s) XPS spectrum of a hard and elastic a-CN_x (deposited at 400 °C) is shown in Figure 8.2. XPS measurements indicate a typical nitrogen concentration of 21 at.%. Before fitting the data, an integral background was calculated by an iterative Shirley
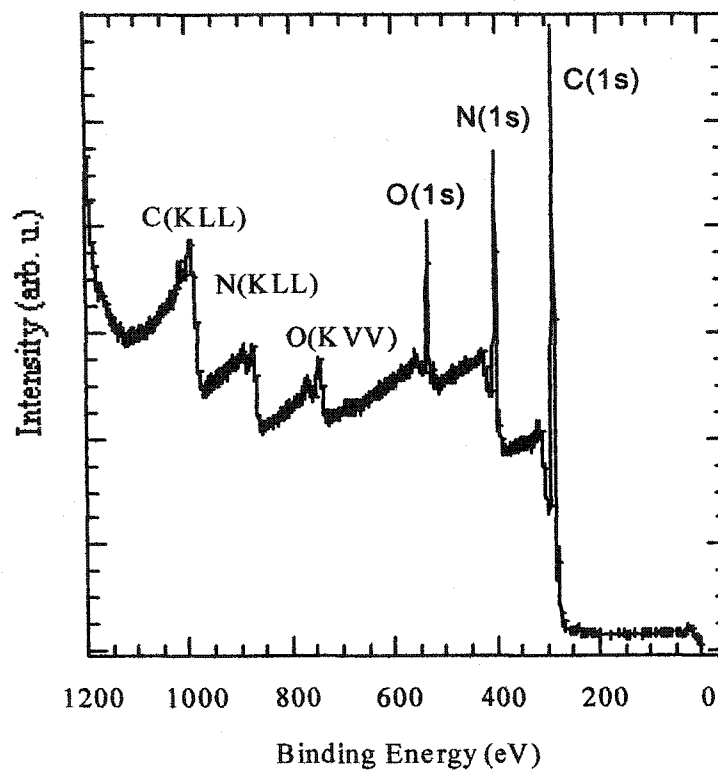
Figure 8.1: XPS survey scan of a typical *a-CN*$_x$ film. The C(1s), N(1s), and O(1s) core-level and C(KLL), N(KLL), and O(KVV) Auger peaks are labeled. The presence of oxygen is the only detectable contaminant appearing in the spectrum, and its presence is expected, since all XPS measurements were performed *ex situ*.
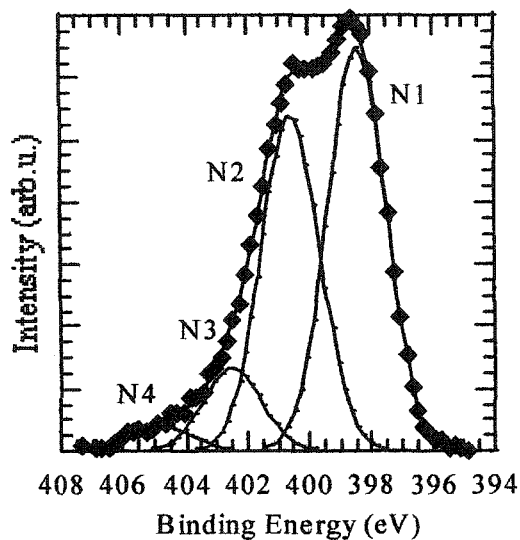
Figure 8.2: N(1s) XPS spectra of a-CN$_x$, deposited at 400 $^\circ$C. The spectra were fit with Gaussian line-shapes after subtracting an integral background.

Table 8.1: Peak-fit parameters and errors are shown for the spectrum shown in Figure 8.2. Note that the FWHM of each peak was constrained to be the same. As indicated by the relative size of the errors, a fit with four Gaussian components is reasonable.

Gaussian Component	Amplitude (arb. u.)	Peak Center (eV)	FWHM (eV)	Fraction (%)
N1	1295 ± 7	398.50 ± 0.01	2.21 ± 0.01	47.6 ± 0.4
N2	1075 ± 8	400.61 ± 0.02	same	39.5 ± 0.4
N3	270 ± 11	402.5 ± 0.1	same	9.9 ± 0.4
N4	83 ± 6	404.8 ± 0.0	same	3.0 ± 0.2

method [14,18] and subtracted from the raw data. Gaussian components were fit to the N(1s) spectra (see Figure 8.2), with each component constrained to have the same FWHM. The peak-fit parameters are displayed in Table 8.1. The N(1s) peak is composed of the components labeled N1, N2, N3, and N4 at 398.5, 400.6, 402.5, and 404.8 eV respectively, and each has a FWHM of 2.2 eV. The relative fractions of N1, N2, N3, and N4 are 48, 39, 10, and 3 %, respectively.

A summary of the N(1s) XPS results on the reference organic compounds is graphically depicted in Figure 8.3. The choice of reference compounds was restricted by the following two constraints: 1) N atoms are directly bonded only to C or N; and 2) only one N bonding configuration per compound. The upper portion of Figure 8.3 displays the N(1s) binding energies of the various reference organic compounds. Structures **A1** and **F** are from the binding-energy calculations by Souto *et al.*,[6] and structure **A2** is from the calculations by Johansson and Stafström.[16] Structures labeled **B-E** are from our experimental XPS measurements. The diamond-capped histograms indicate the N(1s) binding energies for the structures: **(A)** N sp^3 coordinated to sp^3 carbons (calculated); **(B)** N bonded in a pyridine-like configuration; **(C)** N bonded in an sp configuration (nitrile); **(D)** N sp^3 coordinated to aromatic rings; **(E)** N sp^2 bonded in a salt; and **(F)** N bonded to three sp^2 carbons in the interior of a graphite-like segment (calculated). For convenience, Table 8.2 displays the chemical name, structure, N(1s) binding energy, and the experimental vs. expected N/C ratios for the structures **B-E** (Figure 8.3). The comparison of experimental vs. expected N/C ratios suggests that we are primarily measuring the C(1s) component of the compound and not measuring the C(1s) component of adventitious carbon. In addition, the FWHM of the N(1s) peaks for the reference organic
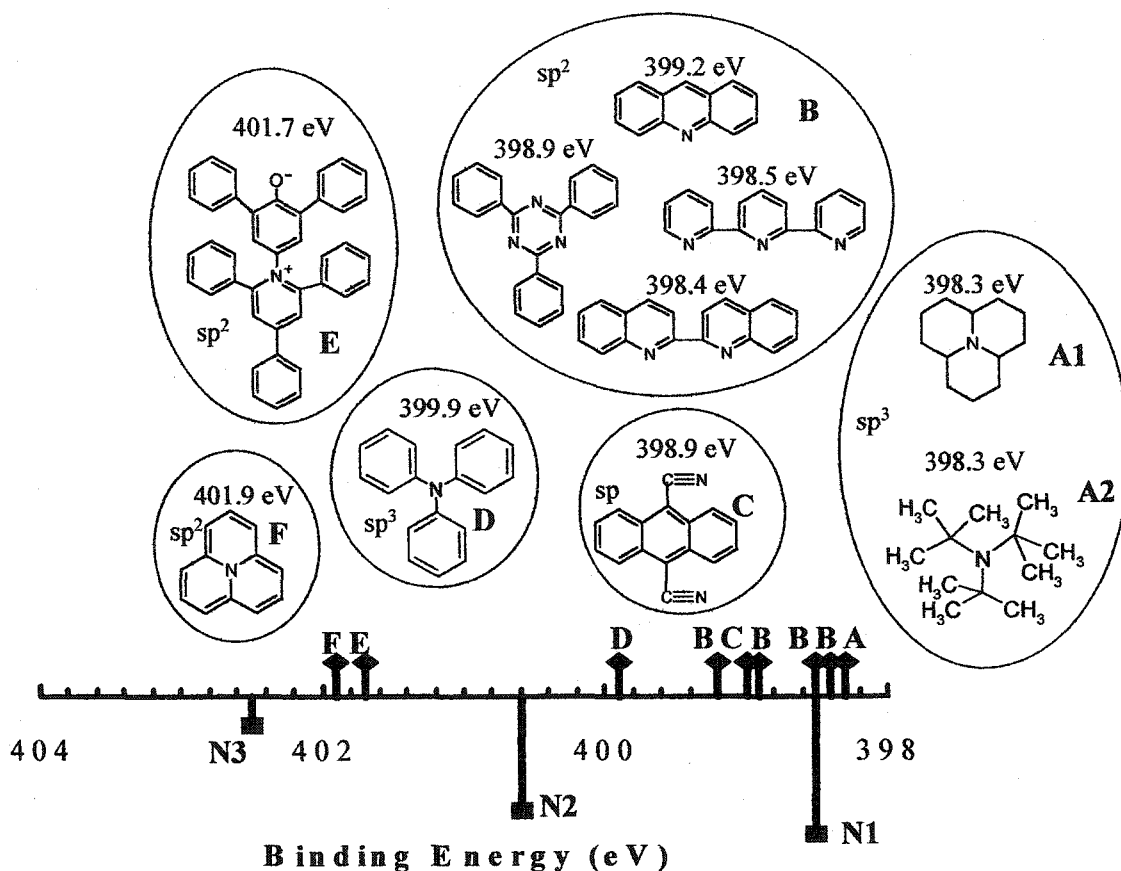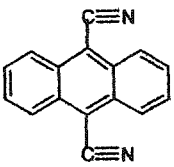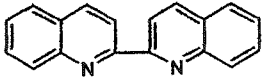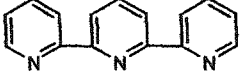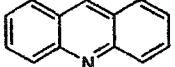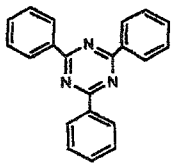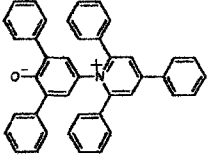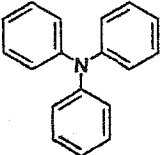
Figure 8.3. **Upper:** N(1s) binding energies for a variety of carbon compounds containing nitrogen. Structures A and F are from the binding energy calculations (A1 and F by Souto *et al.* [6] and A2 by Johansson *et al.* [16]). Structures B-E are from our experimental XPS measurements. The histograms indicate the N(1s) binding energy for the above structures: **(A)** N sp^3 coordinated to sp^3 C; **(B)** N bonded in a pyridine-like configuration; **(C)** N bonded in a nitrile configuration (sp); **(D)** N sp^3 coordinated to aromatic rings; **(E)** N threefold sp^2 bonded in a salt; and **(F)** N threefold coordinated in a graphite-like segment.

Lower: The histograms (capped with filled squares) indicate the position of the N(1s) binding energy for the Gaussian components of a-CN$_x$ (Figure 8.2). The heights of the histograms indicate the relative fractional contribution of a particular Gaussian component.

Table 8.2: The chemical names, N(1s) binding energies, and the experimental vs. expected N/C ratios for the structures B-E in Figure 8.3.

	Name	9,10-Anthracenedicarbonitrile
	N(1s) Binding Energy (eV)	399.0
	N/C measured	0.125
	N/C expected	0.125
	Name	2,2'-Biquinoline
	N(1s) Binding Energy (eV)	398.4
	N/C measured	0.086
	N/C expected	0.111
	Name	2,2':6',2''-Terpyridine
	N(1s) Binding Energy (eV)	398.5
	N/C measured	0.169
	N/C expected	0.200
	Name	Acridine
	N(1s) Binding Energy (eV)	399.2
	N/C measured	0.078
	N/C expected	0.077
	Name	2,4,6-Triphenyl-1,3,5-Triazine
	N(1s) Binding Energy (eV)	398.9
	N/C measured	0.141
	N/C expected	0.143
	Name	Reichardt's Dye
	N(1s) Binding Energy (eV)	401.7
	N/C measured	0.020
	N/C expected	0.024
	Name	Triphenylamine
	N(1s) Binding Energy (eV)	399.9
	N/C measured	0.060
	N/C expected	0.056

compounds were all in the range of 1.8-2.1 eV, except for acridine, which had a FWHM of 3.3 eV. The large FWHM of acridine is attributed to its high vapor pressure.

In the lower portion of Figure 8.3, the histograms (capped with filled squares) denote the N(1s) binding energies for the various Gaussian components N1, N2, and N3 (for simplicity, N4 is not shown), which are shown in Figure 8.2 and quantified in Table 8.1. The heights of the histograms indicate the relative fractional contribution of a particular Gaussian component to the overall spectral intensity.

Next, C(1s) XPS data are surveyed. The C(1s) spectrum of a-CN$_x$ (Figure 8.4) is featureless, but shows an asymmetric broadening toward high binding energies. The carbon-bonded-to-only-carbon component is expected to be near 285.0 eV—a result inferred from countless measurements on a variety of organic compounds.[14] Thus, we attribute the asymmetric broadening of the C(1s) peak toward higher binding energy as due to C-N bonds. To give a measure of the influence of the C(1s) chemical shift due to nitrogen bonding, we present the spectrum of 2,4,6,-triphenyl-1,3,5-triazine in Figure 8.5. The high-binding-energy peak at 286.7 eV is assigned to sp^2 carbons bonded to two sp^2 nitrogen neighbors and has a 2.1 eV chemical shift relative to the low-binding-energy peak (defined at 284.6 eV). The ratio of the areas for the two components is 0.19, which closely agrees with the expected ratio of 3:18 (0.17), as required for 3 carbons bonded to 2 nitrogen neighbors, with the remaining 18 carbons atoms bonded only to carbon.
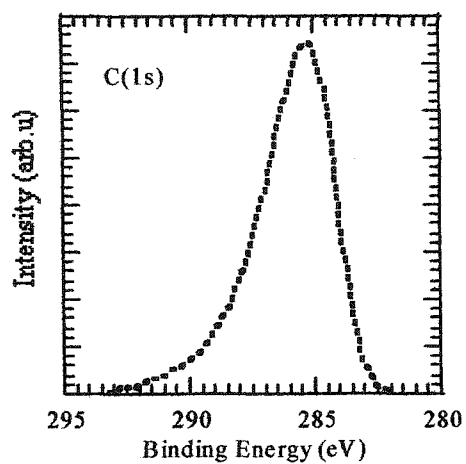
Figure 8.4: C(1s) XPS spectra of an a-CN$_x$ film deposited at 400 °C. An integral background has been subtracted.
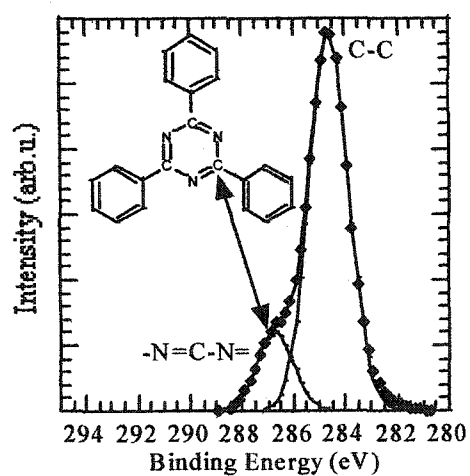
Fig. 8.5: The C(1s) spectrum of 2,4,6,-triphenyl-1,3,5-triazine. The high-binding-energy peak at 286.7 eV is due to sp^2 C bonded to two sp^2 N neighbors and has a 2.1 eV chemical shift relative to the low-binding-energy peak at 284.6 eV.

8.3 Discussion

Binding energy calculations by Johansson and Stafström [16] suggest that the two main N(1s) peaks at 398.5 and 400.6 eV in hard and elastic a-CN_x were due to 1) sp^3 nitrogen bonded to sp^3 hybridized carbon (specifically structure A2); and 2) sp^2 nitrogen substituted in the interior of a graphitic segment (similar to structure F), respectively. Johansson and Stafström's bonding model [16] suggests that the hardness of a-CN_x is due to an increase of sp^3 bonded nitrogen in an sp^3 carbon environment, as in the model amine structure $N(C(CH_3)_3)_3$; i.e., structure A2. However, recent experimental evidence [19] indicated that an sp^3 coordinated carbon environment will relax to sp^2 in the presence of approximately 14% bonded nitrogen. This evidence suggests that the interpretation by Johansson and Stafström [16] may be incorrect.

Computational work by Snis and Matar[17] on the model compound $C_{11}N_4$ offers another interpretation of the ~2 eV chemical shift between the two main components in the N(1s) spectrum. The two types of nitrogen sites in $C_{11}N_4$ are located on the perimeter of a single-atom vacancy, as would be found in a graphite layer missing one atom. These two nitrogen-bonding configurations are described as: 1) sp^2 N bonded to three sp^2 carbons (400.8-401.3 eV); and 2) sp^2 N bonded to two aromatic carbons—pyridine-like—(398.3-398.8 eV).[17] The chemical shift between these two components is consistent with the core-level shift between the two main components in the N(1s) spectra of hard and elastic a-CN_x (Figure 8.2). Both the model by Snis and Matar (Model 1) and the model by Johansson and Stafström (Model 2) can account for the experimentally observed chemical shift between N1 and N2. For further clarity, these models are compared in Figure 8.6.

Model 1

Vacancy Defect Structure

N(1): 400.8–401.3 eV
N(2): 398.3–398.8 eV

Model 2

2.5 eV
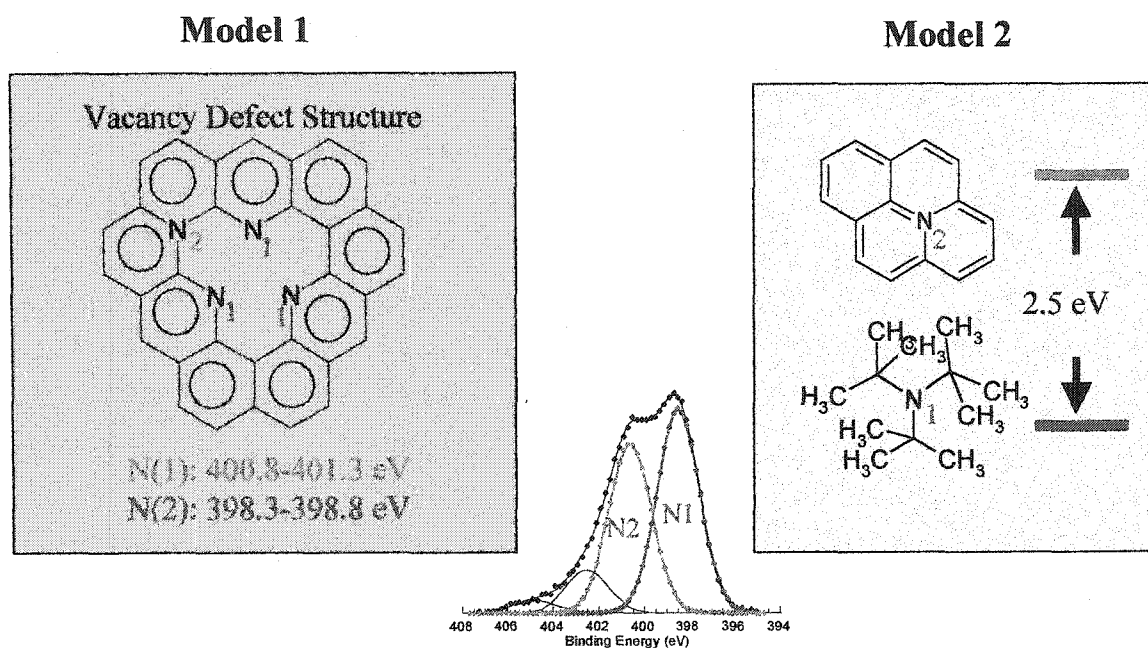
Figure 8.6: A schematic comparison of nitrogen bonding models for a-CN_x. Model 1 is the vacancy-defect-structure model, as suggested by the computational work of Snis and Matar.[17] Model 2 is supported by calculations by Johansson and Stafström.[16] Both models account for the ~2.0 eV chemical shift between the dominant components in the N(1s) spectrum.
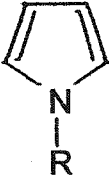
As discussed in the background section, previous experimental work has produced varying interpretations of the N(1s) XPS components. Even in this study, as shown in Figure 8.3, the N(1s) peak of a-CN_x exhibits bonding over the whole range of considered configurations. However, inspection of N(1s) binding energies for the reference compounds (A-F) suggests three primary nitrogen-binding-energy regions: 1) a low-binding-energy region due to sp^3 N bonded to sp^3 carbon (A1 or A2), pyridine-like (B) or

nitrile (C); 2) a midrange-binding-energy region which would include compounds like structure D; and 3) a high-binding-energy region due to sp^2 N bonded in an sp^2 salt-like configuration as in (E) or N bonded to three sp^2 carbons in a graphitic segment as in (F). As indicated in Figure 8.3, a particular bonding configuration may cover a binding energy range of ~1.0 eV; thus, the overlap of spectral intensities between regions is expected. For example, the binding energy range for the pyridine-like compounds (structures labeled B) is 0.8 eV. Thus, the boundaries of the three indicated regions are not absolutely defined. In this discussion, we ignore the high binding energy feature N4, since its overall contribution is very small (~3%).

A discussion of N1 is very limited if only the comparison in Figure 8.3 is considered, since the spectral intensity of N1 overlaps with the regions encompassed by the N(1s) binding energies of the structures A-C. However, previous Fourier transform infrared spectroscopy studies have shown that the fraction of nitrile bonding is small in hard and elastic a-CN_x films that were deposited under similar conditions;[12] therefore, we do not consider this arrangement any further. Disregarding nitrile bonding, Figure 8.3 suggests that the spectral intensity of N1 is due to N bonded in a pyridine-like configuration (B), N bonded to sp^3 carbon (A1 and A2), or a mixture of the two configurations.

Discussion of the binding energy component N2 is complicated by the fact that it does not coincide with one of the three bonding regions depicted in Figure 8.3. The binding energy of N2 at 400.6 eV falls in a range between pyridine-like compounds (B) and nitrogen that is threefold coordinated to sp^2 carbons (E and F). The N(1s) binding energy of triphenylamine (D) at 399.9 eV falls the closest to the binding energy of N2. However, it is not clear from the limited experimental data that N2 can be attributed to

Table 8.3: N(1s) binding energy range for pyrrole-like nitrogens.[15]

Pyrrole-like Nitrogen	Binding Energy Range (eV)
(pyrrole structure with N–R)	400.0-400.6 eV

this configuration. It is interesting to point out that the binding energy of triphenylamine is consistent with other values reported for amines.[15] In addition, XPS analyses of coals and chars by Pels et al.[15] offer another interpretation (see Table 8.3), which suggests that N2 may be due to nitrogen bonded in a pentagon, as in a pyrrole-like configuration. The existence of pentagons has been suggested by Sjöström et al.[1] to account for the buckled graphitic layers that are observed in a-CN$_x$. Another interpretation of N2 is offered by both the computational work by Snis et al.[17] and Johansson et al.,[16] which suggests N2 is due to sp^2 nitrogen bonded to three sp^2 carbon neighbors. At first glance, this assignment seems questionable, since structures E and F indicate that this bonding configuration should appear at higher binding energy. Moreover, measurements on 3,5,11,13-tetraazacycl[3.3.3]azine suggest a value closer to 401.3 eV (Figure 8.7).[20] However, computational work by Casanovas et al.[21] supports the assignment for N2 as due to nitrogen substituted in a graphene sheet. Casanovas' work indicates that the binding energies associated with sp^2 nitrogen bonded to three sp^2 carbons in graphene segments
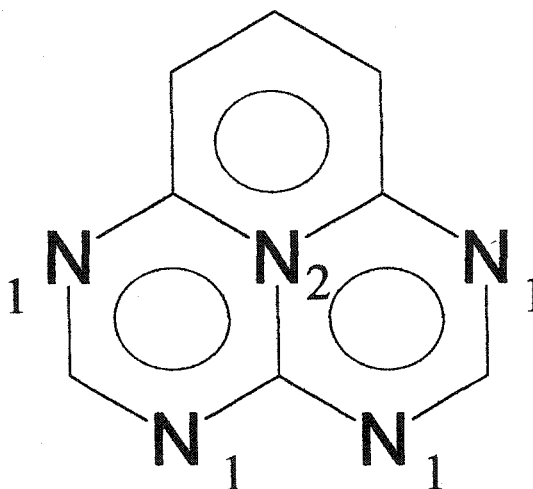
Figure 8.7: A schematic of the structure of 3,5,11,13-tetraazacycl[3.3.3]azine. The pyridine-like bonding configurations (N1) have an XPS binding energy of 398.3 eV, and the threefold coordinated sp^2 N configuration (N2) has a binding energy of 401.3 eV.[20]

can fall in a broad range of 400.5-402.7 eV. We speculate that this broad range reflects the extent that the nitrogen's π electrons are delocalized in the various structures studied by Casanovas *et al.* [21] In light of the available evidence, it is possible that N2 could be ascribed to amine, pyrrole-like, nitrogen substituted in a graphene segment, or a mixture of all these configurations. We emphasize that precise bonding assignment is impossible without further experimental data.
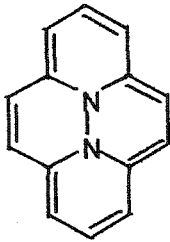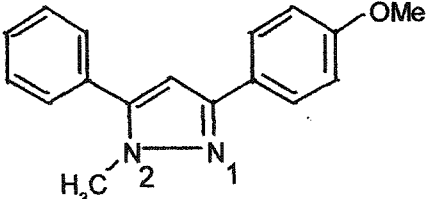
As with peak N2, the binding energy of N3 does not coincide with one of the three bonding regions in Figure 8.3. The binding energy of N3 at 402.5 eV is ~1 eV higher than structures E and F. The peak component N3 is most likely due to threefold coordinated sp^2 N bonded to aromatic carbon. There are several possible bonding situations that would fall in this category: 1) N bonded in the interior of a graphene segment (see Figure

8.7 and structure F in Figure 8.3); 2) N bonded at the edge of a graphene segment;[16, 21] and 3) N bonded in a configuration similar to structure E. Although the binding energy of E is 0.8 eV less than N3, we have included this possibility since a range of binding energies is anticipated for similar bonding situations. This bonding assignment for N3 is consistent with computational work by Casanovas et al.,[21] which suggests a broad range for nitrogen in graphene segments (400.5-402.7 eV).

It is worth mentioning that the XPS work by Marton et al.[3] on a-CN_x has attributed the intensity in the range of N3 as due to N-O bonds. Clearly this possibility is not resolvable from the other the features E and F; therefore, we cannot dismiss this possibility. Although we do not consider N-O bonding any further, it is interesting to note that structure E illustrates how charge transfer from distant oxygen can shift the N(1s) component to higher binding energy.

In addition, N3 has been attributed to N-N bonding [3] as well as trapped molecular nitrogen.[10] It is commonly assumed that N-N bonds always appear at the high-binding-energy portion of the spectrum (401-403eV). However, the assumption that nitrogens participating in N-N bonds are always at high binding energy is incorrect. This point is clarified in Table 8.4, where several examples of N-N bonding types are shown. The N(1s) spectrum of 1-methyl-3-p-methoxyphenyl-5-phenyl pyrazole (third entry in Table 8.4) exhibits two well-resolved peaks in its N(1s) spectra, which are separated by 1.8 eV.[22] The two nitrogens in 1-methyl-3-p-methoxyphenyl-5-phenyl pyrazole have different bonding configurations: N1 participates in two σ bonds, 1 π bond, and has a lone pair (pyridine-like); and N2 participates in three σ bonds and two of its valence electrons participate in the π system (pyrrole-like). In most work on carbon nitride, the

Table 8.4: N(1s) binding energies of several N-N bonding configurations.

Structure	Binding Energy (eV)	Source
N_2	403.0 eV	Souto *et al.*[6]
	401.0 eV	Souto *et al.*[6]
	N1: 399.4 eV	Katrib *et al.*[22]
	N2: 401.2 eV	Katrib *et al.*[22]

role of N-N bonding is dismissed or ignored. It is usually argued that the probability of N-N bond formation is very low, since it is kinetically favorable for molecular N_2 to desorb from the film's growth surface, rather than incorporating in the film as an N-N bond.[23] Although the formation of N-N bonds in a-CN$_x$ is not kinetically favored during the growth process, the possibility of N-N bonds as found in 1-methyl-3-p-methoxyphenyl-5-

phenyl pyrazole is interesting. While this work offers no evidence either for or against N-N bonds, a lower limit of N-N bonding in a-CN_x films has yet to be established.

In closing, we emphasize the following important result. We have shown that N(1s) XPS data do not give direct evidence for assigning N1 to nitrogen bonded to sp^3 carbons. The N1 bonding configuration can be equally as well explained by a pyridine-like configuration. This is also supported by Snis and Matar's computational work, [17] which suggests that N1 is due to pyridine-like nitrogen at the perimeter of vacancy defect, as found in $C_{11}N_4$. In fact, the nitrogen bonding situations in $C_{11}N_4$, at the two nonequivalent positions on the vacancy's perimeter (e.g., see vacancy structure Figure 8.6) exhibit a chemical shift in the range of 2.0-3.1 eV. This is consistent with the chemical shift of 2.1 eV between N1 and N2 in our spectra (Figure 8.2). In addition, a vacancy defect in a graphitic structure provides space for the pyridine-like nitrogen's lone pairs. The ability to determine the relative fraction of sp^2 to sp^3 bonded carbons would allow us to determine which assignment for N1 (see Figure 8.6) is most appropriate to describe a-CN_x. However, XPS is not sensitive enough to resolve the sp^2 from the sp^3 fraction of carbon bonded only to carbon. This is an important point; the assignment of N1 as due to nitrogen bonded to sp^3 carbons is only indirectly inferred from N(1s) chemical shift calculations.[1] Direct C(1s) measurement can not confirm this assignment, since the resolution of XPS is too small.

Other researchers have realized the importance of this issue and have used electron energy loss spectroscopy [7,9,24] and near-edge x-ray absorption fine structure spectroscopy [12,25] to determine the relative fractions of sp^2 to sp^3 carbon in a-CN_x. However, no reliable quantitative measurements of the sp^3 carbon component have been reported.

Clearly, the determination of the relative fractions of sp^2 and sp^3 carbon content in a-CN_x is crucial for understanding the bonding in this material. In the next chapter, we address this issue with ^{13}C NMR spectroscopy—a technique capable of resolving the sp^2 and sp^3 carbon contributions.

8.4 Conclusions

In this chapter, we have attempted to elucidate the nature of nitrogen bonding in hard and elastic a-CN_x films by comparing the N(1s) spectra of a-CN_x with the peak positions from a variety of organic compounds. We have also compared our XPS data with XPS work by Pels et al. [15] on nitrogen bonding in coals in chars and with N(1s) binding energy calculations by both Snis et al. [17] and Johansson et al. [16] Our XPS study shows that the N(1s) data do not conclusively support the presence of nitrogen bonded to sp^3 carbons. We show that the N(1s) spectra can be equally as well explained by a vacancy defect model. The presence of single-atom vacancies—similar to those in a graphite layer—is supported by N(1s) XPS chemical shift calculations on $C_{11}N_4$. Furthermore, the presence of pyrrole-like bonding configurations is supported by both the work of Pels et al. [15] and Sjöström et al. [1] This is an interesting possibility, since pyrrole-like nitrogens—specifically, nitrogen in pentagons—would account for the buckling of the graphitic layer. Buckled layers would intersect and cross-link. Sjöström et al. proposed that these cross-links are due to sp^3 carbons—a conjecture supported by the computational work of Johansson and Stafström.[16] However, XPS can not conclusively demonstrate the presence of sp^3 carbons. This issue will be addressed in Chapter 9, where ^{13}C NMR spectroscopy is used to conclusively determine the role of diamond-like (sp^3) carbon in a-CN_x.

8.5 References

1   H. Sjöström, S. Stafström, M. Boman, and J. E. Sundgren, Phys. Rev. Lett. **75**, 1336 (1995).

2   F. Rossi, B. Andre, A. van Veen, P. E. Mijnarends, H. Schut, F. Labohm, M. P. Delplancke, H. Dunlop, and E. Anger, Thin Solid Films **253**, 85 (1994).

3   D. Marton, K. J. Boyd, A. H. Al-Bayati, S. S. Todorov, and J. W. Rabalais, Phys. Rev. Lett. **73**, 118 (1994).

4   H. Sjöström, L. Hultman, J. E. Sundgren, S. V. Hainsworth, T. F. Page, and G. Theunissen, J. Vac. Sci. Technol. A **14**, 56 (1996).

5   W. T. Zheng, K. Z. Xing, N. Hellgren, M. Logdlund, A. Johansson, U. Gelivs, W. R. Salaneck, and J. E. Sundgren, J. Electron Spectrosc. Relat. Phenom. **87**, 45 (1997).

6   S. Souto, M. Pickholz, M. C. Dos Santos, and F. Alvarez, Phys. Rev. B **57**, 2536 (1998).

7   C. Spaeth, M. Kuhn, F. Richter, U. Falke, M. Hietschold, R. Kilper, and U. Kreissig, Diamond Relat. Mater. **7**, 1727 (1998).

8   C. Ronning, H. Feldermann, R. Merk, H. Hofsass, P. Reinke, and J. U. Thiele, Phys. Rev. B **58**, 2207 (1998).

9   N. Hellgren, M. P. Johansson, E. Broitman, L. Hultman, and J. E. Sundgren, Phys. Rev. B **59**, 5162 (1999).

10   P. Hammer, N. M. Victoria, and F. Alvarez, J. Vac. Sci. Technol. A **18**, 2277 (2000).

11   B. C. Holloway, O. Kraft, D. K. Shuh, M. A. Kelly, W. D. Nix, P. Pianetta, and S. Hagstrom, Appl. Phys. Lett. **74**, 3290 (1999).

12   B. C. Holloway, O. Kraft, D. K. Shuh, W. D. Nix, M. Kelly, P. Pianetta, and S. Hagstrom, J. Vac. Sci. Technol. A **18**, 2964 (2000).

13   R. Gago, I. Jimenez, D. Caceres, F. Agollo-Rueda, T. Sajavaara, J. M. Albella, C.-F. A., I. Vergara, J. Raisanen, and E. Rauhala, Chem. Mater. **13**, (2001).

14   D. Briggs, *Surface Analysis of Polymers by XPS and Static SIMS* (Cambridge, New York, 1998).

15   J. R. Pels, F. Kapteijin, J. A. Moulijn, Q. Zhu, and K. M. Thomas, Carbon **33**, 1641 (1995).

16   A. Johansson and S. Stafström, J. Chem. Phys. **111**, 3203 (1999).

17   A. Snis and S. F. Matar, Phys. Rev. B **60**, 10855 (1999).

18   A. Proctor and M. A. Sherwood, Anal. Chem. **54**, 13 (1982).

19   J. Hu, P. Yang, and C. M. Lieber, Phys. Rev. B **57**, R3185 (1998).

20   J. P. Boutique, J. J. Verbist, J. G. Fripiat, J. Delhalle, G. Pfister-Guillouzo, and G. J. Ashwell, J. Am. Chem. Soc. **106**, 4374 (1984).

21   J. Casanovas, J. M. Ricart, J. Rubio, F. Illas, and J. M. Jimenez-Mateos, J. Am. Chem. Soc. **118**, 8071 (1996).

22   A. Katrib, N. R. El-Rayyes, and F. M. Al-kharafi, J. Electron Spectrosc. Relat. Phenom. **31**, 317 (1983).

23   N. Hellgren, K. Macak, E. Broitman, M. P. Johansson, L. Hultman, and J. E. Sundgren, J. Appl. Phys. **88**, 524 (2000).

24   L. Wan and R. F. Egerton, Thin Solid Films **279**, 34 (1996).

25   W. T. Zheng, W. X. Yu, H. B. Li, Y. M. Wang, P. J. Cao, Z. S. Jin, E. Broitman, and J. E. Sundgren, Diamond Related Mater. **9**, 1790 (2000).

Chapter 9—Nuclear Magnetic Resonance Results

The chemical bonding of hard, elastic, amorphous, carbon-nitride (a-CN$_x$) films was examined with solid state ^{13}C, ^{15}N, and ^{1}H nuclear magnetic resonance (NMR) spectroscopy. The ^{13}C NMR results demonstrate that hard, elastic a-CN$_x$ has a structure consisting of sp^2-bonded carbons and that sp^3-hybridized carbons are absent. Results from ^{15}N NMR experiments show that nitrogen bonding in this material is predominantly sp^2 and is incorporated in heterocyclic rings. In addition, the data indicate that our a-CN$_x$ material has a very low hydrogen content and is hydrophilic. Specifically, analysis of ^{15}N and ^{13}C cross polarization magic angle spinning (CPMAS) and ^{1}H NMR experiments suggest that water preferentially protonates nitrogen sites.

Our work conclusively demonstrates that sp^3 bonded carbons are not responsible for the hardness of a-CN$_x$ films. The absence of sp^3 carbons demonstrates that the film-structure model proposed by Sjöström et al.[1] is incorrect. Using insights provided by NMR results, we propose a new film-structure model for hard and elastic a-CN$_x$, which is consistent with both XPS (see Chapter 8) and NMR results. Later in Chapter 10, the plausibility of our model is examined with Hartree-Fock, total-energy calculations.

9.1 Background

When deposited under suitable conditions, a-CN$_x$ films can be fabricated with low elastic modulus and high elastic recovery.[2-5] To account for these properties, Sjöström *et al.* proposed a structure consisting of cross-linked, buckled, graphitic layers.[1] They suggested that the buckling was due to pentagons incorporated in the graphitic layers and that buckling would allow adjacent layers intersect and cross-link. In accord with XPS data and N(1s) XPS binding-energy calculations, they suggested the cross-links were due to sp^3 carbons.[1,6] In the framework of their model, the sp^3 carbons were associated with the mechanical hardness of a-CN$_x$ films. Although their model is reasonable and consistent with the data, it was never verified. In Chapter 8, it was shown that N(1s) XPS data do not conclusively support a film-structure model with nitrogen bonded to sp^3 carbons. Instead, we showed that the two main peak components in the N(1s) XPS spectra are equally as well explained by the chemical shift between 1) sp^2 nitrogen coordinated to two sp^2 carbons (pyridine-like) and 2) sp^2 nitrogen coordinated to three sp^2 carbons.

To address the issue of cross-linking between buckled layers in a-CN$_x$, the role of sp^3 carbons needs to be determined. XPS is not capable of resolving sp^2 from sp^3 carbons in a-CN$_x$. XPS measurements by Sjöström *et al.* only indirectly inferred the presence of sp^3 carbons. They noted that the low-binding-energy component observed in the N(1s) spectra was consistent with the calculated chemical shift of sp^3 nitrogen bonded to sp^3 carbon.[1,6] From this observation, they assumed the presence of sp^3 carbons. In an attempt to resolve this issue, researchers have resorted to other techniques. Both electron energy loss spectroscopy (EELS)[3,7,8] and near-edge x-ray absorption fine structure spectroscopy

(NEXAFS)[5,9] have been used to try to determine the relative fraction of sp^2 to sp^3 carbons in a-CN_x. However, no reliable quantitative measurements of the sp^3-carbon fraction have been reported in the literature. Interestingly, recent molecular dynamic calculations and experimental evidence indicate that sp^3 carbons will relax to sp^2 in the presence of approximately 14% bonded nitrogen.[10] This work suggests that sp^3 carbons are unstable in hard and elastic a-CN_x films, since these films typically have a nitrogen concentration of $\sim$ 20 at.%.[3,5] This controversy needs to be resolved.

In the present study, solid-state NMR spectroscopy was used to elucidate the chemical bonding in a-CN_x. The advantage of NMR is its high sensitivity to the electronic environment, which is reflected in the isotropic chemical shift. In fact, NMR chemical shifts are more sensitive than XPS values and thus provide a better description of bonding. Moreover, the NMR chemical shift between sp^2 and sp^3 carbons that are bonded to other carbons or nitrogen is resolvable. Thus, NMR is capable of determining the sp^3-carbon fraction in a-CN_x.

Unfortunately, NMR has an inherent disadvantage in that a large amount of material ($\sim$100 mg) is needed to make measurements. This makes film fabrication very demanding, and presumably explains the limited attention NMR has received from the carbon nitride community. Only a few reports of NMR on a-CN_x films appear in the literature;[11-14] however, all earlier work has focused on hydrogenated materials or materials deposited at ambient temperature.[11-14] Separate results have shown that either of these deposition conditions produces an a-CN_x material with less robust mechanical properties.[15,16] Mechanical testing results were not reported for any of the materials

previously characterized by NMR.[11-14] Thus, it is doubtful if those materials were the highly elastic and mechanically hard materials of interest.

In this work, the chemical bonding of hard and elastic a-CN$_x$ films was examined with solid state ^{13}C, ^{15}N, and ^{1}H NMR spectroscopy. These films have been characterized by nanoindentation (Chapter 7) in addition to the NMR measurements. Nanoindentation measurements demonstrated that the mechanical properties are uniform across the entire diameter of the 75 mm film. This proves the integrity of our deposition method for producing the large quantity of material needed for the NMR experiments. The ^{13}C NMR results demonstrate sp^3 hybridized carbons are absent in our hard and elastic a-CN$_x$ material. From the ^{15}N NMR measurements, the dominant nitrogen-bonding configurations in a-CN$_x$ were determined. In addition, analysis of ^{15}N and ^{13}C CPMAS and ^{1}H NMR experiments indicate our a-CN$_x$ films have low hydrogen content.

9.2 Nuclear Magnetic Resonance Results

^{13}C NMR

Direct detection and cross polarization ^{13}C MAS spectra are shown in Figure 9.1. The background signal due to the Teflon end-caps (see Section 5.3) has been subtracted from the direct-detection spectra (symbol and solid-line). An estimate for the spin-lattice relaxation time, T_{1z}, was obtained by comparing direct-detection spectra obtained at 6 s and 10 s recycle delays: $T_{1z} \sim 2$ s. To compare relative intensities, the CPMAS spectra (dashed line) has been scaled so that the noise level was equalized to that in the direct-detection spectra. The lower relative intensity of the cross polarization spectrum demonstrates that few protons are bonded to carbons. An assertion further supported by
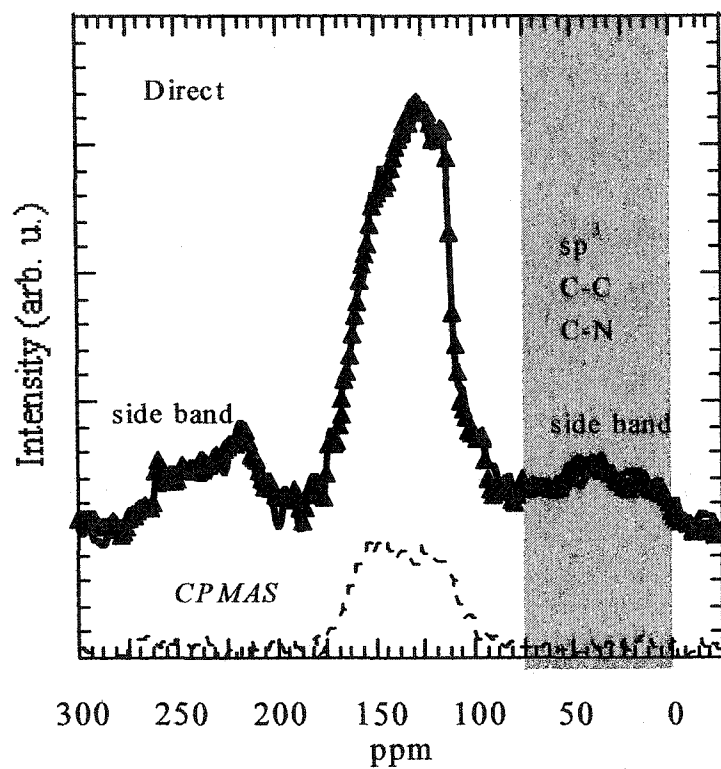
Figure 9.1: ^{13}C Hahn-echo MAS spectra of a-CN$_x$: τ_d = 10 s; τ_e = 125 μs; v_r = 8 kHz; and NS = 4608. Spectra are shown with proton decoupling (triangles) and without (solid line). Note that the background signal due to the Teflon end-caps has been subtracted out (see Chapter 5). The gray shading indicates the region were sp^3 carbon bonded to carbon or nitrogen resonates. The low intensity Hahn-echo CPMAS spectrum (dashed line) was acquired with a 5 ms contact time: τ_d = 1s ; τ_e = 111.11 μs; v_r = 9 kHz; and NS = 10,000. The CPMAS spectrum was scaled so that the noise level was equalized to that in the direct-detection spectra.
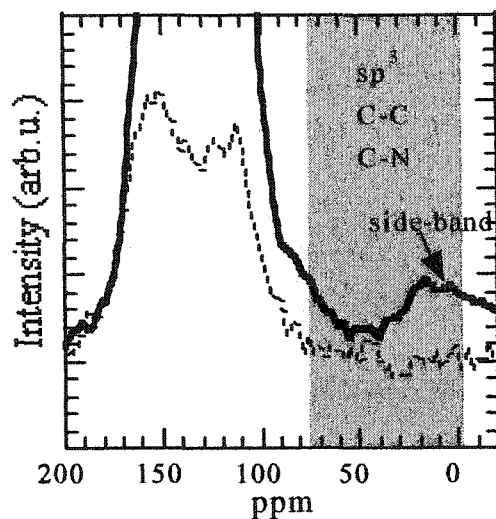
Figure. 9.2: Comparison of TOSS (dashed line, τ_d = 3s; v_r = 6 kHz; and NS = 15,000.) and Hahn echo MAS (solid line, v_r =10 kHz; τ_d = 10s; τ_e = 200 µs; and NS = 10,000.). This comparison shows that the small feature in the shaded sp^3 area of Figure 9.1 is a spinning side band. The spectra were scaled so that the noise level is approximately the same in each.

the fact that the resolution and shape of the direct-detection spectra are unaffected by proton decoupling.

The low intensity lobes that are positioned symmetrically around the central peak of the direct-detection spectra in Figure 9.1 are spinning side bands (106 ppm = 8 kHz). Since the side bands overlap with the spectral region where sp^3 carbon bonded to carbon or nitrogen resonates (0-75 ppm),[17] [13]C MAS experiments were also carried out at higher spinning speeds. A direct-detection spectra (solid line) obtained at v_r =10 kHz is shown in Figure 9.2. In addition, a TOSS sequence (dashed line in Figure 9.2) was also implemented to completely suppress the side bands.[18] No background correction was applied to the TOSS spectra, since the object was merely to examine the region occupied by the side band.
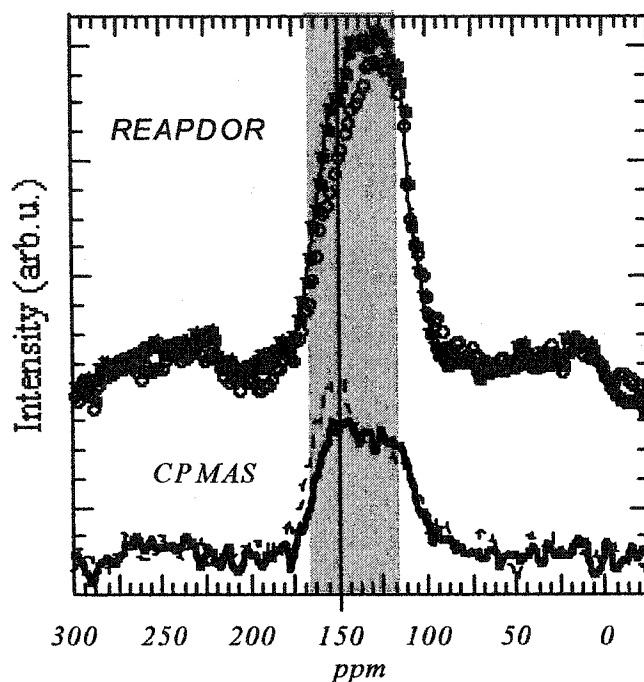
Figure 9.3: Upper traces: REAPDOR spectra were acquired with: τ_d = 3s; v_r = 8 kHz; and NS = 26,000. The full spectrum (filled squares) and attenuated spectrum (open circles) are shown. The gray shading indicates the region of the spectra with carbons directly bonded to nitrogen. Lower traces: Hahn-echo CPMAS spectra obtained using contact times of 1 ms (dashed line) and 5 ms (solid line) (τ_d = 1 s; τ_e = 111.1 μs; v_r = 9 kHz; NS = 10,000, and LB = 200 Hz).

The results of the dipolar dephasing REAPDOR experiment for a-CN_x are shown in Figure 9.3. The full spectrum (filled squares) is compared to the attenuated spectrum (open circles). The attenuated spectrum is obtained by applying an adiabatic-passage pulse to the ^{14}N channel, which results in dipolar dephasing.[19] The gray shaded region indicates the portion of the ^{13}C spectrum that is coupled to ^{14}N nuclei. The largest dephasing occurs at 150 ppm, as indicated by the solid vertical line. In addition, the REAPDOR spectra are also compared with ^{13}C CPMAS measurements (lower traces).

The CPMAS spectra were obtained using contact times of 1 ms (dashed line) and 5 ms (solid line). Note that at short contact times (1 ms), the CPMAS spectra exhibit a sharp peak at ~150 ppm, where the REAPDOR spectra exhibit the largest dephasing.

^{15}N NMR

The direct-detection ^{15}N MAS spectrum is shown in Figure 9.4; this was obtained with 11,160 scans using a 30 s recycle delay. By comparing spectra obtained at 20 s and 30 s recycle delays, the spin-lattice relaxation time was estimated, T_{1z}~15 s. The broad, low-intensity features positioned symmetrically around the central portion of the spectrum are identified as spinning side bands (296 ppm = 9 kHz).

Hahn echo ^{15}N MAS spectra obtained with direct-detection and cross polarization experiments are compared in Figure 9.5. The direct-detection spectra obtained with (solid line) and without (symbols) proton decoupling are indicated in the top traces; proton decoupling has the greatest affect on the spectral intensity of the broad shoulder in the range between -210 to -330 ppm. In fact, without proton decoupling, the spectral feature centered approximately at -295 ppm (top traces) is notably dephased. For comparison, a CP spectrum obtained using a 1 ms contact time (dashed line in lower portion of Figure 9.5) is also displayed. As expected, the highest cross polarization efficiency is observed near -295 ppm (gray line), where the direct-detection spectrum exhibits the highest dephasing without proton decoupling.
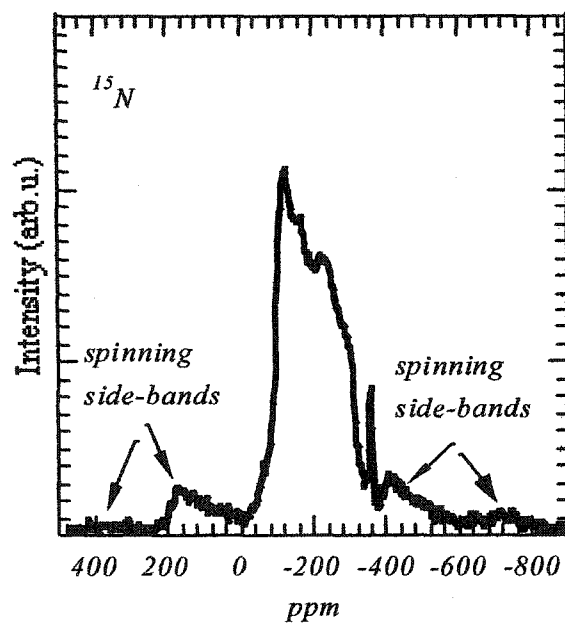
Figure 9.4: ^{15}N Hahn-echo MAS spectrum with proton decoupling (τ_d = 30 s; τ_e = 111.1 μs; v_r = 9 kHz; *NS* = 11,160 transients, and no apodization). The shape of the spectrum suggests at least five bonding configurations at the following estimated positions: -120, -160, -255, -295, and -358 ppm.
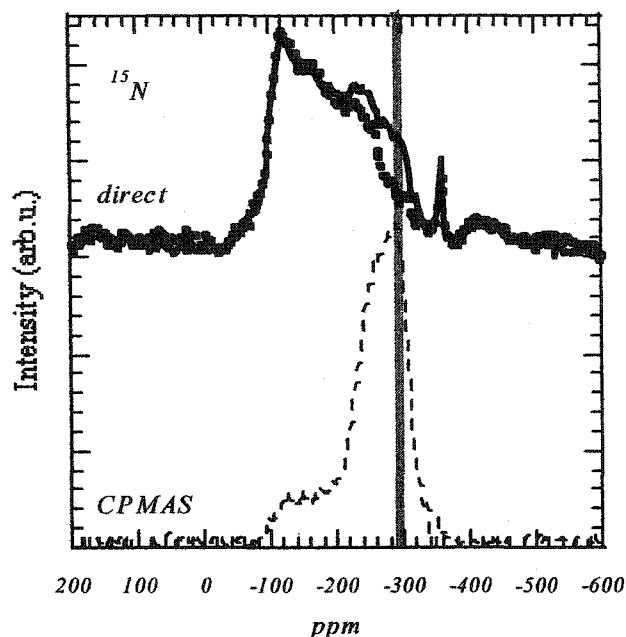
Figure 9.5: ^{15}N Hahn-echo MAS spectra obtained by direct-detection and cross polarization experiments. The direct-detection spectra ($\tau_d = 30$ s; $\tau_e = 111.1$ μs; $v_r = 9$ kHz; $NS = 2480$, and $LB = 50$ Hz) obtained with and without proton decoupling are indicated by the solid line and symbols, respectively. The CPMAS spectrum with 1 ms contact time ($\tau_d = 1$ s; $\tau_e = 111.1$ μs; $v_r = 9$ kHz; $NS = 2480$, $LB = 50$ Hz) is displayed at the bottom and indicated by the dashed line. The spectral feature near -295 ppm (gray line) is markedly dephased in absence of proton decoupling, and this feature coincides with the highest cross polarization efficiency.

CPMAS ^{15}N spectra obtained at 0.1, 1.0, and 5 ms contact times are shown in Figure 9.6a. Evolution of the ^{15}N CPMAS spectra with contact time suggests at least two ^{15}N-^{1}H dipolar-coupling strengths for polarization transfer. Cross polarization is very effective at short contact times (0.1 ms) for the high intensity feature centered near -275 ppm, indicating dipolar coupling to directly bonded protons. However, cross polarization is not efficient for the low-intensity, broad shoulder centered near -160 ppm. The intensity of this shoulder increases up to 1 ms contact time, and remains constant out to at least 5 ms. The low relative intensity and slow build-up of the polarization suggests that these nitrogens have no directly bound protons.
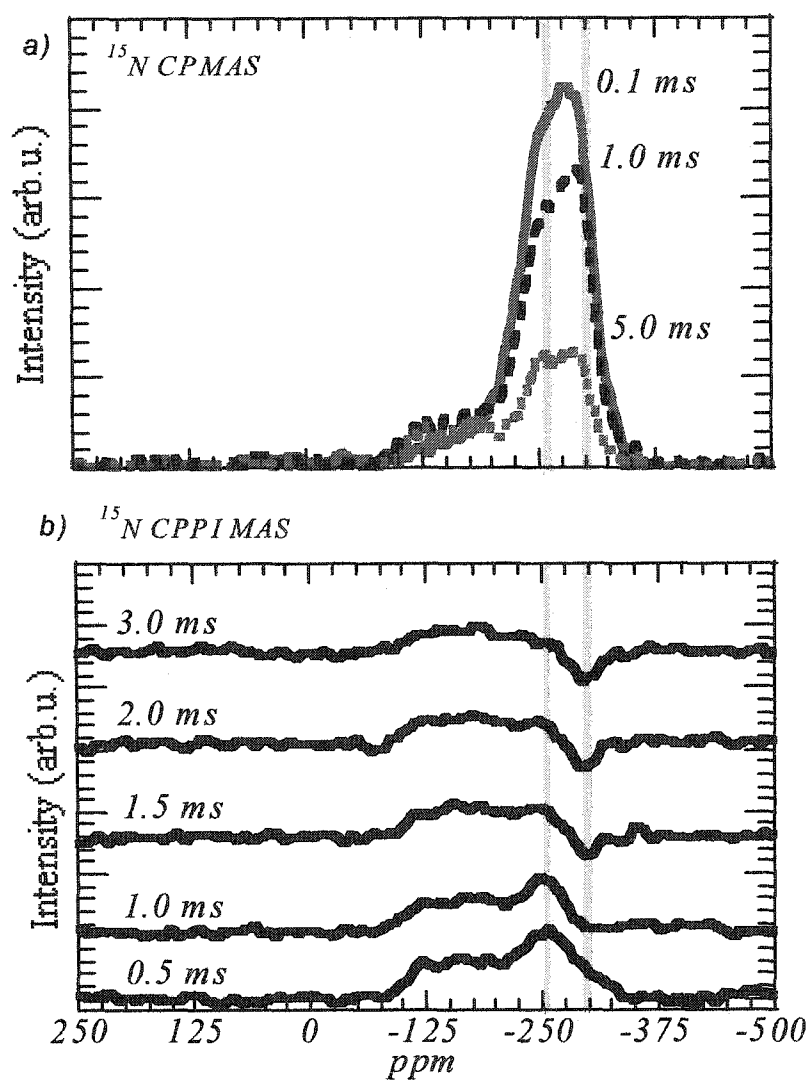
Figure 9.6: a) ^{15}N CPMAS spectra (τ_d = 1 s; τ_e = 111.1 µs; v_r = 9 kHz; NS = 2480, and LB = 50 Hz) obtained at 0.1, 1.0, and 5 ms contact times. The efficient cross polarization of the feature centered at -275 ppm at short contact times indicates that this nitrogen-bonding site is protonated.

 b) ^{15}N CPPI MAS spectra (τ_d = 1 s; τ_e = 111.1 µs; v_r = 9 kHz; NS = 600, and LB = 200 Hz) for various PI times ranging from 0.5 ms to 3.0 ms following an initial 1 ms contact time. Peak positions estimated from the CPPI measurement are indicated by the gray lines at -295 and -255 ppm.

The shape of the peak centered near -275 ppm (Figure 9.6a) suggests at least two nitrogen-bonding configurations. In order to distinguish these, CPPI measurements [20] were performed using a 1 ms initial contact time, as shown in Figure 9.6b. As indicated by the gray vertical lines in the CPPI spectra, the high-intensity feature in the CPMAS spectra suggests two distinct nitrogen-bonding types, which are centered at approximately -255 and -295 ppm. The inversion time for the peak at -295 ppm occurs between 0.5 ms and 1.0 ms PI times, while the other portions of the spectrum retain a positive intensity for PI times greater than 3.0 ms.

^{1}H NMR

The temperature dependence of the ^{1}H MAS NMR spectra of a-CN$_x$ was also investigated, as shown in Figure 9.7. The data were first collected on the as-prepared sample (solid line). Then, the sample was heated inside the probe for 20 min. at 150 $^\circ$C, and this temperature was maintained during data acquisition (~22 minutes). The heat treatment caused a dramatic reduction of the ^{1}H MAS spectral intensity (dashed line) and revealed a previously unresolved feature near 0 ppm.

9.3 Discussion

In Figure 9.1, the lower relative intensity of the ^{13}C CPMAS spectrum (dashed line) as compared to direct-detection^{13}C MAS spectra (symbol and solid line) indicates that the a-CN$_x$ material has low hydrogen content. If the material were predominantly hydrogenated then the CPMAS signal would be larger than the direct detection signal. In a proton-rich environment, the enhancement of the CPMAS signal would be ~4 times
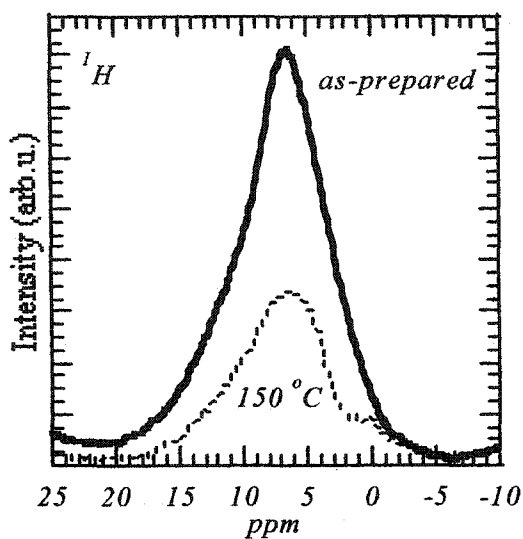
Figure 9.7: Comparison of ^{1}H MAS NMR spectra (τ_d = 1 s; τ_e = 250 μs; v_r = 8 kHz; NS = 1320, and LB = 100 Hz) of the as-prepared material and after heating at 150 ^{o}C, solid and dashed lines, respectively. After heating, the spectral intensity centered at 6.5 ppm is greatly reduced which suggests desorbtion of water.

larger than the direct detection signal. This enhancement is governed by [21] the ratio: γ_{13C}/γ_{1H}. Since no signal enhancement of the CPMAS over the direct-detection signal was observed, this assertion is justified. This assertion is further supported by the fact that the resolution and shape of the direct-detection spectra are unaltered by proton decoupling (symbol and solid line). The amount of carbons with significant ^{13}C-^{1}H coupling is small; thus, proton decoupling had no affect.

The spinning side bands in the ^{13}C MAS spectra (Figure 9.1) obscure the region where sp^3 carbon bonded to carbon or nitrogen resonates (gray shaded region). To push the side bands further away from the central band, experiments were carried out at higher

spinning speeds. Comparison of the direct-detection spectra obtained at 8 and 10 kHz spinning speeds (Figures 9.1 and 9.2, respectively) shows that the low-intensity feature between 0-75 ppm moves with respect to the central band, as expected for a spinning side band. Spinning speeds above 10 kHz were unavailable, so a TOSS sequence was implemented to completely suppress the side bands. The TOSS spectrum (dashed line in Figure 9.2) confirms the absence of sp^3 carbons in hard and elastic a-CN_x.

The REAPDOR results (Figure 9.3) allow portions of the ^{13}C spectrum due to nitrogen bonding to be distinguished. This is facilitated by comparing the full spectrum (filled squares) and the attenuated spectrum (open circles). The full spectrum is obtained in the absence of the adiabatic-passage pulse. When the adiabatic-passage pulse is applied to the ^{14}N channel, dipolar dephasing occurs and the signal is attenuated (open circles). Further details are given in Chapter 5. Since the strength of the dipolar interaction is inversely proportional to the cube of the inter-nuclear bond distance, the carbons bonded closest to the nitrogen experience the strongest dipolar coupling. Thus, the highest dephasing efficiency (signal attenuation) is observed for those carbons directly bonded to nitrogen. The gray shaded region in Figure 9.3 corresponds to the portion of the ^{13}C spectrum that is coupled to ^{14}N. The maximum observed dephasing at ~150 ppm (vertical line) corresponds to carbon directly bonded to nitrogen. However, concise assignment of the broad shoulder in the range of 125-175 ppm is not possible. The ^{13}C chemical shifts in the range of this shoulder are consistent with both sp^2 carbons with nitrogen nearest neighbors as well as those with only sp^2 carbon nearest neighbors. This is situation is clarified with aid of Figure 9.8, which shows the distribution of ^{13}C chemical shifts in several aromatic heterocycles, as measured in solution.[17]
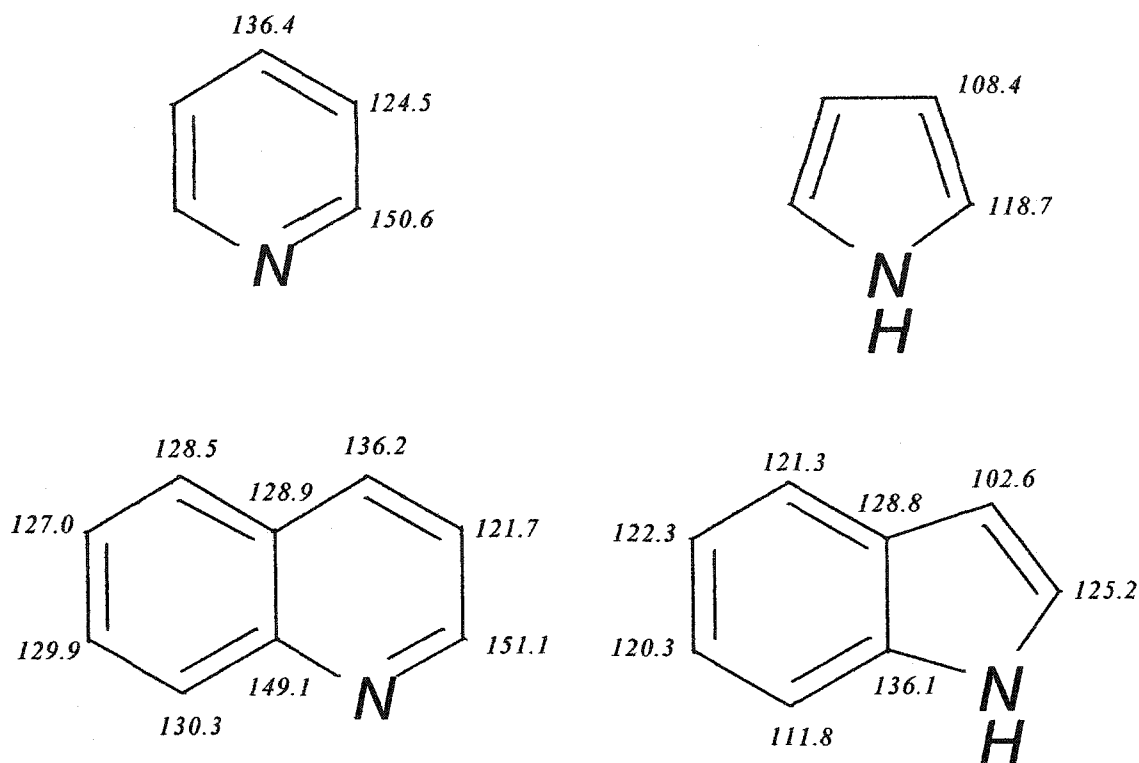
Figure 9.8: ^{13}C isotropic chemical shifts in several heterocyclic rings, as measured in solution.[17]

The CPMAS ^{13}C spectra (Figure 9.3) show that the intensity of the peak observed at 150 ppm (gray line) decreases as the contact time is lengthened from 1 to 5 ms. Since magnetization transfer is mediated by dipolar interactions, cross polarization is more efficient (intensity is higher) for carbons closer to protons. Thus, protonated species are mainly associated with the feature at 150 ppm. Recall that REAPDOR experiments showed the strongest dephasing at 150 ppm. Together, these observations suggest those carbons that are directly bonded to nitrogen are also more likely to be protonated.

The direct-detection ^{15}N MAS spectrum with proton decoupling (Figure 9.4) suggests at least five different bonding environments, positioned approximately at -120,

-160, -255, -295, and -358 ppm, respectively. Estimates of the peak-center values near -120 and -160 ppm were obtained from the zero-crossings of the first derivative spectrum. The values of -255 and -295 ppm were inferred from the CPPI measurements (shown in Figure 9.6b), and the value of -358 ppm for the sharp feature was obtained from its point of maximum intensity.

We have also compared our experimental ^{15}N MAS spectra (Figures 9.4 and 9.5) with two compilations of ^{15}N chemical shifts.[23,24] The isotropic chemical shifts listed in Ref. [23] are based on liquid and solution NMR measurements, while those in Ref. [24] are from solid-state measurements. In addition, Ref. [23] includes some ^{14}N chemical shift data, and these results were included in the comparison.

The reference, chemical-shift data [23,24] are schematically summarized in Figure 9.9. For clarity, pyridine-like and pyrrole-like bonding types are depicted in Figure 9.10. The chemical shifts for pyridine and pyrrole-like nitrogens were taken exclusively from measurements on solutions,[23] and specific examples are shown in Figure 9.9. For compounds with both nitrogen types (as an example see Figure 9.10), only those with R ≠ H were considered in this comparison. Since, if R = H, the chemical shift between the two sites is averaged due to effects of proton tautomerism. An example of this effect is shown in Figure 9.11. N-methyl-pyrazole has two nitrogen-bonding configurations. The pyridine-like nitrogen resonates at -78 ppm, while the pyrrole-like one resonates at -181 ppm.[23] This situation can be compared to pyrazole (Figure 9.11), which exhibits a single resonance at -134.5 ppm, [23] which is close to the average value of the two resonances in N-methyl-pyrazole.
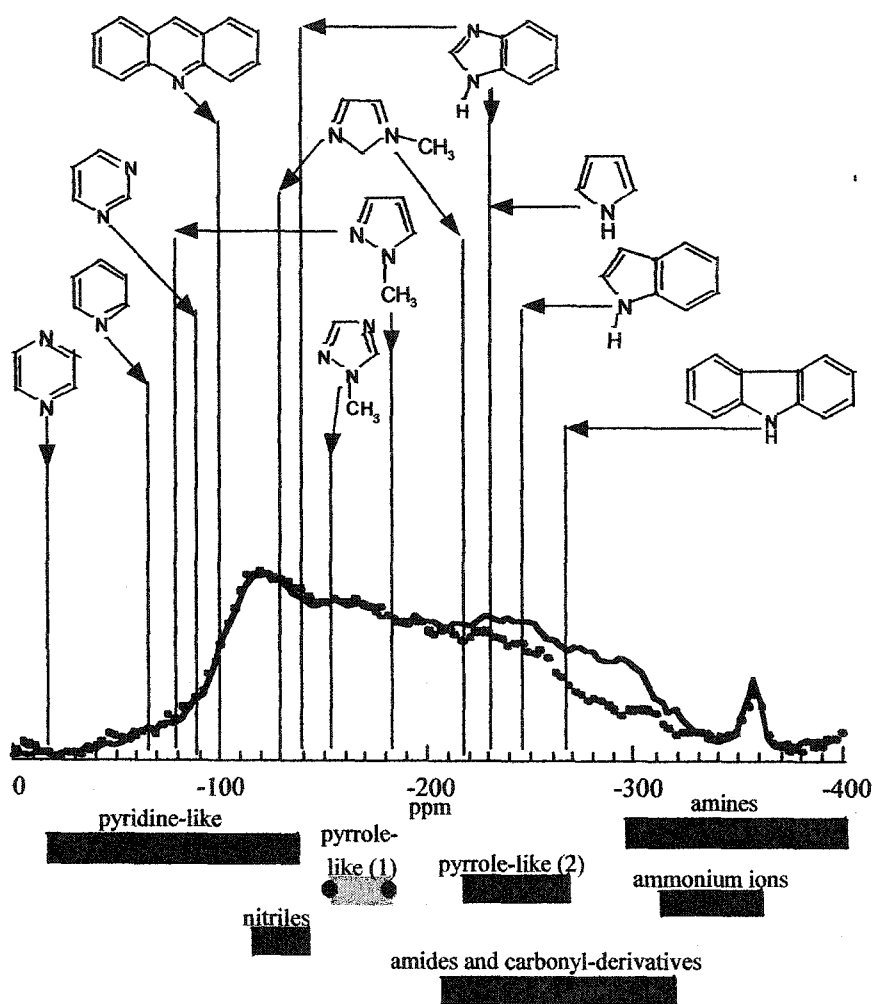
Figure 9.9: A schematic display of ^{15}N isotropic NMR chemical-shift ranges for various bonding configurations.[23],[24] For ease of comparison, the ^{15}N direct-detection spectra from Figure 9.5 are shown.
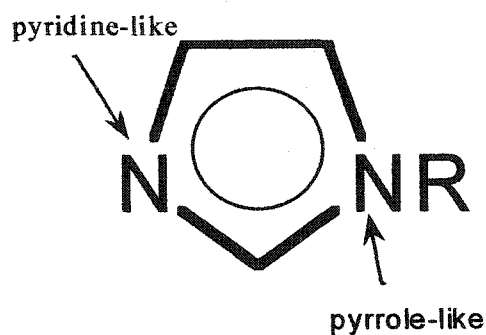
Figure 9.10: Configurations of pyridine-like and pyrrole-like nitrogen.[23]

N-methyl-pyrazole
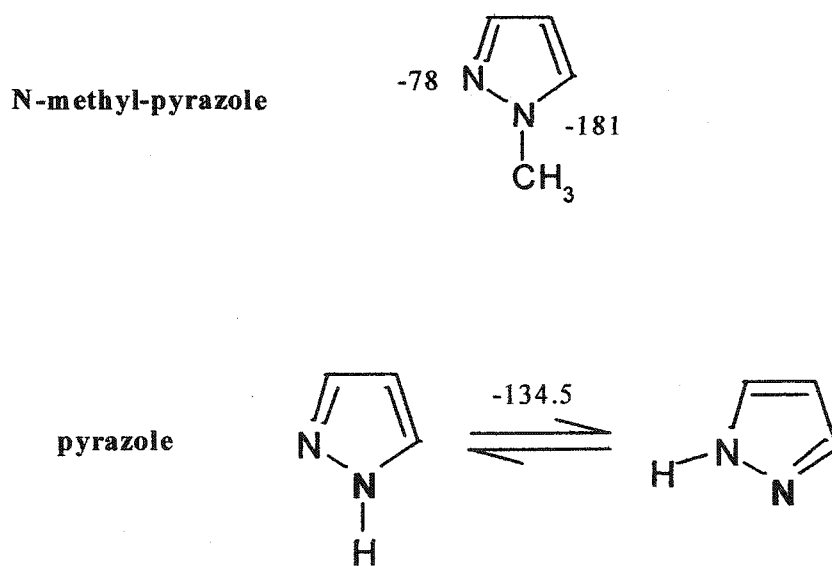
pyrazole

Figure 9.11: The ^{15}N chemical shifts of two pyrazoles are compared. The methylated compound exhibits two ^{15}N resonances, which correspond to the pyridine-like nitrogen (-78 ppm) and the pyrrole-like nitrogen (-181). However, only a single resonance (-134.5 ppm) is observed in the protonated compound. This single value is obtained from an averaging over both sites due to proton tautomerism. These chemical shift values were taken from Ref [23] and are based on solution NMR measurements.

The comparison in Figure 9.9 suggests that the spectral feature at -120 ppm may be due to nitrogen bonded in a pyridine-like or nitrile bonding configuration. The ^{13}C chemical shifts of carbons in a nitrile group (–C≡N) fall in the range of 111-122 ppm [24] and overlap with the resonances of other aromatic carbons. Thus, a clear signature of nitrile bonding can not be conclusively deduced from our ^{13}C or ^{15}N spectra. However, previous Fourier transform infrared spectroscopy work by this group indicates at most a small fraction of nitrile bonds in our material.[5] Therefore, we assume a pyridine-like nitrogen site and do not consider nitrile bonding further.

Furthermore, the spectral features at -160 and -255 ppm are in the range of nitrogens bonded in pyrrole-like configurations. The indicated pyrrole-like range [23] is subdivided into two categories: pyrrole-like nitrogen with (1) or without (2) a directly bonded nitrogen neighbor. The available chemical-shift data for type-(1) nitrogens are very limited,[23] and thus should be considered with caution. In addition, only those type-(1) pyrrole-like nitrogens that are methylated were considered, as opposed to protonated (see above discussion about proton tautomerism). This small data set (two compounds) suggests that type-(1) nitrogens are more deshielded,[23] as schematically indicated by the range of the gray-shaded bar shown in Figure 9.9. If the gray region can completely account for this bonding contribution, then a region of equal intensity for the nitrogen neighbor that is directly bonded to the pyrrole-like N should also appear in the spectrum. These nitrogens can also be described as pyridine-like and have chemical shifts in that range (Figure 9.9).[23] However, we emphasize that the presence of N-N bonding configurations is usually argued to be unlikely, since it more probable for molecular N_2 to desorb from the film's growth surface, rather than incorporating in the film as a N-N

bond. Regardless, no lower experimental limit on N-N bonding has been reported in the literature. To settle the question of N-N bonding, experiments that exploit homonuclear dipole-dipole coupling are required, which is an issue to be taken up by future study.

The comparison in Figure 9.9 suggests that the feature near -295 ppm is perhaps due to nitrogen in amides or carbonyl derivatives. However, this assignment implausible. If this feature in the ^{15}N spectra is associated with a carbonyl group then a corresponding feature due to C=O should appear in the ^{13}C direct-detection spectrum near 168-177 ppm [24] (Figure 9.1). This feature is not evident in the ^{13}C spectrum; clearly more work is required to make a conclusive assignment of this spectral feature. Finally, the sharp feature at -358 ppm falls in the range of amines,[23] ammonium ions,[23] or possibly, isocyanate structures.[24] Since this feature (-358 ppm) makes up a small percentage of the overall integrated intensity, it is not discussed any further.

In direct-detection ^{15}N spectra without proton decoupling (Figure 9.5), the spectral feature near -295 ppm is considerably dephased, and this feature coincides with the highest intensity of the ^{15}N CPMAS spectrum. This shows that this nitrogen site is protonated. This conclusion is further supported by the observation that the CPMAS spectra exhibit the highest efficiency at short contact times (see Figure 9.6a). It is important to note that the other portions of the direct-detection spectra (Figure 9.5) are either unaffected or at most slightly influenced by proton decoupling. Indeed, the overall resolution of the spectra is not greatly affected by proton decoupling. These observations suggest that water adsorption during NMR sample preparation is the most likely source of proton contamination. If the majority of protons had been introduced during film deposition, one would expect the entire ^{15}N spectrum to be influenced by proton

decoupling and dephasing of the entire spectrum to occur. However, we estimate an 8% relative intensity loss due to proton dipolar dephasing, and this shows that only a small fraction of nitrogens are protonated. In addition, this small change indicates that not all of the intensity near -295 ppm arises from protonated nitrogen. Assuming the spectral intensity of protonated nitrogen is completely dephased and lost, an estimate of the atomic percentage of hydrogen in the material can be made. Using the value of 20% for the atomic nitrogen concentration in the material, as inferred from our XPS measurements, the content of directly bonded hydrogen is estimated to be ~2%.

If hydrogenation of the material is due to adsorbed water, the portions of the ^{15}N direct-detection spectrum (Figure 9.5) that are affected by proton decoupling (region between -210 and -330 ppm) may arise from a chemical shift due to protonation by water of sites that are the less-shielded (regions between -30 and -210 ppm). For example, one possible explanation is due to the protonation of pyridine-like nitrogen, which would strongly shield the site and yield a chemical shift of approximately 100 ppm.[23] The ^{15}N CPMAS spectra (Figure 9.6a) exhibit two major features separated by approximately 100 ppm: a peak centered near -275 ppm, and a broad shoulder centered near -160 ppm. This may indicate that the peak near -275 ppm arises from protonation of the species associated with the region near -160 ppm. The observed cross polarization behavior of these peaks (Figure 9.6a) is consistent with this idea. The slow build-up of the CPMAS intensity, as a function of contact time, in the region near -160 ppm indicates remote, weakly coordinated protons. While, high cross polarization efficiency of the intense peak in the region near -275 ppm originates from protonated species.

Proton MAS NMR spectra, before and after annealing at 150 °C, are shown in Figure 9.7. During the heating process, the integrated intensity of the proton line centered at 6.5 ppm dropped by 57%. This suggests that the spectral feature centered at 6.5 ppm is predominantly due to physi-absorbed water. After heating to 150 °C, the proton spectrum shows an additional small feature near 0 ppm. The origin of this small peak may be due to protons bonded to something less electronegative than oxygen, and this is perhaps indicative of protons directly bonded to nitrogen sites in a-CN$_x$. This is plausible, since the ^{13}C spectra (Figure 9.1) indicate that the carbons are not significantly hydrogenated. Alternatively, this small feature may be due, in part, to hydroxyl species.

In summary, our ^{13}C NMR data demonstrate that a-CN$_x$ has an sp^2 carbon structure and that sp^3 carbons are absent. Our comparison with reference, chemical-shift data indicates that nitrogen bonding in a-CN$_x$ is predominately sp^2 and exists in pyridine-like or pyrrole-like configurations. The most consistent bonding structure of our a-CN$_x$ material is one with an aromatic carbon structure with nitrogen bonded in heterocyclic rings. Next, we consider several bonding models that were proposed for a-CN$_x$ and evaluate their plausibility based on our experimental data.

Previous computational work by Johansson and Stafström [6] suggested a bonding model for a-CN$_x$ that incorporates sp^3 carbons to explain the hardness of the material. However, our direct-detection ^{13}C NMR spectra (Figure 9.2) indicate the absence of sp^3 carbons in the signal range of 0-75 ppm. Our observation is thus inconsistent with their model. Also, note that an sp^3 C signal is not observed in the ^{13}C CPMAS spectra shown in (Figures 9.1 and 9.3); this observation rules out protonated sp^3 carbons. Furthermore, Johansson and Stafström's bonding model proposed that those nitrogen bonded to sp^3

carbons were in a tertiary amine configuration, as in their model structure $N(C(CH_3)_3)_3$.

Johansson and Stafström suggested that this configuration could be assigned to the low

binding component in the N(1s) XPS spectrum, which makes up 48% of the spectral

intensity (see Chapter 8). However, our ^{15}N results show that the amount of amine present

is very small (see comparison depicted in Figure 9.9). Our work demonstrates that

Johansson and Stafström's bonding model [6] is not applicable to hard and elastic $a\text{-}CN_x$.

Yoon *et al.* have calculated the chemical shifts of a variety of carbon nitride

phases.[22] Only, the calculated ^{13}C chemical shift (144 ppm) and the ^{15}N chemical shifts

(-166 and -241 ppm) of graphitic C_3N_4 are coincident with the range covered by our

experimental spectra (Figures 9.1 and 9.4). A schematic of a segment from a single layer

of graphitic C_3N_4 is shown in Figure 9.12. The two nitrogen sites are on the perimeter of

a single-atom vacancy in the graphitic layer: a nitrogen bonded to two aromatic carbon

neighbors (-166 ppm), together with nitrogen bonded to three aromatic-carbon neighbors

(-241 ppm). The twofold-coordinated nitrogens (-166 ppm) in this structure exhibit

bonding similar to pyridine. Comparing these calculated ^{15}N chemical shifts with our

experimental ^{15}N spectra (Figure 9.4) suggests that single-atom vacancies as found in

graphitic C_3N_4 may also occur in $a\text{-}CN_x$ films. The suggestion of a material consisting of

sp^2 bonded nitrogens in sp^2 carbon rings is reasonable, since the ^{13}C NMR results rule out

the presence of sp^3 bonded carbons. Moreover, vacancies in graphitic layers can

accommodate pyridine-like nitrogen; the presence of which is inferred from both our [15]N

NMR data and XPS study (Chapter 8).
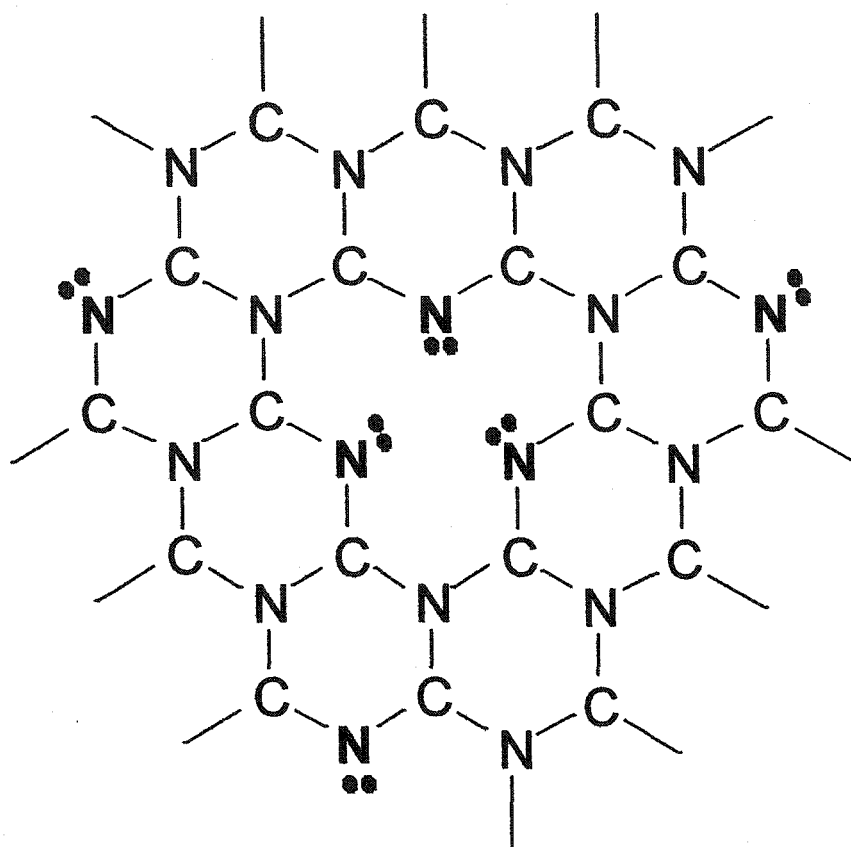
Figure 9.12: Schematic of a segment from a single layer of graphitic C_3N_4. The pyridine-like nitrogen sites have a calculated ^{15}N chemical shift of -166 ppm.[22] The sp^2 nitrogen sites coordinated to three sp^2 carbons have a calculated ^{15}N chemical shift of -241 ppm.[22]

Although, we note that the calculated value of -166 ppm for the pyridine-like nitrogen site in graphitic C_3N_4 appears to be too low (see experimental range for pyridine-like nitrogen in Figure 9.9). Indeed, their calculated ^{15}N chemical shift for pyridine is 43 ppm lower than its experimental value.[22] This suggests that the calculated value of -166 ppm for graphitic C_3N_4 is similarly shifted. Applying the same shift, the value of -166 ppm becomes -123 ppm; note that the value of -123 ppm is very close to the value for the feature at -120 ppm in a-CN_x (Figure 9.4). Additionally, experimental ^{15}N chemical shifts are unavailable for nitrogen coordinated to three carbons in graphene segments. However,

one might anticipate that these isotropic chemical shifts are similar those observed for pyrrole-like nitrogen. Indeed, the calculated ^{15}N chemical shift of -241 ppm for the component in graphitic C_3N_4 due to sp^2 nitrogen bonded to three sp^2 carbons [23] falls in the range of pyrrole-like nitrogens (Figure 9.10).

The suggestion that nitrogen configurations in a-CN$_x$ are similar to the nitrogen bonding at the perimeter of a single-atom vacancy is also supported by Snis and Matar's computational work.[25] Their calculations on the model compound $C_{11}N_4$ give an XPS N(1s) chemical shift of ~2 eV between the sp^2 nitrogen site bonded to two sp^2 carbons and the sp^2 nitrogen site bonded to three sp^2 carbons; both sites are on the perimeter of a single-atom vacancy. Their result is consistent with the experimental XPS chemical shift between the two main N(1s) components in the XPS spectra of hard and elastic a-CN$_x$ (see Chapter 8). Thus, both NMR and XPS data are consistent with the proposal that these vacancies occur in a-CN$_x$ films.

Previous transmission electron microscopy work indicates that hard and elastic a-CN$_x$ consists of buckled graphitic planes that are cross-linked together.[1] Furthermore, our experimental data suggest that nitrogen bonded in a pyrrole-like configuration is present in the material (Figure 9.9). Incorporation of five-membered rings in the material, similar to pyrrole, would allow the graphitic planes to buckle. Thus, we propose a model that incorporates vacancy defects and pentagons; a schematic of one such model is shown in Figure 9.13. This film-structure model allows for the incorporation of pyridine-like nitrogen and for buckling of the graphitic planes. We propose that cross-linking occurs at dangling bond (twofold coordinated) sites on the perimeter of the vacancy. In particular, a twofold-coordinated site on the pentagon is anticipated to be very reactive due to high curvature.
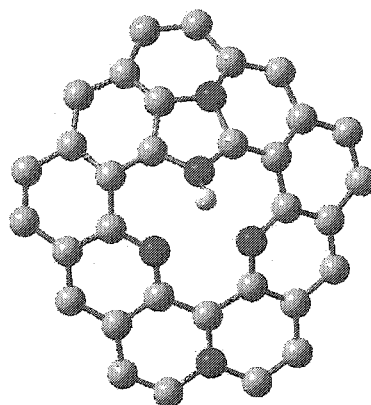
Figure 9.13: Our proposed film-structure model for a-CN$_X$. The gray shaded spheres are carbon atoms, and the blue spheres are nitrogen atoms. The white sphere is a hydrogen atom, which is bonded to the nitrogen in the pentagon on the perimeter of the vacancy defect.

9.4 Conclusions

The ^{13}C NMR study demonstrates that hard, elastic a-CN$_x$ has an sp^2-carbon structure, and that sp^3-hybridized carbons are absent. Using double resonance techniques (REAPDOR), we were able to distinguish the region in the ^{13}C spectra due to carbons bonded to nitrogen from the region due to only sp^2 carbons bonded to other carbons. Comparison of the ^{15}N NMR chemical shifts of a-CN$_x$ was made with tabulated compilations of experimental ^{15}N chemical shifts from various organic molecules.[23, 24] This comparison (Figure 9.9) suggests that the spectral feature near -120 ppm is due to pyridine-like nitrogen and that the features at -160 and -255 ppm are due to pyrrole-like configurations. Thus, we infer that the nitrogen bonding in this material is predominantly sp^2 and incorporates in heterocyclic rings.

It was shown that proton decoupling has a negligible affect on the direct-detection ^{13}C spectra. Thus, it can be inferred that the majority of carbons in a-CN_x are not directly bonded to protons. This is further supported by the low efficiency of ^{13}C CPMAS experiments. However in the ^{15}N direct-detection spectra, proton decoupling has a notable influence on the spectral feature at -295 ppm (Figure 9.5). In particular, the dephasing and high cross polarization efficiency at short contact times indicate that nitrogens corresponding to portions of the spectrum near -295 ppm have protons in close proximity. The most likely proton source in a-CN_x is due to adsorbed water. This conjecture is supported by ^{1}H NMR experiments, which indicate water desorbtion during sample heating. These results indicate that certain nitrogen bonding sites are hydrophilic and are protonated by physi-adsorbed water. In particular, we suggest that portions of the ^{15}N direct-detection spectrum that are affected by proton decoupling may arise from a chemical shift due to protonation by water of the less-shielded portions of the spectrum.

These multinuclear NMR results confirm our conclusions that the structure of a-CN_x lacks sp^3 carbons, and that the interconnecting structure is not hydrogen bonded. Considering our NMR and nanoindentation results from the same a-CN_x material, the most consistent bonding model is an aromatic carbon structure with nitrogen bonded in heterocyclic rings. The similarity of the ^{15}N chemical shifts in graphitic C_3N_4 and in hard and elastic a-CN_x suggests that the same single-atom vacancy defects may occur in a-CN_x. This is consistent with x-ray photoelectron spectroscopy (XPS) chemical-shift calculations of $C_{11}N_4$, which has a vacancy defect structure.[25] Our experimental ^{15}N data are also consistent with nitrogen bonded in a pyrrole-like configuration. Thus, we propose a film-structure model with nitrogen incorporated on the perimeter of vacancy-defect

structures and in pentagons. The incorporation of pentagons would account for the buckling of the graphitic layers—a proposal consistent with both transmission electron microscopy and computational work.[1] In Chapter 10, we explore the plausibility of this sort of film-structure model with Hartree-Fock, total-energy calculations.

9.5 References

1 H. Sjöström, S. Stafström, M. Boman, and J. E. Sundgren, Phys. Rev. Lett. 75, 1336 (1995).

2 H. Sjöström, L. Hultman, J. E. Sundgren, S. V. Hainsworth, T. F. Page, and G. Theunissen, J. Vac. Sci. Technol. A 14, 56 (1996).

3 N. Hellgren, M. P. Johansson, E. Broitman, L. Hultman, and J. E. Sundgren, Phys. Rev. B 59, 5162 (1999).

4 B. C. Holloway, O. Kraft, D. K. Shuh, M. A. Kelly, W. D. Nix, P. Pianetta, and S. Hagstrom, Appl. Phys. Lett. 74, 3290 (1999).

5 B. C. Holloway, O. Kraft, D. K. Shuh, W. D. Nix, M. Kelly, P. Pianetta, and S. Hagstrom, J. Vac. Sci. Technol. A 18, 2964 (2000).

6 A. Johansson and S. Stafström, J. Chem. Phys. 111, 3203 (1999).

7 L. Wan and R. F. Egerton, Thin Solid Films 279, 34 (1996).

8 C. Spaeth, M. Kuhn, F. Richter, U. Falke, M. Hietschold, R. Kilper, and U. Kreissig, Diamond Relat. Mater. 7, 1727 (1998).

9 W. T. Zheng, W. X. Yu, H. B. Li, Y. M. Wang, P. J. Cao, Z. S. Jin, E. Broitman, and J. E. Sundgren, Diamond Relat. Mater. 9, 1790 (2000).

10 J. Hu, P. Yang, and C. M. Lieber, Phys. Rev. B 57, R3185 (1998).

11 L. Dong, C. Yip-Wah, Y. Shengtian, W. Ming-Show, F. Adibi, and W. D. Sproul, J. Vac. Sci. Technol. A 12, 1470 (1994).

12 J. LaManna, J. Braddock-Wilking, S. H. Lin, and B. J. Feldman, Solid State Commun. 109, 573 (1999).

13 S. H. Lin, J. Braddock-Wilking, and B. J. Feldman, Solid State Commun. 114, 193 (2000).

14 J. C. Sanchez-Lopez, C. Donnet, F. Lefebvre, C. Fernandez-Ramos, and A. Fernandez, J. Appl. Phys. 90, 675 (2001).

15 E. Broitman, N. Hellgren, O. Wanstrand, M. P. Johansson, T. Berlind, H. Sjöström, J. E. Sundgren, M. Larsson, and L. Hultman, Wear 248, 64 (2001).

16 N. Hellgren, M. P. Johansson, B. Hjorvarsson, E. Broitman, M. Ostblom, B. Liedberg, L. Hultman, and J. E. Sundgren, J. Vac. Sci. Technol. A 18, 2349 (2000).

17 D. E. Leydon and R. H. Cox, *Analytical Applications of NMR*, Vol. 48 (Wiley, New York, 1977).

18 S. J. Lang, J. Magn. Reson., Ser. A 104, 345 (1993).

19   B. Yong, K. Hsien-Ming, C. P. Grey, L. Chopin, and T. Gullion, J. Magn. Reson. **133**, 104 (1998).

20   X. Wu and K. W. Zilm, J. Magn. Reson., Ser A **102**, 205 (1993).

21   E. O. Stejskal and J. D. Memory, *High Resolution NMR in the Solid State* (Oxford, New York, 1994).

22   Y. Yoon, B. G. Pfrommer, F. Mauri, and S. G. Louie, Phy. Rev. Lett. **80**, 3388 (1998).

23   G. C. Levy and R. L. Lichter, *Nitrogen-15 Nuclear Magnetic Resonance Spectroscopy* (Wiley, New York, 1979).

24   T. M. Duncan, *A Compilation of Chemical Shift Anisotropies* (Farragut Press, Madison, WI, 1990).

25   A. Snis and S. F. Matar, Phys. Rev. B **60**, 10855 (1999).

Chapter 10—Computational Results

In this chapter, a possible film-structure model for amorphous carbon nitride (a-CN_x) is presented. We propose a structure consisting of buckled, graphitic layers that are cross-linked together by sp^2-hybridized carbons. The curvature and cross-linking of the layers are attributed to a compound defect, which is formed by placing a pentagon next to a single-atom vacancy in a graphite layer. This proposed film structure is dubbed the pentagon-with-vacancy-defect (5VD) model and is supported by our theoretical calculations. More importantly, the 5VD film-structure model is compatible with both experimental x-ray photoelectron spectroscopy (XPS) and nuclear magnetic resonance (NMR) results, which were presented in Chapters 8 and 9, respectively.

10.1 Background

Previous transmission electron microscopy (TEM) work on hard and elastic a-CN_x films gave evidence of a microstructure consisting of buckled planes that are cross-linked together.[1-3] Sjöström et al. attributed the curvature of the basal planes to pentagon-inclusion and the cross-linking between planes to sp^3 carbons. They supported their conjecture with experimental XPS measurements [1] and computational modeling.[1,4] Using semi-empirical calculations at the AM1 level, their results indicated that the formation energy of a pentagon is lowered by substituting nitrogen at a pentagon vertex.[1]

188

The results of Sjöström *et al.* are referenced several times in later discussion;[1] therefore, their results are summarized in Figure 10.1. Differences in total energies were compared between clusters with the same stoichiometry.

E(B1,A1): The energy difference between Structures B1 and A1, *E(B1,A1)*, is 3.20 eV; this value indicates the energy cost for putting a pentagon in a graphene segment. These structures ($C_{24}H_{12}$) do not contain nitrogen.

E(B2,A2): The Structures A2 and B2 ($C_{22}H_{12}N_2$) are formed by placing nitrogens (blue spheres) at sites labeled x and x' (see Structures A1 and B1). The energy difference *E(B2,A2)* is 3.07 eV and is very similar to *E(B1,A1)*. The pentagon-formation energy is practically unaltered by placing nitrogens at sites outside the pentagon.

E(B3,A3): In structures A3 and B3, the nitrogens are located at sites x' and y. The y-site in Structure B3 is located at a pentagon vertex. The energy difference is reduced to *E(B3,A3)* = 2.33 eV. Placing a nitrogen in the pentagon reduces its formation energy by ~ 0.8 eV.

E(B4,A4): In Structures A4 and B4, the nitrogens are positioned at sites y and y'; both of these sites in Structure B4 are at pentagon vertices. The energy difference between the two structures, *E(B4,A4)*, is 2.06 eV. Placing nitrogen at two pentagon-vertices lowers the pentagon-formation energy by ~ 1.0 eV.

Collectively, these calculations (Figure 10.1) infer that pentagon formation is more likely in a-CN_x films than in pure carbon films.

The presence of pentagons is also supported by our ^{15}N NMR studies, which indicate pyrrole-like nitrogens are in a-CN_x. However, Sjöström *et al.*'s proposal that

$$E(B_j, A_j) = E_{Bj} - E_{Aj}$$

Structure

Structure
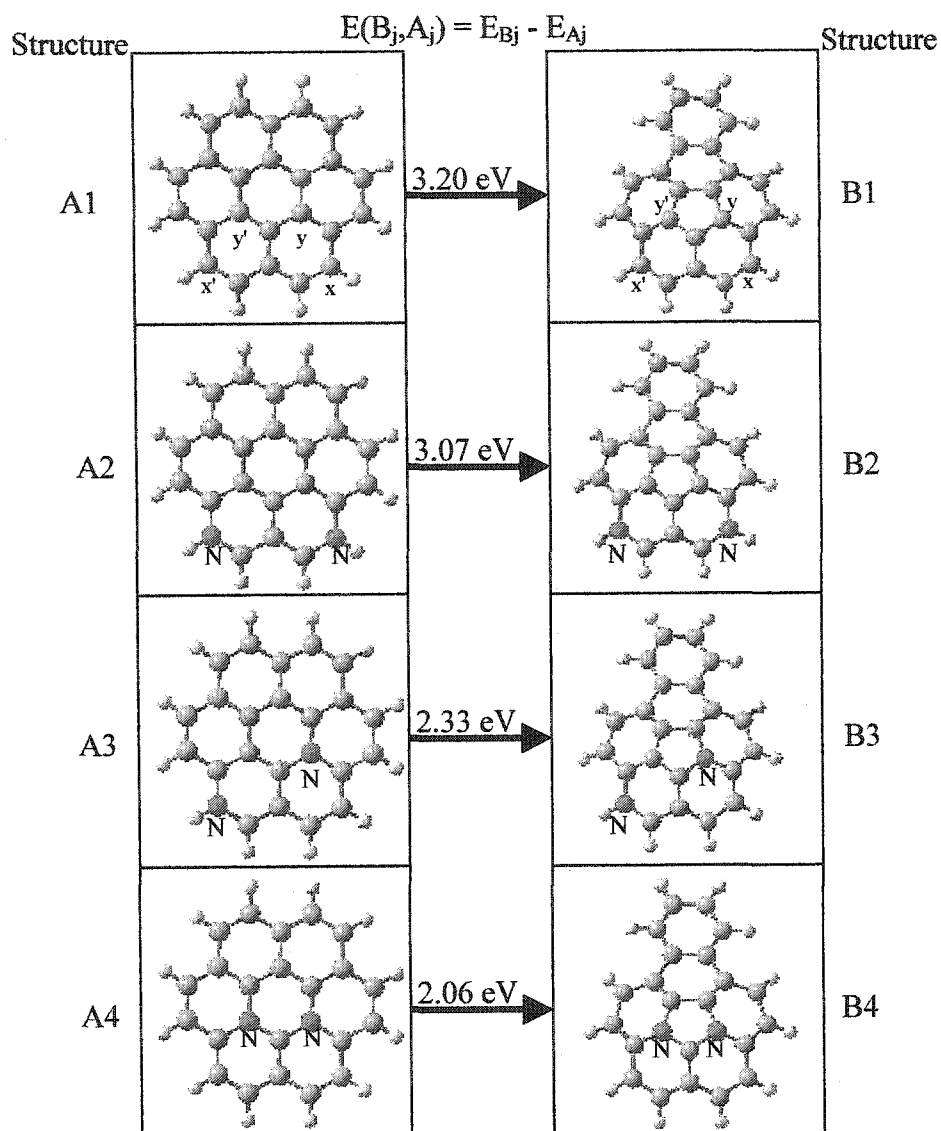
Figure 10.1: Results from total-energy calculations on the series of clusters examined by Sjöström et al.[1] These results are from semi-empirical, AM1 calculations. Comparison of differences between total energies suggests that the formation energy of a pentagon is lowered by substituting nitrogen at pentagon vertices.

cross-linking between basal planes is due to sp^3-hybridized carbon [1] is not supported by our ^{13}C NMR data. Our NMR data demonstrate that sp^3-bonded carbons are absent in a-CN_x films (see Chapter 9). Therefore, film-structure models that incorporate sp^3 carbons will not be considered further. The results that were discussed so far suggest a film-structure consisting of graphitic planes with substituted nitrogens and pentagons. However, the model is still missing two essential ingredients: a defect structure that accommodates pyridine-like nitrogen and a cross-linking mechanism. (Recall that both our ^{15}N NMR and N(1s) XPS data infer the presence of pyridine-like nitrogen.) These issues are considered next.

Dos Santos and Alvarez examined a series of carbon clusters with substituted nitrogen using a semi-empirical, PM3 method.[5] Their results indicated that when the N/C ratio exceeds 0.20, the geometry of a graphene segment changes from planar to slightly wrinkled. At high nitrogen concentration some of the substituted nitrogens are displaced above and below the plane of the cluster by $\sim$ 0.7 Å.[5] Using a valence-effective-Hamiltonian method, they related the disruption in geometry to the localization of electrons in nitrogen lone pairs.[5] The corrugated planes contained nitrogen in two bonding configurations: 1) nitrogen that contributes two electrons to the π system; and 2) nitrogen with a lone pair. When the N/C ratio exceeds 0.20, the formation of lone pairs becomes energetically favorable and causes a corrugated geometry. The nitrogens with lone pairs have three σ bonds, similar to amines. However, our ^{15}N NMR results indicate that the presence of amine configurations is small in a-CN_x (see Chapter 9). In addition, our ^{15}N NMR data demonstrate that nitrogen bonding in a-CN_x is not completely described by simple substitutional sites in a graphene segment—sites that are threefold

coordinated. Both N(1s) XPS and ^{15}N NMR data indicate the presence of pyridine-like nitrogen—two-fold coordinated nitrogen.

A single-atom vacancy in a graphitic sheet can account for a pyridine-like bonding configuration by placing nitrogens at sites on the vacancy-perimeter with only two nearest neighbors. Furthermore, the geometry instability, described by Dos Santos and Alvarez, is circumvented by the inclusion of vacancy defects in a-CN$_x$. For example, consider the calculated geometry of graphitic C$_3$N$_4$, which consists of planar layers with nitrogens positioned at sites on the edge of a single-atom vacancy (see Figure 9.9).[6] The N/C ratio of graphitic C$_3$N$_4$ is nearly seven times greater than Dos Santos and Alvarez's threshold for corrugation. Furthermore, XPS chemical-shift calculations by Snis and Matar [7] also support the inclusion of single-atom vacancies in a-CN$_x$. Their calculations show that the two non-equivalent nitrogen sites on the perimeter of a vacancy have an XPS chemical shift in agreement with the two dominant components found in the N(1s) spectra of a-CN$_x$ (see Figure 8.6). Collectively, these results suggest that a reasonable film-structure model must also include vacancy defects. The presence of vacancies is consistent with our experimental observation of pyridine-like nitrogen in a-CN$_x$, as inferred from both XPS and ^{15}N NMR data.

All the evidence indicates that the graphitic planes in a-CN$_x$ have both pentagons and vacancy defects. Therefore, we propose that the curvature and cross-linking of the basal planes are attributed to a type of compound defect that is formed by placing a pentagon next to a single-atom vacancy. As before, we refer to this structure as a pentagon-with-vacancy-defect (5VD). Cross-linking is proposed to occur at the twofold-coordinated pentagon-vertex, which lies on the vacancy's perimeter. Carbons at these

sites are proposed to form sp^2-hybridized cross-links between adjacent *planes*—see Figures 10.6 and 10.7. The chemical bonding of a-CN$_x$, as inferred from our XPS and NMR measurements, is consistent with the 5VD model.

In this chapter, we show that the 5VD model is also supported by theoretical calculations. Unless otherwise noted, our computational results were first obtained at the UHF/STO-3G//UHF/STO-3G level of theory. Then, we performed a second set of calculations at the UHF/3-21G//UHF/3-21G level. The UHF/STO-3G geometry was used as the starting geometry for the second set of calculations. (Computational details are given in Chapter 6.) All clusters are hydrogen terminated.

Since the STO-3G basis set is minimal basis set, total energies computed with this basis are not accurate. However, comparison between systems, which are computed at the same level of theory with the STO-3G basis, can be expected to elucidate semi-quantitative trends. Larger basis sets provide a better mathematical description of the total electronic wave function. Thus, our comparison between calculations that were obtained using the STO-3G basis with those using the larger 3-21G basis provides an indication of the validity of our trends. In this study, our objective is to establish these trends and to motivate future work. Here, we establish a plausible model for film structure.

10.2 Results

Comparison of Various Computational Methods

We have repeated the calculations by Sjöström et al. on Structures A1 and A2. In Figure 10.2, results are shown that were obtained using the semi-empirical, unrestricted AM1 (UAM1) method, specifically UAM1//UAM1. We have obtained: E(B1,A1) = 3.54

Structure A1

Structure B1

$$E(B1,A1) = E_{B1} - E_{A1}$$
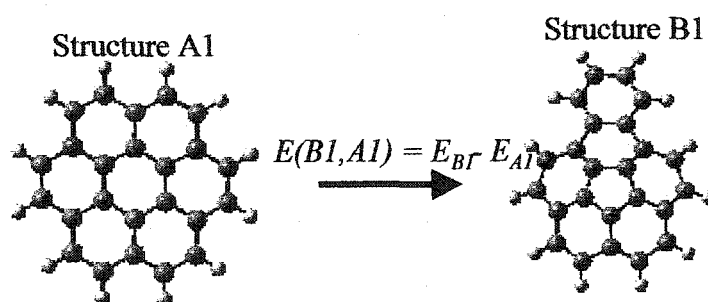
E(B1,A1)	Level of Theory
3.54 eV	UAM1//UAM1
4.23 eV	UHF/STO-3G//UHF/STO-3G
3.67 eV	UHF/3-21G//UHF/3-21G
3.55 eV	UHF/6-31G(d)//UHF/3-21G

Level of Theory	EA1 (Hartrees)	EB1 (Hartrees)
UHF/STO-3G//UHF/STO-3G	-904.9670	-904.8116
UHF/3-21G//UHF/3-21G	-910.8745	-910.7397
UHF/6-31G(d)//UHF/3-21G	-916.0054	-915.8749

Figure 10.2: The results indicate the cost of pentagon formation in carbon clusters, as computed from various methods. Total-energy differences that are computed with the STO-3G basis set overestimate the pentagon-formation energy.

eV, which is in close agreement to their value (see Figure 10.1). We compare this result with *ab initio* Hartree-Fock calculations at various levels of theory, also shown in Figure 10.2. At the UHF/STO-3G//UHF/STO-3G level of theory, we obtain 4.23 eV, which is ~ 0.7 eV higher. As the level of theory is increased, the computed cost of pentagon formation in these structures decreases. In particular, we obtain 3.55 eV at the level of UHF/6-31G//UHF/3-21G, which agrees identically with the semi-empirical method. The

results show that the cost of pentagon inclusion as calculated with the STO-3G basis is too high, which may be due to the small size of the basis set. Moreover, the UHF/3-21G//UHF/3-21G result seems to be adequate.

The agreement of *ab initio* with semi-empirical calculations as the level theory increases may be fortuitous. Our result indicates that semi-empirical, AM1 calculations provide a reasonable estimate of pentagon-formation energy in a pure carbon clusters. To prove the validity of the AM1 method for nitrogen containing clusters, a similar comparison with other structures in Figure 10.1 would have to be made. Such a comparison was not made due to limitations in computer time.

Influence of Pentagon-Formation Energy on Nitrogen Placement

Clusters with a pentagon defect and two nitrogens—placed at strategic sites—are shown in Figure 10.3. For reference, the total energies in Hartrees are displayed in Table 10.1; the conversion between Hartrees and electrons volts (eV) is

$$1 \text{ Hartree} = 27.2116 \text{ eV}.$$

Comparison of total energies (Table 10.1) demonstrates that nitrogen prefers substitutional sites in the pentagon. Results from both the UHF/3-21G//UHF/3-21G and the UHF/STO-3G//UHF/STO-3G methods are found in Figure 10.3 and Table 10.1. The UHF/STO-3G//UHF/STO-3G values are in parentheses.

E(P2,P1): In Structure P1, the nitrogens are positioned at sites 1 and 2, away from the pentagon. Structure P2 is similar but with nitrogens at sites 1 and 3; site 3 is a vertex in the pentagon. The energy difference between these configurations is *E(P2,P1)* = -1.17 eV (-1.62 eV).

Structure P1

Structure P4

$E(P4,P1) =$
-0.68 eV

(-1.90 eV)

$E(P2,P1) = -1.17$ eV
(-1.62 eV)

$E(P3,P1) = -1.71$ eV

(-2.85 eV)

$E(P3,P2) =$
-0.54 eV

(-1.23 eV)

Structure P2

Structure P3
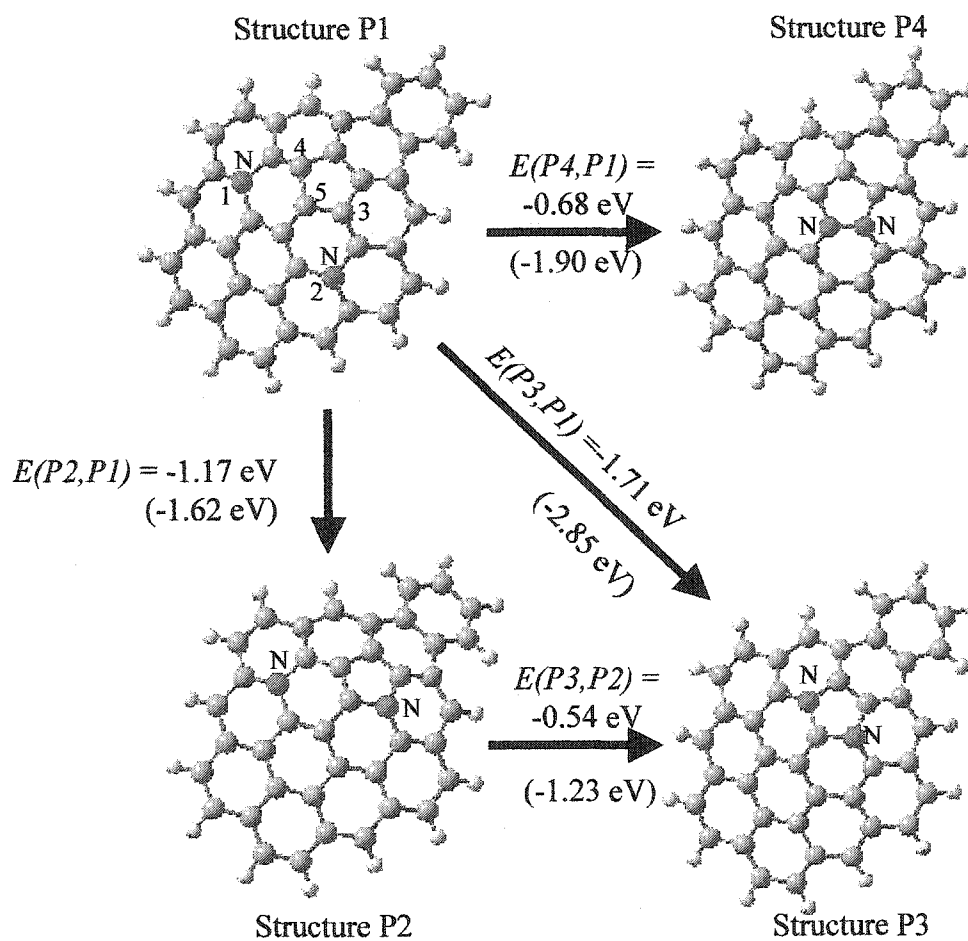
Figure 10.3: The total energies among these clusters are compared as a function of nitrogen placement in the cluster. Results from both UHF/3-21G//UHF/3-21G and UHF/STO-3G// UHF/STO-3G are shown. The values obtained with the STO-3G basis set are in parentheses. This comparison demonstrates that nitrogen prefers to reside at sites in the pentagon. This result suggests that nitrogen substitution at pentagon vertices lowers the pentagon's formation energy.

Table. 10.1: The total energies and stoichiometries of the clusters shown in Figure 10.3. The energies were calculated at both the UHF/3-21G//UHF/3-21G and UHF/STO-3G// UHF/STO-3G (values in parentheses).

Structure	Energy (Hartrees)	Stoichiometry
P1	-1623.8936 (-1613.2707)	$C_{40}H_{16}N_2$
P2	-1623.9366 (-1613.3304)	$C_{40}H_{16}N_2$
P3	-1623.9565 (-1613.3755)	$C_{40}H_{16}N_2$
P4	-1623.9187 (-1613.3406)	$C_{40}H_{16}N_2$

E(P3,P1): Structure P3 is formed by positioning both nitrogens at pentagon vertices: sites 3 and 4. Placement of both nitrogens in the pentagon stabilizes the cluster: $E(P3,P1) = -1.71$ eV $(-2.85$ eV$)$.

E(P4,P1): Structure P4 is formed by placing both nitrogens as nearest neighbors at pentagon sites. Despite the direct N-N bonding, the total energy of the cluster is reduced: $E(P4,P1) = -0.68$ eV $(-1.90$ eV$)$. The N-N bond distance is 1.46 Å (1.49 Å). These results are consistent with previous computations by Sjöström et al. (Figure 10.1), which suggests the validity of our computational method. Moreover, the magnitude of the energy differences $E(Pi,Pj)$ that are computed with the STO-3G basis set is always higher, which is consistent with the result in Figure 10.2.

Pentagon and Vacancy Defects in Graphene Clusters

Calculations on a series of carbon clusters (all hydrogen terminated), using the UHF/3-21G//UHF/3-21G and the UHF/STO-3G//UHF/STO-3G methods, are shown in Figure 10.4. For reference, the total energies and stoichiometries of the various clusters in Figures 10.4 are presented in Table 10.2. Results obtained with the STO-3G basis are in parentheses. For reference purposes, we give the average C-C bond distance in Structure 1: 1.41 Å (1.43 Å). The total energy differences are compared among the four configurations (Figure 10.4).

E(3,1): The energy difference between Structure 3 and Structure 1 provides an indication of the energy cost to place a pentagon in a graphene cluster; this difference is given by $E(3,1) = 4.37$ eV (4.78 eV).

E(2+C,1): The *v*-site carbon is removed from Structure 1 to form a vacancy defect (Structure 2). The binding energy of the displaced carbon is $E(2+C,1) = 13.51$ eV (15.73 eV).

E(4+C,3): The *v*-site carbon is removed from Structure 3 to form a 5VD (Structure 4): $E(4+C,3) = 12.38$ eV (14.37 eV).

E(4,2): The energy of Structure 2 (with a single-atom vacancy) is compared to Structure 4 (with a 5VD): $E(4,2) = 3.24$ eV (3.41 eV).

Comparison among results with the 3-21G and STO-3G basis sets shows that the all energy differences computed with the STO-3G basis are higher. We attribute this to the small size of the STO-3G basis set (see results Figure 10.2).

By replacing the carbons at sites labeled *x*, *y*, and *z* (see Figure 10.4) with nitrogens, an analogous set of calculations was carried out. These four configurations are displayed

in Figure 10.5 (the nitrogen sites, blue spheres, are now labeled *Na*, *Nb*, and *Nc*). For future reference, the *Na* site in Structure 8 at the pentagon-vertex is labeled *p*. The total energies and stoichiometries of these clusters are listed in Table 10.2.

E(7,5): The energy difference between Structure 7 and Structure 5 is given by *E(7,5)* = 1.34 eV (3.74 eV).

E(6+C,5): A vacancy defect (Structure 6) was formed by removing the *v*-site carbon in Structure 5; the binding energy of this carbon is *E(6+C,5)* = 3.08 eV (6.22 eV).

E(8,6): The energy difference between the vacancy structures (Structure 6 and 8) is given by *E(8,6)* = 3.83 eV (3.75 eV).

E(8+C,7): A 5VD (Structure 8) was formed from Structure 7 by removing the *v*-site carbon; this carbon's binding energy is *E(8+C,7)* = 5.57 eV (6.24 eV).

Comparison among these data (see Figures 10.4 and 10.5) suggests that the binding energy of the *v*-site carbon is reduced by at least a factor of ~2 by placing nitrogens at sites *x*, *y*, and *z*. We hypothesize that single-atom vacancy defects are stabilized by nitrogen placement at the twofold-coordinated sites on the vacancy's perimeter.

Film-Structure Model for a-CN$_x$

A model to explain cross-linking between buckled graphitic planes is shown in Figure 10.6. The two clusters (Structures CL1 and CL2) have the same stoichiometry, as shown in Table 10.3. The total energies were computed at both the UHF/3-21G//UHF/3-21G and UHF/STO-3G//UHF/STO-3G levels of theory. The UHF/STO-3G//UHF/STO-3G values are in parentheses. Structure CL1 is a planar structure with two nitrogens (blue
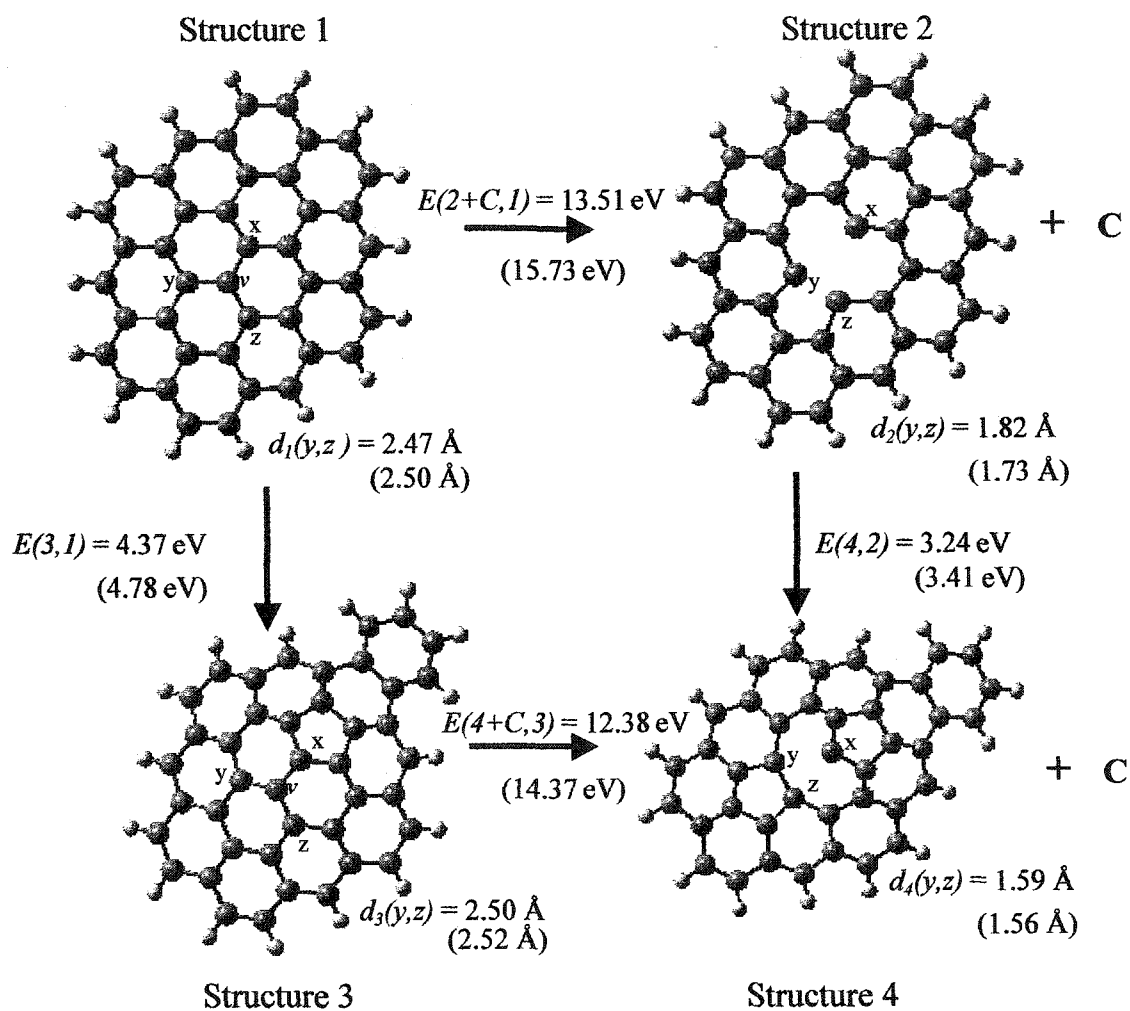
Figure. 10.4: A comparison of total energies among carbon containing clusters. Results are from both UHF/3-21G//UHF/3-21G and UHF/STO-3G//UHF/STO-3G calculations. The values from UHF/STO-3G//UHF/STO-3G calculations are in parentheses The $d_i(y,z)$ indicate the distance between carbons at sites y and z.
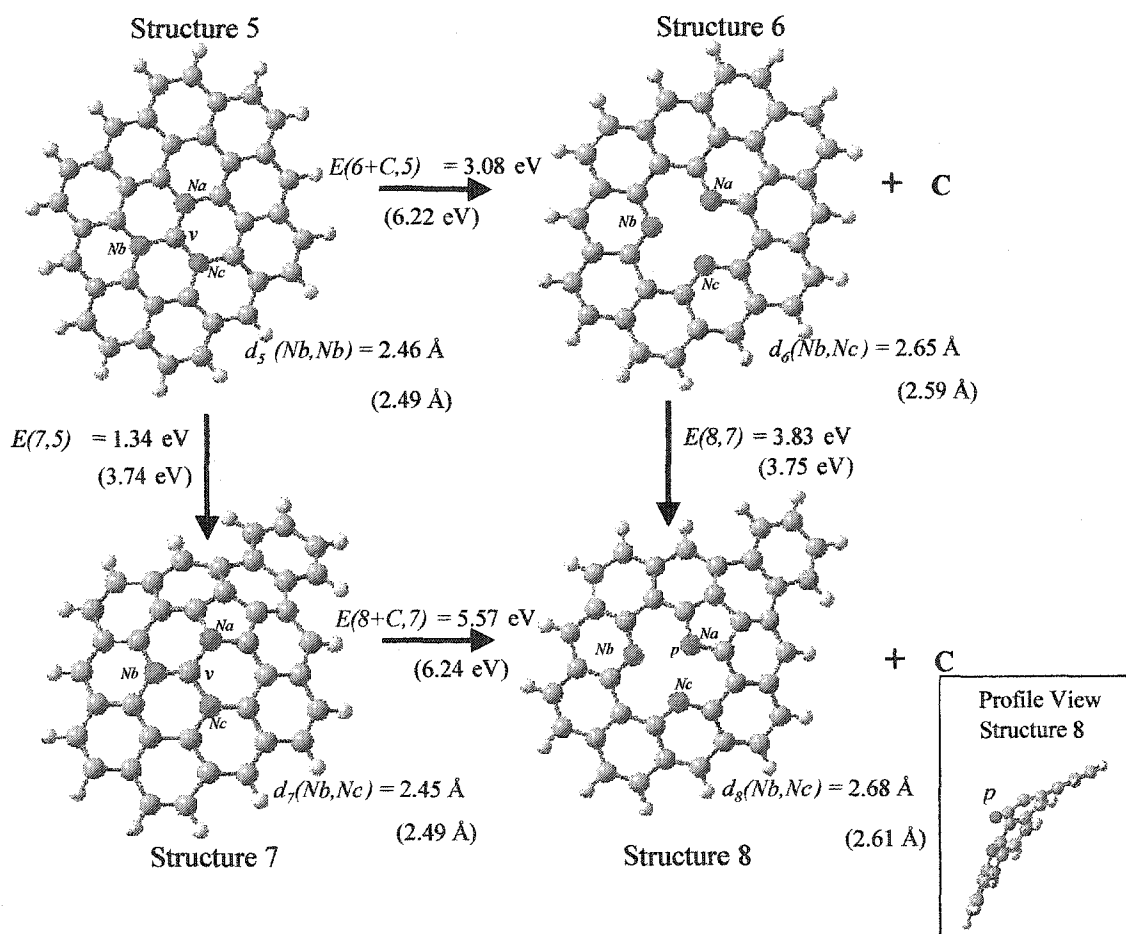
Figure 10.5: A comparison of total energies of carbon clusters with substituted nitrogens. These results suggest that vacancy defects are stabilized by substituting nitrogen at the twofold coordinated sites on the vacancy's perimeter. Results are from both UHF/3-21G//UHF/3-21G and UHF/STO-3G//UHF/STO-3G calculations. The values obtained with the STO-3G basis are in parentheses. The profile view of Structure 8 shows the p-site nitrogen protruding from the cluster. The $d_i(Nb,Nc)$ indicate the distance between nitrogens at sites Nb and Nc.

Table 10.2: The total energies and stoichiometries of the clusters shown in Figures 10.4-10.5. The energies were computed at both the UHF/3-21G//UHF/3-21G and the UHF/STO-3G//UHF/STO-3G levels of theory. Values listed in parentheses denote the UHF/STO-3G//UHF/STO-3G results.

Structure	Energy (Hartrees)	Stoichiometry
1	-1591.1959 (-1580.9115)	$C_{42}H_{16}$
2	-1553.2489 (-1543.1712)	$C_{41}H_{16}$
3	-1591.0352 (-1580.7360)	$C_{42}H_{16}$
4	-1553.1298 (-1543.0456)	$C_{41}H_{16}$
5	-1640.4291 (-1629.7442)	$C_{39}H_{16}N_3$
6	-1602.8655 (-1592.3536)	$C_{38}H_{16}N_3$
7	-1640.3800 (-1629.6069)	$C_{39}H_{16}N_3$
8	-1602.7247 (-1592.2156)	$C_{38}H_{16}N_3$
Carbon Atom	-37.4505 (-37.1621)	C
Nitrogen Atom	-54.0316 (-53.6368)	N
Hydrogen Atom	-0.4961 (-0.4666)	H

Table. 10.3: The total energies and stoichiometries of the clusters shown in Figure 10.6. Both UHF/3-21G//UHF/3-21G and UHF/STO-3G//UHF/STO-3G energies are shown; the UHF/STO-3G//UHF/STO-3G values are in parentheses.

Structure	Energy (Hartrees)	Stoichiometry
CL1	-2231.2135 (-2216.6571)	$C_{56}H_{24}N_2$
CL2	-2231.1725 (-2216.6277)	$C_{56}H_{24}N_2$

spheres, also labeled N) positioned next to the site labeled v. Formation of Structure CL2 from CL1 is envisioned by four steps:

1) Removal of the v-site carbon to form a vacancy; 2) incorporating a pentagon next to the vacancy, forming a 5VD structure; 3) cross-linking a phenyl group (C_6H_5) at the site labeled p (the p-site carbon in Structure CL2 is a pentagon vertex on the vacancy's perimeter); and 4) removal and rearrangement of carbons and hydrogens on the edge of Structure CL1 (to ensure stoichiometry is preserved).

Several perspectives of the cross-linked cluster (Structure CL2) are shown in Figure 10.7. The carbon sites labeled a and b (also indicated by red dots) are part of the phenyl group and serve as reference points. Comparison of the energies (Figure 10.6) suggests that incorporation of a 5VD structure with a cross-link in a graphene segment costs ~1.0 eV. Obviously, since the Structures CL1 and CL2 are different, edge effects will also contribute to this energy difference, but we did not explore this issue.

Structure CL1

1.10 eV
(0.80 eV)
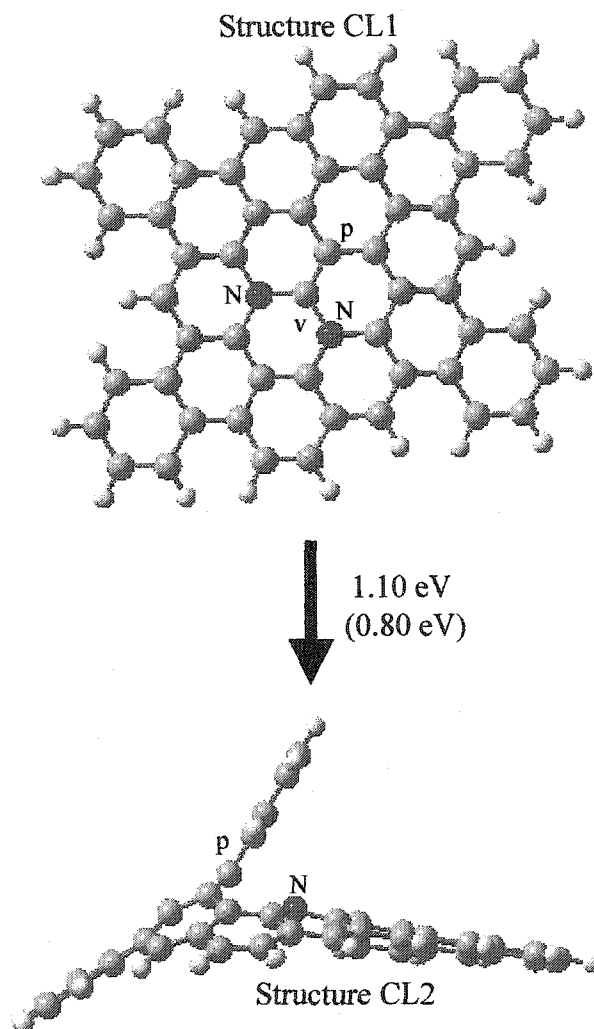
Structure CL2

Figure. 10.6: This comparison of total energies suggests that the formation of a 5VD structure with a cross-link costs ~ 1.0 eV. The total energies from UHF/3-21G//UHF/3-21G and the UHF/STO-3G//UHF/STO-3G calculations are shown for comparison. The UHF/STO-3G//UHF/STO-3G result is shown in parentheses. The nitrogens in Structure CL2 are substituted at twofold sites along the vacancy's perimeter. We propose that Structure CL2 may account for cross-linking between the basal planes in a-CN_x films.
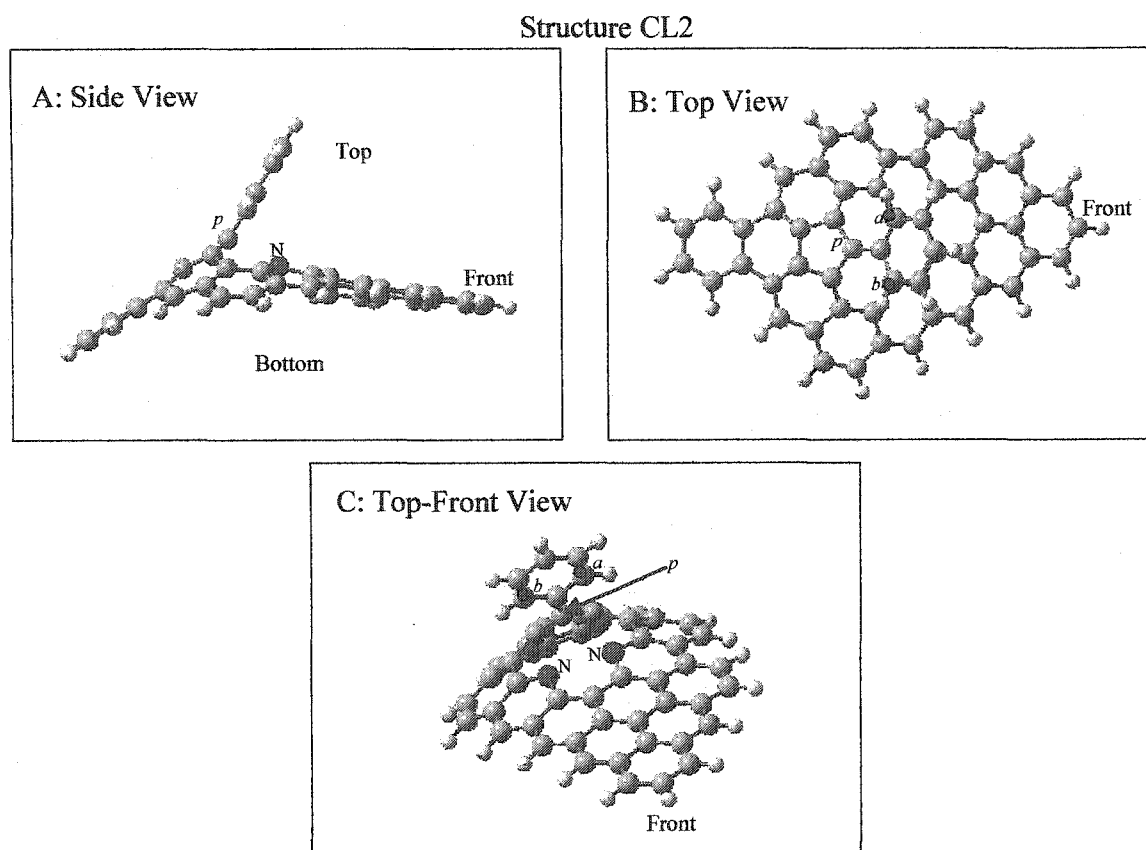
Structure CL2

Figure 10.7: Several perspectives of Structure CL2.

10.3 Discussion

In this study, we have computed the total energies of a variety of carbon clusters with and without nitrogen. Our comparison of energies at the UHF/3-21G//UHF/3-21G and UHF/STO-3G//UHF/STO-3G levels shows that the STO-3G basis set is capable of elucidating semi-quantitative trends in these systems. Overall, the UHF/3-21G//UHF/3-21G and UHF/STO-3G//UHF/STO-3G calculations indicate similar trends. Thus, in the remainder of this discussion, we will focus only on our UHF/3-21G//UHF/3-21G results.

Since the binding energy of the v-site carbon is notably reduced (compare Figure 10.4 with Figure 10.5), we infer that single-atom vacancies are stabilized by replacing the carbon at twofold-coordinated sites with nitrogen. Unfortunately, a direct way of comparing cohesive energies among clusters (Figures 10.4 and 10.5) is not available, since their stoichiometry (Table 10.2) and hydrogen termination vary. One possibility is to compare the cohesive energies per valence electron among these clusters. However, we made no attempt was made at such a comparison, since more expensive calculations with larger basis sets would be required to demonstrate the validity of this comparison. This is an intriguing prospect for future study.

Comparison of Figures 10.4 and 10.5 shows another interesting observation. The distance, $d(y,z)$, between carbons at sites y and z decreases from Structure 1 to 2 and from Structure 2 to 4 (Figure 10.4). Incorporating a vacancy in Structure 1 results in a contraction: $d_1(y,z) \sim 2.5$ Å shrinks to $d_2(x,z) \sim 1.8$ Å, which we assume is a mechanism to eliminate dangling bonds. Placing a pentagon next to the vacancy to form a 5VD structure (Structure 4), pinches the carbon sites closer together: $d_4(y,z) = 1.6$ Å. This contraction of bond distance may explain the lower pentagon formation energy in Structure 2 as compared to Structure 1 (compare $E(3,1) = 4.37$ eV with $E(4,2) = 3.24$ eV). The pentagon in Structure 4 squeezes the carbon sites y and z together, which allows bond formation between sites y and z, thus lowering the cost of pentagon incorporation. In contrast, this contraction in bond distance is unobserved for the nitrogen-containing clusters in Figure 10.5; in fact, an opposite effect is observed. The corresponding bond distances are now labeled $d(Nb,Nc)$. The increase in bond distance is attributed to repulsion among the nitrogen lone pairs (Structures 6 and 8).

The series of calculations, shown in Figure 10.3, agree with the results by Sjöström *et al.* that the formation energy of a pentagon is lowered by nitrogen incorporation.[1] Next, consider the energy difference between Structures 1 and 3 (Figure 10.4). *E(3,1)* suggests that the cost of incorporating a pentagon in Structure 1 is ~ 4.4 eV. Calculations by Sjöström *et al.*[1] indicate that this formation energy is nearly independent of nitrogen substitution at sites outside the pentagon (see Figure 10.1). Assuming their result is basically correct, the energy difference *E(P3,P1)* demonstrates that the pentagon with two nitrogens (Structure P3 in Figure 10.3) is stabilized by ~ 1.7 eV; this implies a pentagon-formation energy of ~ 2.7 eV in Structure P3. Interestingly, pentagons with two nitrogens with direct N-N bonding are further stabilized by ~ 0.7 eV. However, in almost all work on a-CN_x, the possibility of N-N bonding is ignored. It is commonly assumed that the N-N bonds that form during the deposition process are immediately desorbed as molecular N_2.[8] Therefore, N-N bonding is not considered any further.

From the above discussion, our computational results suggest a film-structure model for a-CN_x that contains both pentagons and vacancy defects. The stabilization of single-atom vacancies by nitrogens that are positioned at twofold-coordinated sites along the vacancy's perimeter is consistent with our experimental results. Both our XPS and NMR data are consistent with the presence of pyridine-like nitrogen. However, single-atom vacancies do not account for the curvature in the graphitic layers in a-CN_x, as inferred from TEM data.[1] Buckling of the graphitic layers in a-CN_x can be readily accounted for by pentagon incorporation. A conjecture supported by both computational work and our ^{15}N NMR data. Using semi-empirical, AM1 calculations, Sjöström *et al.* showed that the pentagon-formation energy in carbon-nitride systems is lower.[1]

Nitrogens placed at pentagon vertices substantially lower the formation energy. Our calculations are consistent with this result (Figure 10.3). In addition, incorporation of pentagons in a-CN_x may account for the presence of pyrrole-like nitrogen as inferred from our ^{15}N NMR results. Thus, a film-structure model with single-atom vacancies and pentagons would account for the presence of pyridine-like nitrogen, as well as buckling. Both of these features are accounted for by Structure 8 (Figure 10.5). By placing a pentagon next to the vacancy, a 5VD structure is formed (Structure 8). However, cross-linking between the buckled layers is still not accounted for.

By examining the geometry of Structure 8, a mechanism for cross-linking is readily suggested. In particular, note the profile view shown in the inset on Figure 10.5. The nitrogen site at the pentagon vertex (site labeled p in Structure 8) is at a point of high curvature and is the highest point protruding out of the cluster. Consider the replacement of the p-site nitrogen with a carbon; this configuration would allow the formation of sp^2 carbon cross-links between basal planes (corresponding cross-links with nitrogen were not considered in this study). The geometry of a cluster with a 5VD structure motivates the calculations shown in Figure 10.6; these results indicate that the formation energy of a 5VD with a cross-link is ~ 1.0 eV. We compare this value with the formation energy of a pentagon with nitrogens at two vertices (Structure P3 in Figure 10.3), which is estimated to be ~ 2.7 eV (see above). Interestingly, these calculations (Figure 10.3) suggest that the formation energy of the 5VD structure with cross-linking may be further lowered by incorporating nitrogen in the pentagon; this possibility will be explored in future study. In summary, our total energy calculations confirm the plausibility of a 5VD, film-structure model.

10.4 Conclusions

The 5VD, film-structure model is consistent with both our XPS (Chapter 8) and NMR (Chapter 9) measurements. In this model, pentagon incorporation next to a vacancy accounts for both buckling of the basal planes and cross-linking between them by sp^2 carbons. Our calculations demonstrate that a pentagon with a nitrogen substituted at its vertex has a lower formation energy; this result is consistent with earlier work by Sjöström et al.[1] In addition, cross-links by sp^2 carbons are suggested, since ^{13}C NMR experiments confirm sp^3 carbons are absent. The 5VD model also allows for the incorporation of pyridine-like nitrogen—consistent with both XPS and ^{15}N NMR measurements. Calculations suggest that a single-atom vacancy is stabilized by replacing the twofold-coordinated carbons with nitrogen to form pyridine-like nitrogen sites. Furthermore, ^{15}N NMR measurements also suggest the presence of pyrrole-like nitrogens; placing nitrogens in pentagons may account for this configuration.

10.5 References

1   H. Sjöström, S. Stafström, M. Boman, and J. E. Sundgren, Phys. Rev. Lett. 75, 1336 (1995).

2   N. Hellgren, M. P. Johansson, E. Broitman, L. Hultman, and J. E. Sundgren, Phys. Rev. B 59, 5162 (1999).

3   J. Neidhardt, Z. Czigany, L. F. Brunell, and L. Hultman, J. Appl. Phys. 93, 3002 (2003).

4   A. Johansson and S. Stafström, J. Chem. Phys. 111, 3203 (1999).

5   M. C. dos Santos and F. Alvarez, Phys. Rev. B 58, 13918 (1998).

6   Y. Yoon, B. G. Pfrommer, F. Mauri, and S. G. Louie, Phys. Rev. Lett. 80, 3388 (1998).

7   A. Snis and S. F. Matar, Phys. Rev. B 60, 10855 (1999).

8   N. Hellgren, K. Macak, E. Broitman, M. P. Johansson, L. Hultman, and J. E. Sundgren, J. Appl. Phys. 88, 524 (2000).

Chapter 11—Summary

11.1 Summary

In this research, DC magnetron sputtering was used to fabricate amorphous, carbon-nitride (a-CN_x) films that are both hard and elastic. All films were deposited with a 99.999% pure graphite target in a pure nitrogen discharge (4-8 mTorr) on S(001) substrates. During deposition, the substrates were electrically grounded and heated to at least 300 °C. The chemical bonding in our a-CN_x films was characterized by x-ray photoelectron spectroscopy (XPS) and solid-state ^{13}C, ^{15}N, and ^{1}H nuclear magnetic resonance (NMR) spectroscopy. The differences in deposition conditions for our XPS and NMR studies were explained in Chapter 3. For the NMR study, the a-CN_x films were deposited on whole, 75-mm-diam., Si wafers study, since large substrate areas were required to fabricate enough material (~100mg) for NMR measurements. In addition, for the ^{15}N NMR measurements, the a-CN_x films were ^{15}N enriched by using an $^{14}N_2$/$^{15}N_2$ gas mixture during fabrication.

Justification of the growth conditions (Chapter 3) was provided by nanoindentation testing (Chapter 7). The hardness and elastic modulus of our films were determined by the Oliver-Pharr method,[1] which confirmed these films have a low elastic modulus and resist plastic deformation. Typically, these films exhibit a hardness of ~ 5 GPa and an elastic modulus in the range of 38-47 GPa. Furthermore, comparison of

indentations between center and edge of the 75-mm-diam., NMR films showed that the deposition process created material that is mechanically similar over the whole substrate area.

X-ray Photoelectron Spectroscopy Results

The results from our XPS study were presented in Chapter 8. The N(1s) spectra of a-CN$_x$ are dominated by two main components: one at low binding energy (N1) near 398.5 eV and the other at high binding energy (N2) near 400.6 eV. In an attempt to make assignments to these components, we compared the N(1s) XPS spectra of hard and elastic a-CN$_x$ films with the peak positions from a variety of reference compounds. Additionally, we compared the N(1s) XPS data with a variety of previously published experimental and computational results.

In early work, Sjöström *et al.* proposed that the component N1 was due to sp^3 nitrogen bonded to sp^3 carbons.[2] Their conjecture was supported by N(1s) XPS chemical-shift calculations by Johansson and Stafström.[3] Their interpretation was widely accepted in the literature, since sp^3 (diamond-like) carbon could be attributed to the improved mechanical hardness of a-CN$_x$. The important point is that the presence of sp^3 carbons was only indirectly inferred from N(1s) chemical-shift calculations. Direct measurement of the C(1s) spectra can not confirm this assignment, since the chemical shift between sp^2 and sp^3 carbons is too small to resolve. In our XPS study, we demonstrated that the assignment of N1 to nitrogen bonded to sp^3 carbons is inconclusive.

We offered an alternate interpretation for N1 that was based on a comparison of a-CN$_x$ data with reference N(1s) spectra. We showed that the N1 bonding configuration

could be equally as well explained by a pyridine-like configuration. Our assignment is consistent with Snis and Matar's computational work,[4] which indicated N1 may be due to pyridine-like nitrogen on the perimeter of a single-atom vacancy, as found in a graphite layer. It is emphasized that our XPS data do not dismiss the possibility of sp^3 carbons in a-CN_x films. Instead, we showed that the presence of sp^3 carbons could not be conclusively inferred from the N(1s) spectra. Our data showed that the spectral intensity of N1 could be due to a pyridine-like configuration, nitrogen bonded to sp^3 carbon, or a mixture of these two configurations. The ability to determine the relative fraction of sp^2 to sp^3 bonded carbons would allow us to determine which bonding configuration is the most appropriate to describe N1. This issue was addressed by our ^{13}C NMR study.

Furthermore, we demonstrated that unambiguous interpretation of the high-binding-energy component N2 is impossible by XPS analysis, since a variety of nitrogen configurations yield chemical shifts that are consistent with N2. Our experimental comparison with reference compounds suggested that N2 (400.6 eV) could be attributed to a nitrogen configuration as found in triphenylamine (399.9 eV). In contrast, XPS analyses of coals and chars by Pels et al.[5] offered another interpretation, which suggested that N2 might be due to nitrogen bonded in a pentagon, as in a pyrrole-like configuration. Another possibility is offered by the computational works of both Snis et al.[4] and Johansson et al.[3] These calculations suggested that N2 is due to threefold-coordinated sp^2 nitrogen to sp^2 carbons; nitrogen at a substitutional site in a graphite layer is an example of this configuration. Collectively all the available evidence indicates that N2 is limited to the following possibilities: an amine configuration (sp^3 N) or threefold coordinated sp^2 nitrogen in carbon rings.

Nuclear Magnetic Resonance Spectroscopy

The chemical bonding of our hard and elastic a-CN_x films was further examined with solid-state ^{13}C, ^{15}N, and ^{1}H NMR spectroscopy. NMR chemical shifts are more sensitive than XPS values and thus provide a better description of bonding. Our NMR study (Chapter 9) serves to remove the ambiguities from our XPS interpretation of possible bonding assignments in a-CN_x. For example, the NMR chemical shift between sp^2 and sp^3 bonded carbons is resolvable—unlike XPS.

The role of diamond-like (sp^3) carbon in a-CN_x is of paramount importance, since the sp^3-carbon component is commonly assumed to be associated with the hardness of carbon nitride. The primary objective of the ^{13}C NMR study was to determine the sp^3 carbon content, if any, in hard a-CN_x films. Our ^{13}C magic angle spinning (MAS) NMR measurements, as obtained by direct-detection, indicated a predominantly sp^2 carbon bonded structure. Unfortunately, the spinning side bands in the ^{13}C MAS direct-detection spectra partially obscured the region where sp^3 carbon bonded to carbon or nitrogen resonates (0-75 ppm; relative to TMS = 0ppm).[6] Thus, we used a total suppression of spinning side bands (TOSS) technique to eliminate the side bands. The TOSS measurements demonstrated the absence of sp^3 carbons in direct-detection spectra. In addition, cross polarization (CP) measurements showed that protonated sp^3 carbons are also absent. Thus, sp^3 carbons in C-C or C-N bonding configurations are absent in hard and elastic a-CN_x films.

Our ^{15}N NMR experiments indicated that nitrogen bonding in a-CN_x is predominantly sp^2 and incorporated in heterocyclic rings. We inferred these bonding configurations by comparing our experimental data to a variety of ^{15}N and ^{14}N reference

chemical-shifts data from organic compounds in liquids or solutions. Specifically, this comparison suggested that nitrogen bonding in a-CN_x is predominately in pyridine-like or pyrrole-like configurations. In addition, this comparison suggested that nitrogens in an amine configuration make up a small portion of the overall bonding.

Besides providing information on carbon and nitrogen bonding, the multinuclear NMR study gave insight into the nature and extent of hydrogen bonding in our material. Specifically, we demonstrated that proton decoupling has a negligible effect on the direct-detection ^{13}C spectra. Thus, it was inferred that the majority of carbons in a-CN_x are not directly bonded to protons. This conjecture was further supported by the low efficiency of ^{13}C CPMAS experiments.

In contrast to the ^{13}C NMR results, proton decoupling had a notable influence on the ^{15}N MAS direct-detection spectra near the feature at c.a. -295 ppm ($CH_3NO_2 = 0$ ppm)—see Chapter 9. The spectral feature at -295 ppm was considerably dephased without proton decoupling. Indeed, ^{15}N CPMAS measurements showed that this feature has a high cross-polarization efficiency, indicating that protonated nitrogens are associated with this feature. It is important to note that the other portions of the ^{15}N direct-detection spectra were either unaffected or at most slightly influenced by proton decoupling. These observations suggested that water adsorption during NMR sample preparation is the most likely source of proton contamination. This conjecture was supported by ^1H NMR experiments, which indicated water desorbtion during sample heating (150°C). Interestingly, our comparison between REAPDOR and ^{13}C CPMAS spectra suggested that those carbons that are protonated are also more likely to be directly bonded to nitrogen. This result was consistent with our observation that nitrogen sites

exhibit the highest level of protonation. Collectively, analysis of ^{15}N and ^{13}C CPMAS and ^{1}H NMR experiments indicated that our a-CN_x material has a very low hydrogen content and is hydrophilic; physi-absorbed water preferentially protonates nitrogen sites.

Development of a Film-Structure Model

Previous transmission electron microscopy (TEM) work on hard and elastic a-CN_x films suggested a microstructure consisting of a network of buckled graphitic segments that are cross-linked together.[2,7,8] This microstructure readily accounts for the hardness and high elasticity of a-CN_x films. The graphitic layers are consistent with the material's high elasticity, while the cross-linking between layers explains the material's resistance to permanent deformation (hardness). Early work by Sjöström and co-workers suggested that the curvature in the layers could be accounted for by pentagon incorporation.[2] They supported their conjecture of pentagon inclusion with semi-empirical, AM1 calculations, which indicated the formation energy of a pentagon in a planar, carbon cluster is substantially lowered by placing a nitrogen at a pentagon vertex. Their results indicated that the formation of pentagons is more likely in a-CN_x films than in pure carbon films. They concluded that nitrogen incorporation induces buckling, which is responsible for the intersection of the adjacent layers and therefore cross-linking. Sjöström et al. further conjectured that the cross-linking was due to sp^3 (diamond-like) bonded carbon.[2] XPS chemical shift calculations supported the presence of sp^3 carbons by indicating that the low binding energy component observed in the N(1s) spectra of a-CN_x was consistent with the chemical shift of sp^3 nitrogen bonded to sp^3 carbons.[2,3] The above film-structure model is reasonable and consistent with a variety of experimental

and computational data. However, in this research, our ^{13}C NMR study demonstrates that sp^3 carbons are absent and therefore do not account for cross-linking. Based on the chemical bonding assignments as inferred from our ^{15}N NMR and N(1s) XPS studies, we proposed a new film-structure model for a-CN$_x$.

The absence of sp^3 carbons in hard and elastic a-CN$_x$ supports our assignment of the low binding energy component (398.5 eV) in the N(1s) XPS spectra to pyridine-like nitrogen. Thus, both N(1s) XPS and ^{15}N NMR data indicated the presence of pyridine-like nitrogen. We proposed that a single-atom vacancy, as found in a graphite layer, accounts for the pyridine-like bonding configuration. Our conjecture was supported by both N(1s) XPS and ^{15}N NMR chemical-shift calculations.[4,9] Snis and Matar [4] have calculated the N(1s) XPS chemical shifts of the model compound C$_{11}$N$_4$. In their model, the two types of nitrogen sites in C$_{11}$N$_4$ are located on the perimeter of a single-atom vacancy; the nitrogens are positioned at either twofold or threefold coordinated sites to sp^2 carbon. The chemical shift between these two components is consistent with the core-level shift between the two main components in the N(1s) spectra of hard and elastic a-CN$_x$. Yoon et $al.$ have calculated the ^{15}N NMR chemical shifts of a variety of C$_3$N$_4$ phases.[9] Only the calculated ^{13}C and ^{15}N chemical shifts of the graphitic phase of C$_3$N$_4$ are coincident with the range covered by our experimental ^{13}C and ^{15}N NMR spectra. The two types of nitrogen sites in graphitic C$_3$N$_4$ are positioned on the perimeter of a single-atom vacancy: sp^2 nitrogen sites that are either twofold or threefold coordinated to sp^2 carbon. Our Hartree-Fock calculations, using both the STO-3G and 3-21G basis sets, added further support to the plausibility of single-atom vacancies in a-CN$_x$ films. Specifically, we showed that the energy cost (binding energy) to remove a carbon from a

graphitic layer, thus forming a vacancy, is substantially reduced by replacing carbons at twofold-coordinated sites with nitrogen (Chapter 10). Thus, we inferred that single-atom vacancies are stabilized by placing nitrogen at twofold-coordinated sites (pyridine-like nitrogen). Summarizing, we have presented a variety of experimental and computational data lending support to single-atom vacancy defects in a-CN_x films.

However, single-atom vacancies can not account for the curvature in the graphitic layers of a-CN_x, as inferred from TEM data.[2,7,8] As already mentioned, buckling of the graphitic layers can be readily accounted for by inclusion of pentagons.[2] This is a reasonable conjecture, since pentagons are responsible for the curvature in fullerenes. Furthermore, incorporation of pentagons in a-CN_x is consistent with presence of pyrrole-like nitrogen, as inferred from our ^{15}N NMR results. Moreover the conjecture of pentagon incorporation is consistent with computational work by Sjöström et al.[2] They showed that the pentagon-formation energy in a carbon-nitride system is lower; nitrogen placed at pentagon vertices lowers its formation energy. Our Hartree-Fock calculations are consistent with their result; we demonstrated that carbon clusters with nitrogen and a pentagon are stabilized by placing the nitrogen at pentagon vertices (Chapter 10).

We showed that a reasonable film-structure model for a-CN_x should include both single-atom vacancies and pentagons. A very simple structure to account for these features is obtained by placing a pentagon next to a single-atom vacancy in a graphitic cluster. We call such a structure a pentagon-with-vacancy defect (5VD). If a pentagon vertex occupies one of the twofold-coordinated sites on the vacancy's perimeter, a mechanism for cross-linking is readily suggested. In such a configuration, the twofold-coordinated site in the pentagon is at a point of high curvature (e.g., see Structure 8 in

Figure 10.5). It is anticipated that such a site is highly chemically reactive and provides a site for cross-linking between adjacent layers. To simulate an sp^2 carbon cross-link, we attached at phenyl ring to this site. Our Hartree-Fock calculations, with both the STO-3G and 3-21G basis sets, indicated that the formation energy of a 5VD with a cross-link is ~1.0 eV. To demonstrate the plausibility of this film-structure model, we compared this value with the formation energy of a pentagon with nitrogens at two vertices, which was estimated to be ~2.7 eV (Chapter 10). Our calculations demonstrated that a 5VD with cross-link is comparable to the cost of pentagon formation; therefore, confirming the plausibility of our film-structure model.

In summary, a film-structure model was proposed for hard and elastic a-CN$_x$. We attributed the curvature and cross-linking of the basal planes to a compound defect, a 5VD with cross-link. The 5VD, film-structure model is compatible with our experimental XPS and NMR data as well as nanoindentation results. The graphitic layers account for the high elasticity, while the cross-linking accounts for resistance to permanent deformation.

11.2 Future Work

There are several possible directions for future work. In particular, NMR techniques such as adiabatic-passage, Hartmann-Hahn, cross polarization (APHH-CP) may allow for an improvement in the confidence of making peak assignments as well as in resolving spectral components.[10, 11] For example, APHH polarization transfer from ^{15}N to ^{13}C (and acquiring the ^{13}C signal) would enable an improved correlation between the

observed ^{13}C chemical shift and the particular C-N bonding configuration associated with that site. Another possibility is isotopic enrichment of the ^{13}C spins; this would entail using an enriched carbon target during the film-fabrication process. The advantage of ^{13}C enrichment is obvious for future chemical bonding studies with NMR; less material would be required; thus, making it possible to fabricate several samples deposited under different conditions, which would enable a correlation between chemical bonding and process parameters. If the ^{13}C enrichment is high enough, one can envision doing NMR experiments on a-CN$_x$ with the film still bonded to the substrate. Careful annealing studies of these samples may allow for a correlation between NMR spectra and relaxation of compressive stress in the film. As the sample is annealed, the stress is relaxed and, perhaps, may be observed as a small change in NMR line-width (FWHM).

Lastly, in the course of work for this dissertation, several hundred milligrams of a-CN$_x$ powder were produced. What should be done with this material? The original interest in carbon nitride stemmed from Liu and Cohen's theoretical work on the hypothetical compound β-C$_3$N$_4$, which was predicted to be metastable, with a bulk modulus comparable to diamond.[12] The predicted low compressibility of β-C$_3$N$_4$ implied that its hardness may exceed that of diamond. Thus, it seems worthwhile to use the a-CN$_x$ powder as a precursor in an attempt of high-pressure synthesis of super-hard carbon nitride; experiments using a diamond micro-anvil might be suitable for this task.

11.2 References

1   W. C. Oliver and G. M. Pharr, J. Mater. Res. **7**, 1564 (1992).

2   H. Sjöström, S. Stafström, M. Boman, and J. E. Sundgren, Phys. Rev. Lett. **75**, 1336 (1995).

3   A. Johansson and S. Stafström, J. Chem. Phys. **111**, 3203 (1999).

4   A. Snis and S. F. Matar, Phys. Rev. B **60**, 10855 (1999).

5   J. R. Pels, F. Kapteijin, J. A. Moulijn, Q. Zhu, and K. M. Thomas, Carbon **33**, 1641 (1995).

6   D. E. Leydon and R. H. Cox, *Analytical Applications of NMR*, Vol. 48 (Wiley, New York, 1977).

7   N. Hellgren, M. P. Johansson, E. Broitman, L. Hultman, and J. E. Sundgren, Phys. Rev. B **59**, 5162 (1999).

8   J. Neidhardt, Z. Czigany, L. F. Brunell, and L. Hultman, J. Appl. Phys. **93**, 3002 (2003).

9   Y. Yoon, B. G. Pfrommer, F. Mauri, and S. G. Louie, Phys. Rev. Lett. **80**, 3388 (1998).

10   D. Rovnyak, M. Baldus, B. A. Itin, M. Bennati, A. Stevens, and R. G. Griffin, J. Phys. Chem. B **104**, 9817 (2000).

11   M. Baldus, D. G. Geurts, S. Hediger, and B. H. Meier, J. Magn. Reson., Ser. A, **118**, 140 (1996).

12   A. Y. Liu and M. L. Cohen, Science **245**, 84 (1989).

VITA

Wesley Jason Gammon

Born in Richmond, Virginia, September 29, 1971. Graduated from Lee Davis High School in June 1989; B.S. Chemistry, Virginia Commonwealth University, 1994; M.S. Physics; Virginia Commonwealth University, 1997. After completing his M.S., he worked at the Medical College of Virginia until enrolling in the Ph.D. program at the College of William & Mary in the fall of 1998. He completed his Ph.D. in Physics in 2003.